

Study on mechanical deterioration and structural response due to internal swelling reactions of concrete

(内部膨張反応によるコンクリートの力学的劣化と構造応答に関する研究)

Joshi Nirmal Raj

A Dissertation Submitted to
Saitama University
in Partial Fulfillment of the Requirements for
The Degree of Doctor of Philosophy

Supervisor
Associate Professor Shingo Asamoto

Graduate School of Science & Engineering
Saitama University
Saitama, Japan
September 2021

Abstract

In many countries, severe deterioration of concrete structures has been observed instigated by expansion related to alkali-silica reaction (ASR) and/or delayed ettringite formation (DEF). The past studies on ASR and DEF are mainly focused on the chemical and material aspects which have laid the ground for the formulation of various codes and guidelines. As a result, ASR and DEF can generally be avoided in the new construction. However, the safety and serviceability evaluation of the structures that have been infected remains dubious due to a lack of understanding of the mechanical behaviour of affected concrete. To address this gap of understanding, a study was initiated to carry out various laboratory experiments and numerical analysis related to change in the mechanical properties caused by expanding concrete.

In the first part of the study, experiments were done to understand the interaction between restraints and DEF/ASR expansion. The external restraint could reduce the expansion by up to 45% while at the same time, restraining steel experienced stress of up to 132 N/mm^2 . It was noticed that despite having a larger free expansion, the stress instigated by combined DEF and ASR (DA) expansion remained lower than due to DEF in restrained cases. Similar behaviour was found in reinforced concrete in which an internal restraint was provided by rebar. The rebar experienced a tensile strain of up to 0.05%, after which the strain gradually reduced indicating a deterioration of interface between concrete and rebar.

To check the change in the bond due to expansion, a pullout test was conducted. The pullout strength slightly improved when expansion was small which is ascribed to the pre-stressing effect caused by the confinement from shear and main rebars. The large expansion deteriorated the pullout strength to about 60% of the original. After an expansion of about 0.5%, there was no significant drop in the pullout strength even though the compressive strength was reduced to 20% which indicated that the pullout strength is not directly related to the compressive strength.

A small expansion in the ASR specimen improved the compressive strength. The dynamic Young's modulus, however, deteriorated even at small expansion. This indicated that even though there is an increase in load capacity, there could be a larger deflection of structure that is affected by ASR. DEF and DA specimens had a larger expansion, and such effects were not observed. Their bond and compressive strength decreased rapidly with expansion. The expanded concrete also showed a large plastic strain which was attributed to the closing of pre-existing gaps in the direction of loading by X-ray CT. The failure of the highly expanded concrete was caused by the opening of cracks in the direction perpendicular to the loading.

In the second part of the dissertation, a numerical modelling approach is proposed that can be used to evaluate the structural performance of expanding concrete. The model is a combination of Mazar's model of concrete damage and the time-dependent expansion model of Larvae. The expansion-dependent variables such as the peak strength and elastic modulus were treated as a Gaussian function. The numerical model was implemented in Code Aster for FEM analysis. The model was fairly accurate at the lower expansion but at larger expansion, there was some deviation. The model needs to be further calibrated and fine-tuned to get better results.

A numerical study was also done to highlight the effect of expansive concrete on the serviceability of a massive dam. This study is based on the work of previous researchers who had identified ASR expansion in the dam based on the petrographic analysis and had conducted a time-dependent FEM simulation. This study enhanced the previous study by incorporating probabilistic approaches for the prediction of dam deflection and stresses. A sensitivity analysis was also carried out to examine the effect of varying ultimate strain and time-dependent variables on dam behaviour. The maximum deflection was predicted to be 54–66 mm towards the upstream direction with a standard deviation of 28 mm at the age of 100 years. The principal stress distribution in the dam showed that it is predominantly in compression and safe against cracking at the current rate of reaction. It was predicted that some cracks may occur in the downstream face if the expansion continues.

Table of Contents

List of Figures.....	vii
List of Tables.....	xiii
List of abbreviations and symbols	xiv
1. Introduction	1
1.1. Background.....	1
1.2. Problem statement.....	3
1.3. Objectives of research.....	5
1.4. Dissertation outline	6
2. Literature review	8
2.1. A brief history of concrete deterioration	8
2.2. Alkali-silica reaction	9
2.2.1. Factors Influencing ASR.....	10
2.2.2. Test method for ASR.....	11
2.3. Mechanical effect of ASR expansion.....	12
2.3.1. Change in compressive strength.....	14
2.3.2. Change in tensile strength	16
2.3.3. Change in bond strength	16
2.3.4. Change in modulus of elasticity.....	17
2.3.5. Change in shear strength.....	18
2.3.6. Change in flexure strength.....	18
2.4. Delayed ettringite formation	18
2.4.1. Factors influencing DEF	19
2.4.2. Test methods for DEF	21
2.5. Mechanical effect of DEF expansion.....	22
2.5.1. Change in compressive strength.....	23
2.5.2. Change in tensile strength	24
2.5.3. Change in bond strength	24
2.5.4. Change of modulus of elasticity.....	24
2.5.5. Change in shear capacity.....	25
2.5.6. Change in flexure capacity.....	25
2.6. Combination of ASR and DEF.....	25
2.7. Evolution of damage and mechanical tests	26

2.8.	Numerical modelling of ASR and DEF	27
2.8.1.	Numerical modelling of ASR.....	27
2.8.2.	Model description	27
2.8.3.	Numerical modelling of DEF.....	29
3.	Effect of internal restraints on ASR/DEF expansion.....	34
3.1.	Background	34
3.2.	Methodology	34
3.2.1.	Specimen dimension	34
3.2.2.	Concrete	35
3.2.3.	Steel.....	37
3.2.4.	Heat treatment for DEF sample	37
3.2.5.	Measurement.....	38
3.2.6.	ASR detection	39
3.3.	Results.....	39
3.3.1.	Evolution of strain in concrete	39
3.3.2.	Evolution of strain in steel	40
3.3.3.	Evolution of mass gain.....	41
3.3.4.	Evolution of dynamic modulus of elasticity	41
3.3.5.	Evolution of cracks	42
3.3.6.	ASR distribution	43
3.4.	Discussion	44
3.4.1.	Expansion behaviour.....	44
3.4.2.	Effect of reinforcement in concrete expansion	44
3.4.3.	Relation between steel and concrete strains.....	45
3.4.4.	Effect of reinforcement in mass gain	47
3.5.	Summary	47
4.	Effect of external restraints on ASR/DEF expansion	48
4.1.	Background	48
4.2.	Methodology	48
4.2.1.	Specimen dimension	48
4.2.2.	Concrete	49
4.2.3.	Heat treatment for DEF sample	50
4.2.4.	Application of restraint	51

4.2.5.	Measurement.....	51
4.3.	Results.....	52
4.3.1.	Evolution of strain in the longitudinal direction.....	52
4.3.2.	Evolution of strain in the lateral direction.....	54
4.3.3.	Evolution of strain in retraining steel.....	54
4.3.4.	Evolution of cracks.....	55
4.4.	Discussion.....	56
4.4.1.	Expansion behaviour.....	56
4.4.2.	Interaction between external restraint and concrete expansion.....	57
4.4.3.	Strain from concrete and strain gauge.....	58
4.5.	Summary.....	60
5.	Evolution of bond and compressive strength due to ASR/DEF expansion.....	61
5.1.	Background.....	61
5.2.	Methodology.....	61
5.2.1.	Specimen dimension.....	61
5.2.2.	Concrete.....	62
5.2.3.	Heat treatment for DEF sample.....	64
5.2.4.	Conditioning of the specimens.....	64
5.2.5.	Measurement.....	65
5.2.6.	Strength test.....	66
5.2.7.	Sufficiency of coupler.....	67
5.3.	Results.....	68
5.3.1.	Free expansion of cylinders.....	68
5.3.2.	Expansion in pullout specimens.....	69
5.3.3.	ASR distribution.....	71
5.3.4.	Evolution of compressive strength.....	71
5.3.5.	Incremental loading and internal damage.....	76
5.3.6.	Evolution of bond strength.....	80
5.4.	Discussion.....	84
5.4.1.	Comparison of the evolution of strain.....	84
5.4.2.	Interaction of ASR and DEF reaction and expansion mechanism.....	86
5.4.3.	Relation between bond strength and compressive strength.....	87
5.4.4.	Relation between expansion and strength.....	88

5.4.5.	Evolution of damage in the affected concrete	90
5.5.	Summary	91
6.	Investigation in internal damage by X-ray CT	93
6.1.	Methodology	93
6.1.1.	Specimens	93
6.1.2.	Mechanical tests	94
6.1.3.	X-ray CT scan	95
6.2.	Specimen condition before the mechanical test	96
6.3.	Measurement of elasticity	97
6.4.	Crack characterization.....	97
6.4.1.	Separation of cracks and air voids	98
6.4.2.	Crack volume	99
6.4.3.	Crack width.....	99
6.5.	Results.....	101
6.5.1.	Stress-strain relationships of concrete with DEF expansion under various compressive loading patterns	101
6.5.2.	Crack distribution and propagation after various loading	103
6.5.3.	Crack volume and crack size based on X-ray CT scan	106
6.6.	Discussion	111
6.6.1.	Crack propagation.....	111
6.6.2.	Distribution of cracks.....	111
6.6.3.	Relating SDI and PDI with internal damage.....	112
6.6.4.	Effect of sustained load.....	114
6.6.5.	Changes in elasticity	114
6.7.	Summary	115
7.	Numerical modelling	117
7.1.	Background	117
7.2.	Time dependent expansion model of Larvie	117
7.3.	Strength model of Mazar.....	117
7.3.1.	Change in peak strength.....	120
7.3.2.	Change in Young's modulus.....	121
7.3.3.	Change in peak strain.....	121
7.4.	Model implementation	122
7.5.	Application of the model.....	122

7.5.1.	Concrete prism with and without steel.....	122
7.5.2.	Compressive strength of concrete cylinders at various ages.....	125
7.5.3.	Evolution of loading capacity of DEF affected beam.....	128
7.6.	Summary.....	130
8.	Case Study: Structural response of massive structure by internal expansion reaction.....	132
8.1.	Background.....	132
8.2.	Diagnosis of the problem.....	133
8.2.1.	Petrographic analysis.....	134
8.2.2.	Residual expansion test.....	137
8.3.	Numerical analysis for time-dependent deformation.....	138
8.3.1.	Model implementation.....	138
8.4.	Model calibration.....	141
8.5.	Sensitivity analysis.....	142
8.5.1.	Effect of elasticity.....	142
8.5.2.	Effect of varying monthly temperature.....	143
8.5.3.	Effect of ambient temperature.....	144
8.5.4.	Effect of strain.....	146
8.6.	Deflection prediction.....	146
8.7.	Crack susceptibility.....	148
8.8.	Summary.....	150
9.	Conclusion and recommendation.....	151
9.1.	Part A: Experimental works.....	151
9.2.	Part B: Numerical modelling for strength and serviceability evaluation.....	153
9.3.	Recommendation for future study.....	154
	References.....	155
	Appendix.....	167
A.	Effect of cement type on the free expansion.....	168
B.	Photographs of specimens of Chapter 3 (Internal restrains).....	170
C.	Photographs of specimens of Chapter 4 (External restrains).....	175
D.	Photographs of specimens of Chapter 5 (Bond test).....	183
E.	Alternate analysis of prism based on random nodes.....	193
F.	Sample script of Code-Aster used in Chapter 8.....	196
G.	List of some infrastructures infected by internal expansion reaction.....	203

List of Figures

Figure 1-1 Mechanism of alkali-silica reaction	1
Figure 1-2 Mechanism of delayed ettringite formation	1
Figure 1-3 Current status of research in ASR/DEF.....	4
Figure 2-1 Occurrence condition for ASR.....	9
Figure 2-2 Mechanism of alkali-silica reaction (based on Kreitman, (2011))	10
Figure 2-3 Variation of compressive stress with ASR expansion	15
Figure 2-4 Expansion due to ASR and hydration of normal concrete based on Price (1951) and Ahmed et al. (2003).....	15
Figure 2-5 Splitting strength of ASR affected concrete	16
Figure 2-6 Change in bond strength with the expansion of ASR.....	17
Figure 2-7 Change in modulus of elasticity due to ASR expansion (Giaccio et al., 2008).....	18
Figure 2-8 Mechanism of delayed ettringite formation	19
Figure 2-9 Curing temperature cycle used in (a)Fu’s method and (b)Kelhem’s method	22
Figure 2-10 Reduction in compressive strength due to DEF	24
Figure 2-11 Reduction in tensile strength due to DEF based on Rocco et al.....	24
Figure 2-12 Relationship between reduction of dynamic modulus and expansion.....	25
Figure 2-13 Definition of τ_c and τ_L based on the ASR extent with time.....	28
Figure 2-14 Relationship between expansion and DEF index (a) based on Zhang et al. (2002) (b) normalized for strain	30
Figure 2-15 (a) Comparison of experiment and numerical values; (b) Evolution of strain by Baghdadi.....	32
Figure 2-16 Evolution of strain for various temperatures and duration of curing condition (Martin et al. (2012))	32
Figure 3-1 Specimen type (a) with rebar and (b) without rebar.....	35
Figure 3-2 Photographs of the specimens during casting	35
Figure 3-3 Particle size analysis of aggregates.....	37
Figure 3-4 Heat treatment at an early age for DEF samples	38
Figure 3-5 Strain measurement in steel during heat treatment	38
Figure 3-6 (a) cutting of specimen, (b) setup for ASR detection	39
Figure 3-7 Expansion strain of concrete without steel reinforcement (a) ASR, (b) DEF and (c) DA ..	40
Figure 3-8 Expansion strain of concrete with steel reinforcement (a) ASR, (b) DEF and (c) ASR+DEF (DA).....	40
Figure 3-9 Stress in steel.....	41

Figure 3-10 Mass gain in the sample with (a) without steel and (b) with steel	41
Figure 3-11 Evolution of dynamic Young's modulus of elasticity.	42
Figure 3-12 Typical crack pattern of DA specimens at the age of about 300 days (a) unreinforced specimen and (b) reinforced specimen.....	42
Figure 3-13 Typical crack pattern of DEF specimens at the age of about 300 days (a) unreinforced specimen and (b) reinforced specimen.....	43
Figure 3-14 ASR detection in DA specimens (a) unreinforced and (b) reinforced specimen.....	43
Figure 3-15 Strain evolution in (a) free specimen and (b) reinforced specimen.....	44
Figure 3-16 Comparison of strain in ASR, DEF and DA specimens for unreinforced and reinforced specimens.....	45
Figure 3-17 (a) Evolution of strain in steel and concrete in reinforced specimens and (b) interaction between concrete and steel strains affected by ASR.....	46
Figure 3-18 (a) Evolution of strain in steel and concrete in reinforced specimens and (b) interaction between concrete and steel strains affected by DEF.....	46
Figure 3-19 (a) Evolution of strain in steel and concrete in reinforced specimens and (b) interaction between concrete and steel strains affected by ASR+DEF.....	46
Figure 4-1 External restraints.....	48
Figure 4-2 Heat treatment at the early age for DEF and DA samples.....	50
Figure 4-3 Steel frame used for restraining the expansion	51
Figure 4-4 Specimens for (a) free and (b) restraint expansion.....	51
Figure 4-5 Measurement of strain in the longitudinal and lateral direction. The direction 1-1 was measured with a contact gauge while the direction 2-2 was measured with a laser device.....	52
Figure 4-6 Evolution of strain in (a) free specimen (b) restrained specimen for normal, ASR, DEF and DA cases.....	53
Figure 4-7 Evolution of lateral strain in concrete for (a) free specimens (b) restrained specimens.....	54
Figure 4-8 Evolution of strain in steel rods of restraining frame in (a) Normal, (b) ASR, (c) DEF and (d) DA specimens. The grey lines show the variation and the continuous line shows the average strain.....	55
Figure 4-9 Crack distribution in free and restrained specimens for (a) DEF and (b) DA specimens ...	56
Figure 4-10 Evolution of strain in (a) free specimen (b) restrained specimen.....	56
Figure 4-11 Comparison of average strain in (a) Normal, (b) ASR, (c) DEF and (d) DA specimens for unreinforced and reinforced specimens. The broken line shows the restrained case.....	58
Figure 4-12 Comparison of stress in steel rods of the restraining frame (E=200GPa) and stress in concrete.....	58
Figure 4-13 Strain steel rod and concrete	59
Figure 4-14 (a) Relation between strain in concrete and steel rod ; (b) deformed shape of steel frame due to the expansion of concrete.....	59

Figure 5-1 Pull out specimen preparation	62
Figure 5-2 Photographs of the specimen during casting	62
Figure 5-3 Heat treatment at an early age for DEF and DA specimens	64
Figure 5-4 Temperature controlled water pool.....	65
Figure 5-5 Temperature variation in pool	65
Figure 5-6 (a) Strain measurement in cylindrical, (b) strain measurement of cubic specimens and (c) measurement of dynamic Young's modulus with the acoustic method.....	66
Figure 5-7 Setup for (a) uniaxial compressive strength test and (b) pull out test in Universal Testing Machine (UTM).....	67
Figure 5-8 Testing of the coupler for force transfer	68
Figure 5-9 Force transfer between main specimen rebar and connecting bar via coupler	68
Figure 5-10 Evolution of free expansive strain in (a) Normal, (b) ASR, (c) DEF and (d) DA cylindrical specimens. The grey lines show the actual measurements and the color continuous line show the average strain	69
Figure 5-11 Evolution of expansive strain in pullout specimens	70
Figure 5-12 ASR detection in cylindrical and pullout specimens	71
Figure 5-13 Uniaxial compressive strength in 28 days	73
Figure 5-14 Uniaxial compressive strength in 90 days	74
Figure 5-15 Uniaxial compressive strength in 150 days	75
Figure 5-16 Stress-strain relation and resonance frequencies for cyclic loading at 28 days.....	77
Figure 5-17 Stress-strain relation and resonance frequencies for cyclic loading at 90 days.....	78
Figure 5-18 Stress-strain relation and resonance frequencies for cyclic loading at 150 days.....	79
Figure 5-19 Bond stress and corresponding stress in steel rebar at 28 days	81
Figure 5-20 Bond stress and corresponding stress in steel rebar at 90 days	82
Figure 5-21 Bond stress and corresponding stress in steel rebar at 150 days	83
Figure 5-22 Peak pull out the stress of all specimens at 28 days, 90 days and 150 days.....	84
Figure 5-23 Evolution of strain in Normal, ASR, DEF and DA cylindrical specimens.....	85
Figure 5-24 Evolution of strain in Normal, ASR, DEF and DA pullout specimens	85
Figure 5-25 Distribution of ASR gel in ASR and DA cylinders	86
Figure 5-26 (a) Stress- slip curve and (b) stress in the embedded steel during pullout test at 28 days.	87
Figure 5-27 Relation between compressive strength and bond strength in (a) experiment and (b) based on JSCE code	88
Figure 5-28 (a) Absolute compressive strength and (b) absolute peak pull out stress at various expansion levels based on specimens that did not yield	89
Figure 5-29 (a) Relative compressive strength and (b) relative peak pull out stress at various expansion levels based on specimens that did not yield	89

Figure 5-30 Mechanism of bond strength reduction.....	90
Figure 5-31 Impact on dynamic Young’s modulus due to loading on affected structures.	91
Figure 6-1 Heat treatment of the specimens	94
Figure 6-2 Strain and weight change of specimen over time.....	94
Figure 6-3 Types of loading procedure adopted during the experiment (a) stepped incremental loading, (b) cyclic loading (c)cyclic and sustained loading and (d) incremental sustained loading. The circular dot shows the timing of acquiring CT image.....	95
Figure 6-4 Setup for compression test	95
Figure 6-5 X-Ray CT scan setup.....	96
Figure 6-6 Condition of specimens before the mechanical test	96
Figure 6-7 Dynamic Young’s Modulus and maximum DEF strain of specimens before the mechanical test used for various loading types.....	97
Figure 6-8 Steps for image analysis.....	98
Figure 6-9 Sensitivity of thresholding for specimens after failure for mid stack	98
Figure 6-10 Crack detected at threshold values of 0-110, 0-120 and 0-130	98
Figure 6-11 Process of separating air voids and cracks	100
Figure 6-12 3d view of voids and cracks	101
Figure 6-13 Determination of crack width.....	101
Figure 6-14 Relationships between stress and strain under various compressive loading patterns	102
Figure 6-15 Enlarged initial stress-strain relationship for monotonic loading.....	103
Figure 6-16 X-ray CT and binary image showing crack propagation due to stepwise loading	104
Figure 6-17 CT and Binary images showing crack propagation due to cyclic loading of 20 kN (= 2.40 N/mm ²).....	105
Figure 6-18 CT and Binary images showing crack propagation due to cyclic loading of 30 kN (= 3.61 N/mm ²).....	106
Figure 6-19 Crack volume under various compressive loading patterns for mid 5 cm	107
Figure 6-20 Crack volume under various compressive loading patterns for mid 10cm	108
Figure 6-21 Crack count of various widths under different compressive loading patterns for mid 5 cm	109
Figure 6-22 Crack count of various widths under different compressive loading patterns using mid 10 cm.....	110
Figure 6-23 Crack distribution for threshold values of 0-110, 0-120 and 0-130	110
Figure 6-24 Distribution of crack from the core to the surface of cylindrical specimen before and after loadings	112
Figure 6-25 Definition of stiffness damage index and plastic damage index (a) for step loading (b) for cyclic loading in this study	112

Figure 6-26 Damage index and plastic damage index for steeped incremental loading.....	113
Figure 6-27 Damage index, plastic damage index and change in crack volume for cyclic loading of (a) 20kN and (b) 30 kN	113
Figure 6-28 Evolution of specific strain.	114
Figure 6-29 Reduction in elasticity at various levels of loading.....	115
Figure 7-1 Evolution of (a) compressive strength and (b) Young’s modulus with expansion in ASR affected concrete	119
Figure 7-2 Evolution of (a) compressive strength and (b) Young’s modulus with expansion in DEF affected concrete	120
Figure 7-3 Evolution of Gaussian function.....	120
Figure 7-4 Dimension of prismatic specimens used in the simulation	123
Figure 7-5 Evolution of free expansion of ASR infected concrete with and without reinforcement..	123
Figure 7-6 Evolution of free expansion of DEF infected concrete with and without reinforcement..	124
Figure 7-7 Evolution of principal strain at the age of 150 days for free specimen	124
Figure 7-8 Evolution of strain in steel-concrete interface due to concrete expansion	125
Figure 7-9 Evolution of free expansion in ASR and DEF specimens.....	126
Figure 7-10 Comparison of uniaxial compressive test for ASR specimens at 90 days and 150 days.	126
Figure 7-11 Comparison of uniaxial compressive test for DEF specimens at 90 days and 150 days.	127
Figure 7-12 Damage evolution in (a) ASR and (b) DEF specimens due to uniaxial compression at 90 days and 150 days	127
Figure 7-13 Damage in (a) ASR and (b) DEF specimens in experiment due to uniaxial compression at 150 days	128
Figure 7-14 Beam for analysing (a) flexure failure and (b) shear failure	128
Figure 7-15 Simulated stress-strain relation of a DEF affected cylinder at various expansion	129
Figure 7-16 Load deflection curve for (a) flexure failure (b) shear failure.....	130
Figure 7-17 Stress in steel for (a) flexure failure (b) shear failure.....	130
Figure 8-1 Location of the dam in Thailand. The distribution of maximum average temperature is also shown based on Souris (2000)	132
Figure 8-2 Location of deflection measurement station in the dam.....	133
Figure 8-3 (a) Deflection of the dam at the crest (based on Bui Anh (2018)) and (b) mechanism of expansion	133
Figure 8-4 Cutting surface and magnified surface of C1 core sample (based on (Joshi et al., 2021)).	135
Figure 8-5 Cutting surface and magnified surface of C2 core sample (based on (Joshi et al., 2021)).	136
Figure 8-6 Polarizing microscopic observation of coarse aggregate in the C2 core sample (based on (Joshi et al., 2021)).....	136
Figure 8-7 SEM observation of ASR gel and qualitative analysis by EDS in the coarse aggregate of C2	

sample (based on (Joshi et al., 2021)	137
Figure 8-8 Expansion owing to accelerated ASR test for core samples taken from a depth of 30 cm (C1) and 100 cm (C2) (based on (Sriprasong, 2020)	138
Figure 8-9 Fluctuation of temperature from 2014 to 2020; (b) average annual temperature fluctuation used in the numerical model	139
Figure 8-10 Temperature distribution inside the dam body at various months	139
Figure 8-11 Age of dam when ASR occurred in various dams	140
Figure 8-12 Water level comparison between Bui (2018) and Thongthamchart & Raphitphan (n.d.)	141
Figure 8-13 (a) Calibration of the model at a water level of 120 m; (b) estimation of deflection for various water levels; the full line is the calculated values while the observed values are shown by dots	142
Figure 8-14 (a) Effect of modulus of elasticity on the evolution of deflection, and (b) deflection of the dam for a water level of 120 m along its height at the age of 100 years.....	143
Figure 8-15 (a) Evolution of deflection overtime for a water level of 120 m; (b) the deflection pattern of the dam at the age of 100 years	144
Figure 8-16 Evolution of maximum radial deflection at the crest for various temperatures and water level of 120 m owing to (a) ASR strain (b) ASR strain combined with the thermal strain.....	145
Figure 8-17 (a) Evolution of deflection owing to various levels of ASR strain for a water level of 120 m; (b) deflection of the dam for various water levels at the age of 100 years	146
Figure 8-18 (a) Prediction of deflection of the dam at the age of 70 years and 100 years using a deterministic approach for the water level of 120 m; (b) deflection of the dam for various ages (Joshi et al., 2021).....	148
Figure 8-19 (a) Probabilistic prediction of the deflection of the dam for the water level of 120 m; (b) deflection for various water levels with the standard error at the age of 100 and 70 years. (Joshi et al., 2021)	148
Figure 8-20 Distribution of major principal stress in the dam body without the effect of ASR and with ASR at the age of 50 years, 70 years and 100 years for hydrostatic loading of 120 m (Joshi et al., 2021)	149

List of Tables

Table 1-1 Some reported cases of ASR and DEF	2
Table 2-1 Chronology of the various degradation in concrete	8
Table 2-2 Grading Requirements for ASTM C1260	12
Table 2-3 ASTM C 1260 identification for the expansion	12
Table 2-4 Summary of research on the mechanical effect of ASR expansion	13
Table 2-5 Summary of research about the mechanical effect of ASR expansion	23
Table 3-1 Concrete mix proportion	35
Table 3-2 Cement composition	36
Table 3-3 Physical properties of aggregate	36
Table 4-1 Concrete mix proportion	49
Table 4-2 Cement composition	49
Table 4-3 Physical properties of aggregate	50
Table 4-4 Absolute displacements in concrete and steel rods	59
Table 5-1 Concrete mix proportion	63
Table 5-2 Cement composition	63
Table 5-3 Physical properties of aggregate	64
Table 5-4 Average peak strength and corresponding strain.....	72
Table 5-5 Resonance frequency (f) and dynamic Young's modulus(E_d) at various ages	76
Table 5-6 Peak pullout strength and slip	84
Table 5-7 Expansive strain in cylindrical and pull out specimens	86
Table 6-1 Mix Proportion of DEF/ASR specimens	94
Table 7-1 Gaussian parameters for time-dependent strength analysis	122
Table 7-2 Strain evolution parameters for free expansion of prismatic specimens.....	123
Table 7-3 Strain evolution parameters for free expansion of cylindrical specimens	125
Table 8-1 Parameters used for analysis.....	140
Table 8-2 Standard error of estimation of deflection for various water level	142
Table 8-3 Comparison of deflection with and without thermal strain for various water levels and temperature	145
Table 8-4 Variation of input and output parameters.....	147

List of abbreviations and symbols

Abbreviations

A	ASR specimens
AAR	Alkali Aggregate Reaction
AD	see DA
ASR	Alkali Silica Reaction
ASTM	American Society for Testing and Materials
BS	British Standards
BSI	British Standards Institution
CSA	Canadian Standards Association
CT	Computerized Tomography
D	DEF specimens
DA	ASR+DEF combined specimens
DEF	Delayed Ettringite Formation
DIC	Digital Image Correlation
DRI	Damage Rating Index
EDS	Energy Dispersive Spectroscopy
EL	Expansion Limit
FEM	Finite Element Method
FFT	Fast Fourier Transform
HPC	High Performance Cement
HPCM	High Performance Cement Mortar
IFSTTAR	French Institute of Science and Technology for Transport, Development and Networks
ISE	The Institution of Structural Engineers
ITZ	Interfacial Transition Zone
MIN	Minimum
NA	Not Applicable
NDT	Non Destructive Test
OPC	Ordinary Portland Cement
PARI	Port and Airport Research Institute (Kanagawa, Japan)
PDI	Plastic Deformation Index
PVC	Polymer of Vinyl Chloride

RH	Relative Humidity
RILEM	The International Union of Laboratories and Experts in Construction Materials, Systems and Structures (in French)
SCMs	Supplementary Cementing Materials
SDI	Stiffness Damage Index
SDT	Stiffness Damage Test
SEM	Scanning Electron Micrographs
SEM	Scanning Electron Microscopy
SN	Serial Number
TC	Technical Committee
THM	Thermo Hydro Mechanical
UK	United Kingdom
USA	United State of America
UTM	Universal Testing Machine
XCT	X-ray Computerized Tomography

Symbols

Φ , dia.,d	diameter
μm	micrometre
$^{\circ}\text{C}$	degree Celsius
$^{\circ}\text{F}$	degree Fahrenheit
M	molarity
MPa	megapascal (equals to N/mm^2)
fbs	characteristic bond strength
α	coefficient
β	coefficient
c	cover
f_t	tensile strength
%wt	percentage by weight
∂	derivative
θ	temperature
K	thermal conductivity
C	heat capacity

ξ	rate of ASR reaction
τ	characteristic or latent time
ϵ	strain
E	Young's modulus of elasticity
d_{asr}	damage factor
Cp	specific heat capacity
h	hydration degree
λ	Lame's coefficient
ρ	density
μ	Lame's coefficient
σ	stress
mm	millimetre
ml	millilitre
GPa	gigapascal
Hz	Hertz
w/c	water-cement ratio
kN	kilo Newton
kg	kilogram
kJ	kilo Joule
W	watt

1. Introduction

1.1. Background

Concrete generally has a long life and is considered as a maintenance-free material. However, it is not immune to deterioration and a large amount of resources has to be allocated for repair, maintenance or replacement of deteriorated structures. Deterioration can be either due to physical phenomena such as abrasion and thermal cracking or it could be due to chemical changes such as carbonation and corrosion. Among the chemical deteriorations, time-dependent expansions caused by Alkali Silica Reaction (ASR) and Delayed Ettringite Formation (DEF) are two key phenomena that have been identified in various structures such as dams, bridges and pre-cast concrete such as railway sleepers. Some problems caused by ASR and DEF are listed in Table 1-1.

Alkali Silica Reaction (ASR) is a slow time-dependent deleterious chemical reaction that occurs due to the reaction between alkali (KOH, NaOH) in pore solution and the reactive silica (SiO_2) in aggregates as shown in Figure 1-1. During the chemical reaction, the ASR gel absorbs moisture and causes expansive stress in the concrete which results in the cracking of concrete. Delayed Ettringite Formation (DEF) occurs when the concrete is exposed to elevated temperatures (over 70°C) in its early age. During the early hydration process, the elevated temperature decomposes ettringite into mono-sulphate releasing sulphate which is absorbed by C-S-H as shown in Figure 1-2. Later in the hardened stage, mono-sulphate recrystallize by absorbing the sulphate forming ettringite. The larger volume of ettringite causes expansive stress in concrete. Although ASR and DEF have a different chemical process, both phenomena have similar expansion kinetics at the macro level. Therefore, DEF and ASR are often studied together.

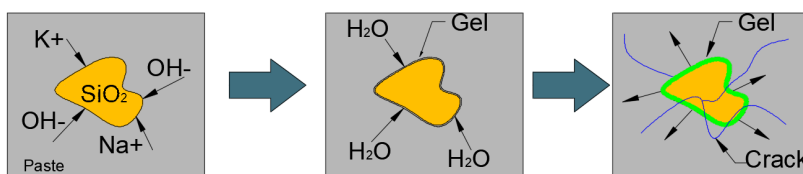


Figure 1-1 Mechanism of alkali-silica reaction

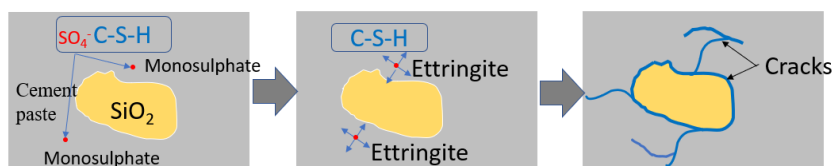


Figure 1-2 Mechanism of delayed ettringite formation

ASR has been investigated in the United States for more than five decades. It became a concern in Japan in the 1980s as a result of identification of various highways

structures affected by ASR. Based on the experience, guidelines and specifications have been compiled mainly by academic associations to analyze the causes, preventive standards, and repair measures. DEF was initially identified in Europe and has been considered as the cause of degradation in various bridges where concrete was cast-in-place. In Japan, however, reports on DEF are mainly confined to precast concrete. Nevertheless, DEF is of great concern among Southeast Asia countries because of their hot climate. Among the studies carried out, most of them are focused on unreinforced cases with the focus on prevention in a new structure. In reality, reinforcement is present in most concrete structures. The study on the effect of restraints on internal expansion has not been studied well. The possibility of combined DEF and ASR interaction has also been pointed out where there is a possibility of inclusion of reactive aggregates in the concrete mix. Thus, it has become important to understand the effect of internal expansion reaction by ASR/DEF on the concrete structures in order to take appropriate measures when excessive expansion occur.

The objective of this thesis is to understand the structural capacity and serviceability of structures that exhibit internal expansion reactions. The study focuses on the internal expansion reaction of concrete caused by ASR and DEF and experimentally investigates the expansion behaviour under internal and external restraints, the adhesion strength of reinforcing bars and the strength reduction of concrete due to expansion. A model for numerical simulation is also proposed.

Table 1-1 Some reported cases of ASR and DEF

SN	Problems	Country	Reported Year	Reference
Alkali silica reaction (ASR)*				
1	A double-decker elevated highway in Johannesburg, constructed in 1963 started to crack in a corner in 1970s. The deteriorated corner of the frame was rebuilt in 1991.	South Africa	1963	Alexander et al., (1992); Talley (2009)
2	Several of the bridge columns of A26 highway in Northeast France built in the 1970s were affected by ASR cracking. The stiffness was reduced to about 10% of the original although the overall structural stiffness was high. The bridges were repaired by coating to stop moisture ingress.	France	1970s	Baillemont et al. (2000)
3	Crack in spillway and powerhouse were found in Furnas Dam	Brazil	1970	Sims & Poole (2017)

SN	Problems	Country	Reported Year	Reference
4	The concrete cores taken from the Hanshin Expressway in Japan showed a reduction of 35% of its strength and 78% of its stiffness due to ASR cracking	Japan	1982	Imai et al. (1986)
5	The spillway of Kleinplass dam showed swelling and carking at horizontal joints in	South Africa	1982	Sims & Poole (2017)
6	The ASR expansion in Rihand Dam in Northern India caused misalignment of machinery resulting in problems in the operation of gates, cranes and passenger lifts	India	1987	Mullick (1991)
Delayed Ettringite Formation (DEF)				
1	Various bridge piers where mass concreting was done was found to be infected with DEF expansion. Map cracking was a distinct feature.	France	1999	Godart & Divet (2012)
2	The steam cured railway sleepers produced between 1992 and 1996 started to show DEF cracks in 1999.	Sweden	2004	Sahu & Thaulow (2004)
3	Various bridges in Maryland	USA	2007	Ceary (2007)
4	The steam cured railway sleepers showed map cracking due to DEF expansion.	India	2017	Awasthi et al., (2017)
5	A combination of DEF and ASR caused damage to railway track slabs in China railways.	China	2017	Ma et al. (2017)

* additional list of structures infected with expansive concrete is given in the Appendix.

1.2. Problem statement

ASR and DEF are multiscale phenomena that can be studied from the reaction product level to the structural level as shown in Figure 1-3. In the case of ASR, most of the past studies are focused on the reaction product level, aggregate level and laboratory specimen while there are relatively fewer studies on the structural level (Esposito & Hendriks, 2019). The studies are evolving over time. For example, based on the early

researches on ASR mechanism, ASTM C 289 chemical test was drafted. Over time it was found that this test could not give a correct result and eventually, in 2016 it was withdrawn (Figueira et al., 2019; P. Thomas et al., 2019) and replaced with ASTM C1260 and ASTM C1293 in conjunction with petrographic analysis using ASTM C295. Similarly, IFSTTAR (France) published recommendations for the prevention of DEF in 2007, which was revised in 2017 (Godart & Divet, 2017). And, in Japan a technical committee has been formed to work on the DEF mechanism (Hanehara et al., 2019).

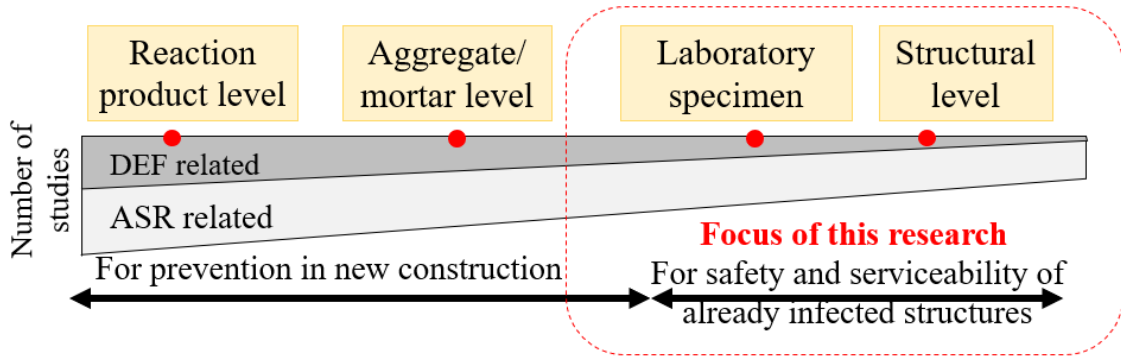


Figure 1-3 Current status of research in ASR/DEF

The study on the chemical mechanism is applicable for new construction to inhibit the expansion however, it cannot be applied to already affected structures. Many structures, mainly those exposed to moisture absorption, have been identified to be infected by ASR (Charlwood & Sims, 2017). Similarly, railway sleepers, bridges were found to be infected with DEF (Ceary, 2007; Godart & Divet, 2013). In some cases, the ASR expansion was strong enough to rupture steel reinforcement (Miyagawa et al., 2006). These infected structures are either monitored continuously as done in the European countries or discretely inspected at some time interval as in Japan. The monitoring is generally carried out by visual inspection or non-destructive tests (NDT). The monitoring data are invaluable, however, the interest of practising engineers and the owner of the structure lies in assessing the safety and serviceability of the structures which cannot be reliably predicted based on inspecting tools alone.

To estimate the safety and serviceability of infected structures, experimental studies are required at the structural level. There are a fairly large number of studies on ASR related deterioration in structural level compared to DEF as indicated in Figure 1-3 because of a relatively larger number of reported cases. Based on the case studies and laboratory experiments, recommendations have been prepared to estimate the loss of compressive strength, tensile strength and bond strength such as by *ISE* (1992).

In comparison to ASR, the study on mechanical properties of DEF infected concrete is relatively low. Because of similar expansion kinetics, the DEF affected concrete has a similar attribute of ASR deterioration, however, there are some major differences. The first main difference is the origin of expansion. The ASR expansion is caused by swelling

of reaction gel near aggregate interface which results in cracking of aggregate while the DEF expansion is caused by ettringite formation in the cement paste which causes cracking of cement matrix. Thus, the stress instigated by the two phenomena could be different. This can make a considerable difference in steel-concrete interaction because micro-cracks by DEF can completely damage the adhesion between steel and concrete rapidly than ASR. Such comparative studies have not been done yet. The second difference is the rate of reaction. The laboratory investigation indicates that the loss of strength by DEF deterioration is much rapid than ASR which means the structure, especially the unreinforced ones, can become unsafe within a short period. Such expansive forces can also result in overstressing of prestressed tendons in pre/post-tensioned components.

Besides safety concerns, ASR/DEF expansion can adversely impact the serviceability of the infrastructures by developing unwarranted deflection and cracks (Fournier et al., 2010). Cracks are formed due to a change in the stress distribution inside the structure. Depending on the boundary condition, even a small expansion can induce tensile or compressive stress, causing unwarranted cracks. The expansion can also cause other problems such as water leakage from expansion joints or maloperation of equipment (Charlwood & Sims, 2016). Thus, the serviceability of the infected infrastructures also needs a due attention.

Based on the above discussion, it can be concluded that there is a necessity to understand the mechanical behaviour of ASR/DEF infected concrete for safety evaluation. The effect on the serviceability of the structures (mainly cracking) also needs to be understood. This dissertation is focused to answer these pertaining questions.

1.3. Objectives of research

In the previous section, it was indicated that there is a necessity to expand the study on the changes in mechanical properties of concrete due to ASR and DEF and their combination. This research aims to provide insight on the effect of ASR and DEF expansion on strength, bonding and internal and external restrains. These objectives are achieved by dividing the dissertation into two main parts.

The first part of the research is focused on the experimental studies to check the alteration of mechanical properties of concrete affected by ASR/DEF. Mainly four types of experiments are carried out as listed below:

- (1) Experiment to understand the effect of internal restraint on ASR/DEF expansion
- (2) Experiment to understand the effect of external restraints on ASR/DEF expansion
- (3) Experiment to measure the change in bod and compressive strength by ASR/DEF expansion
- (4) Experiment to understand the crack propagation and failure mechanism

In the second part of the research, the finding of experimental works and previous studies are used to develop a model for numerical analysis that can be implemented in FEM software for the safety evaluation of infected structures. Besides strength, the serviceability of the structures can be of prime importance, hence to understand the effect on serviceability due to the time-dependent expansion, an analysis of a massive dam is carried out.

The finding of this dissertation can be used to evaluate the safety and serviceability of the plain, reinforced and post-tensioned structure that has been affected by the expansive reaction of ASR/DEF. The numerical model can be implemented in FEM software to predict the time-dependent response of the affected structure.

1.4. Dissertation outline

This dissertation is organized as follows:

Chapter 1 accumulates the introduction, objective of the study, problem statement, and organization of the dissertation.

Chapter 2 presents the literature review of the past studies on the Alkali Silica Reaction and Delayed Ettringite Formation. The review will provide information on the chemical nature, however, the main focus will be on the mechanical aspects. Any specific exploration of literature required for a part of the thesis is provided in the corresponding chapters.

Chapters 3 and 4 explore the effect of restraints on the ASR/DEF expansion. In chapter 3, the result of the experimental study done with reinforced concrete is reported. In chapter 4, the effect of external restraints is explored. The experimental results and their usability for application on real structures are discussed in the respective chapters.

Chapter 5 presents the study on bond deterioration due to ASR/DEF expansion.

Chapter 6 presents the study on failure mechanism and crack propagation of highly expanded concrete under uni-axial loading. The damage observed using an X-Ray CT image analysis is reported.

Chapter 7 presents the development of numerical modelling to associate time-dependent expansion with mechanical properties for FEM analysis. Some verification examples are shown. A typical application of the numerical model to analyze a reinforced beam is provided.

Chapter 8 presents a case study of a concrete dam that has been affected by ASR. A method is shown to systematically diagnose the problem and conduct a thermo-mechanical analysis based on data collected from past studies. Then after a prediction is made on the future performance of the dam using FEM analysis. The main purpose of this study is to understand the effect of various parameters contributing to ASR and on

the serviceability of a massive structure.

Chapter 9 forms conclusions about the main findings of this research.

2. Literature review

2.1. A brief history of concrete deterioration

Historically, most of the early scientific works on concrete is directed towards increasing its strength which is inspired by the requirement of war where concrete had to resist the impact of the projectile from the enemy (Powter, 1978). From the mid 20th century, concrete was massively used for the construction of public and private infrastructures in the European, North American countries and Japan. With the ageing of those structures, researchers started identifying various problems. The most well-recognized problem was corrosion of steel reinforcement inside the reinforced concrete that was closely linked with the moisture and gas transport through pores and cracks in the concrete. Various other deterioration phenomena were also identified, some of which are listed in Table 2-1. The deterioration processes are well recognized and have been listed in national codes and guidelines. For example, the British concrete code (BS7543) recognizes temperature, radiation, carbonation, air contaminants, freezing/thawing, abrasion, biological attack, varying stresses, chemical attack, etc as the source of deterioration. In addition, concrete can get deteriorated by two or many of these phenomena simultaneously (BS 7543, 2015). To respond to these phenomena, durability requirement for 50 years and 100 years of service life has been provided in BS 8500-1:2006.

Among various types of deterioration phenomena, Alkali Silica Reaction (ASR) and Delayed Ettringite Formation (DEF) are time-dependent expansions that can cause internal swelling in concrete and result in cracking and deterioration of strength. ASR was first identified in 1914 in Denmark while DEF was first reported in Finland in 1987. ASR and DEF are studied together in this research because they have similar expansion kinetics. Also, they can co-exist due to their chemical inter-dependence related with the pH of the pore solution. Furthermore, various cases have been identified where both DEF and ASR were present in the same structure, although the main cause of damage remains still ambiguous.

Table 2-1 Chronology of the various degradation in concrete

Year	Focus	Description
1824	General	Joseph Aspdin patented for Portland Cement
1910	General	Emil Morsch, a German engineer, formulated Elastic theory of structure for reinforced concrete
1913	Corrosion	Bureau of Standards, Washington published a book on electrolysis of concrete written by a team of physicists E. B. Rosa, Burton McCollum, and O. S. Peters, Assistant Physicist. Mechanical stress due to the expansion of rust was measured.

Year	Focus	Description
1914	ASR	<p>ASR phenomenon was first presented by Poulsen in January 1914 to the Institution of Danish Civil Engineers.</p> <p>The phenomenon was further studied in the 1930s in the USA and presented by Stanton in 1940 by giving examples of structures in California. Stanton also demonstrated the expansive nature of this reaction.</p> <p>The ASR phenomenon was gradually discovered in other countries such as Denmark (1950s), Germany (1960s), UK (1970s), France (1970s), South Africa (1976), Norway (1980s), Japan (1980s), etc.</p>
1987	DEF	<p>DEF was identified in steam cured precast railway sleepers in Finland in 1987. It was also identified in mass concrete in 1999 in France in various bridge piers in 1999. (Godart & Divet, 2013) (Colleparidi, 1999)</p>

2.2. Alkali-silica reaction

Alkali Silica Reaction (ASR) is one of the sub-set of Alkali Aggregate Reaction (AAR). ASR refers to a reaction between the alkali in pore solution with the highly reactive silica in aggregate. The reaction forms an expansive gel around the reactive aggregate. This gel in the presence of moisture causes expansion of concrete and cracking. The basic requirement of ASR is reactive aggregate, high alkali level and availability of moisture.

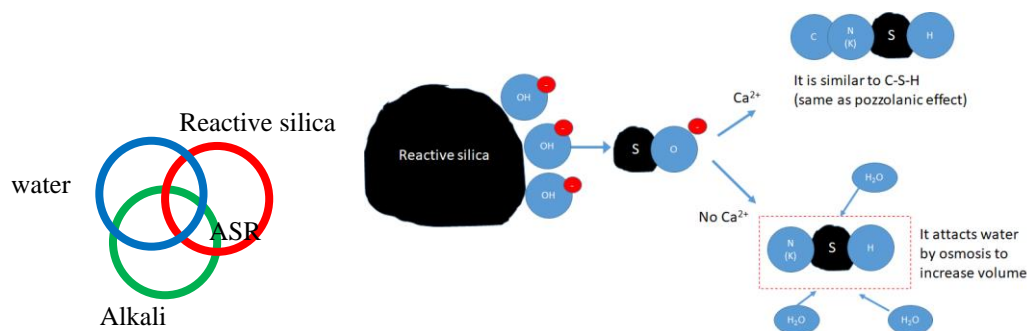


Figure 2-1 Occurrence condition for ASR

ASR has been reported in various concrete structures around the world (Sims & Poole, 2017). It is frequently reported in hydraulic structures such as dams and foundations because of the easy moisture availability. Reports by Charlwood & Sims (2016) and Sellier et al. (2017) have catalogued various examples of ASR in these types of structures. Some of them has been provided in Appendix G.

The chemical mechanism of ASR related to concrete deterioration was systematically studied by Dent Glasser & Kataoka (1981). Various other researchers have also worked on the mechanism of ASR such as by Chatterji & Christensen (1990) and Diamond (1989). According to Dent-Glasser and Kataoka, in highly alkaline cement paste some of the silicate, aluminate or sulphate ions are balanced by high alkali metals (Na^+ or K^+) instead of alkali earth metals (Ca^{2+}), causing high pH in the pore solution. The hydrolysis of weak anions acids and the formation of insoluble calcium salts instead of calcium hydroxide were identified to contribute to the formation of Hydroxyl ions (OH^-). OH^- ions gradually penetrate the poorly crystallized silica aggregates in the presence of Na^+ or K^+ ions. This causes rupture of the siloxane groups (Si-O-Si). The reaction processes can be represented stoichiometrically as follows:



The ASR gel itself does not have a degrading effect. However, this gel is hydrophilic and absorbs moisture easily and swells. This swelled ASR gel exerts outward expansion pressure. With the increase in the expansive pressure, ASR gel causes aggregate and cement matrix to crack. The crack near the concrete surface can act as a route for additional water and leading to further ASR. The mechanism is shown in Figure 2-2.

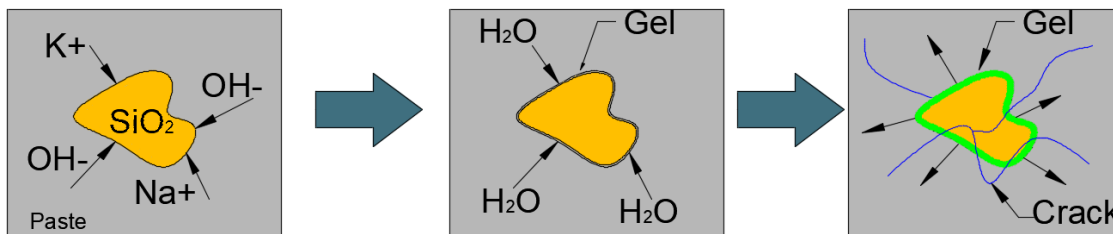


Figure 2-2 Mechanism of alkali-silica reaction (based on Kreitman, (2011))

To prevent the likelihood of ASR, a low alkali level cement or pozzolanic cement (e.g. fly ash) can be used. The reactivity of the aggregates can be tested according to ASTM C227, ASTM C1260, and ASTM C1293.

2.2.1. Factors Influencing ASR

ASR is mainly influenced by alkali content, silica type, moisture availability, temperature, and porosity. These are briefly described in the following sections.

a. Alkali content

The alkali is present in cement in the form of sodium and potassium oxides. Besides cement, chemical admixtures, supplementary cementing and aggregates also contribute to the alkali concentration in the concrete (Diamond, 1989). The equivalent alkali content is expressed in terms of mass percentage calculated as an equivalent sodium oxide (Na_2O) as:

$$\text{Na}_2\text{O}_{\text{eq.}} = \text{Na}_2\text{O} + (0.658) \text{K}_2\text{O}$$

According to ASTM C150, any cement with $\text{Na}_2\text{O}_{\text{eq}}$ below 0.6% is defined as a low-alkali cement. However, concrete prepared with low-alkali cement may still exhibit ASR expansion if the aggregate used is highly reactive.

b. Silica in the aggregates

The reactivity of silica (SiO_2) depends upon its crystallization and presence of impurities (M. Thomas et al., 2013). Aggregates that are poorly crystallized, amorphous, glassy, and micro-porous, can easily be attacked by alkali, while well-crystallized silica is less reactive. Highly strained crystals are also reactive which is attributed to a large amount of strain energy stored in the crystal lattice that could help to accelerate the chemical reaction. The rate of reaction is much slower compared to the aggregates composed of glassy or amorphous silica.

In the study by Diamond & Thaulow, (1974), they noted that 20-30 μm aggregate had a larger expansion in a short time compared to larger aggregates. For specimens with aggregates of size 20-30 μm , ASR expansion terminated within a few months while the specimens having a coarser size of 125 μm (the same type of aggregate) experienced a prolonged expansion. Hobbs & Gutteridge (1979) also concluded that the smaller aggregate particle size can lead to the larger expansion in a short duration.

c. Moisture

Relative humidity above 80% is favourable for ASR. The use of a low water-cement ratio or supplementary cement materials can lead to a reduction of permeability and slowing the rate of reaction (Multon et al., 2005; Multon & Toutlemonde, 2010; Ulm et al., 2000). Farny & Kosmatka, (1997) showed that in any specimens that have undergone ASR, the moisture uptake can be initiated even at the later stage resulting in expansion.

d. Temperature

The temperature has a significant effect on ASR expansion. According to the study of Larive & Laboratoire Central des Ponts et Chaussees (1998), the temperature effect could be modelled using the Arrhenius equation. Locher & Sprung (1973) found the largest expansion occur with the pessimum value of 38°C while the increase of temperature resulted in a decrease of expansion. A similar result was found by Chatterji & Christensen (1990). The reduction could probably be due to increased solubility of silica and reduced solubility of $\text{Ca}(\text{OH})_2$. However, this claim is controversial because larger expansions were found at a higher temperature in several studies.

2.2.2. Test method for ASR

Chemical test with ASTM C1260

This method is recommended by the American Society for Testing and Materials (ASTM) as a rapid test for the identification of reactivity of aggregate for potential ASR. The method was developed by Oberholster & Davies (1986) in South Africa.

In the test, the mortar bar specimen is prepared with aggregate having a standard

gradation (Table 2-2). The mould is removed after 24 hours and the specimen is submerged in tap water at 80 °C for the next 24 hours. At this point, zero readings are taken. Then, the specimen is conditioned in 1M NaOH solution for 14 days. The length is measured again which is reported as the final strain. The reactivity is identified by comparing this value with the standard values of Table 2-3. For supplementary cementing materials (SCMs), the expansion limit is set at 0.10%.

Because of the highly alkaline submerged solution and high curing temperature, the test is severe and may identify some non-reactive aggregates as reactive. Thus, the test result should be used cautiously and the aggregates should not be rejected solely based on ASTM C1260. It should be used in conjunction with the petrographic examination (ASTM C 295).

Table 2-2 Grading requirements for ASTM C1260

Sieved Size		% Mass
Passing	Retained On	
No. 4	No. 8	10
No. 8	No. 16	25
No. 16	No. 30	25
No. 30	No. 50	25
No. 50	No. 100	15

Table 2-3 ASTM C 1260 identification for the expansion

% Expansion	Description
< 0.1 %	Non-Reactive
0.1-0.2 %	Potentially Reactive
>0.2 %	Reactive

2.3. Mechanical effect of ASR expansion

The engineering properties of concrete is affected by ASR expansion mainly due to the internal swelling and formation of cracks. Since ASR depends on reactive aggregates, large variability in expansion can occur even within the same structure (Wood et al., 1986). A summary of representative studies done in the field related to mechanical damage due to ASR is given in Table 2-4. The conditions of experiments in those studies are also shown because it can affect the outcome.

Table 2-4 Summary of research on the mechanical effect of ASR expansion

Author (year)	Specimen conditioning	Specimen type and findings
Fan & Hanson (1998)	38 °C in 0.5 N NaOH	<p>Specimen type: Reinforced concrete beams and concrete cylinder</p> <ul style="list-style-type: none"> • Mechanical properties started to deteriorate after the appearance of visible cracks. At the age of 6 months, compressive strength, splitting strength, and dynamic modulus were reduced by 24, 38, and 31 percent, respectively. • At an age of one year, the rate of reduction slowed down. • The reinforced beams experienced visible cracking due to ASR; however, the flexural loading capacity was in the same range as that of the control beams.
Ahmed et al. (2003)	38 °C in water	<p>Specimen type: Prisms and cylinders</p> <ul style="list-style-type: none"> • The compressive strength was not reduced. It was concluded that strength is not a good indicator of the degree of reaction. The tensile strength was reduced by 50% to 80%. • The static modulus of elasticity was used as an indicator for the degree of deterioration. • The loss in flexural strength was between 48-60%.
Marzouk & Langdon (2003)	NaOH solution and de-ionized water at 80 °C	<p>Specimen type: Prisms and cylinders</p> <ul style="list-style-type: none"> • The modulus of elasticity, tensile, compressive, and flexural strength varied with ASR expansion. • With high strength concrete, the deterioration was small
Giaccio et al. (2008)	ASTM C1293	<p>Specimen type: Prisms and cylinders</p> <ul style="list-style-type: none"> • Compressive strength did not increase when highly reactive aggregates were used, however, there was a reduction in modulus of elasticity and Poisson's ratio. • In the specimen with low reactive aggregate, the compressive strength was increased, however, the modulus of elasticity and Poisson's ratio were reduced. • The shape of the stress-strain curves showed increased non-linearity and a more gradual softening.
Yurtdas et al. (2013)	60 °C and 95% RH	<p>Specimen type: Prisms and cylinders</p> <ul style="list-style-type: none"> • The compressive strength of reactive mortars was found higher than non-reactive by about 23–34%. • The tensile strength, modulus of elasticity, and Poisson's ratio were significantly affected by the ASR and decreased.

Author (year)	Specimen conditioning	Specimen type and findings
Li et al. (2016)	80 °C in tap water, and 80 °C in 1 N NaOH solution	Specimen type: High-performance cementitious mortar <ul style="list-style-type: none"> The loss in the flexural strength of HPCM was observed with an increase in the alkali content of the cement. The addition of fly-ash reduced ASR deterioration
Shi et al. (2017)	ASTM C1260	Specimen type: Activated slag mortars <ul style="list-style-type: none"> The degree of hydration for slag increased with an increase in alkali content, which led to a higher compressive strength even though there was an increase in ASR.
Islam & Ghafoori (2018)	20°C in water and 80 °C in 1.0 M NaOH	Specimen type: Mortar bars and concrete cylinders <ul style="list-style-type: none"> ASR caused a significant reduction in modulus of elasticity They categorized reactivity with loss of stiffness as – the specimen losing 18% stiffness at 26 weeks.
Barbosa et al. (2018)	Field condition	Specimen type: Concrete cores <ul style="list-style-type: none"> The orientation of ASR cracks affected the compressive strength. The compressive strength in the direction perpendicular to ASR cracks (vertical drilling) was significantly lower than in the direction parallel to ASR cracks (horizontal drilling). The compressive strength for cores with perpendicular ASR cracks was reduced up to 67% and for cores with ASR cracks parallel to the load direction was up to 56%.

*Summarized from Mohammadi et al. (2020)

2.3.1. Change in compressive strength

Compressive strength is the most important parameter for the design of the concrete structure. It is used to estimate various other parameters using empirical relationships. It is invaluable information for any constitutive models required for numerical simulation and safety evaluation.

It has been reported that the reduction in the compressive strength of concrete affected by ASR is not pronounced compared to tensile and modulus of elasticity such as by (*ISE*, 1992). In the study by Munir et al. on a cube of 25 mm using ASTM C 227 and ASTM C1260 for exposure up to 6 months, only about 22% to 25% strength was retained (Munir et al., 2017). Other studies have reported a reduction of up to 60% (Canadian Standards Association, 2000; Fournier et al., 2010; *ISE*, 1992). The study by Hobbs on 14 years old cubes found a reduction of about 15% strength for cubes that had undergone 1500 to 3000 microns expansion (Hobbs, 1986). In a similar study, Swamy found a reduction of strength by 63% at the end of one year (Swamy & Al-Asali, 1986). It must be noted that the compressive strength depends on the

degree of expansion. A comparison of these studies and some additional studies is shown in Figure 2-3.

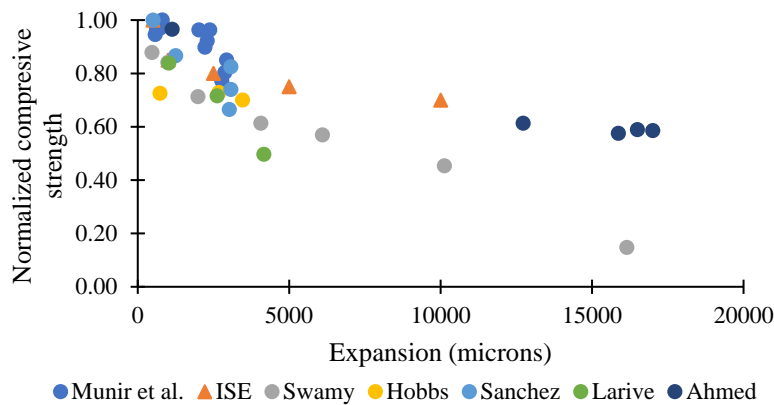


Figure 2-3 Variation of compressive stress with ASR expansion

The change in strength and ASR expansion is likely to be related to the hydration reaction. When the hydration graph (which is a curve showing strength gain over time for normal concrete) is plotted together with the expansion graph of ASR affected specimen, we can see that the expansion is accelerated in the same period when the hydration is attaining its ultimate value. Figure 2-4 shows one such figure by plotting data from Price (1951) and Ahmed et al. (2003). If hydration continues along with ASR, the degradation due to ASR could be compensated with the formation of new hydration products. This could be a reason for not a significant reduction in compressive strength, especially when ASR is accounted as a slow reaction in the field. Even in a laboratory setting, ASR expansion is significantly slower compared to DEF.

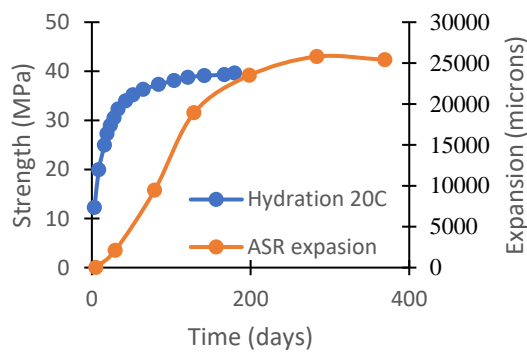


Figure 2-4 Expansion due to ASR and hydration of normal concrete based on Price (1951) and Ahmed et al. (2003)

The degree of reactivity of aggregates directly influences the compressive strength. The study by Marzouk & Langdon (2003) showed the reduction in strength is more significant in highly reactive aggregates compared to the moderately reactive aggregates. In the field study by Yurtdas et al., the cores taken from ASR affected structures showed an increase in compressive strength compared to 28-day compressive strength for mild and moderate reactive aggregate (Yurtdas et al., 2013). Barbosa et al.'s field study on severely damaged bridge slabs

indicated that the compressive strength is directly affected by the orientation of the cracks produced by ASR. The compressive strength parallel to the ASR cracks was found to be higher than the compressive strength in the perpendicular direction (Barbosa et al., 2018).

2.3.2. Change in tensile strength

ASR causes a significant reduction in the unrestrained tensile strength of concrete. The reduction depends on the level of expansion. The splitting tests done by Hobbs with 100 mm cubes (Hobbs, 1986) found about 20% reduction in strength when expansion reached about 5000 micros (0.5%). In a similar study, Swamy and Al-Asali tested cylinders of 100 mm diameter x 200 mm height and found a reduction of about 60% in compressive strength (Swamy & Al-Asali, 1986). These data are shown in Figure 2-5. The rate of reduction in the splitting strength was higher than the reduction in compressive strength.

Smaoui et al. found that the concrete with high alkali can reduce the tensile strength (direct tensile strength test or splitting test). Similar to compressive strength, there was a gradual decrease in tensile strength over time (Smaoui et al., 2005). However, the expansion data is missing in their study, hence a direct comparison with other studies cannot be made.

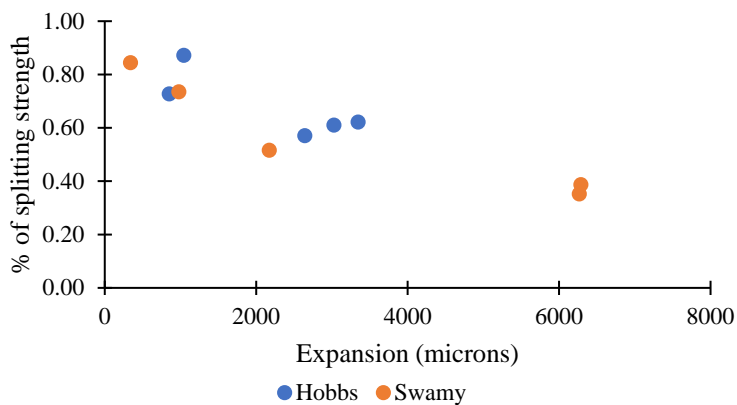


Figure 2-5 Splitting strength of ASR affected concrete

2.3.3. Change in bond strength

The early experiments by Chana reported that ASR does not have a detrimental effect on the bond strength of plain bars, in fact, there is an increase in bond strength. In the case of the ribbed bar, the bond was reduced by 40% when the concrete expansion was in the range of 4000 microns (the maximum strain observed in the UK at the time of the experiment) (Chana, 1989). Chana also observed that the bond strength of bars in the core regions was reduced, even though no explanation was provided for the reduction. Further studies have indicated that ASR cracking could be the main reason for the reduction in bonding capacity. ASR has shown to cause delamination of the cover concrete meaning a complete loss of bonding between concrete and steel. Cracks wider than 0.3 mm can cause complete loss of bond. According to CSA, expansion of 6000 microns can cause loss of bonding. Another study by Ahmed et al. showed that ASR had an insignificant influence on the bonding of spliced reinforcement especially when they were short because the failure was controlled by the load-carrying capacity rather

than the bond itself (Ahmed et al., 1999). For longer laps greater than twelve times the bar diameter, the ASR caused about a 20% loss in bond strength. The ISE also proposed a relationship to take the effect of the bond as follows:(ISE, 1992)

For ribbed bar

$$f_{bs} = \alpha(0.5 + c/d) * f_t$$

For plain bar

$$f_{bs} = \beta * f_t$$

Where f_{bs} =characteristic bond strength

α = coefficient between 0.60 to 0.30

β = coefficient between 0.33 to 0.65

c = cover

d = bar diameter

The recent study by Li et al. (2020) indicated that there is a threshold value of about 350 microns (0.035%) in the ASR expansion up to which the bond strength was improved, which they attributed to the pore pressure. After exceeding the threshold, the bond strength gradually decreased.

Huang et al. (2014) developed a probabilistic model for steel-concrete bond behaviour considering the effects of ASR based on load testing data of bridge columns. A finite element model was established to assess the parameters in the bond-slip model through a Bayesian approach. It was found that the bond strength initially increases with the increase of ASR effects but decreases when ASR deterioration reaches a certain level as shown in Figure 2-6.

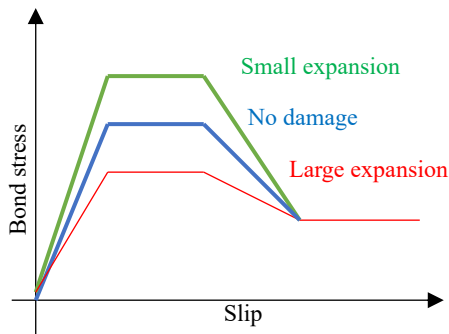


Figure 2-6 Change in bond strength with the expansion of ASR

2.3.4. Change in modulus of elasticity

Elasticity is the main material parameter needed for predicting the deflection of the structure. It has been found that the unrestrained concrete shows a significant loss in modulus of elasticity. A collection of data on the reduction of strength based on Giaccio et al. and some other authors is shown in Figure 2-7. The reduction can be 30-80% (Monette et al., 2002). In the case of reinforced concrete, ASR did not have a significant effect. (Canadian Standards Association, 2000)

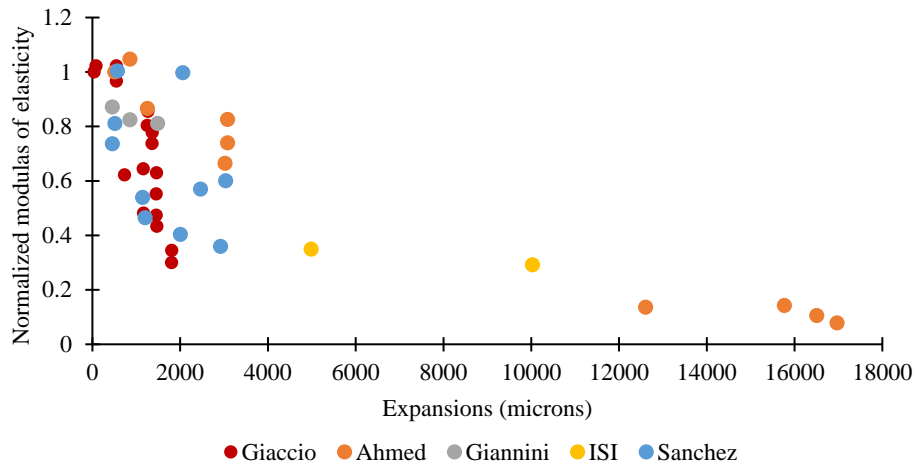


Figure 2-7 Change in modulus of elasticity due to ASR expansion (Giaccio et al., 2008)

2.3.5. Change in shear strength

The ISE reported that with a presence of about 0.2% shear stirrup, ASR did not affect the shear capacity (*ISE*, 1992). A similar study by Deschenes et al. has shown that if adequate shear reinforcement is provided, ASR does not cause a loss of shear strength. (Deschenes et al., 2009). In their study, even at the expansion level of 5400 microns, there was no reduction in shear strength with a stirrup ratio of 0.15% and 0.31%.

2.3.6. Change in flexure strength

The flexure capacity of the reinforced beam was not affected by ASR even though there was a decrease in the elastic modulus and tensile capacity (Monette et al., 2002). In the experiment, Monette et al. initiated ASR expansion of about 3000 microns and did the structural test. Regardless of expansion level, the beams failed at a similar load to that of non-affected beams even though the stiffness of ASR affected cylinders was much lower than the control cylinders. Monette et al. found that the damage rating index values for given elastic modulus had no reliable relationship with the ultimate flexural load or the compressive strengths of the cylinder.

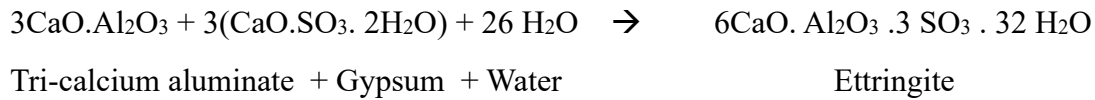
2.4. Delayed ettringite formation

Delayed ettringite formation (DEF) is an expansive reaction associated with the alteration of the chemical composition of concrete that have been subjected to elevated temperatures while it was solidifying. DEF can be found mostly in precast concrete that is steam cured; however, cast-in-place concrete might also have this kind of problem especially in mass concrete in which the heat of hydration could raise the temperature of concrete. The ambient temperature in hot regions of tropical countries can be over 30 °C during all seasons, which can cause the concrete temperature to rise above the limiting temperature. In a tropical climate such as Sri Lanka, map cracking was discovered in a massive concrete pile (Nanayakkara, 2011). In India, it has been suggested that DEF could occur in precast concrete sleepers due to a high curing temperature over 70 °C (Awasthi et al., 2017).

DEF occurs when the internal temperature of the concrete reaches about 70 °C or higher

during the early hydration. The high temperature decomposes ettringite into mono sulphate. The excess sulphate is trapped in the early hydrates, mainly in the calcium silicate hydrate (C-S-H). The sulphate is then released back into the hardened stage and monosulphate is crystallized to form ettringite. The expansive force causes cracking in the cement paste. A simplified DEF mechanism is illustrated in Figure 2-8.

At 20°C



At 70°C or higher

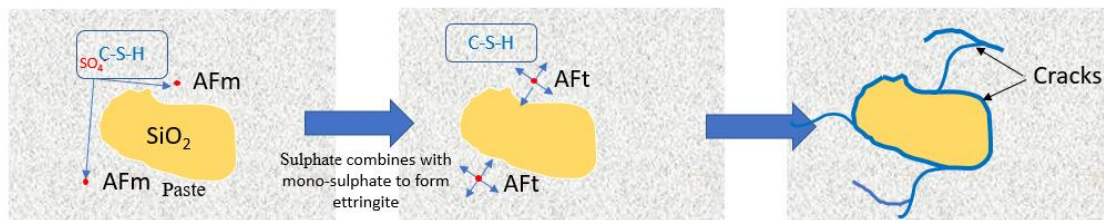
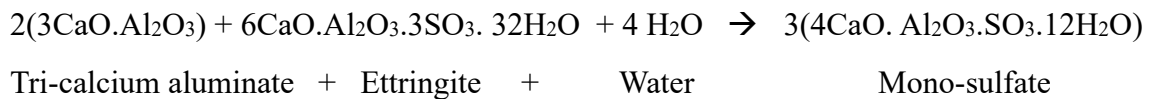


Figure 2-8 Mechanism of delayed ettringite formation

Odler (1981), and Fu (1996) postulated that sulphates and calcium aluminates were trapped by physical adsorption in C-S-H gel layered, where hydration has been accelerated as a result of heat curing. A curing temperature of about 70 °C causes acceleration of C-S-H formation which helps to trap sulphates. The remaining sulphates form ettringite and monosulphate. At the hardened stage, the sulphates slowly diffuse out of the C-S-H gel and enter into the pore solution. The diffusion acts as an internal source of sulphate and triggers the reformation of ettringite. Scrivener & Lewis (1997) verified this trapping theory by using an SEM/EDS. Scanning electron micrographs (SEM) show that ettringite occurs in concrete in various forms, often as clusters of ettringite crystals. Many studies indicated that there was an expansion during subsequent storage in the water of the mortars cured at high temperatures (70-90 °C) while lack of moisture did not cause any expansion. Thus, similar to ASR, the availability of moisture is one of the main requirements for DEF (Hanehara & Oyamada, 2010).

2.4.1. Factors influencing DEF

a. Curing temperature

An elevated curing temperature greater than 70 °C is the main cause of DEF. Higher temperature destabilizes ettringite and gets transformed into monosulphate. Stark & Bollmann (1999) postulated that the ettringite transforms to monosulphate at a temperature between 70 and 90 °C. There is an experimental agreement that 70°C is the threshold temperature, below that temperature, the probability of DEF expansion is low. Ramlochan et al. (2003), found that

the ultimate expansion of mortars increases with the increase of curing temperatures. Similar results were found by Kelham (2004) and by Taylor et al.(2001). Other researchers have found that the DEF can occur even at a lower temperature (Diamond, 1996).

b. Chemical composition of cement

It has been suggested that the risk of DEF expansion can be reduced by using low alkali cement or low in SO₃, C₃A, and C₃S Ramlochan et al. (2003). Zhang et al., (2002a) suggested that high SO₃ content in cement and SO₃ / Al₂O₃ molar ratio could be the main factor for DEF because, without SO₃, ettringite cannot be formed. Some ettringite can be present at the end of the heat treatment in the presence of excess SO₃. In the absence of Al₂O₃, ettringite cannot be formed. However, if Al₂O₃ content is high, ettringite could be absent. Taylor et al. (2001) suggested that the pessimum of SO₃ trends to increase with the content of Al₂O₃. Zhang et al.'s (2002b) result indicated that the maximum expansion occurs when the molar ratio is about 1.00 which led to the concept of DEF index as given below.

$$\text{DEFIndex} = \left(\frac{\text{SO}_3}{\text{Al}_2\text{O}_3}\right)_a \times \left[\frac{(\text{SO}_3 + \text{C}_3\text{A})_b}{10}\right] \times \sqrt{\text{Na}_2\text{O}_{\text{eq}}} \quad 2-1$$

where; (SO₃ / Al₂O₃)_a is the molar ratio of SO₃ to Al₂O₃ of the cement,

(SO₃ + C₃A)_b is the combination of SO₃ and C₃A %wt in the cement

$\sqrt{\text{Na}_2\text{O}_{\text{eq}}}$ is the square root of Na₂O_{eq} %wt in the cement

Expansion is favoured by high alkali cement that has high SO₃ content as well. Taylor et al.(2001) suggested that the increased alkali content tends to increase the rate of alite (C₃S) hydration at early ages and absorbs SO₃. This helps the formation of ettringite later causing an increase in expansion. Zhang et al.(2002a) suggested that high C₃A content is required for DEF development.

c. Specific surface area

The heat of hydration of cement and DEF susceptibility increases with the increase of cement fineness. Experiment with mortars specimens indicated that there is a potential increase in expansion with increasing specific surface area (Kelham, 1996). Another similar experiment by Tosun (2006) with 3 different fineness of 3000, 4000 and 5000 cm²/g showed that the effect of specific surface area has no significance in the short period; however, the rate of expansion of mortars prepared with finer cement exceeded those of the coarser ones in long duration.

d. Properties of aggregates

Aggregate properties also have effects on DEF. Grattan-Bellew et al.(1998) experimented with mortar bars made with six different types of aggregate. The results indicated that only the mortar bars made with quartz aggregate showed significant expansion, and the expansion had an inverse relationship with the particle size. Similar results were obtained by Fu et al. (1997). They also found that mortar bars made with finer sand containing high quartz content had larger expansion than those made with limestone. Brunetaud et al. also found that the specimen did not swell beyond 0.2% (2000 microns) and dynamic modulus of elasticity was not affected

(Brunetaud et al., 2008).

Al Shamaa et al. tested the mortars bars made with limestone filler as aggregates. They found that limestone filler had no effect on the delayed ettringite formation. The filler only changed the kinetics of the swelling. Larger filler size aggregated increased the swelling (Al Shamaa et al., 2016) which is contrary to the result by Fu et al. Similarly, the larger proportion of limestone filler only increased the rate of swelling, however, the final swelling remained similar for all mix.

e. Pore solution

The DEF expansion was suppressed when the specimens were stored in saturated air rather than in tap water. Storing specimens in an alkali solution could reduce the expansion. In both cases, the reduction of the expansion is due to a lack of the prevention of alkali leaching. The alkali leaching drastically alters pore solution chemistry and influences the DEF-related expansion. However, storage in an alkali solution might have a possibility to accelerate ASR as mentioned in the ASR chapter.

f. Microcracks

Microcracks are fully or partially responsible for DEF expansion. Shimada (2005) had shown that the ettringite preferred to form in crack tips rather than on the surfaces, thus the critical sites of expansion are the existing cracks. The study by Ekolu et al., (2007) also found that microcracking can promote DEF.

2.4.2. Test methods for DEF

There are no specific tests advised by codes for DEF. One of the tests that were extensively used was the Duggan test. The test was initially developed as an accelerated test for the potential alkali aggregate reactivity. Careful observation from this test can be used to determine that DEF as well. The test involves the following procedure (Day, 1992).

- Concrete cores with a diameter of 25 mm and height of 65 mm are taken from real structures or cast in a laboratory. The specimens are cut to 50 mm length making both ends smooth and parallel and the initial length is measured.
- Specimens are then submerged in distilled water for 3 days at 70 °F in a closed container.
- After 3 days, the specimen is placed in an oven at 180 °F for 1 day.
- Then the specimens are cooled for 1 hour and placed back in distilled water for 1 day.
- A second cycle is performed by heating the sample for 1 day heating and soaking it for 1 day.
- Next, the third cycle is performed. In this cycle, the specimens are left in the oven at 180 °F for 3 days.
- At the end of the third heating cycle, the cores are removed from the oven and allowed to cool for 1 hour, and the reading is taken to use as the zero points for further strain readings.
- The specimens are submerged in distilled water at 70 °F and the length measurement is

done at an interval of 3 to 5 days

The Duggan test has been progressively abandoned because Lawrence et al. (1999) pointed out that Duggan’s heating cycle does not represent practical heating regimes, and the heating cycle is severe. Later, test methods by Fu (1996) and Kelham (1997) were developed considering the shortcomings of previous methods.

a. Fu’s Method

Fu (1996) developed a DEF acceleration test by following a typical precast concrete curing cycle. Fu’s method includes an extreme drying cycle to trigger microcracking as illustrated in Figure 2-9. The specimens are pre-cured in a moist environment for 1 hour followed by curing temperature within the next hour. The specimens are held for 12 hours at the desired curing temperature, and then the temperature is dropped to 20 °C within 4-hour. Next, the moulds are removed, and the specimens are stored in water for 6 hours before taking a zero reading. And then, the specimens are exposed to a drying cycle for 24 hours at a temperature of 85 °C. This drying cycle is used to introduce microcracks in the cement paste.

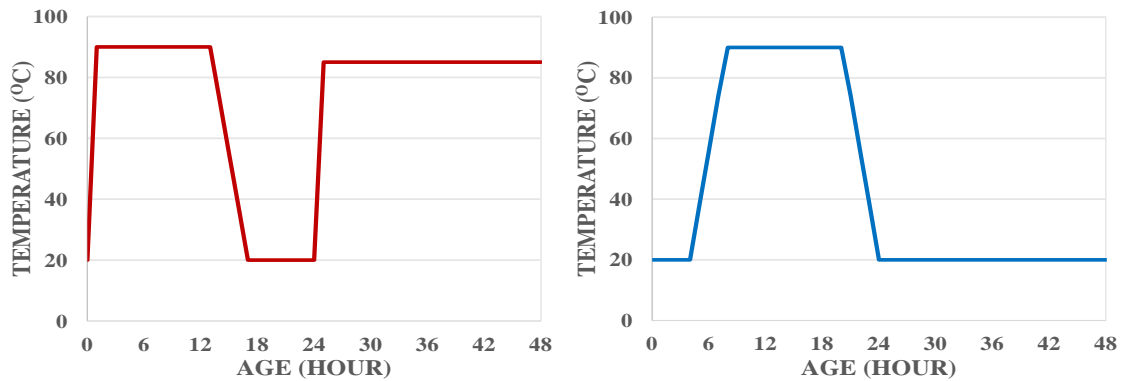


Figure 2-9 Curing temperature cycle used in (a)Fu’s method and (b)Kelhem’s method

b. Kelham’s Method

Kelham (1997) method is similar to Fu’s method except that the specimens are not subjected to the drying cycle. Kelham tested more than 70 cement compositions and evaluated the expansion in different curing temperatures of 23, 70, 75, and 90° C. The results indicated that the only temperature which consistently provided the expansions is the temperature of 194 °F (90 °C). He concluded that expansion tends to increase with the increase of cement fineness, alkali content, C₃A and C₃S content, and also MgO content. He also suggested an equation to account for the fineness and chemical composition of the cement as follows:

$$\text{Expansion at } 90\text{ }^{\circ}\text{C} = (0.00474 \times \text{SSA}) + (0.0768 \times \text{MgO}) + (0.217 \times \text{C}_3\text{A}) + (0.0942 \times \text{C}_3\text{S}) + (1.267 \times \text{Na}_2\text{O}_{\text{eq}}) - (0.737 \times \left[\text{SO}_3 - 3.7 - [1.02 \times (\text{Na}_2\text{O})_{\text{eq}}] \right]) - 10.1$$

2.5. Mechanical effect of DEF expansion

The mechanical studies on DEF affected structures are limited. Due to a close relation of DEF with ASR, sometimes the studies in DEF are also combined with ASR. A list of recent

publications in the field of DEF focusing on mechanical behaviour is listed in Table 2-5.

Table 2-5 Summary of research about the mechanical effect of ASR expansion

Author (Year)	Studied properties and description
Rocco et al.(2004)	Specimen type: Concrete prism(100×75×400 mm) At an expansion of 1.56% (15600), a drop of 60% tensile strength and an 80% drop in elastic modulus were found.
Brunetaud et al.(2008)	Specimen type: Concrete cylinder (ϕ110×220 mm) In 700 days the concrete expanded by 1.28% (12800 microns) and strength was reduced from 41.3 N/mm ² to 14 N/mm ²
Bouzabata et al., (2012b).	Specimen type: Mortar prisms (40×40×40 mm) At the expansion of 1.69% (16900 microns), the strength of concrete reduced from 46.5 N/mm ² to 25.6 N/mm ²
Al Shamaa et al. (2014)	Specimen type: Concrete cylinder (ϕ 110×220 mm) At the expansion of 0.27% (2700 microns), the strength of concrete changed from 31.1 N/mm ² to 31.6 N/mm ²
Martin et al.(2017)	Specimen type: Concrete cylinder (ϕ 110×220 mm) In 600 days the concrete expanded by 1.4% (14000 microns) and strength was reduced from 31.5 N/mm ² to 3.5 N/mm ²
Giannini et al., (2018)	Specimen type: Concrete cylinder (ϕ 100×200 mm) At the expansion of 1.01% (10100 microns) the strength of concrete changed from 27.4 N/mm ² to 15.9 N/mm ² and elasticity reduced from 23.1 N/mm ² to 5.8 N/mm ² At the expansion of 0.45% (4500 microns), the strength of concrete changed from 33 N/mm ² to 25.1 N/mm ² and elasticity reduced from 23.6. N/mm ² to 9.6 N/mm ²
Sanchez et al., (2018)	Specimen type: Concrete cylinder (ϕ 100×200 mm) At the expansion of 1.9% (19000 microns), the strength of concrete changed from 35 N/mm ² to 17.85 N/mm ²
Karthik et al.(2018)	Numerical models were proposed to capture expansion due to DEF

2.5.1. Change in compressive strength

The study by Yan et al.(2004) on reinforced specimens noted that although some specimens exceed four hundred micro strains, no cracks were observed. They concluded that DEF does not result in the deterioration of affected structures. This observation is however not justified by other observations. One reason is that their specimen did not expand enough. The

data from Brunetaud et al. (2008), Al Shamaa et al. (2014) and other researchers have shown that there is a gradual reduction of strength reaching up to 34% at an expansion of about 13,000 microns (1.3%). The strength reduction by these authors and some other authors are shown in Figure 2-10. It can be observed that there is a scattering of data, nonetheless, the trend is a gradual loss of compressive strength.

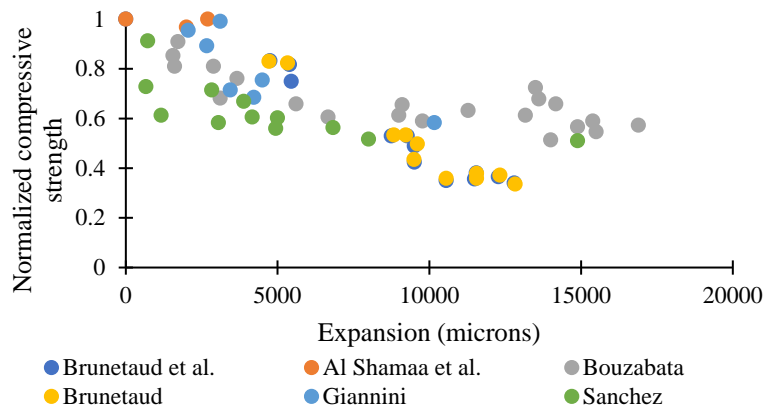


Figure 2-10 Reduction in compressive strength due to DEF

2.5.2. Change in tensile strength

There are very few tests done to measure the tensile strength of concrete affected by DEF. In a test by Rocco et al., a reduction of 60% tensile strength was recorded at an expansion of 1.56% (15600 microns) as shown in Figure 2-11 (Rocco et al. 2004)

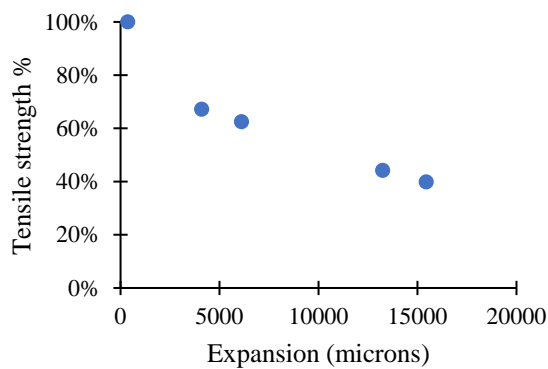


Figure 2-11 Reduction in tensile strength due to DEF based on Rocco et al.

2.5.3. Change in bond strength

No studies were found related to the reduction in flexure strength due to DEF to this researchers' knowledge and study at the time of writing this thesis.

2.5.4. Change of modulus of elasticity

In the study of the deterioration by DEF, Bergol et al. (2003) employed ultrasonic pulse velocity to correlate the deterioration with the dynamic modulus and apparent fracture toughness of concrete by curing the specimens at 95 °C.

It was expected that, with the onset and propagation of DEF, the resulting damage to the

concrete would result in reduced toughness. However, some specimens showed an increase in fracture toughness with time, while others decreased. Thus, there was no clear conclusion.

Zhang et al. (2002a) measured the dynamic young modulus of heat-treated mortar bars using the resonance frequency method. In the specimens with expansion beyond 1300 microns (0.13 %), there was a reduction in the dynamic modulus. This reduction was about 40% at an expansion of 1.7% (17000 microns). Based on the findings, they proposed a numerical correlation between expansion and reduction in dynamic modulus. A similar reduction was observed by other authors. The data from various authors are shown in Figure 2-12.

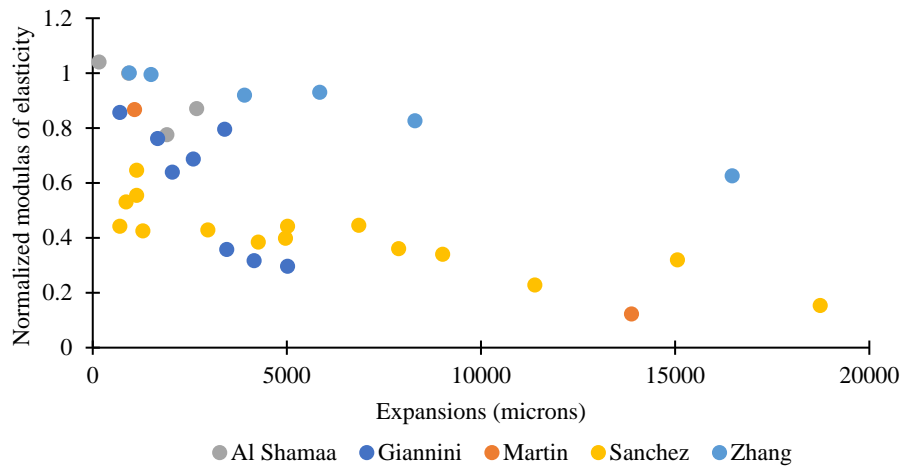


Figure 2-12 Relationship between reduction of dynamic modulus and expansion

2.5.5. Change in shear capacity

In the experiment by Deschenes et al. a full-scale beam was tested for combined DEF/ASR expansion, it was found that the expansion was capable to yield the reinforcing steel. The confinement provided by the shear reinforcement was critical to maintain the structural integrity and the concrete that was confined inside the shear reinforcement did not show any visible deterioration. This result showed a slight increase in the shear capacity of the beam (Deschenes et al., 2009). The increase could be due to the prestressing effect.

2.5.6. Change in flexure capacity

Not many studies were found related to a reduction in flexure strength by DEF. A beam test by Giannini et al. that was affected by combined ASR and DEF found that there is was no significant reduction in flexure capacity of the beam, even though the expansion had reached 6000 microns (0.6%) to 8000 microns (0.8%) (Giannini, 2012).

2.6. Combination of ASR and DEF

Although ASR and DEF have different origins and are generally studied separately, the mechanical damage process for both cases are similar. Recent studies have found that ASR and DEF could be interrelated. Thiebaut et al. (2018) observed that ASR is a prerequisite while DEF only played a contributory role in the overall expansion, in other words, DEF can occur only if the concrete has potential for ASR. Another study by (M. Thomas, 1998) also concluded

that ASR acts as a primary cause for cracking, while DEF can only act as a secondary cause for the damage. This view is based on the chemical observation that ASR causes a reduction in pH that enables precipitation of ettringite (Brown & Bothe, 1993). On the contrary, other researchers have pointed out that the formation of ettringite can increase the alkalinity of pore solution that might enhance ASR (Scrivener & Lewis, 1997). Due to a chemical interconnection between ASR and DEF, the concrete is sometimes misdiagnosed. For example, the concrete in concrete sleepers which was first diagnosed as ASR infected by Ahmad Shayan & Quick (1994) was later found to be infected with DEF and freeze-thaw action.

In a 20 years old concrete in Thailand, Baingam et al., (2012) observed ASR and DEF gel around the aggregates, voids and cracks. Another study in Thailand by Jensen & Sujjavanich (2016) also suggested a concurrent occurrence of DEF and ASR in foundation concrete. In the USA, Thomas et al. (2008) found that some concrete columns of an expressway had evidence of both ASR and DEF. Besides field observation, laboratory observations are also contradictory. Shayan & Ivanusec (1996) concluded that ASR is the main cause for expansion. In their experiment, steam-cured concrete without reactive aggregate did not show DEF even in the presence of CaSO_4 , while DEF expansion occurred when reactive aggregate was added. However, on the contrary, the study by Kelham (1996) and Sriprasong et al. (2020) found that raised CaSO_4 content caused a mild expansion while K_2SO_4 caused rapid DEF expansion. All these studies have tried to come up with some explanation to suggest which occurs first, whether it is ASR or DEF. However, it is only a hypothesis and there is no clear way to prove or reject the explanation.

From a structural viewpoint, it does not matter which phenomena occur first. The deterioration due to either of the reaction can be a concern. However, there have not been many studies on the combined cases of ASR and DEF. The early study by Sanchez et al. (2018) identified that the damage process can be divided into four stages consisting of initial cracking at the strain of about 0.05%. Then, cracks propagate from the coarse aggregate through the cement paste and ITZ in the case of ASR while for DEF, the cracks propagate from ITZ to cement paste up to 0.3% strain forming a crack network. Thereafter, debonding and disaggregation of the aggregate particles take place. The deterioration of mechanical properties due to the ASR and DEF combination remains unexplored.

2.7. Evolution of damage and mechanical tests

Sanchez et al. studied the coupled mechanical properties of concrete with expansion due to ASR, DEF and freezing and thawing with the internal microscopic damage based on the observation of stereoscopy for microcrack. In the case of DEF, the cracks formed at interfacial transition zone (ITZ) can be locally observed until an expansion of 0.12 % (1200 microns) which mainly results in a reduction of elastic modulus. At the expansion of 0.3%, the existing cracks propagate to continuously reduce the compressive strength and for expansion beyond 0.40 % (4000 microns), a strong network of crack is formed in the cement paste. And, at the expansion levels $> 0.5\%$, the debonding and disaggregation of aggregate particles occurred (Sanchez et al., 2018).

Based on the Stiffness Damage Test (SDT) proposed by Chrisp et al. (1993), Sanchez et

al. developed a method called stiffness damage index (SDI) and plastic deformation index (PDI) to evaluate the damage in the affected concrete (Sanchez et al., 2018). It must be noted that this method was first used in ASR affected concrete and then extended for DEF affected concrete. The global analysis charts to relate expansion and modulus of elasticity with SDI and Damage Rating Index (DRI) obtained by SDT were proposed for the overall distress assessment of ageing concrete. Although the mechanical degradation was associated with the internal damage at different expansion levels, the specimens need to be explicitly examined for changes in the petrographic features and DRI needs to be measured.

2.8. Numerical modelling of ASR and DEF

Due to the multiscale nature of the phenomenon from chemical reaction products level up to the structural level, the numerical models to simulate ASR and DEF have been developed with different purposes which are reviewed and categorized by Esposito & Hendriks (2019). In this thesis, the focus is on the structural level, thus the focus of the numerical models is on the evolution of expansion and strength at a given point of time. The available numerical models used for ASR and DEF are discussed in the following sections.

2.8.1. Numerical modelling of ASR

One simple method to carry out the numerical analysis of ASR affected structure is by applying an equivalent thermal expansion to imitate the ASR expansion as done by Larsen et al. (2008). A more sophisticated numerical model proposed by Ulm et al. (2000) uses thermo-chemo-mechanics which is originally based on the model by Larive & Laboratoire Central des Ponts et Chaussées (1998). This method incorporates temperature, start time, and duration of the reaction. This model was successfully used by Pourbehi & Zijl (2019) to simulate ASR expansion of Kleinplaas dam and by Pan et al. (2013) to simulate Kariba dam. Saouma et al. (2007) showed that the stress distribution can be captured correctly using this model in a parametric study. The model of Larive is described next. Due to similar expansion kinetics, the evolution of DEF expansion can also be modelled with a similar approach.

2.8.2. Model description

Thermal modelling

The temperature distribution inside the structure due to its environment can be determined using the following Equation.

$$\frac{\partial(\theta-\theta_o)}{\partial t} = D_{\theta} \cdot \text{div} \{ \text{grad}(\theta - \theta_o) \} \quad (2-1)$$

where $D_{\theta} = K/C$ is the thermal diffusivity,

K = thermal conductivity,

C = heat capacity of concrete,

θ = actual temperature, and

θ_o = reference temperature.

The boundary conditions (i.e., the surface temperature) of the dam will be in equilibrium

with the air or water temperature immediately near it, while the inner core temperature will depend on the thermal properties of the concrete.

Strain evolution due to ASR

The reaction rate of ASR at any time ‘t’ is provided by Equation 2, based on the model proposed by Ulm et al. (2000).

$$\dot{\xi}(t) = \frac{e^{\frac{t}{\tau_c}} \left(e^{\frac{\tau_L}{\tau_c} + 1} \right)}{\tau_c \left(e^{\frac{t}{\tau_c}} + e^{\frac{\tau_L}{\tau_c}} \right)^2} \quad (2-2)$$

where τ_L and τ_c are the latency and characteristics times respectively. It is shown in Figure 2-13. The latency time represents the duration required for nucleation, initiation of reaction and partial acceleration of reaction while the characteristics time represents the duration during which the reaction is accelerated and concrete starts deteriorating rapidly Saouma et al. (2015) The characteristics time $\tau_c(\theta)$ and latency period $\tau_L(\theta)$ depend on the actual temperature (θ) and the reference temperature (θ_o) as follows:

$$\tau_c(\theta) = \tau_c(\theta_o) e^{\left(U_c \left(\frac{1}{\theta} - \frac{1}{\theta_o} \right) \right)} \quad (2-3)$$

$$\tau_L(\theta) = \tau_L(\theta_o) e^{\left(U_L \left(\frac{1}{\theta} - \frac{1}{\theta_o} \right) \right)} \quad (2-4)$$

where U_c and U_L are activation energies obtained by

$$U_c = 5400 \pm 500 K, \text{ and } U_L = 9400 \pm 500K \quad (2-5)$$

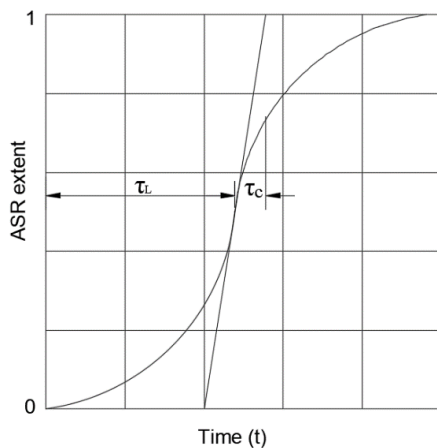


Figure 2-13 Definition of τ_c and τ_L based on the ASR extent with time

The reaction rate should be integrated over time to obtain the total reaction. The stress-free expansion owing to ASR is calculated by multiplying with the maximum possible strain $\epsilon(\infty)$.

$$\epsilon(t) = \epsilon(\infty) * \xi(t) \quad (2-6)$$

Equations 2-3 and 2-4 indicates that the ASR increases exponentially with temperature following the Arrhenius equation (Alnaggar et al., 2013).

Modulus of elasticity

The deterioration of elastic stiffness (E_0) by the ASR can be estimated using Equations 7 and 8 (Capra & Sellier, 2003).

$$E = E_0 * (1 - d_{asr}) \quad (2-7)$$

The ASR damage factor given by d_{asr} is a function of the maximum ASR strain at that time, expressed as

$$d_{asr} = 1 - \frac{E}{E_0} = \frac{\max(\epsilon(t)^{asr})}{\max(\epsilon(t)^{asr}) + B} \quad (2-8)$$

Where B is the calibration parameter approximated to 0.3%.

According to the study by Saouma et al. (2007), the degradation of Young's modulus has a small effect on the long-term deflection.

2.8.3. Numerical modelling of DEF

Similar to ASR expansion, to simulate the expansion of concrete due to DEF, three important parameters are latency time, characteristics time and final expansion. These are described in the following paragraphs.

Strain evolution due to DEF

Based on the observation that DEF expansion has similar kinetics as ASR in macro scale, Martin et al. (2012) extended the equation of Larive & Laboratoire Central des Ponts et Chaussees (1998). The strain at any instant is given by:

$$\epsilon(t) = \epsilon_\infty * \frac{1 - e^{-\frac{t}{\tau_c}}}{1 + e^{-\frac{t - \tau_L}{\tau_c}}} \left(1 - \frac{\varphi}{\delta + t}\right) \quad (2-9)$$

and the rate equation is given by differentiation the second part of the right-hand side term

$$\dot{\xi}(t) = \frac{e^{-\frac{t}{\tau_c}} \left[-\tau_c \varphi \left(1 + e^{-\frac{\tau_L - t}{\tau_c}}\right) \left(1 - e^{-\frac{t}{\tau_c}}\right) + (\delta + t)(\delta - \varphi + t) \left(1 + e^{-\frac{\tau_L}{\tau_c}}\right) \right]}{\tau_c * (\delta + t)^2 * \left(1 + e^{-\frac{\tau_L - t}{\tau_c}}\right)^2} \quad (2-10)$$

where τ_c and τ_L are the characteristics and latency times respectively. The quantity $(1 - \varphi/(\delta + t))$ is a scaling term used for curve correction, the effect of which gets diminished as t increases. From the FEM formulation perspective, this term can be neglected and the correction can be incorporated by suitably modifying τ_c and τ_L . Thus the modified rate equation will be

$$\dot{\xi}(t) = \frac{e^{-\frac{t}{\tau_c}} \left(e^{-\frac{\tau_L}{\tau_c}} + 1\right)}{\tau_c \left(e^{-\frac{t}{\tau_c}} + e^{-\frac{\tau_L}{\tau_c}}\right)^2} \quad (2-11)$$

Effect of chemical composition on expansive strain

The expansion due to DEF depends significantly on the quantity of sulphate (SO_3), aluminate (Al_2O_3) and alkalinity of the solution. Zhang et al. (2002) proposed an empirical index based on his experiment and findings from previous studies given by the following equation.

$$DEF_{Index} = (\text{SO}_3/\text{Al}_2\text{O}_3)_m \times [(\text{SO}_3 + \text{C}_3\text{A})_w / 10] \times \sqrt{\text{Na}_2\text{O}_{eq}} \quad (2-12)$$

Where,

$(\text{SO}_3/\text{Al}_2\text{O}_3)_m$ is the molar ratio of SO_3 to Al_2O_3 of the cement;

$(\text{SO}_3 + \text{C}_3\text{A})_w$ is the sum of weight percentage of SO_3 and Bogue-calculated C_3A in the cement, and

Na_2O_{eq} is the weight percentage of alkali in the cement.

Zhang et.al. plotted the expansion of cement paste as a function of the DEF index at the age of 800 days and 1400 days. The actual data of Zhang and its normalized form are shown in Figure 2-14. From their data, the expansion strain can be seen to have a linear correlation with the DEF index. The relationship can be represented by Equation 2-11. The correlation coefficient is about 0.757 for this equation.

$$\omega = \begin{cases} 0 & \text{for } DEF_{index} < 1.16 \\ -1.03 + 0.88 * DEF_{index} & \text{for } DEF_{index} \geq 1.16 \end{cases} \quad (2-13)$$

And thus, the final expansion can be represented as:

$$\epsilon_{DEF}(t) = \epsilon(t) * \omega \quad (2-14)$$

where $\epsilon_{DEF}(t)$ is the corrected strain incorporating DEF index and $\epsilon(t)$ is the predicted strain without correction.

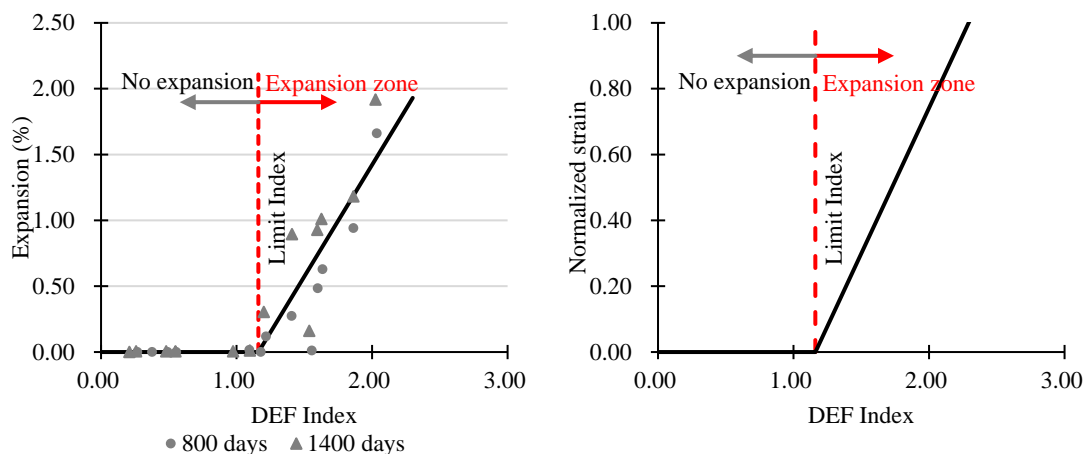


Figure 2-14 Relationship between expansion and DEF index (a) based on Zhang et al. (2002) (b) normalized for strain

Effect of early temperature and duration of temperature on maximum expansive strain

The magnitude and duration of the temperature applied while concrete is setting is the most important factor determining the rate and magnitude of DEF expansion. The limiting temperature is found to be about 65-70 °C, below this temperature DEF does not occur (Tracy et al., 2004). Experiments have shown that specimen which is cured below 65 °C, however long period, has a negligible expansion, hence this temperature can be set as the limit temperature for expansion to initiate (Brunetaud et al., 2007). Above 65 °C, the expansion effect grows exponentially with temperature. This experimental observation can be represented mathematically as :

$$\epsilon_{\infty} = \begin{cases} 0 & \theta_o \leq 338 K \\ \epsilon_{\infty o} & \theta_o > 338 K \end{cases} \quad (2-15)$$

Where $\epsilon_{\infty o}$ is the uncorrected final strain which can be estimated using Baghdadi's law (Seignol & Baghdadi, 2009) as:

$$\epsilon_{\infty o} = \alpha \int_0^{t_o} \begin{cases} 0 & \text{if } \theta < \theta_{lim} C \\ e^{\left(\frac{E_a}{R} \cdot \frac{1}{T(t)-T_o}\right)} dt & \theta \geq \theta_{lim} \end{cases} \quad (2-16)$$

Where,

$$\alpha = 6.9E10^{-4} /h ;$$

$$E_a = 438.50 \text{ J/mol} ;$$

$$\theta_{lim} = 43.30 \text{ } ^\circ\text{C};$$

$$R = 8.3145 \text{ J/mol/}^\circ\text{K and}$$

t_o is heat treatment duration in hours.

Martin et al. performed experiments to check the effect of temperature and duration of heat treatment (Martin et al., 2012). The maximum strain from their experiments is shown in Figure 2-15(a). The results from numerical prediction given by Equation 2-16 are also shown in the same figure. This indicates that Baghdadi's method is in good agreement with the experiment values. Figure 2-15 (b) shows the limiting DEF strains for various temperatures treated for one to five days in the range of 0 to 100 °C which indicates the possible cases for heating conditions. It can be seen that though the limiting temperature set in Equation 2-16 is 43.30 °C, the actual evolution of DEF expansion starts when the temperature is above 60-65 °C.

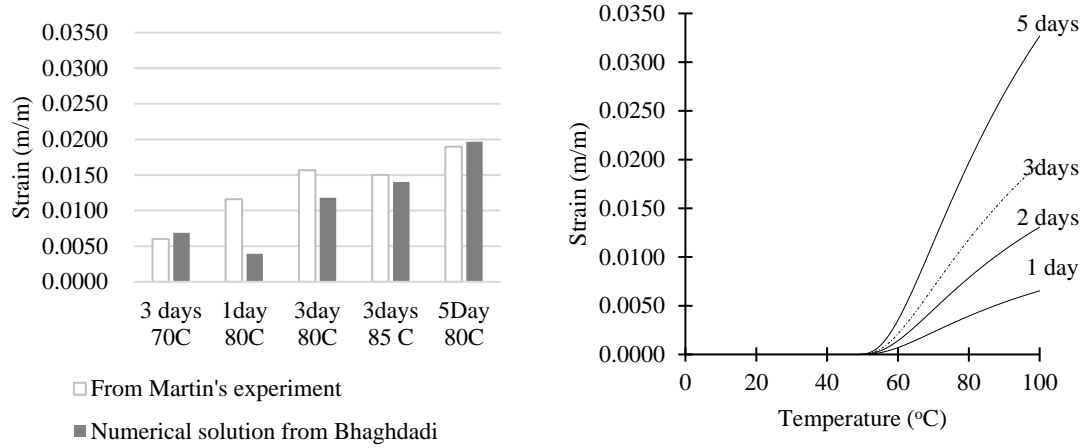


Figure 2-15 (a) Comparison of experiment and numerical values; (b) Evolution of strain by Baghdadadi.

Effect of early temperature and duration of temperature on the rate on expansion evolution

The rate of evolution of DEF expansion also depends on the early heating temperature and heating duration which is defined by the characteristics time (τ_c) and latency time (τ_L). Figure 2-16 shows the evolution kinetics of DEF strain in various specimens that were treated at various temperatures and heating duration Martin et al. (2012). To capture the effect, certain modifications should be applied to the characteristics time and latency time.

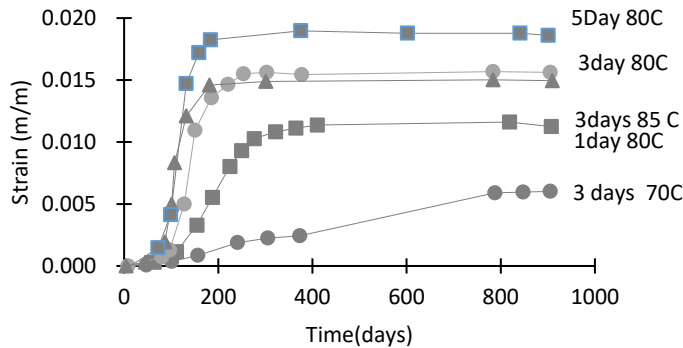


Figure 2-16 Evolution of strain for various temperatures and duration of curing condition (Martin et al. (2012))

These modifications can be done by defining two parameters α and γ and rewriting the equation for τ_c and τ_L as follows:

$$\begin{aligned} \tau_C &= \tau_{C0} * \alpha_1 * \gamma_1 \\ \tau_L &= \tau_{L0} * \alpha_2 * \gamma_2 \\ \epsilon_{\infty} &= \epsilon_{\infty 0} * \alpha_3 * \gamma_3 \end{aligned} \tag{2-17}$$

Where τ_c and τ_L are the base value for characteristics and latency time respectively.

A regression analysis from Martin's equation gives the following equation for

modification parameters :

$$\begin{aligned}\alpha_1 &= \frac{1}{0.597 + 0.018 * t_o} & \gamma_1 &= \frac{1}{-165 + 0.487 * \theta_o} \\ \alpha_2 &= \frac{1}{0.834 + 0.007 * t_o} & \gamma_2 &= \frac{1}{-38.89 + 0.116 * \theta_o} \\ \alpha_3 &= 0.845 + 0.007 * t_o & \gamma_3 &= -32.42 + 0.098 * \theta_o\end{aligned}\quad (2-18)$$

Where,

t_o = duration of heat treatment

θ_o = temperature of heat treatment in °K

Effect of external temperature and humidity

In the solid state, DEF expansion is suppressed by higher temperatures. Christensen et al. found that the increased temperature beyond 48°C in a hardened state prevents the reformation of ettringite experimentally (Christensen et al., 2004). Lothenbach et al. successfully verified the experimental result using a thermodynamic simulation (Lothenbach et al., 2008). Lothenbach et al. also predicted the inaccuracy in measurement at which monosulphate can be transformed to ettringite is in the range of ± 0.1 log units which transforms into 42-54°C. It can be noted that this temperature is very close to the limiting temperature of Baghdadadi (43.3 °C). Hence for generality, we can use the same limit. Based on the discussion, we can write a step function for DEF expansion as

$$F = \begin{cases} 1 & \theta \leq 316.15 \text{ K (43°C)} \\ 0 & \theta > 316.15 \text{ K (43°C)} \end{cases} \quad (2-19)$$

The temperature distribution inside the concrete volume can be calculated by the steady-state solution of the following equation

$$\frac{\partial(\theta - \theta_o)}{\partial t} = D_\theta \frac{\partial(\theta - \theta_o)}{\partial x^2} \quad (2-20)$$

where $D_\theta = K/C$ is thermal diffusivity, K is thermal conductivity and C is the heat capacity of concrete. Factor F can be multiplied directly with ϵ_∞ .

The effect of saturation can be considered exponential, as proposed by (Karthik et al., 2016). Higher the saturation, the faster the D

$$G = e^{(1 - \frac{1}{S})} \quad (S > 0) \quad (2-21)$$

Where S is the degree saturation of concrete lying between 0 and 1. The factor G is used to transform τ_L as $G * \tau_{Lo}$. The saturation by moisture can be due to permeability which can be modelled by using Darcy's equation (Xi et al., 1994).

A further description of the numerical modelling is given in the respective chapter.

3. Effect of internal restraints on ASR/DEF expansion

3.1. Background

As described in Chapter 2, the expansive behaviour of concrete due to ASR and DEF and their combined effect on unreinforced concrete have been studied by many authors such as by Yurtdas et al. (2013) and Z. Zhang et al. (2002a). However, in reality, most concrete structures use reinforcement. Thus, studies on the effect of reinforcement on expansion are important.

Thiebaut et al. (2018) studied the effect of reinforcement in laboratory level specimens and concluded that DEF expansion is isotropic for plain concrete and anisotropic in reinforced conditions. However, the anisotropy defined by them is not due to change in material properties in each direction but due to the presence of unequal steel percentage in each direction. Nonetheless, from their experiment, it can be observed that the restraint by internal reinforcement can substantially change the expansion behaviour of concrete. The effect of restraint on the manifestation of ASR and DEF reaction was also studied by Morenon et al. (2017) and Bouzabata et al. (2012b) respectively. Studies by Allard et al. (2018) and Karthik et al. (2016) focused on strength of beams and slabs. They found that there is no substantial decrease in beam capacity if sufficient reinforcement is provided. Given the fact that expansion can reduce the strength parameters such as compressive strength, tensile strength and elasticity significantly, the findings that large beam has no effect due to expansion indicates there are some missing links.

It must be noted that there the strength of reinforced concrete mainly depends upon the bonding between steel and concrete. There are many studies on the bond deterioration of ASR related expansion, and guidelines have recommended the ways to deal with it which is described in Chapter 2. However, there are only not many studies on the interaction between steel and concrete for DEF and combined ASR and DEF infected reinforced concrete.

Thus to fill the study gap, experimental work was carried out to study the expansive behaviour of ASR, DEF and combined cases of expansion in the presence of steel reinforcement. The main objectives of this experiment are:

- a) to study the effect of steel reinforcement on expansion strain, cracking, moisture absorption, etc. due to ASR, DEF and their combined swelling
- b) to study the effect of expansion on the bonding between steel and concrete

3.2. Methodology

3.2.1. Specimen dimension

Prismatic specimens with the dimension of 100 mm x 100 mm x 400 mm were cast for each case of ASR (A), DEF (D) and combined (DA). In the reinforced specimen, the steel rebar was placed in the longitudinal direction passing through the centre of the specimen as shown in Figure 3-1 and Figure 3-2.

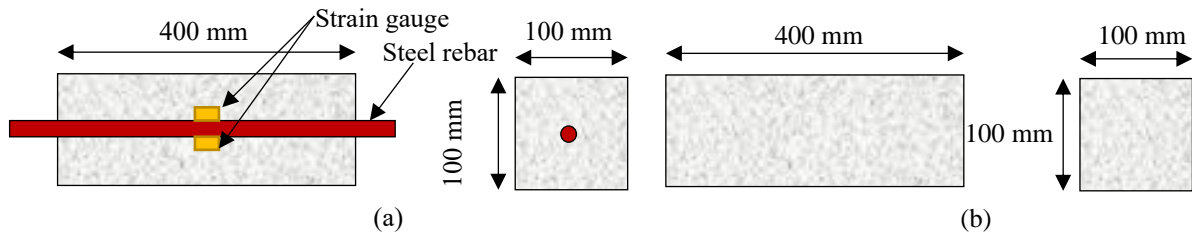


Figure 3-1 Specimen type (a) with rebar and (b) without rebar.



Figure 3-2 Photographs of the specimens during casting

3.2.2. Concrete

Three types of mix proportion were used to initiate ASD, DEF and their combination. The mix proportion is shown in Table 3-1. To initiate ASR, 30% of the coarse aggregate was replaced with the reactive aggregate. Similarly, to initiate DEF, potassium sulphate was added. In the mix to initiate both ASR and DEF simultaneously, reactive aggregate and additional potassium sulphate were added.

Table 3-1 Concrete mix proportion

SN	Sample	w/c ratio	Cement (kg/m ³)	Normal aggregate (kg/m ³)	Reactive aggregate (kg/m ³)	Fine aggregate (kg/m ³)	Water reducer (ml/m ³)	K ₂ SO ₄ (2.5% of cement, kg/m ³)
1	ASR (A)	0.50	348	602	258	770		
2	DEF (D)	0.50	348	860	-	770	1087	18.94
3	ASR+DEF (DA)	0.50	348	602	258	770	1087	18.94

Cement

High-performance cement (HPC) was used in the experiment. The main reason for using HPC is because it is used in places where faster strength is required such as in precast concrete industries. HPC generates more heat of hydration and thus there is a high risk of DEF. The composition of cement is shown in Table 3-2. For comparison, the composition of OPC is also

given in the same table.

Table 3-2 Cement composition

SN	Chemical composition	Percentage by mass	
		HPC	OPC
1	Loss on ignition (ig.loss)	0.77	2.25
2	Silicon Dioxide (SiO ₂)	20.49	20.61
3	Aluminum Oxide (Al ₂ O ₃)	5.13	5.11
4	Iron Oxide (Fe ₂ O ₃)	2.58	3.04
5	Calcium Oxide (CaO)	64.82	64.27
6	Magnesium Oxide (MgO)	1.48	0.95
7	Sulphur Trioxide (SO ₃)	3.01	2.05
8	Sodium Oxide (Na ₂ O)	0.30	0.35
9	Potassium Oxide (K ₂ O)	0.38	0.30
10	Chloride (Cl ⁻)	0.005	0.023

Aggregate

Two types of aggregate were used viz. normal non-reactive aggregate and reactive aggregate. The reactive aggregate consisted of opal, cristobalite and volcanic glasses (Kawabata et al., 2019). Sandstone was used as the non-reactive coarse aggregate. The physical properties of aggregate are given in Table 3-3. The specific density of normal aggregate was 2.66 g/cm³ and that of the reactive aggregate was 2.47 g/cm³. The maximum size of coarse aggregate was 19 mm. River sand was used as the fine aggregate with a specific density of 2.62 g/cm³ and an average particle size (D_{50%}) of 0.72 mm. The particle size distribution of aggregates is shown in Figure 3-3.

Table 3-3 Physical properties of aggregate

Physical Properties	Aggregate		
	Fine	Non-Reactive coarse	Reactive coarse
Maximum Grain Size (mm)	1.18	19	19
D ₅₀ (mm)	0.72	13.26	12.93
Specific gravity	2.62	2.66	2.47

were taken and immersed in a water tank filled with tap water at 20 °C.

Heat treatment was not done for ASR specimens. They were also stored in a water tank filled with tap water at 20 °C after 24 hours of casting.

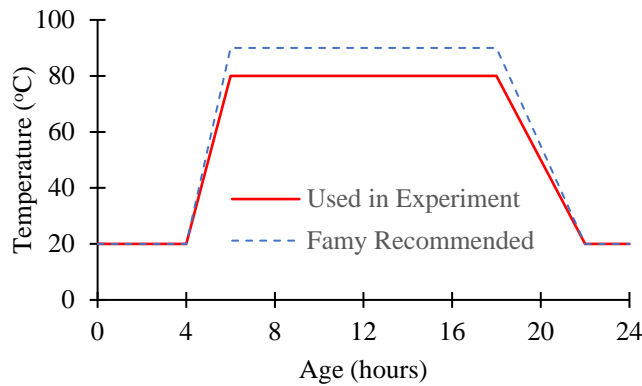


Figure 3-4 Heat treatment at an early age for DEF samples

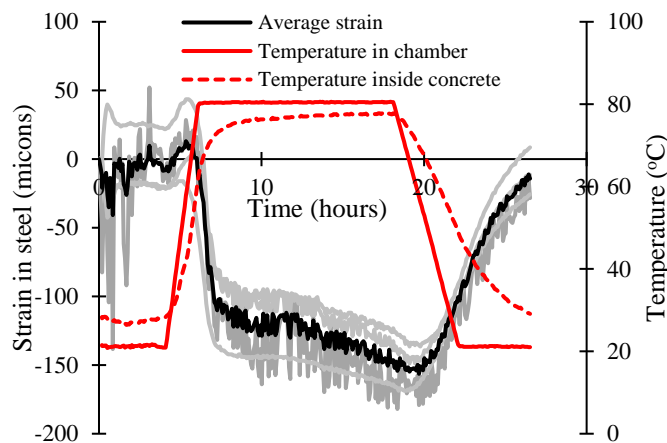


Figure 3-5 Strain measurement in steel during heat treatment

3.2.5. Measurement

The initial measurement of strain, mass and dynamic modulus was taken after 24 hours of casting the specimens. Then after measurement was taken at regular intervals. The frequency of measurement was high in the early stage, the frequency was reduced at the later stage when expansion was stabilized.

The length was measured with a contact gauge having an accuracy of 0.001 mm and a base length of about 100 mm. The mass was measured with an accuracy of 1 gram.

The dynamic Young's modulus was measured employing an acoustic method using the device MIN-011-0-10 (Serial No. 09126). Based on the resonance frequency, the dynamic Young's Modulus was calculated using Equation (3-1). The measurement complies with ASTM-E1875 -08.

$$E_d = 9.47 \times 10^{-4} \frac{L^3 T}{bt^3} mf^3 \quad (3-1)$$

where,

- E_d : Dynamic Young's Modulus (N/mm²)
- L : Length (mm)
- T : Coefficient determined by K and L
- b : Section length (mm)
- t : Vibration direction length (mm)
- m : Mass (kg)
- f : Primary resonance frequency (Hz)

3.2.6. ASR detection

To verify the occurrence and distribution of ASR, the efflorescence technique was used (Natesaiyer & Hover, 1988; Rivard et al., 2000). In this method, the specimen is cut and uranyl acetate solution is applied to its surface. After allowing about 5 minutes for reaction, the surface is dried by blowing warm air. When the surface is observed under ultraviolet (UV) light by taking a long exposure photograph. The ASR affected area glows in green colour in the photographs. The setup of the experiment is shown in Figure 3-11.

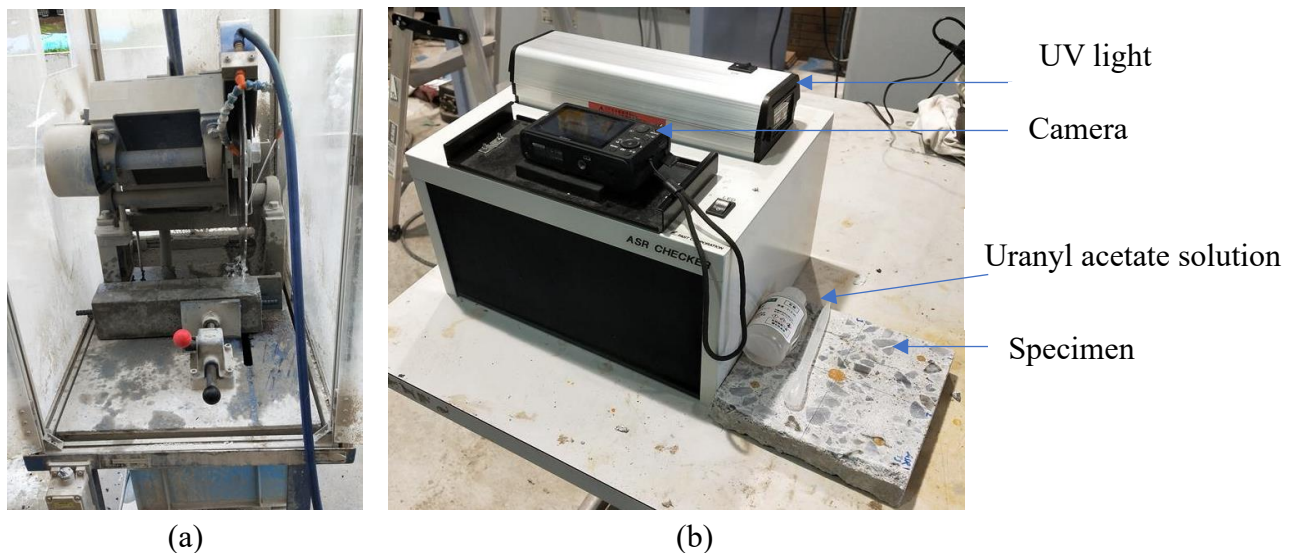


Figure 3-6 (a) cutting of specimen, (b) setup for ASR detection

3.3. Results

3.3.1. Evolution of strain in concrete

The expansion strain of the concrete prism without reinforcement is shown in Figure 3-7. The error bar shows the standard error. The combined ASR and DEF (DA) specimen had the maximum expansion reaching about 18,000 microns (1.8%) in about 150 days. The expansion was exponential between about 40-130 days. The maximum magnitude of the expansion in the DEF specimen was about 9000 microns (0.9%), the expansion was initiated between about 100 and 170 days. The ASR specimen had the lowest expansion in the range of about 300 microns

and the expansion was seen to start within few days and in about 70 days the expansion converged.

The expansion strain of concrete with reinforcement steel is shown in Figure 3-8. The expansion in the ASR specimen was much lower. The DA and DEF specimen had similar expansion reaching about 5,000 microns (0.5%) in about 180 days and 250 days respectively. Similar to the unreinforced case, the DA specimen started expansion earlier than the DEF specimen. The ASR specimen had the lowest expansion in the range of about 300 microns and the expansion was seen to start within few days similar to the unreinforced case.

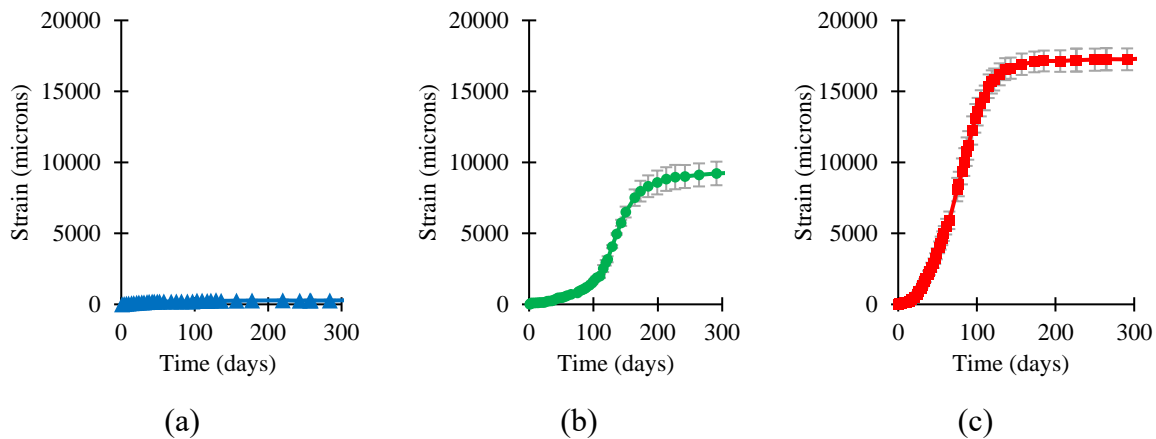


Figure 3-7 Expansion strain of concrete without steel reinforcement (a) ASR, (b) DEF and (c) DA

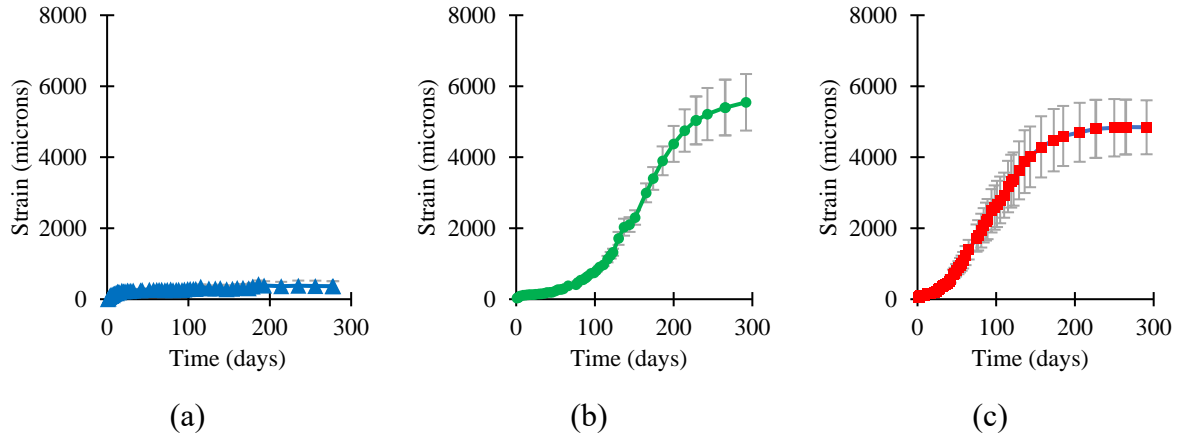


Figure 3-8 Expansion strain of concrete with steel reinforcement (a) ASR, (b) DEF and (c) ASR+DEF (DA)

3.3.2. Evolution of strain in steel

The evolution of strain in reinforcing steel is shown in Figure 3-9. The strain in steel increased gradually. Similar to the concrete strain, in the DA sample specimen, the strain evolution began ahead of DEF and ASR specimens. In DA and DEF specimens the tensile strain increased up to about 650 and 420 microns respectively. Then, the strain gradually reduced and continued to the compression side almost similar to tensile strain. In the case of ASR, the tensile strain was gradually increased and was stable after about 150 days.

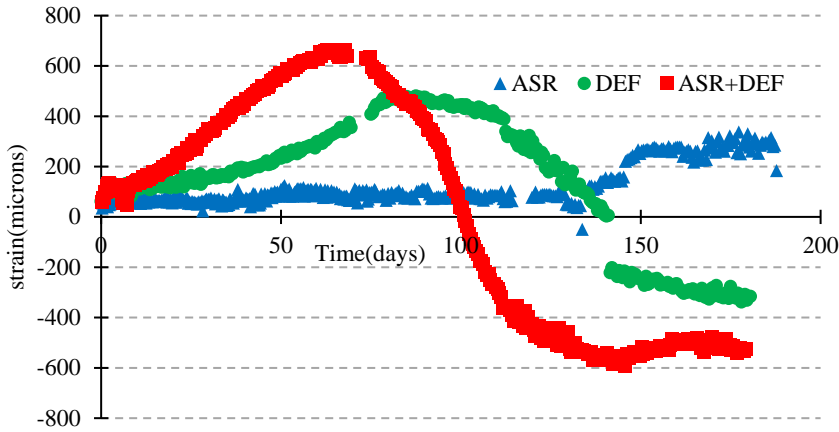


Figure 3-9 Stress in steel

3.3.3. Evolution of mass gain

Figure 3-10 shows the average mass gain (moisture absorption) for concrete for unreinforced and reinforced concrete. DA and DEF specimens absorbed more moisture than ASR. The mass gain was similar for both reinforced and unreinforced cases even though the expansion was significantly different.

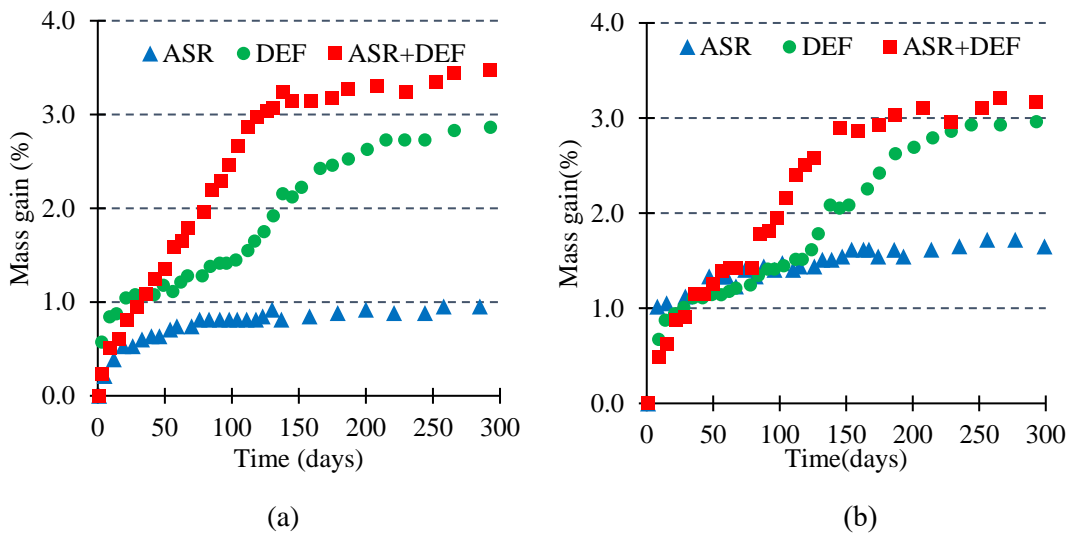


Figure 3-10 Mass gain in the sample with (a) without steel and (b) with steel

3.3.4. Evolution of dynamic modulus of elasticity

The evolution of dynamic Young's modulus of elasticity (E_d) is shown in Figure 3-11. The reduction of E_d in DA samples started from about 20 days while in DEF specimen E_d increased for about 100 days followed by a gradual decrease until it reached a minimum. After reaching a minimum value there was again mild gain. In the case of the ASR specimen, E_d continued to increase.

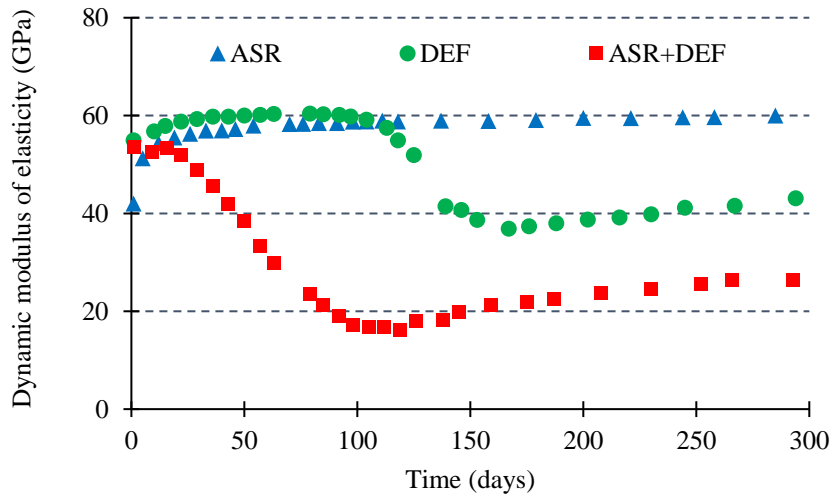


Figure 3-11 Evolution of dynamic Young's modulus of elasticity.

3.3.5. Evolution of cracks

The typical evolution of crack pattern for unreinforced and reinforced DA specimen is shown in Figure 3-12 which was prepared at the end of about 300 days. The first crack was observed in the face of unreinforced DA prisms when the strain was about 500 microns. The specimen without reinforcement had larger cracks which were distributed all over the prism body, while the specimen with reinforcement showed few cracks. The cracks in reinforced specimens were aligned in the direction parallel to the steel.

For unreinforced DEF specimens, the number of cracks was significantly less than DA specimens as shown in Figure 3-13. Similarly, for the unreinforced ASR specimens, the cracks were even less than that of DEF specimens. The photographs of the crack pattern for ASR specimens is shown in the Appendix.

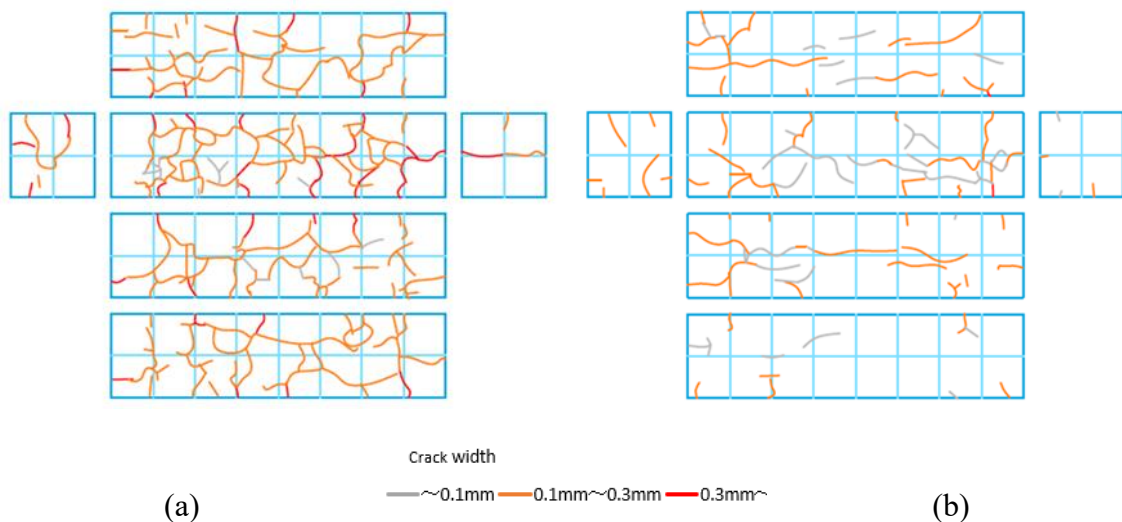


Figure 3-12 Typical crack pattern of DA specimens at the age of about 300 days (a) unreinforced specimen and (b) reinforced specimen

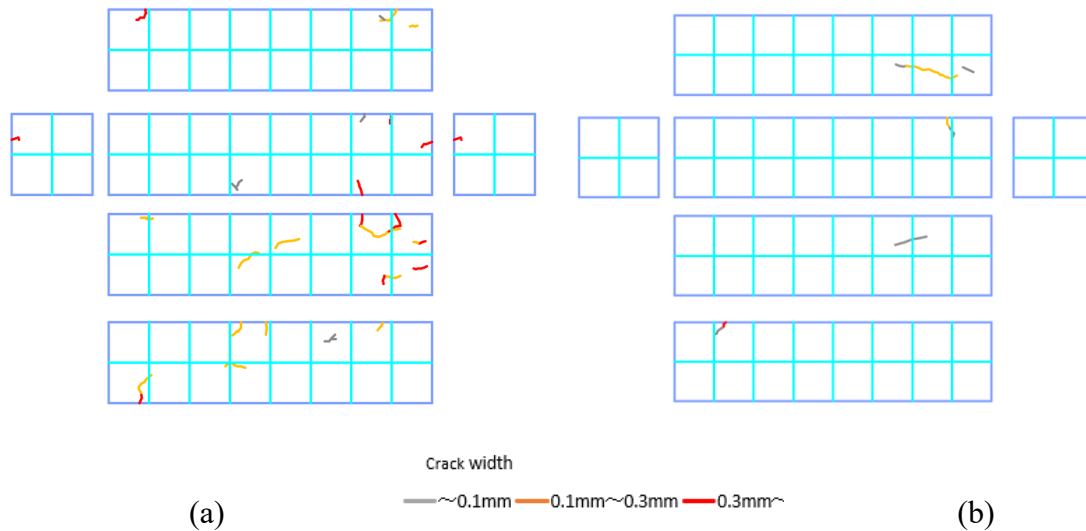
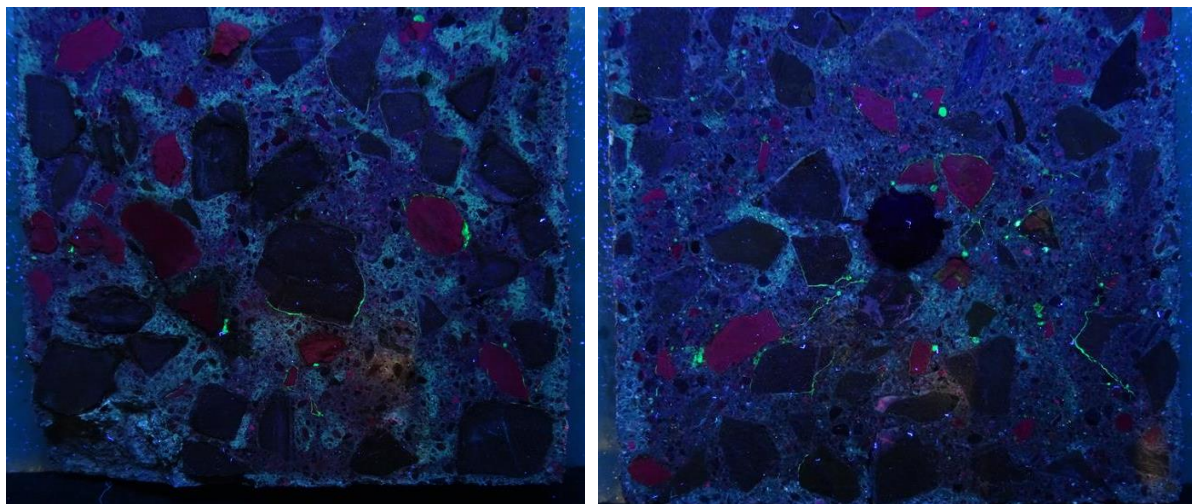


Figure 3-13 Typical crack pattern of DEF specimens at the age of about 300 days (a) unreinforced specimen and (b) reinforced specimen

3.3.6. ASR distribution

The efflorescence photographs for unreinforced and reinforced DA specimen is shown in Figure 3-14. It can be seen that both reinforced and unreinforced specimens had undergone ASR. The spatial distribution of ASR was more in the reinforced specimen compared to an unreinforced specimen. The reason for the higher content and distribution of ASR gel in the reinforced case is attributed to the larger cracks in unreinforced specimens from which the ASR gel is leached out by moisture. A similar observation was made in the experiment of Chapter 5.



(a) unreinforced specimen

(b) reinforced specimen

Figure 3-14 ASR detection in DA specimens (a) unreinforced and (b) reinforced specimen

3.4. Discussion

3.4.1. Expansion behaviour

It can be seen in Figure 3-15 (a) that the DA specimen had the maximum expansion reaching about 18,000 microns (1.8%) followed by DEF (9000 microns (0.9%)) specimen and ASR specimens (300 microns (0.3%)). This indicates that the combined effect of ASR and DEF could give rise to a very high expansion in unreinforced concrete. It must be noted that in this experiment the temperature was set at 80 °C during curing. In the similar experiment, reported in Chapters 4 and 5 of this thesis, the temperature was 90 °C for which the expansion for DEF reached a comparable range to DA specimen. This indicates that curing temperature has a significant effect on the free expansion for DEF. On the other hand, in DA specimens, the reaction was activated even at 80 °C and it could expand rapidly.

In the presence of reinforcement, the expansion for DEF and DA specimens became almost similar reaching about 5000 microns (0.5%) as shown in Figure 3-15 (b). The reason for a similar strain level is discussed in the next section.

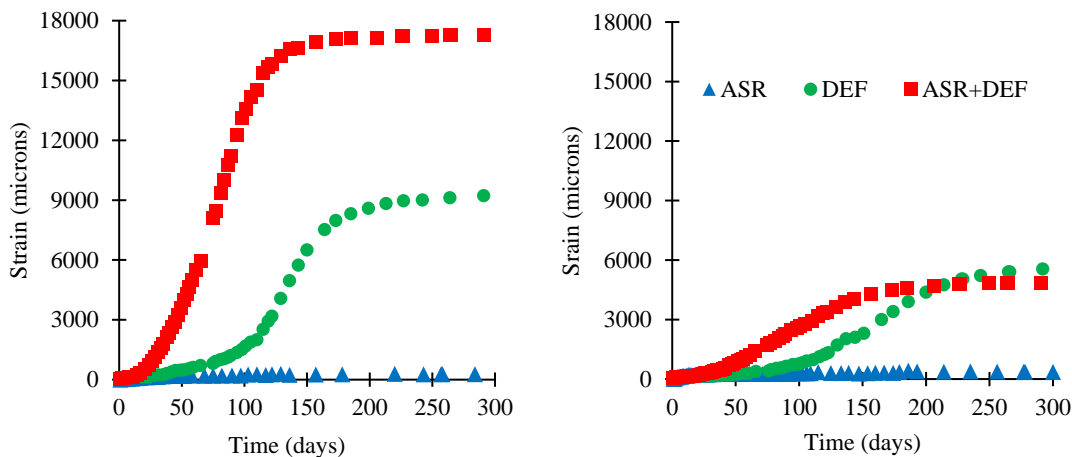


Figure 3-15 Strain evolution in (a) free specimen and (b) reinforced specimen

3.4.2. Effect of reinforcement in concrete expansion

Figure 3-16 shows the comparison of average strain between unreinforced and reinforced specimens for ASR, DEF and DA specimens. In the case of the ASR specimen, the evolution of strain was slow and the specimens with and without steel reinforcement were not significantly different as shown in Figure 3-16(a). In fact, an increase in strain was observed for the reinforced case. In DEF and DA specimens, the overall strain was higher in the absence of steel. Initially, the expansion was equal, however, on reaching about 50 and 20 days, there was a rapid increase in DEF and DA specimens respectively. The maximum strain in the reinforced case was limited to about 5000 microns (0.5%).

If the expansion of the reinforced case only is compared as shown in Figure 3-15 (b), it can be observed that the expansion of DEF and DA converge to a similar range in the reinforced case. The stress developed in the steel remains in a similar range as well (Figure 3-9). These observations indicate that the DA expansion cannot induce additional stress compared to DEF.

In other words, the additional expansion is possible only in the absence of restraints. The reason for a similar level of stress and strain for reinforced case in DA specimen even though free specimen has significantly larger expansion is unclear at this stage, however, the following phenomena is hypothesized. In the unreinforced specimen, at the early stage of expansion, both ASR and DEF contribute to the expansion. When cracks become large due to continuous expansion, ASR gel is leached out and expansion is contributed by DEF alone. The void left by ASR gel remains almost intact when the reaction progresses and hence, the expansion in DA cases becomes larger in unreinforced cases. A similar process should occur in the reinforced case at an early age, however, due to the presence of restraint, any void formed by ASR leaching is later used to accommodate the DEF expansion. This closes the previous cracks and prevents further leaching of ASR gel. Hence in the reinforced case, the apparent expansion of DEF and DA specimens reaches a similar level. Additional verification of this explanation is given in Section 5.4.2.

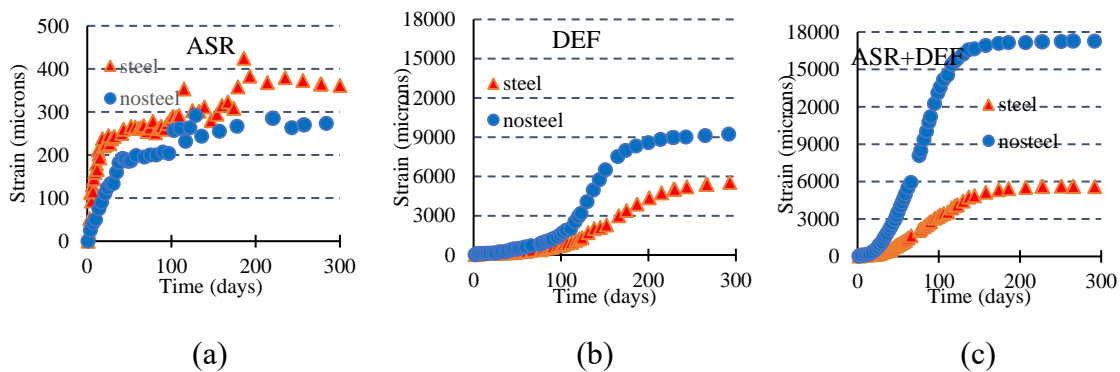
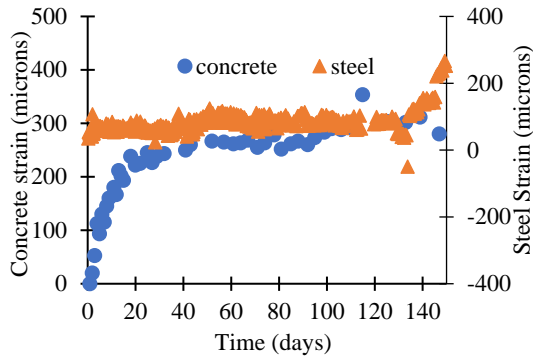


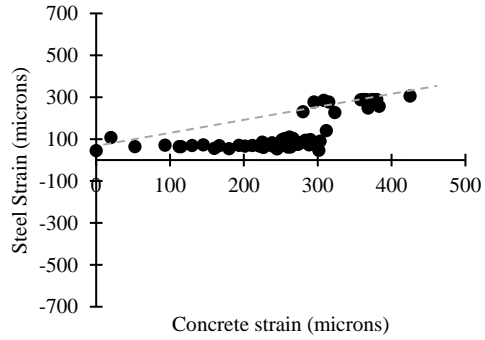
Figure 3-16 Comparison of strain in ASR, DEF and DA specimens for unreinforced and reinforced specimens

3.4.3. Relation between steel and concrete strains

The evolution of strain over time in concrete and steel and the interaction between steel and concrete strain is shown in Figure 3-17, Figure 3-18, Figure 3-19 for ASR, DEF and DA specimens respectively. In the ASR specimen, the strain is relatively small in both concrete and steel (less than 400 microns). There seems to exist a linear relationship within this stress range. In DEF and DA specimens, the concrete strains are large and the strain in steel is linear in the initial stage however, it becomes non-linear as the strain in concrete progresses. The linear relation seems to hold for up to the strain of about 500 microns. When the strain exceeded about 500 microns, strain gradually reduced. This indicates slipping of steel rebar possibly due to micro-cracking of concrete in the steel-rebar interface. Once the strain in concrete exceeds about 2000 to 3000 microns, the steel rebar experiences compressive stress.

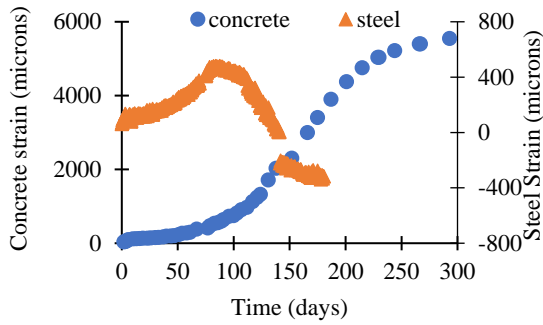


(a)

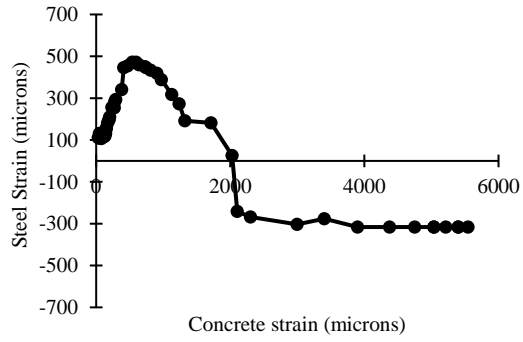


(b)

Figure 3-17 (a) Evolution of strain in steel and concrete in reinforced specimens and (b) interaction between concrete and steel strains affected by ASR

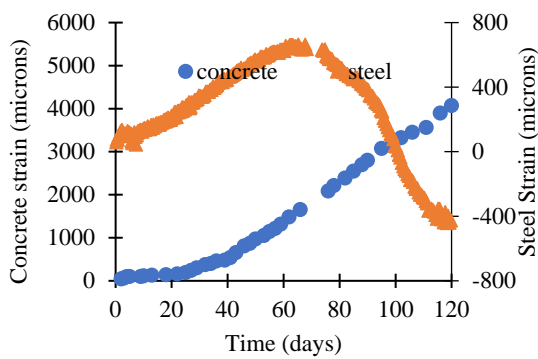


(a)

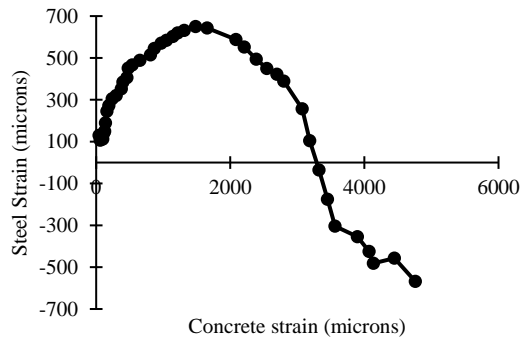


(b)

Figure 3-18 (a) Evolution of strain in steel and concrete in reinforced specimens and (b) interaction between concrete and steel strains affected by DEF



(a)



(b)

Figure 3-19 (a) Evolution of strain in steel and concrete in reinforced specimens and (b) interaction between concrete and steel strains affected by ASR+DEF

3.4.4. Effect of reinforcement in mass gain

As shown in Figure 3-10(a) and Figure 3-10(b), there was no significant difference between the unreinforced and reinforced concrete regarding moisture absorption. Since there is a significant difference in the expansion of unreinforced and reinforced concrete, it implies that there is no direct relationship between moisture absorption and expansion. However, the presence of moisture is necessary for expansion to occur, i.e. dry specimen does not expand.

3.5. Summary

In this chapter, the swelling effect of ASR, DEF and DA in reinforced and plain concrete were studied. Based on the study, the following conclusions are drawn:

- 1) In the case of HPC, the free expansion in DA specimens were significantly higher, reaching a range of about 18,000 microns (1.8%). The expansion could reach the plateau in about 150 days. The expansion in the DEF specimen was about 9000 microns (0.9%), in about 200 days. The evolution of expansion in the ASR specimen was the lowest, lying in a range of about 300 microns.
- 2) The moisture absorption for ASR was lowest and highest for DA specimens. The presence of reinforcement did not affect the moisture absorption, even though the expansion was significantly different.
- 3) There is a significant reduction in expansion due to the presence of steel for DEF and DEF+ASR combined specimens. For ASR only samples, the steel did not influence to reduce the concrete expansion significantly.
- 4) It was observed that steel can sustain a tensile strain of up to about 500 microns due to concrete expansion. When concrete expanded more, the strain in steel was reduced which is attributed to micro cracking between steel and concrete interface.

Note 1: The findings of this experiment was partially published in the ConMat20 conference titled “Study on swelling effect due to ASR and DEF on reinforced concrete”.

Note 2: The difference in expansion and other properties while using OPC and comparison with HPC is given in Appendix A.

4. Effect of external restraints on ASR/DEF expansion

4.1. Background

The restraints to the expansion can be instigated not only by the internal reinforcement as discussed in Chapter 3, but also by external elements such as by adjacent columns or by post-tensioning steel plates and tendons as shown in Figure 4-1. It must be noted that pre/post-tensioned elements are widely manufactured by steam curing such as railway sleepers. Due to elevated temperature for curing, there is a high risk of DEF.

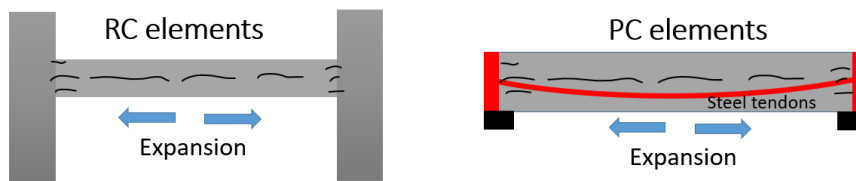


Figure 4-1 External restraints

Past studies on ASR expansion has shown that the increase in stress in the loaded direction leads to an increase in strain in the unloaded direction (Gautam & Panesar, 2017; Multon & Toutlemonde, 2010). While in the case of DEF, the stress in one direction has no (or very little) effect on the strain in the unloaded direction (Bouzabata et al., 2012b; Thiebaut et al., 2018). The behaviour of external restraint on expansion is still controversial. Moreover, there are almost no studies on the combined effect of ASR+DEF (DA) on externally restrained concrete.

To clarify the effect of external restraints, this experimental study was initiated. The main objectives of the experiment are:

- to study the swelling behaviour of ASR, DEF and DA specimens when they are externally restrained
- to distinguish the stress generated by ASR, DEF and DA expansion
- to compare the behaviour of expansion between internally and externally restrained specimens

4.2. Methodology

Prismatic concrete specimens were used in the experiment. A set of three specimens were used to measure the free strain which served as the base case and another set of three specimens were used for restraint expansion cases.

4.2.1. Specimen dimension

Six specimens with a dimension of 160 mm x 40 mm x 40 mm were cast for each case of ASR (A), DEF (D) and combined ASR+DEF cases (DA).

4.2.2. Concrete

Three types of mix proportion were used to initiate ASR, DEF and combination of ASR+DEF in the same way as described in Chapter 3 and as shown in Table 4-1. For ASR initiation, 30% of the coarse aggregate was replaced with reactive aggregate. In the concrete to initiate DEF, potassium sulphate was added. In the mix to initiate both ASR and DEF simultaneously, reactive aggregate and potassium sulphate were added.

Table 4-1 Concrete mix proportion

SN	Sample	w/c ratio	Cement (kg/m ³)	Normal Aggregate (kg/m ³)	Reactive Aggregate (kg/m ³)	Fine aggregate (kg/m ³)	Water reducer (ml/m ³)	K ₂ SO ₄ (2.5% of cement, kg/m ³)
1	ASR (A)	0.50	348	602	258	770		
2	DEF (D)	0.50	348	860	-	770	1087	18.94
3	ASR+DEF (DA)	0.50	348	602	258	770	1087	18.94
4	Normal (N)	0.50	348	860	-	770	1087	-

Cement

To accelerate the rate of reaction high-performance cement (HPC) was used. The composition of cement is shown in Table 4-2.

Table 4-2 Cement composition

SN	Chemical composition	Percentage by mass
		HPC
1	Loss on Ignition (ig.loss)	0.77
2	Silicon Dioxide (SiO ₂)	20.49
3	Aluminum Oxide (Al ₂ O ₃)	5.13
4	Iron Oxide (Fe ₂ O ₃)	2.58
5	Calcium Oxide (CaO)	64.82
6	Magnesium Oxide (MgO)	1.48
7	Sulphur Trioxide (SO ₃)	3.01
8	Potassium Oxide (K ₂ O)	0.38
9	Sodium Oxide (Na ₂ O)	0.30
10	Chloride (Cl ⁻)	0.005

Aggregate

Two types of aggregate were used viz. non-reactive aggregate and reactive aggregate. The reactive aggregate consisted of opal, cristobalite and volcanic glasses (Kawabata et al.,

2019). The non-reactive coarse aggregate consisted of sandstone. The physical properties of aggregate are shown in Table 4-3. The specific density of normal aggregate was 2.66 g/cm³ and the reactive aggregate had a specific density of 2.47 g/cm³. The maximum size of coarse aggregate was 9 mm. River sand was used as the fine aggregate with a specific density of 2.62 g/cm³ and an average particle size (D_{50%}) of 0.72 mm.

Table 4-3 Physical properties of aggregate

Physical Properties	Aggregate		
	Fine	Non-Reactive coarse	Reactive coarse
Maximum Grain Size (mm)	1.18	9	9
D50 (mm)	0.72	13.26	12.93
Specific gravity	2.62	2.66	2.47

Accelerator and Admixtures

Laboratory grade potassium sulphate in powder form was used to increase the sulphate content in the mix to accelerate the DEF reaction. 2.5% by weight of cement was used in the mix to initiate DEF.

Water reducing agent (BASF Master Pozoris ‘マスターポゾリス’ No.70 11288) was added based on the manufacturer's recommended dose as indicated in Table 4-1. This admixture reduces the unit amount of water in concrete by dispersing action of cement and air entrainment.

4.2.3. Heat treatment for DEF sample

To accelerate DEF, the maximum temperature for exposure was set at 90 °C (Famy et al., 2002) as shown in Figure 4-2. After casting the specimen, they were pre-cured at 20 °C for 4 hours under sealed conditions. After that, the specimen was exposed to 90°C for the next 12 hours. Then, the temperature was gradually reduced to 20 °C. After the heat treatment, the specimen was taken out of the mould. In normal and ASR specimens, heat treatment was not applied.

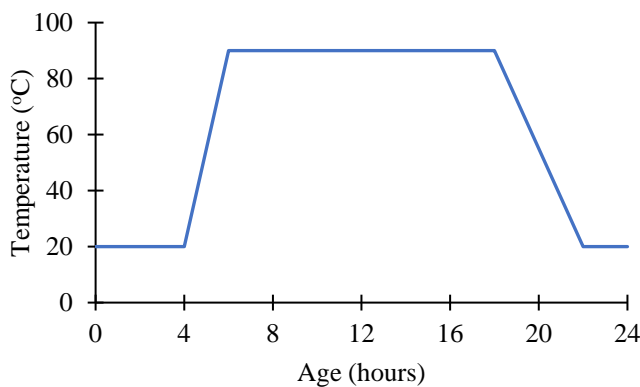


Figure 4-2 Heat treatment at the early age for DEF and DA samples.

4.2.4. Application of restraint

Steel frames were prepared with dimensions as shown in Figure 4-3. Each frame consisted of two end plates tied together by four steel rods. The strain gauge glued on the steel rod measured the evolution of strain in the steel.

After curing the specimens for seven days in tap water at 20°C, they were put in the steel frame and stress was applied in two ends by tightening the screws of each steel rod. The specimens were then conditioned in tap water at 20°C in the climate control room as shown in Figure 4-4 and measurements were taken at regular intervals.

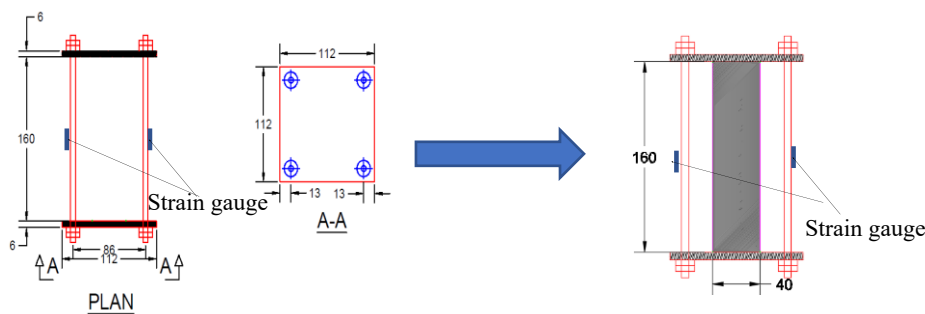


Figure 4-3 Steel frame used for restraining the expansion



Figure 4-4 Specimens for (a) free and (b) restraint expansion

4.2.5. Measurement

The initial measurement of strain and mass was taken after 24 hours of casting the specimens. Then after, strain measurement was taken at a regular interval.

The length change in the concrete specimen was measured with a contact gauge having an accuracy of 0.001 mm and a base length of about 100 mm in the direction 1-1 as shown in Figure 4-5. The lateral measurement in 2-2 direction was done with a laser device. The change in mass was measured with an accuracy of 1 gram.

The strain in steel was measured with 2 mm strain gauges by connecting it with a data logger (Model: TDS 302).

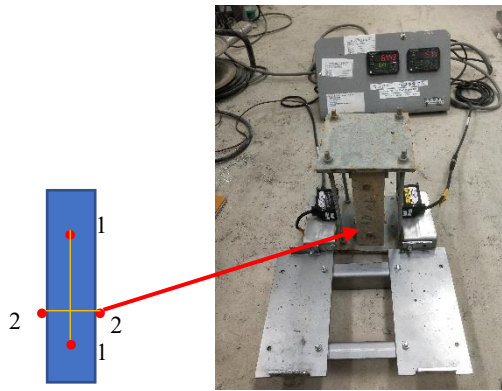


Figure 4-5 Measurement of strain in the longitudinal and lateral direction. The direction 1-1 was measured with a contact gauge while the direction 2-2 was measured with a laser device.

4.3. Results

4.3.1. Evolution of strain in the longitudinal direction

The evolution of strain in the free specimen and the restrained specimen is shown in Figure 4-6. The average of three specimens is shown with a continuous line in the figure while the individual specimens' data is shown by a broken line.

In Norma (N) and ASR specimens, the expansion was similar and reached to value of about 300 microns. In DEF specimens, the average free expansion reached about 16,000 microns (1.6%) while the restrained expansion was about 5500 microns (0.55%). Similar to the DEF specimen, the combined ASR and DEF (DA) specimen showed a free expansion of about 16,000 microns (1.6%) while the restrained expansion was about 4100 microns (0.41%).

The rate of strain evolution in the ASR specimen was much lower and did not show expansion. In the DEF specimen, the rate of evolution became rapid from about the 50th day. DA specimen also had similar kinetics, except that the strain evolution started earlier compared to the DEF specimen. The free strain was much higher for the DEF and DA case compared to the restrained specimen.

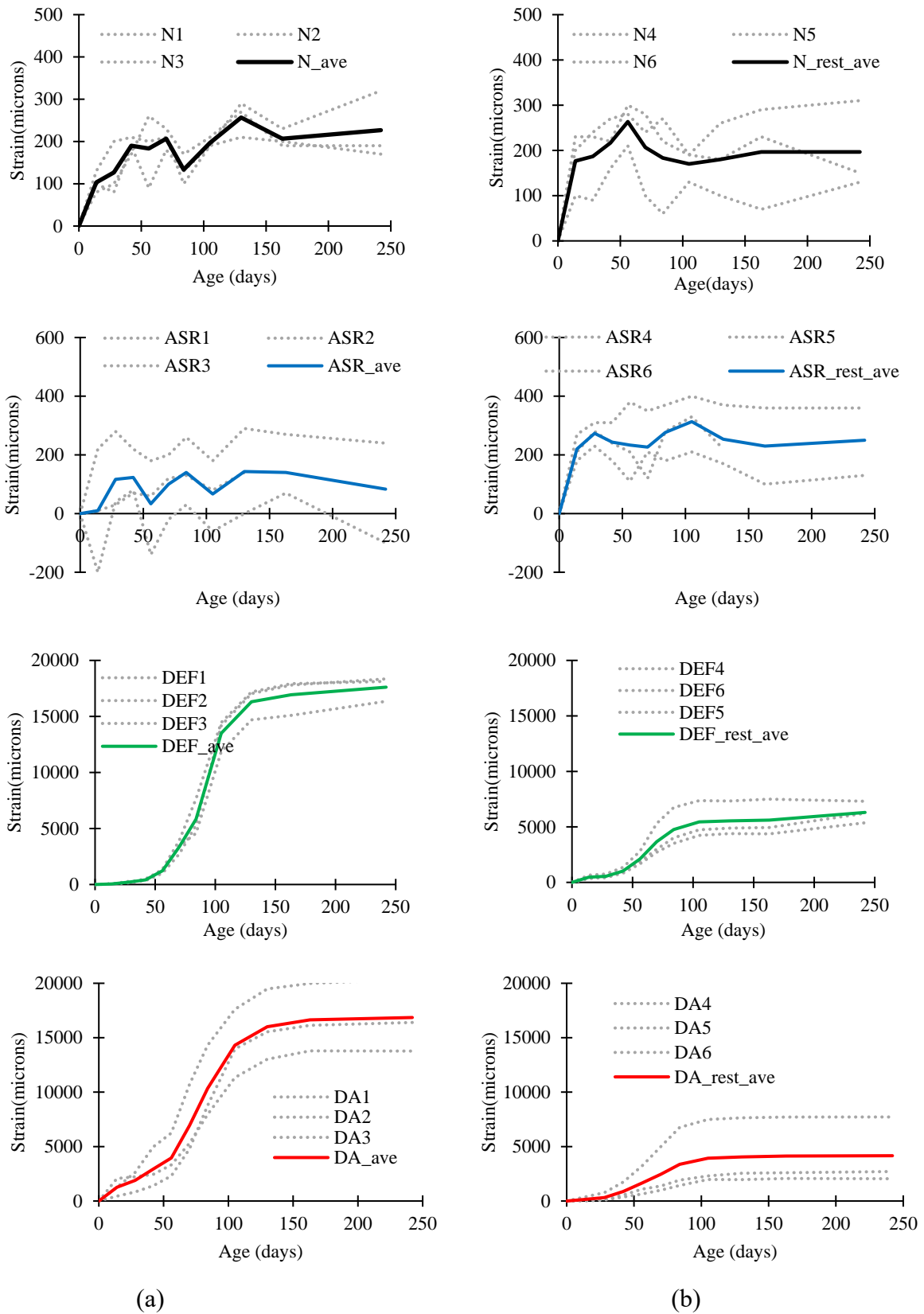


Figure 4-6 Evolution of strain in (a) free specimen (b) restrained specimen for normal, ASR, DEF and DA cases

4.3.2. Evolution of strain in the lateral direction

Figure 4-7 shows the average expansive strain in the lateral direction (direction 2-2 in Figure 4-5). Though the measurement was taken with a high precision laser device, there was a large scattering of data mainly because of the small size of specimens (the width was 40 mm in the direction of measurement). The absolute magnitude of the strain is not recommended for detailed analysis, nonetheless, tentative characteristics of the expansion in the lateral direction can be inferred from the figure.

In unrestrained cases, the expansion in the lateral direction in both DEF and DA specimens reached a range of about 23,000 microns (2.3%) at 150 days. The longitudinal strain was about 18,000 microns (1.8%). The larger values of strain in the transverse direction could be due to ease of moisture availability in this direction or it could be due to the measurement error. For confirmation, further experiments are required.

In the restrained cases, the expansion in the lateral direction was about 16,500 microns (1.65%) which is comparable to the free expansion in the longitudinal direction indicating that the expansion in the lateral direction is not much affected by the presence of the restraint. The slight reduction could be due to plate friction at the restrained ends.

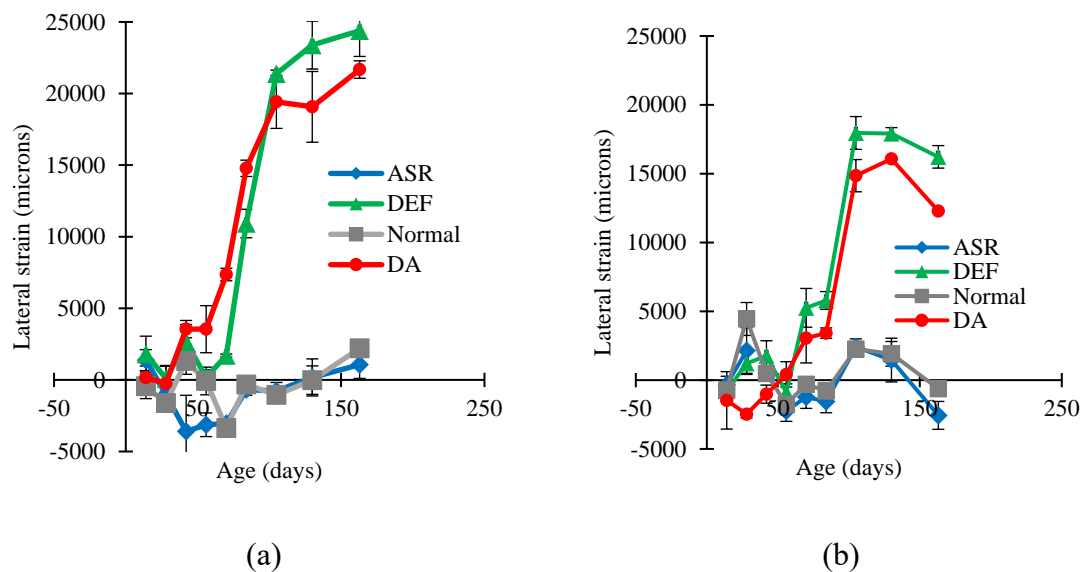


Figure 4-7 Evolution of lateral strain in concrete for (a) free specimens (b) restrained specimens

4.3.3. Evolution of strain in restraining steel

The evolution of strain in the steel rod of the restraining frame is shown in Figure 4-8. The grey lines show the variation measured from each strain gauge and the continuous line shows its average. The discrete peak indicates approximately the day on which the specimen was taken out from the water to measure the strain in concrete, typically every fortnight. These peaks disappeared when the specimen was put back in the water. It can be seen that for the Normal and ASR specimens, there was little or no evolution of strain. The DEF expansion could cause the strain in steel to rise to about 700 microns (0.07%) and the DA expansion could cause about 400 microns (0.04%) strain in the steel.

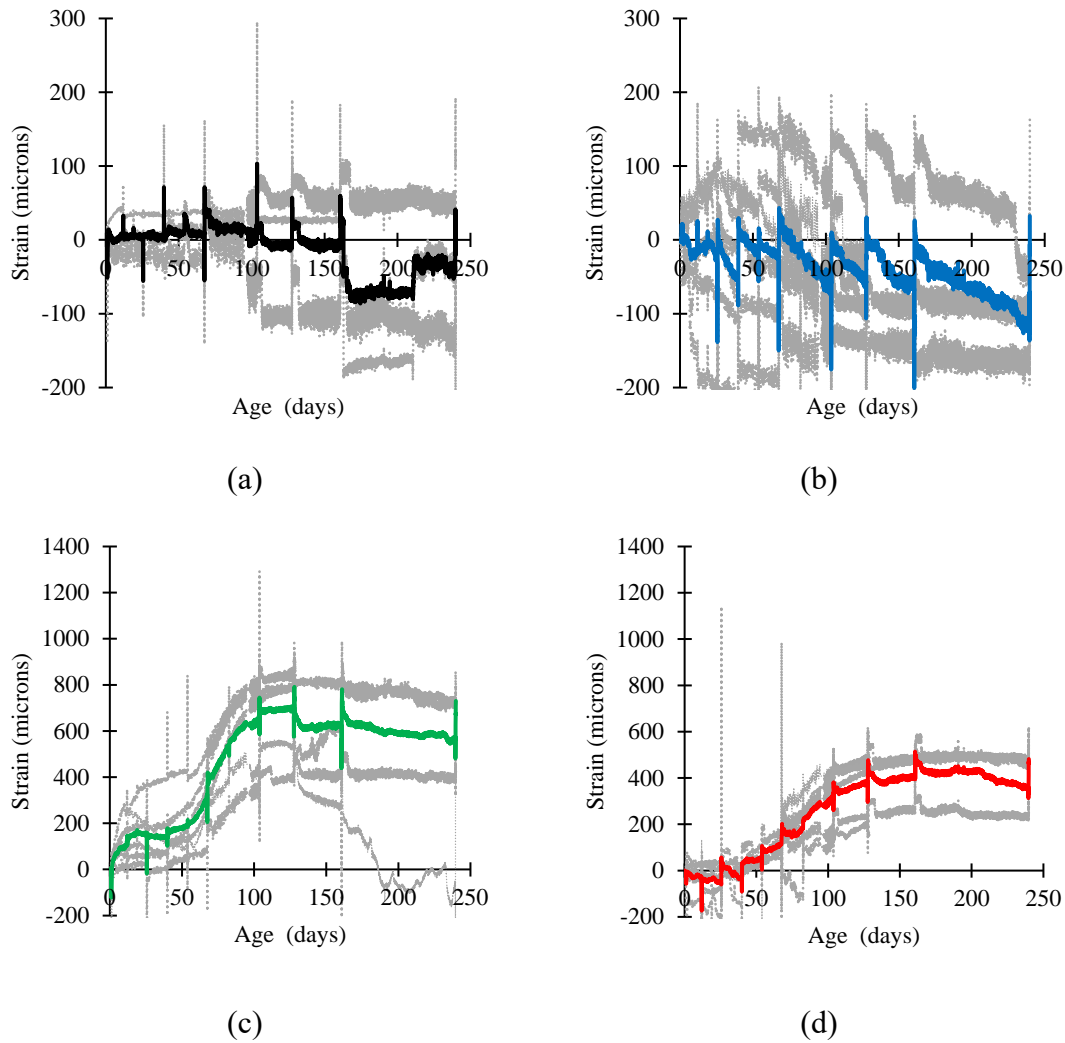


Figure 4-8 Evolution of strain in steel rods of restraining frame in (a) Normal, (b) ASR, (c) DEF and (d) DA specimens. The grey lines show the variation and the continuous line shows the average strain.

4.3.4. Evolution of cracks

A typical crack that appeared on the DEF and DA specimen in the free and restrained cases are shown in Figure 4-9. The evolution of cracks in other specimens during the experiment is given in the Appendix. It can be seen that the crack in the free specimen was random similar to a map-type of crack. In the restrained case, the cracks were parallel to the restraining direction in DA specimens indicating compressive stress. Cracks were not apparent in the DEF or other specimens in the restrained case.

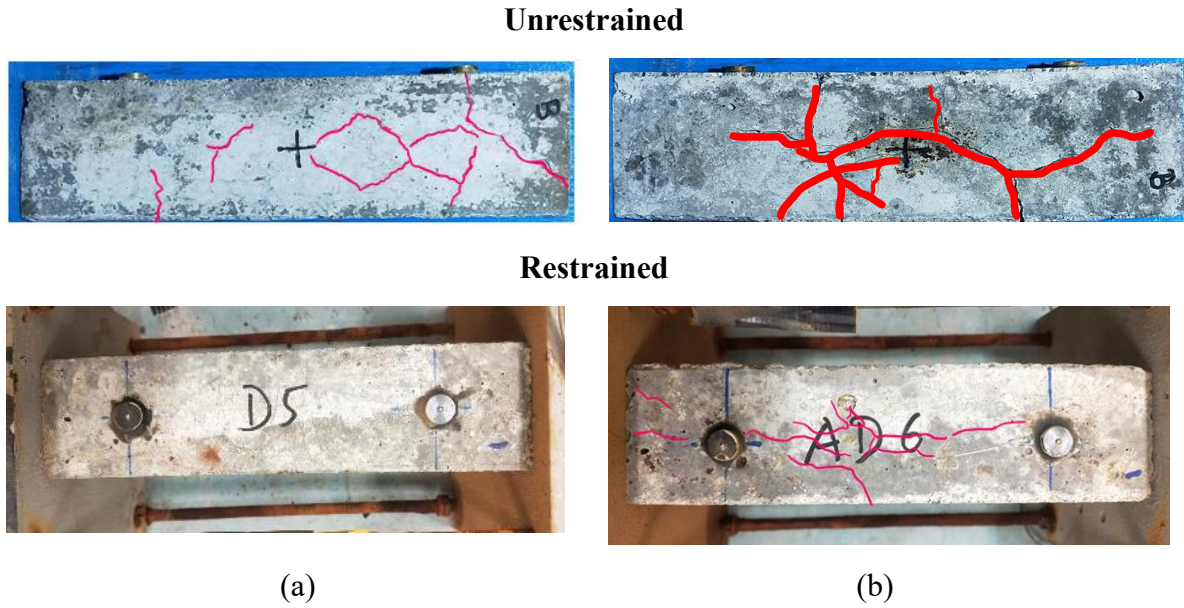


Figure 4-9 Crack distribution in free and restrained specimens for (a) DEF and (b) DA specimens

4.4. Discussion

4.4.1. Expansion behaviour

Figure 4-10 shows the evolution of average strain in ASR, DEF and DA specimens. If we compare the expansion in free and restrained cases in Figure 4-10(a) and (b), we can observe that, within the limit of error, the strains in DEF and DA specimen converged at about 15,000 microns (1.5%) in free expansion and about 4,500 microns (0.45%) in restrained case. For the DEF specimen, the reduction was about 66% and for the DA specimen, the reduction was about 75%. This observation is similar to the one made by (Kawabata, Ueda, et al., 2021), where the reduction in expansion was in the range of 82-87% for the DEF specimen. The difference can arise due to differences in the concrete mix and the amount of steel used for restraining. In Chapter 3, a similar observation was made for specimens with internal restraints. In both internal and external restrained cases, the DEF expansion exceeded the DA expansion.

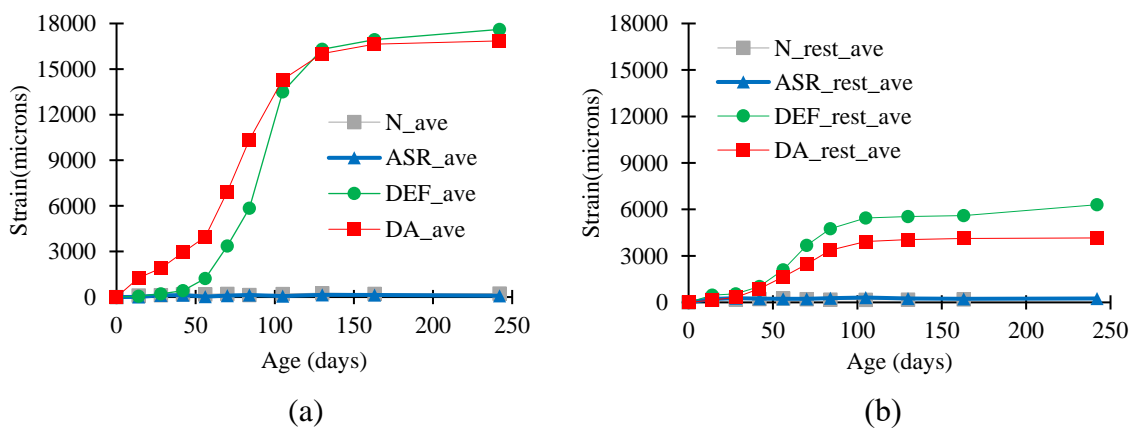


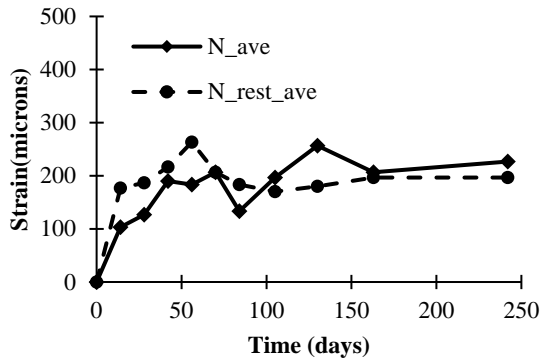
Figure 4-10 Evolution of strain in (a) free specimen (b) restrained specimen

4.4.2. Interaction between external restraint and concrete expansion

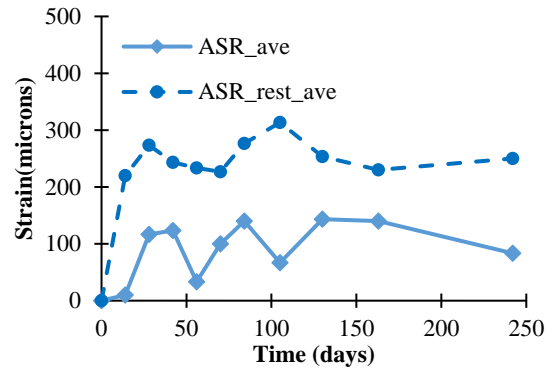
Figure 4-11 shows the comparison of average strain between unreinforced and reinforced specimens for Normal, ASR, DEF and DA specimens. In the case of the Normal and ASR specimens, the evolution of strain was slow and the specimens with and without steel reinforcement were not significantly different as shown in Figure 4-11 (a) and (b) respectively. It must be noted that the expansion of normal and ASR specimens in the restrained case was found to be higher. A similar trend was observed in the internal restrained case in Chapter 3. This behaviour is contrary to the normal hypothesis that the restraint reduces the expansion. Experiments by Gautam et al. had reported that the restraint in one direction results reduction in strain in that direction and an increase in strain in other perpendicular directions (Gautam et al., 2017). In the case when there is an equal finite restraint (non-zero) in all directions, the strain could be higher in one direction (possibly it could lie within the measurement tolerance). They had kept the stress at a constant level. In the current experiment, stress could vary depending on the expansion. This behaviour should be clarified in future studies.

In DEF and DA specimens, shown in Figure 4-11 (c) and (d) respectively, the restraint caused reduction in overall expansion although the initiation time of expansion was similar. The expansion was rapid in between 50 and 120 days.

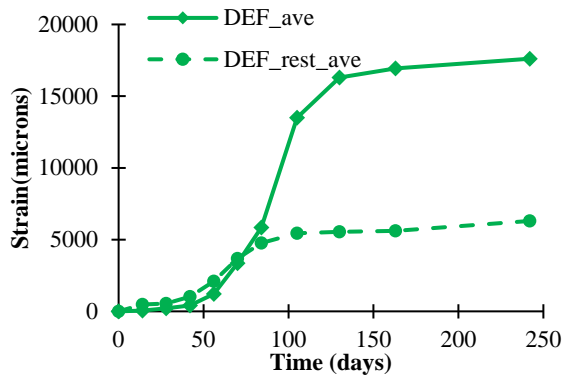
The corresponding average stress calculated in the steel rods and internal stress in concrete is shown in Figure 4-12. The stress was calculated by taking Young's modulus as 200 GPa. The stress induced by normal and ASR specimens was small due to the lower strain. The stress induced by the DEF and DA specimens was however significantly higher. The stress in steel due to DEF and DA expansion was about 132.0 N/mm^2 and 79.5 N/mm^2 respectively and the corresponding stress in concrete was about 6.7 N/mm^2 and 4.1 N/mm^2 respectively. It is noted that although the DEF and DA specimen had a similar expansion in the free case, the DA instigated less stress in steel compared to DEF owing to smaller strain in the restrained case. In a similar experiment published recently by Kawabata et al, the stress measured by a loadcell due to DEF expansion was in the range of $1.9\text{-}3.9 \text{ N/mm}^2$ (Kawabata et al., 2021). They had used steel of 1-6% which is less than the steel used in this experiment (7.1%). In general, a larger steel content should reduce strain and increase expansive stress, however, they did not get a consistent result. The expansive stress in the load cell while restraining the concrete by 17mm steel bar was larger than for 26 mm steel rebar. This shows the expansive stress could depend on other factors as well. Kawabata et.al had used a hollow specimen to pass a rod through it and attach a load cell, which could allow more space for lateral expansion towards the hole due to Poisson's effect. However, this needs to be verified with further experiments.



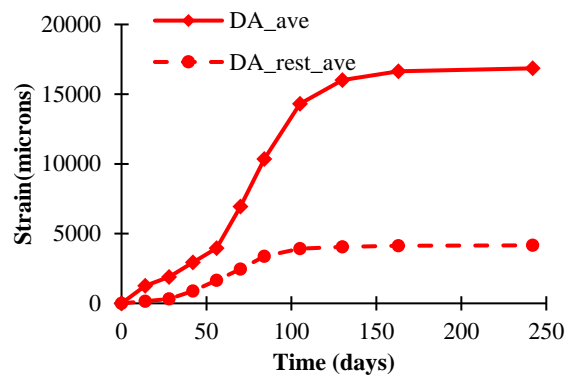
(a)



(b)



(c)



(d)

Figure 4-11 Comparison of average strain in (a) Normal, (b) ASR, (c) DEF and (d) DA specimens for unreinforced and reinforced specimens. The broken line shows the restrained case.

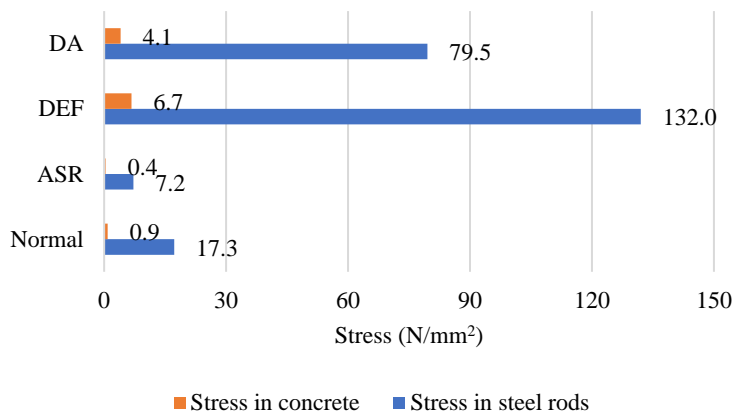


Figure 4-12 Comparison of stress in steel rods of the restraining frame ($E=200\text{GPa}$) and stress in concrete.

4.4.3. Strain from concrete and strain gauge

Figure 4-13 shows the maximum strain measured in concrete prism with contact gauge and strain measured in steel rods by the strain gauge. The numerical value is shown in Table 4-4. For the normal and ASR specimens, the difference is small and for DEF and DA, the

difference is large. This difference arises due to the location of the measurement of strain. The strain in concrete is measured in the concrete body while the measurement with strain gauge was measured in the steel rods which lies at an offset distance from the longitudinal axis of the concrete prism. This causes bending of the restraining end plates (Figure 4-14 (b)) and the strain in the steel rods is reduced. This was verified by a numerical analysis. Figure 4-14(a) shows the relationship between displacement in concrete and displacement in steel rods from the experiment (dots) and the result of linear static analysis (broken line). Figure 4-14 (b) shows the deformed shape. It can be seen that the experiment and numerical analysis matches well. Also, note that two displacements are linearly correlated because the stress was less than the yield stress of steel.

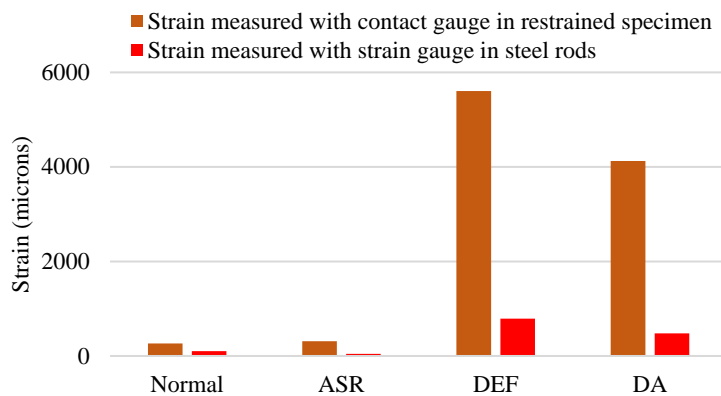


Figure 4-13 Strain steel rod and concrete

Table 4-4 Absolute displacements in concrete and steel rods

Cases	Normal	ASR	DEF	DA
From contact gauge in concrete (mm)	0.042133	0.050133	0.8864	0.648533
From strain gauge in steel rod (mm)	0.01717	0.007164	0.13138	0.079159

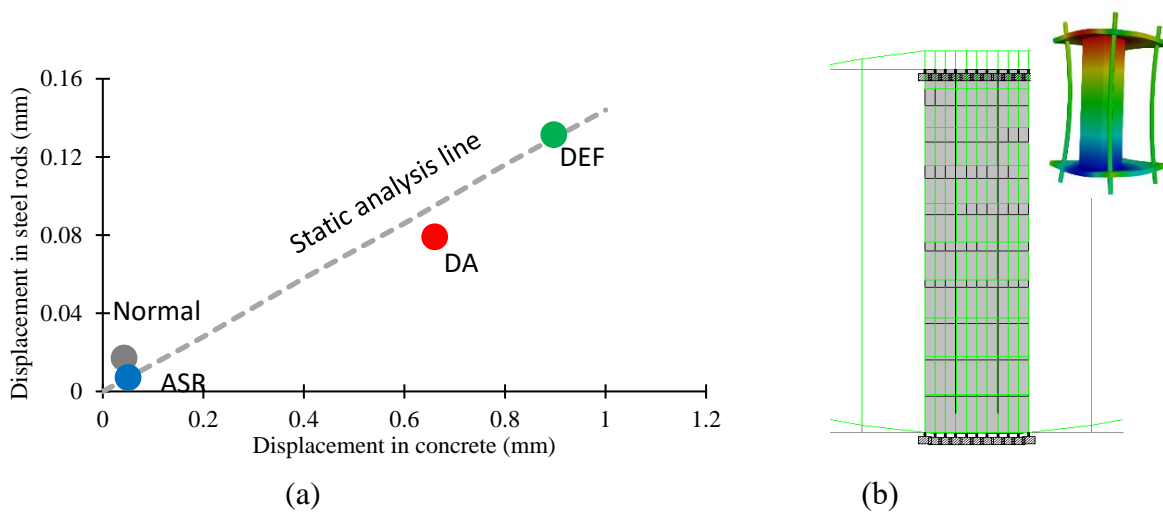


Figure 4-14 (a) Relation between strain in concrete and steel rod ; (b) deformed shape of steel frame due to the expansion of concrete

4.5. Summary

In this chapter, the expansion behaviour of Normal, ASR, DEF and ASR+DEF under externally restrained conditions were studied. Based on the experiment and observations, the following conclusions are made.

- 1) The strains in the DEF and DA specimen converged at about 15,000 microns (1.5%) in free expansion and about 4500 microns (0.45%) in the restrained case. For DEF the reduction was about 66% and for DA the reduction was about 75%.
- 2) It appears that the expansion in the lateral direction is not affected by the presence of restraint. The expansion in DEF and DA specimens reached a similar range of about 20,000 microns (2%) at 130 days in the free expansion case and about 16,000 microns (1.6%) in the restrained case. The difference could be due to the high scattering of data because of the small size of the specimen.
- 3) The external restraint can significantly reduce the expansion by DEF and DA. The restraining caused an increase in stress in the steel. The stress was about 158.3 N/mm^2 and 95.4 N/mm^2 in DEF and DA specimens respectively and the corresponding stress in concrete was about 11.2 N/mm^2 and 6.7 N/mm^2 respectively. The high stress could bend the restraining end plates which were verified by a numerical calculation.
- 4) In the ASR specimens, the expansion was higher in the restrained case. Similar behaviour was observed for the case of the internal restrained case in chapter 3. The actual reason for such behaviour is unclear at this stage.

5. Evolution of bond and compressive strength due to ASR/DEF expansion

5.1. Background

It was verified in Chapter 3 that the expansion of concrete by ASR/DEF induces tensile stress in steel reinforcement which was attributed to micro cracking between steel and concrete interface. This indicated that the bonding between concrete and steel could be affected by ASR/DEF expansion.

In the case of ASR, Chana (1989) had reported that ASR expansion increases the bond strength for plane bars and ribbed bars when the expansion was small. The bond was reduced by 40% when the expansion was about 4000 microns (0.4%). The recommendation from the studies has been incorporated in codes and guidelines such as *ISE*,(1992). A recent study by Li et al. (2020) also indicated that up to about 350 microns (0.035%), the bond strength was improved, which they attributed to the pore pressure. After exceeding the threshold, the bond strength gradually decreased.

In the case of DEF and DA infected concrete, there are no published data to the knowledge of this author as of writing this thesis. It is speculated that the DEF and DA specimens could also exhibit a similar tendency as ASR because of similar expansion kinetics, however, it has not been verified yet. Thus, an experiment was designed for the bond test of ASR, DEF and DA infected concrete at various levels of expansion. The change in bond strength was compared with the normal concrete specimen that was not infected with ASR/DEF. The main objectives of this experiment are as follows:

- a) Study the change in bond strength due to ASR/DEF expansion
- b) Study the change in compressive strength and plastic strain due to ASR/DEF expansion
- c) Study the relation between bond strength and compressive strength if any

5.2. Methodology

A set of prismatic concrete specimens were prepared to induce ASR, DEF and their combination (referred to as DA). Specimens were also prepared with normal concrete for comparison. Three cylindrical and three pullout specimens were prepared for each case of normal (which is defined as a specimen without reactive aggregate and high-temperature curing), ASR, DEF and DA. The cylindrical specimens were used to measure the free expansion, strength and dynamic Young's modulus.

5.2.1. Specimen dimension

The cylinder specimen had a diameter of $\phi 100$ mm and a height of 200mm. These were used to find the free expansion, uniaxial compressive strength and dynamic Young's modulus. The cylindrical specimens were not reinforced.

The pullout specimen had a dimension of 150mm x 150 mm x 150 mm. A 300 mm long steel rebar with a diameter of $\phi 13$ mm was placed in the middle of the specimen for the bond test. Rectangular stirrups, prepared with $\phi 6$ mm rebars, were placed in the corner of the cube. To prevent surface cracking during the pullout test, a 2 cm PVC pipe was placed at the ends of the cube as shown in Figure 5-1(a). Because of the limit of the size of the heating chamber, the length of the pullout rebar had to be limited to 300 mm. However, the tensile test had to be done in the UTM with the arrangement shown in Figure 5-1(b) which needed a longer rebar. The extension was done by connecting separate steel rebar ($\phi 13$ mm) using a mechanical coupler of size 50mm x 25 mm. The force transmission from the extension rebar to the main rebar via mechanical coupler was tested separately and was found that the set-up had a satisfactory performance.

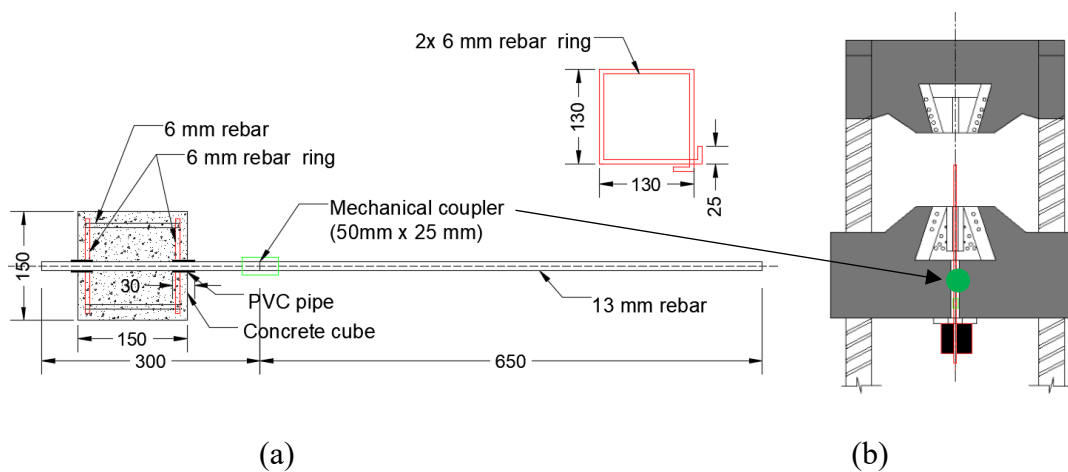


Figure 5-1 Pull out specimen preparation



Figure 5-2 Photographs of the specimen during casting

5.2.2. Concrete

Four types of mix proportion were used to prepare concrete. The first was normal concrete without any additive. The ASR specimens had reactive aggregate (30%) while the DEF had an addition of sulphate. The DA specimens had both reactive aggregate (30%) and sulphate. The quantity of each fraction is shown in Table 5-1.

Table 5-1 Concrete mix proportion

SN	Sample	w/c ratio	Cement (kg/m ³)	Normal aggregate (kg/m ³)	Reactive aggregate (kg/m ³)	Fine aggregate (kg/m ³)	Water reducer (ml/m ³)	K ₂ SO ₄ (2.5% of cement, kg/m ³)
1	ASR (A)	0.50	348	602	258	770		
2	DEF (D)	0.50	348	860	-	770	1087	18.94
3	ASR+DEF (DA)	0.50	348	602	258	770	1087	18.94
4	Normal	0.50	348	860	-	770	1087	-

Cement

To accelerate the reaction, high-performance cement (HPC) was used. The composition of cement is shown in Table 5-2.

Table 5-2 Cement composition

SN	Chemical composition	Percentage by mass
		HPC
1	Loss on ignition (ig.loss)	0.77
2	Silicon Dioxide (SiO ₂)	20.49
3	Aluminum Oxide (Al ₂ O ₃)	5.13
4	Iron Oxide (Fe ₂ O ₃)	2.58
5	Calcium Oxide (CaO)	64.82
6	Magnesium Oxide (MgO)	1.48
7	Sulphur Trioxide (SO ₃)	3.01
8	Potassium Oxide (K ₂ O)	0.38
9	Sodium Oxide (Na ₂ O)	0.30
10	Chloride (Cl ⁻)	0.005

Aggregate

Two types of aggregate were used viz. normal non-reactive aggregate and reactive aggregate. The reactive aggregate consisted of opal, cristobalite and volcanic glasses (Kawabata et al., 2019). Sandstone was used as the non-reactive coarse aggregate. The physical properties of aggregate are shown in Table 5-3. The specific density of normal aggregate was 2.66 g/cm³ and the reactive aggregate had a specific density of 2.47 g/cm³. The maximum size of coarse aggregate was 20 mm. River sand was used as the fine aggregate with a specific density of 2.62 g/cm³ and an average particle size (D_{50%}) of 0.72 mm.

Table 5-3 Physical properties of aggregate

Physical Properties	Aggregate		
	Fine	Non-Reactive coarse	Reactive coarse
Maximum Grain Size (mm)	1.18	20	20
D50 (mm)	0.72	13.26	12.93
Specific gravity	2.62	2.66	2.47

Accelerator and Admixtures

Laboratory grade potassium sulphate in powder form was used to increase the sulphate content in the mix to accelerate the DEF reaction. 2.5% by weight of cement was used in the mix to initiate DEF.

Water reducing agent (BASF Master Pozoris ‘マスターポゾリス’ No.70 11288) was added based on the manufacturer's recommended dose as indicated in Table 5-1. This admixture reduces the unit amount of water in concrete by dispersing action of cement and air entrainment.

5.2.3. Heat treatment for DEF sample

For DEF and DA initiation, the maximum temperature for exposure was set at 90 °C as recommended by Famy et al. (2002) which is shown in Figure 5-3. After casting the specimen, they were cured at 20 °C for 4 hours under sealed conditions. After that, the specimen was exposed to 90 °C for the next 12 hours. Then, the temperature was gradually reduced to 20 °C. After the heat treatment, the specimens were taken out of the mould and placed in tap water. In normal and ASR specimens, heat treatment was not applied.

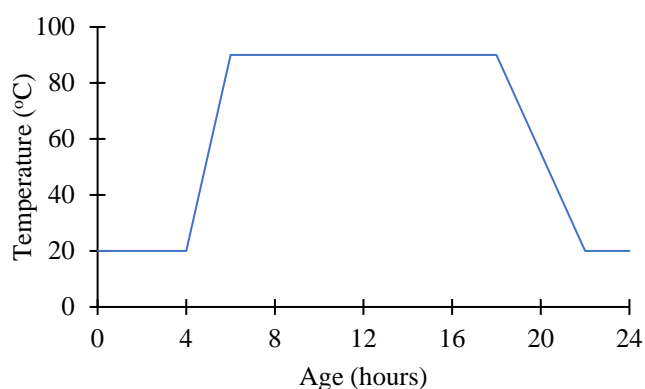


Figure 5-3 Heat treatment at an early age for DEF and DA specimens

5.2.4. Conditioning of the specimens

After taking the initial measurement, all the specimens were placed in tap water at 20 °C in a temperature-controlled water pool as shown in Figure 5-4. The temperature of the pool was monitored using a K-type thermocouple and data was recorded in a data logger. The water temperature in the pool and air temperature adjacent to it is shown in Figure 5-5. The average temperature of the pool was 21.7 °C with a standard deviation of 1.45 °C. The data between 90-115 days were lost due to error.

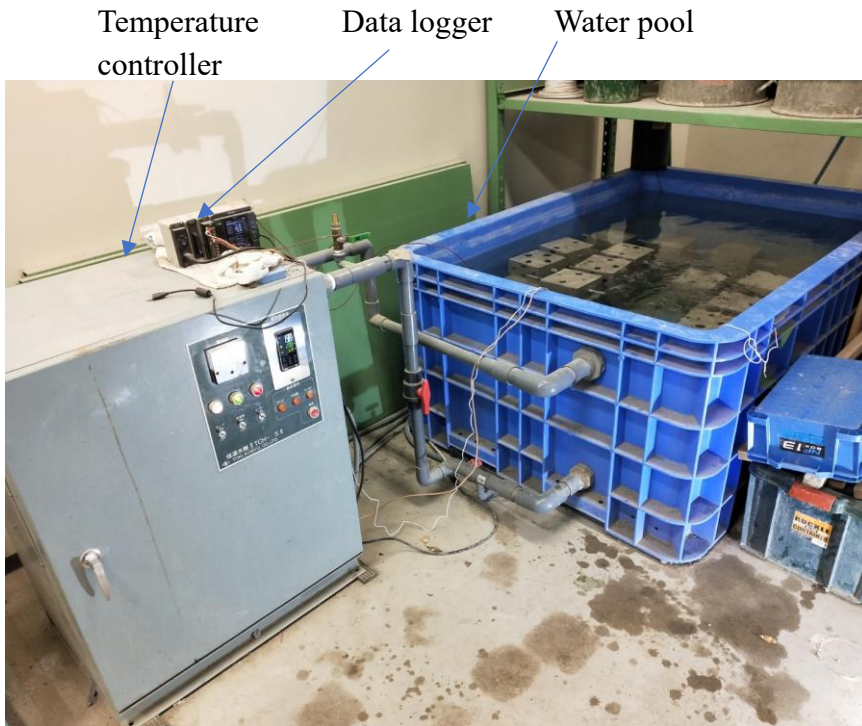


Figure 5-4 Temperature controlled water pool

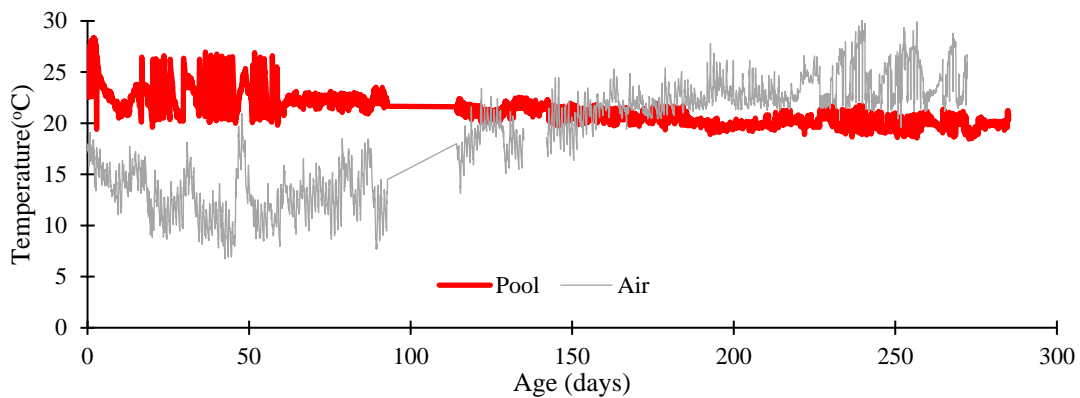


Figure 5-5 Temperature variation in pool

5.2.5. Measurement

The initial measurement of strain, mass and dynamic modulus was taken after 24 hours of casting the specimens. Then, the measurement was taken at regular intervals, typically every fortnight.

The length was measured with a contact gauge having an accuracy of 0.001 mm and a base length of about 100 mm as shown in Figure 5-6 (a) and (b). The change in mass was measured with an accuracy of 1 gram.



(a)



(b)



(c)

Figure 5-6 (a) Strain measurement in cylindrical, (b) strain measurement of cubic specimens and (c) measurement of dynamic Young's modulus with the acoustic method

The dynamic Young's modulus was measured using an acoustic frequency measurement equipment (Model No: MIN-011-0-10 and Serial No. 09126). Based on the resonance frequency, the dynamic Young's Modulus was calculated using Equation (5-1). The measurement complies with ASTM-E1875 -08. The setup is shown in Figure 5-6 (c).

$$E_d = 4 * L^2 * f^2 * \rho \quad (5-1)$$

where,

E_d : Dynamic Young's Modulus (N/m²)

L : Length (m)

ρ : density (kg/m³)

f : Primary resonance frequency (Hz)

5.2.6. Strength test

Strength tests were scheduled to be carried out at the age of 28, 90 and 150th day which is based on the evolution of expansion observed in the previous experiments.

The compressive strength of deteriorated concrete specimens was measured by carrying out a uniaxial compressive test on the cylindrical specimens as shown in Figure 5-7(a). The specimen was encased in a compressometer and load was applied. The load-displacement values were recorded in the data logger. In each set, one of the cylindrical specimens was used for stepwise (incremental cycle) loading to check the extent of internal damage (dynamic Young's modulus) at the various stress level by measuring the resonance frequency after each unloading. The average compressive strength is calculated as the average of all specimens including the one used for cyclic loading.

The pullout test was done in Universal Testing Machine (UTM) machine with the arrangement shown in Figure 5-7 (b). The applied load, displacement, and stress in the steel values were recorded using a data logger.



Figure 5-7 Setup for (a) uniaxial compressive strength test and (b) pull out test in Universal Testing Machine (UTM)

5.2.7. Sufficiency of coupler

As mentioned earlier, a steel coupler was used to extend the specimen's steel for setup in the UTM. Thus, it was necessary to conduct a test to confirm that the couple can efficiently transfer the force from UTM to the pullout specimen. This was done using an arrangement shown in Figure 5-8. The result of the tensile test is shown in Figure 5-9. It can be seen that in the range of 0 to 40 kN, where the bond test is expected to lie, the force transfer is linear as shown in Figure 5-9(b). Furthermore, the stress in the couple was well below yielding stress even when the pullout rod had yielded as indicated in Figure 5-9(a). Thus, it was verified that using the coupler will not affect the bond test. The average yield stress of the rebar was found to be about 332 N/mm².

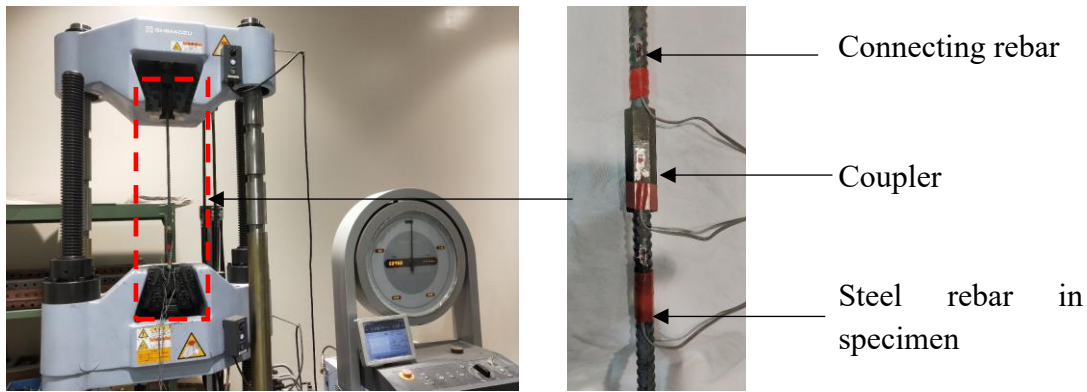


Figure 5-8 Testing of the coupler for force transfer

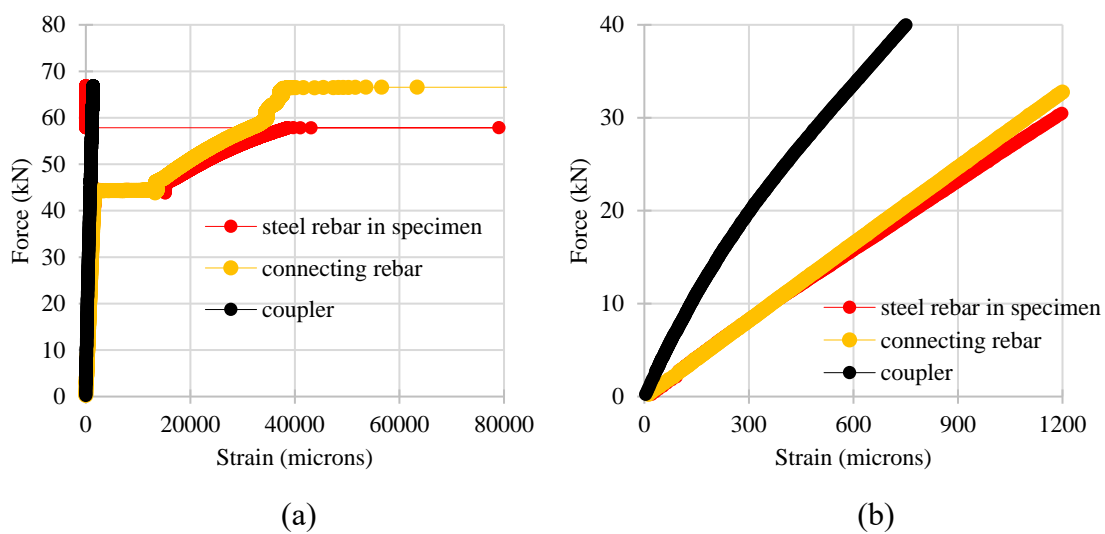


Figure 5-9 Force transfer between main specimen rebar and connecting bar via coupler

5.3. Results

5.3.1. Free expansion of cylinders

The average expansion evolution in the cylindrical specimen is shown in Figure 5-10. The grey line in the figure indicates the actual measurement and the color continuous line show their average. As expected, the strain in the Normal specimen was just a fluctuation of measurement error and some swelling due to moisture absorption. The expansion strain in the ASR specimen converged at about 1,800 microns (0.18%). The expansion strain in DEF and DA specimens converged at about 15,000 (1.5%) and 18,000 (1.8%) respectively. The expansion due to DEF and DA was rapid compared to the ASR specimen.

The specimens started to show fine cracks at the strain level of about 500 microns. These cracks were visible as the expansion continued. The photos of the specimens showing the crack are attached in the Appendix.

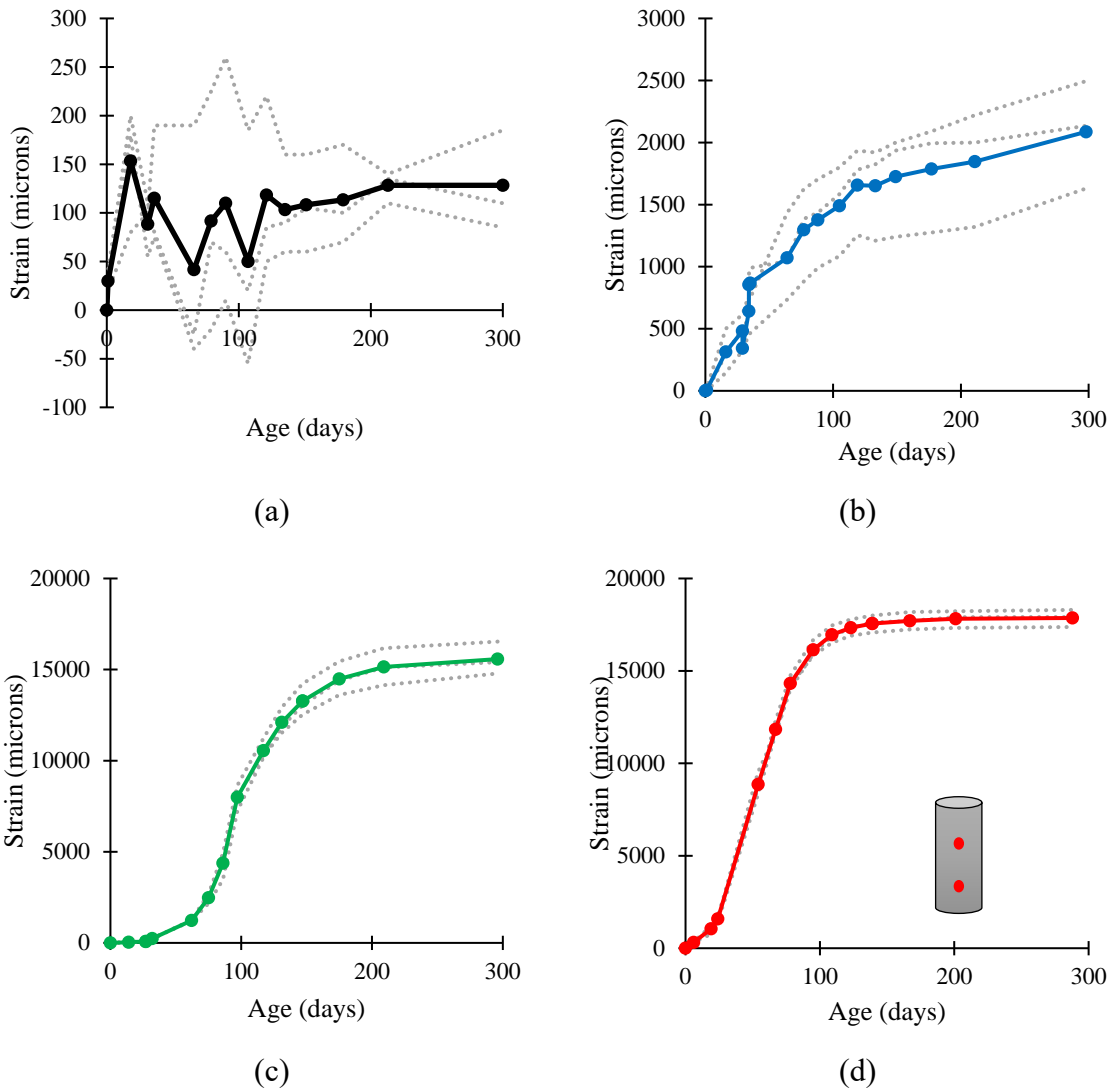


Figure 5-10 Evolution of free expansive strain in (a) Normal, (b) ASR, (c) DEF and (d) DA cylindrical specimens. The grey lines show the actual measurements and the color continuous line show the average strain

5.3.2. Expansion in pullout specimens

Figure 5-11 shows the expansion in the pull-out specimens. The grey line in the figure indicates the actual measurement and the color continuous line show their average. The longitudinal direction indicates the direction along which the main rebar was laid. It can be seen that the strain in the longitudinal direction was slightly lower than in the lateral direction. The Normal pullout specimen had a small expansion and the relative scattering was high which is due to measurement fluctuation at low strain. The expansion strain in ASR averaged at about 2,200 microns (0.22%) and 3000 microns (0.3%) in longitudinal and lateral directions respectively. It was 8900 (0.89%) and 10,000 microns (1%) in DEF and 10,000(1%) and 13000 microns (1.3%) in DA specimens respectively.

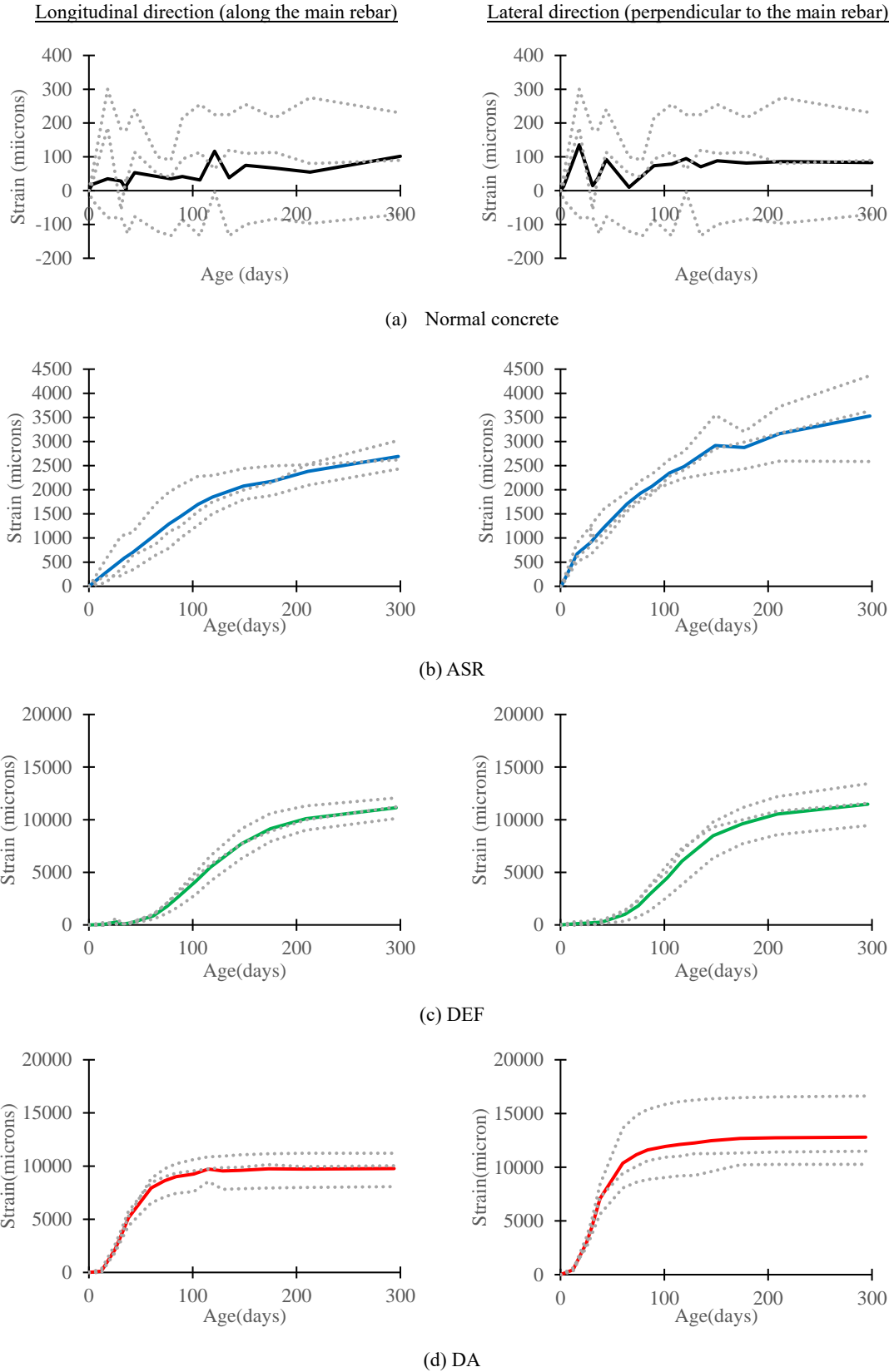
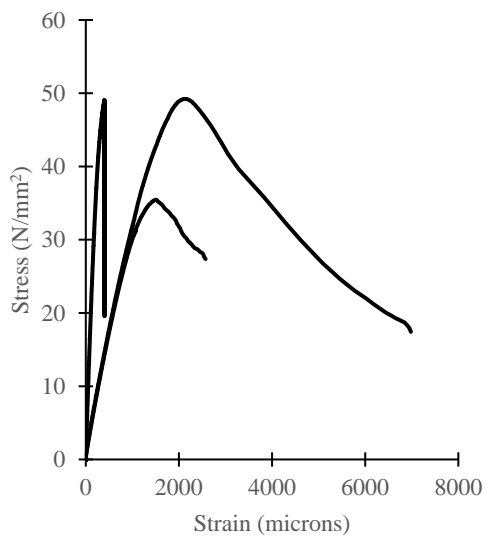


Figure 5-11 Evolution of expansive strain in pullout specimens

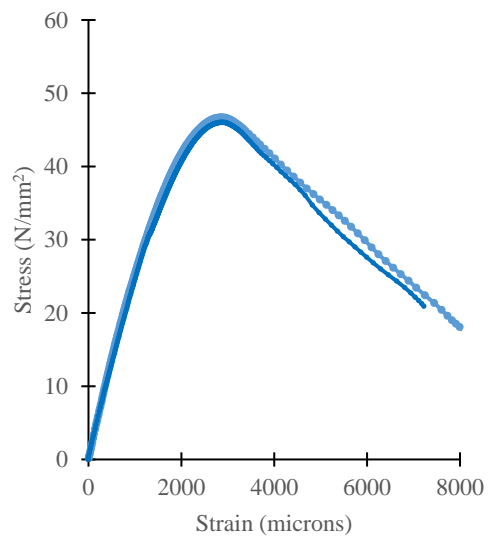
specimens at 28, 90 and 150 days respectively. The peak strength and peak strain are shown in Table 5-4. At 28 days, the peak strength of the normal specimen was close to about 45 N/mm² and the strain at the peak load was about 1300 microns (0.13%). Its strength gradually increased along with the peak strength. At the age of 150 days, the average strength was close to 60 N/mm². The strength of ASR specimens had a peak strength of about 47 N/mm² which slightly decreased on the 150th day. Its peak strain did not change significantly. In DEF and DA specimens, the peak strength was smaller than Normal and ASR specimens even at 28 days. The strength then deteriorated rapidly. For the DEF specimen, the peak strength of about 38 N/mm² on 28 days was reduced to about 7 N/mm² on the 150th day. For the DA specimen, the reduction in strength was even more drastic. In the 90 days, the strength reduced from about 39 N/mm² to 9.94 N/mm² and by 150 days the peak strength was only about 7 N/mm². In DEF and DA specimens, the average peak strain was also increased significantly reaching about 8000 microns (0.8%) and 12,000 microns (1.2%) respectively in 150 days as shown in Table 5-4. Also, the stress-strain curve got flat with age, indicating a significant increase in the plastic strain.

Table 5-4 Average peak strength and corresponding strain

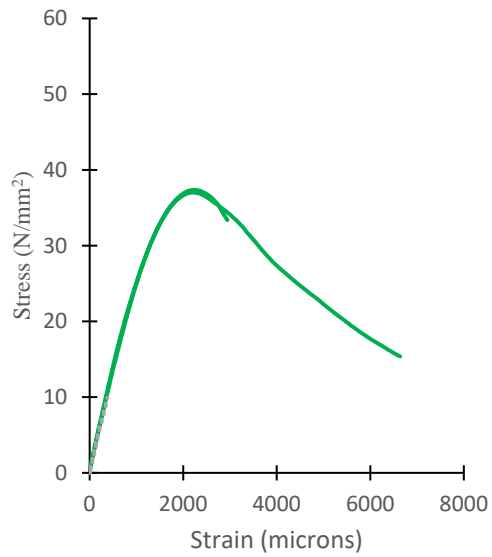
	Normal	ASR	DEF	DA
Age 28 days				
Peak strength (N/mm²)	44.81	47.09	37.95	38.90
Peak strain (microns)	1,288	2,859	4,378	3,735
Age 90 days				
Peak strength (N/mm²)	47.76	47.15	28.47	9.94
Peak strain (microns)	1,651	2,695	4,378	7,835
Age 150 days				
Peak strength (N/mm²)	60.59	45.48	6.69	6.82
Peak strain (microns)	2,256	3,184	8,195	12,786



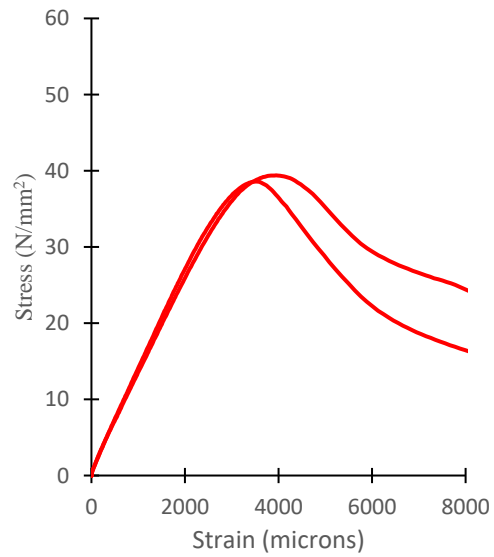
(a) Normal



(b) ASR

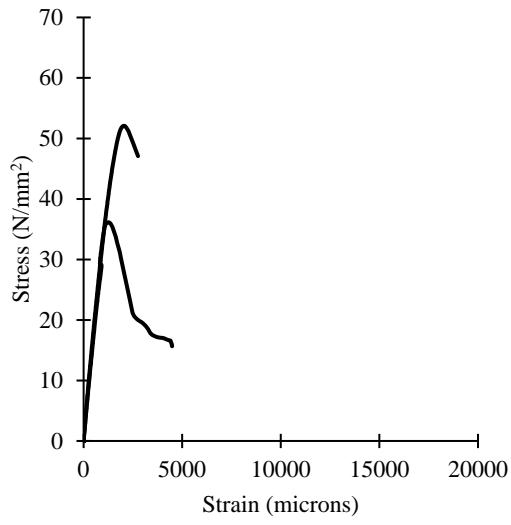


(c) DEF

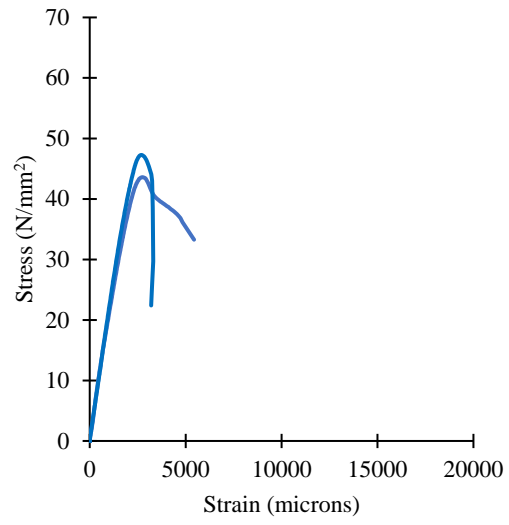


(d) DA

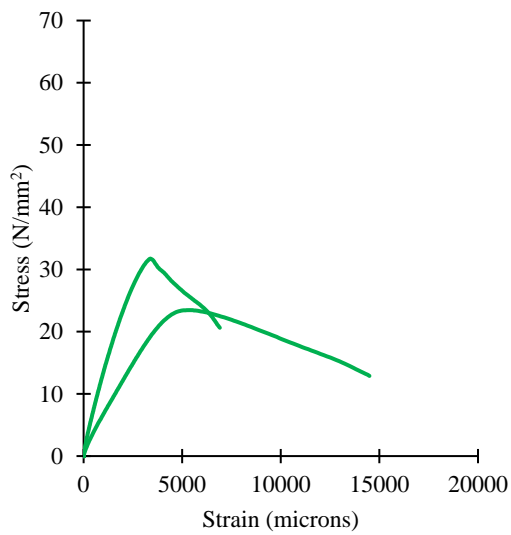
Figure 5-13 Uniaxial compressive strength in 28 days



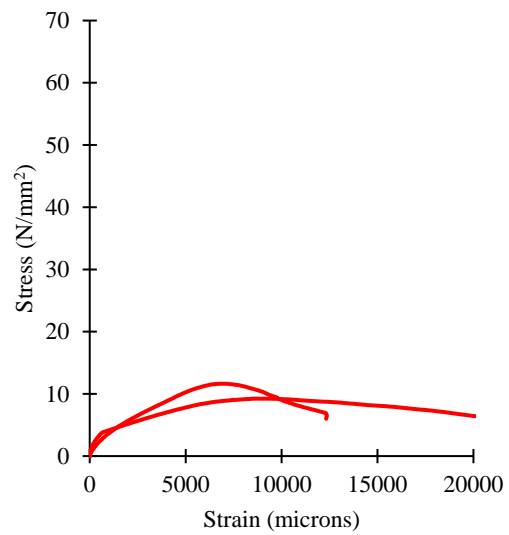
(a) Normal



(b) ASR

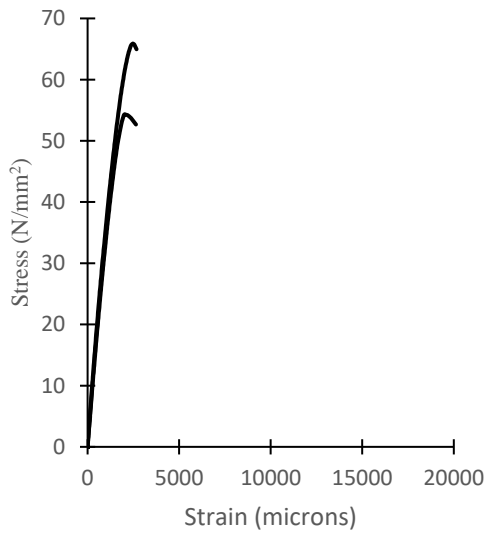


(c) DEF

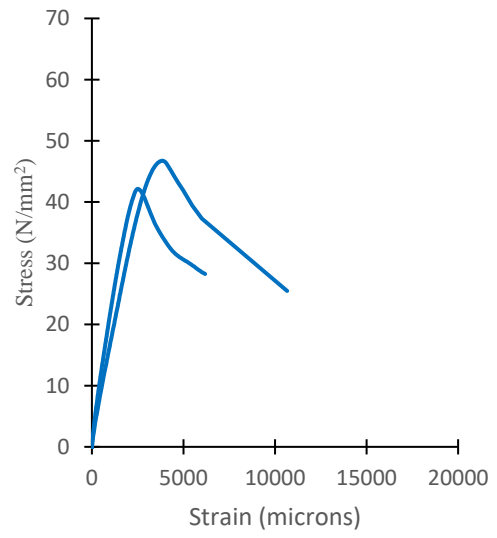


(d) DA

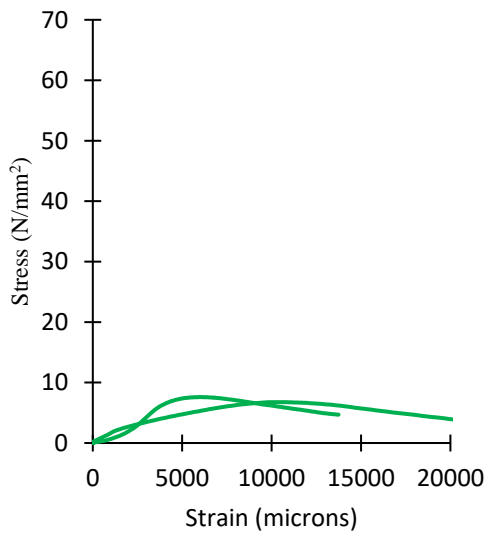
Figure 5-14 Uniaxial compressive strength in 90 days



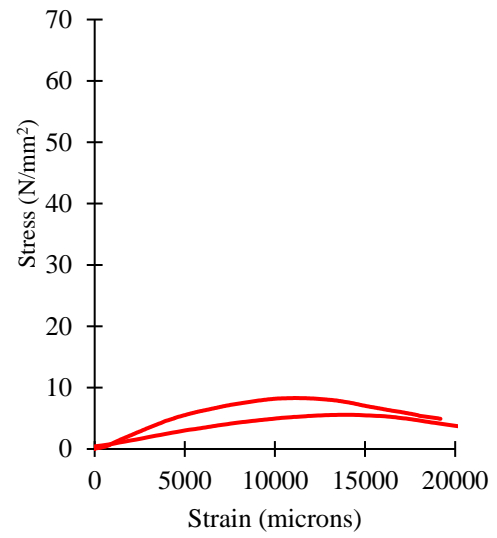
(a) Normal



(b) ASR



(c) DEF



(d) DA

Figure 5-15 Uniaxial compressive strength in 150 days

5.3.5. Incremental loading and internal damage

The incremental loading test was done to estimate the gradual damage in concrete at various levels of stress. The damage is estimated by calculating the change in dynamic Young's modulus of elasticity (E_d) which indirectly indicates the internal cracking qualitatively (refer to Chapter 6 for details). Figure 5-16, Figure 5-17 and Figure 5-18 show the stress-strain relationship and corresponding damages for stepwise loading on one specimen of each kind at 28 days, 90 days and 150 days respectively. The load was applied at the approximate stress level of 25%, 50% and 75% based on the average stress obtained in Section 5.3.3.

The resonance frequency and corresponding E_d of the specimens before the loading are shown in Table 5-4 which serves as the base case for each time step. As can be seen, the DEF and DA specimens had already a low value of E_d before loading at the age of 90 and 150 days. When the axial load was applied to the specimens, the resonance frequency gradually decreased as shown on the right-hand side of the figures. The shifting of resonance frequency was minimal for the ASR specimen while it was maximum for DEF and DA specimen especially at the age of 90 days and 150 days.

Table 5-5 Resonance frequency (f) and dynamic Young's modulus(E_d) at various ages

Age	Normal		ASR		DEF		DA	
	f (Hz)	E_d (GPa)						
28 days	10,683	42.15	10,046	39.21	9,923	28.32	8,721	28.84
90 days	10,882	45.16	9,742	36.30	7,807	24.37	5,108	9.78
180 days	10,771	43.35	9,447	30.98	4,444	6.19	4,462	6.11

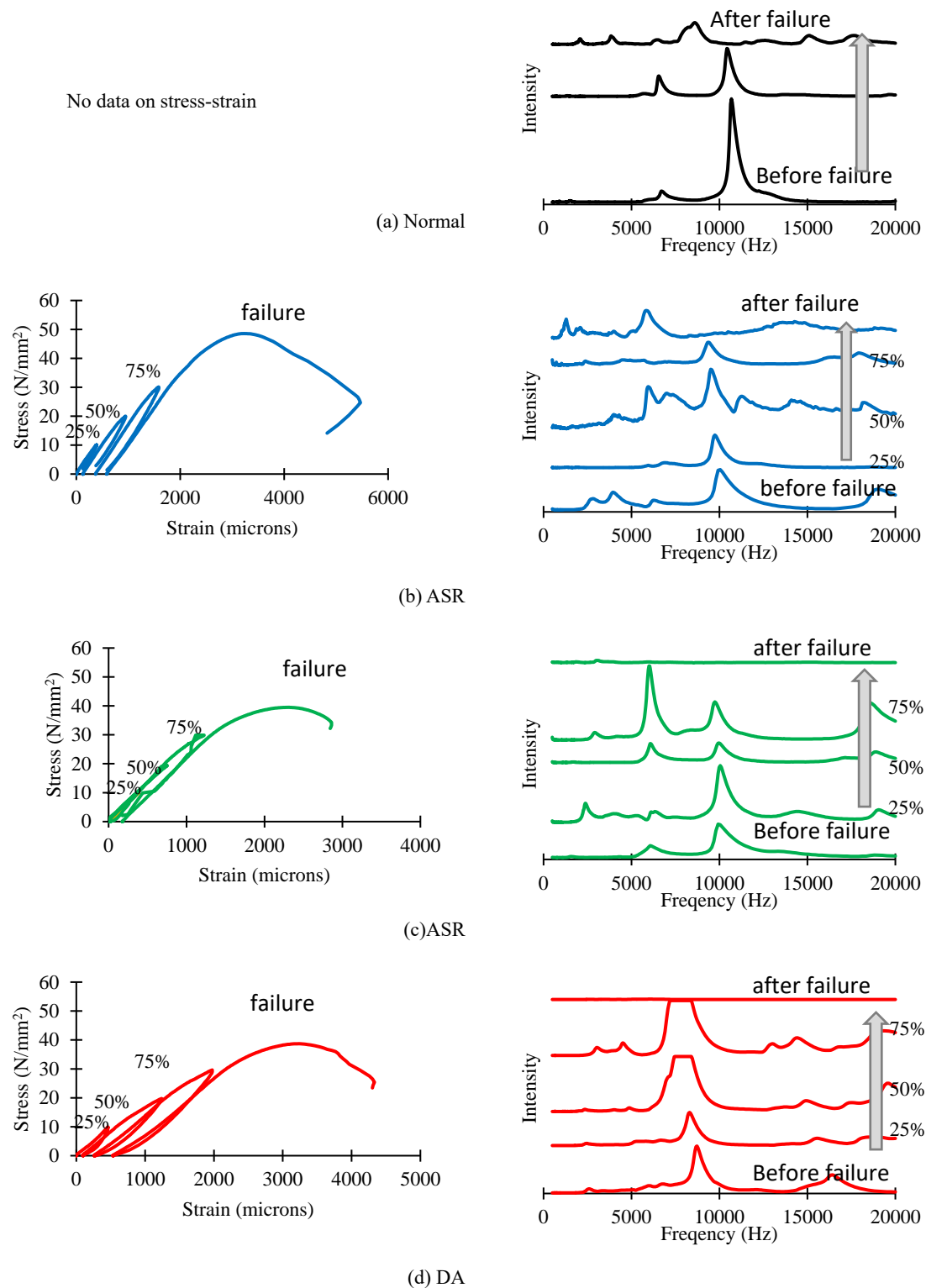
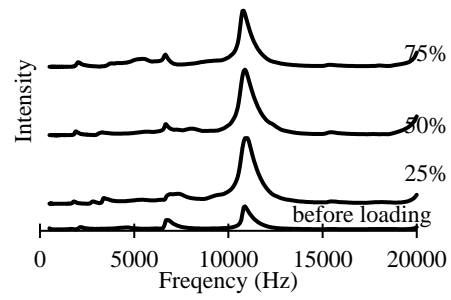
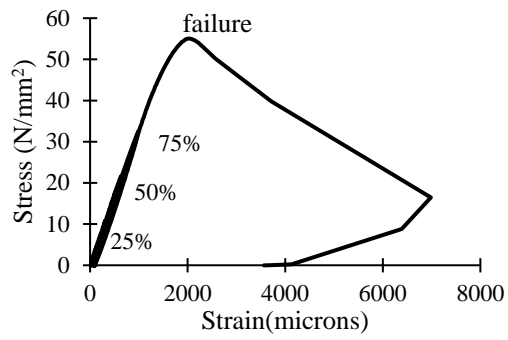
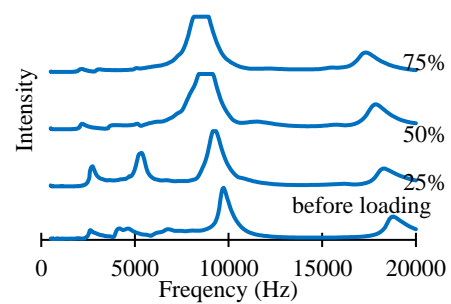
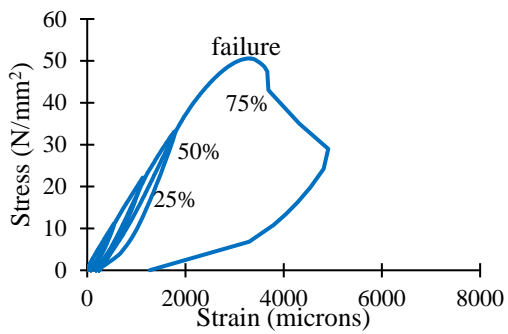


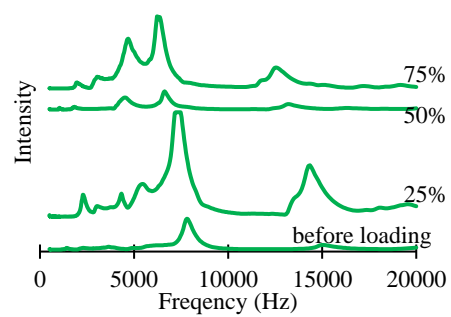
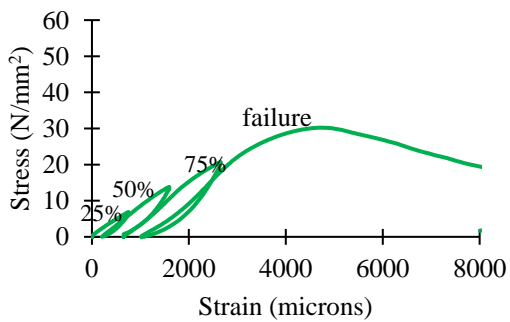
Figure 5-16 Stress-strain relation and resonance frequencies for cyclic loading at 28 days



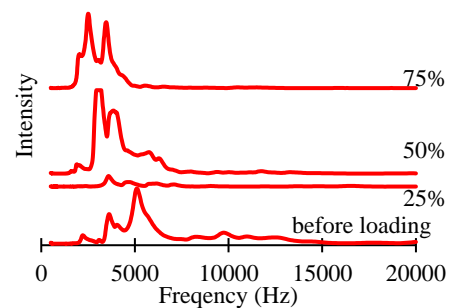
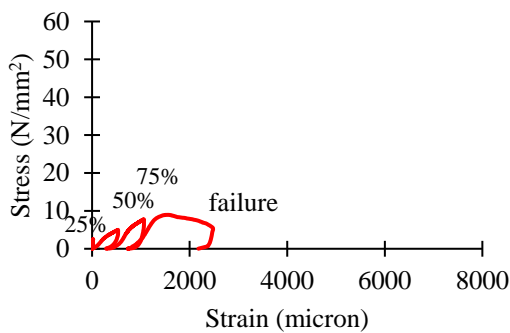
(a) Normal



(b) ASR

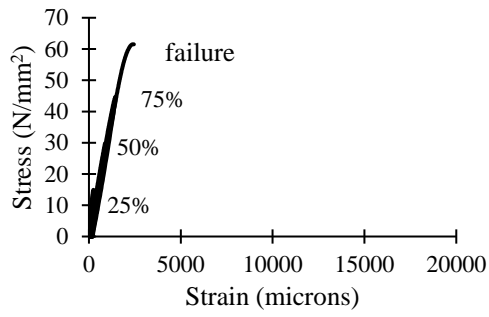


(c) DEF

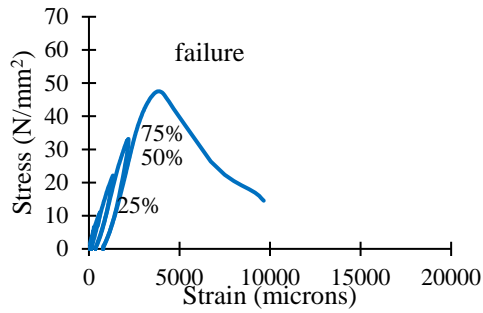
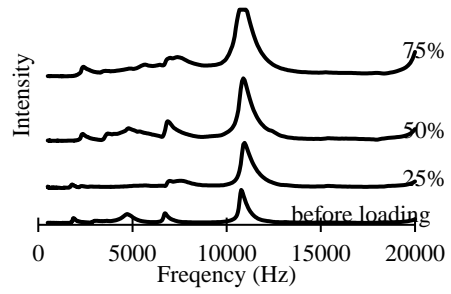


(d) DA

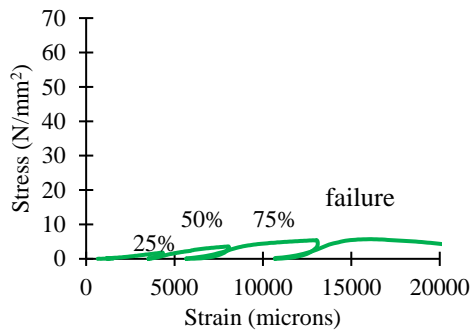
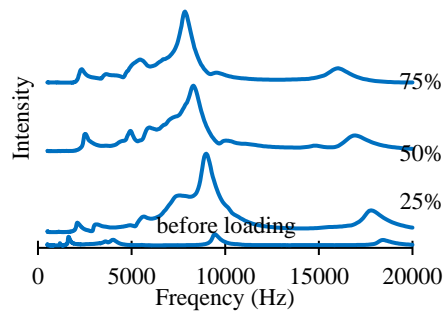
Figure 5-17 Stress-strain relation and resonance frequencies for cyclic loading at 90 days



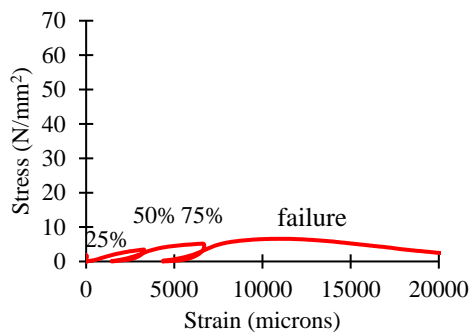
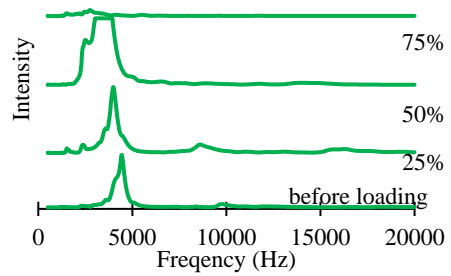
(a) Normal



(b) ASR



(c) DEF



(d) DA

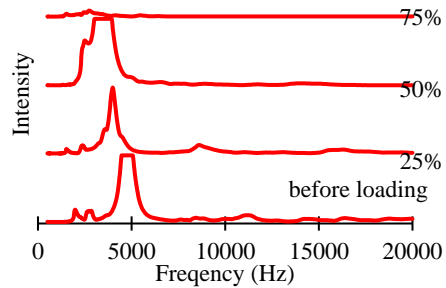


Figure 5-18 Stress-strain relation and resonance frequencies for cyclic loading at 150 days

5.3.6. Evolution of bond strength

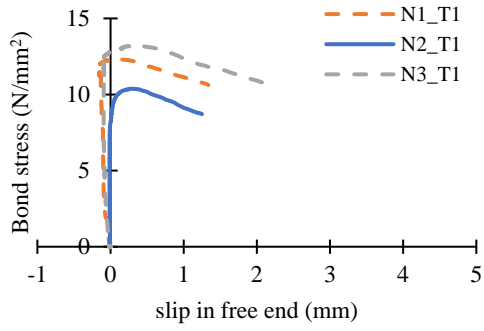
The result of the pullout test at 28 days, 90 days and 150 days are shown in Figure 5-19, Figure 5-20 and Figure 5-21 respectively. The right-hand side of the figure shows the stress-strain relationship of the pullout steel. The numerical values of the pull-out strength and slip values are shown in Table 5-6. The peak strength of all pullout tests is shown in Figure 5-22. It shows that in some of the specimens, the rebar yielded. In the cases when the rebars yielded, the actual bond strength cannot be calculated and thus, such values were discarded for further calculations. The yielding of rebar was due to the underestimation of bond strength using the relation provided in the design codes. For example, JSCE states the relation between bond strength (f_b) and compressive strength (f_{ck}) as $f_b=0.28*f_{ck}^{2/3}$ (JSCE, 2007). For a strength of 45 N/mm^2 , this relation gives a value of about 3.54 N/mm^2 . If a material safety factor of 1.3 is included the ultimate bond strength is about 4.61 N/mm^2 . In case the British Standards is used, the relation is $f_b=0.5*f_{ck}^{1/2}$ for a deformed bar in tension (BSI, 1997), which results in bond strength of 3.35 N/mm^2 . The bond strength calculated in this experiment was about 11.86 N/mm^2 for the normal specimens, which is much higher than the anticipated values. It was realized in the latter part of the experiment that other researchers also obtained similar values of bond strength (P. Li et al., 2020). Fortunately, the ultimate bond strength lied in approximately in the borderline, hence the strength of some of the specimens in which steel did not yield could be used for bond strength analysis. The rest of the specimens, in which the steel yielded (shown by broken lines in the figure), could not be considered for the quantitative analysis, these specimens, however, can be used for qualitative analysis of bond strength evolution. The following discussion is based on the specimens in which steel did not yield.

From Figure 5-19, Figure 5-20 and Figure 5-21, it can be observed that in Normal specimens, the peak pullout force also did not change much.

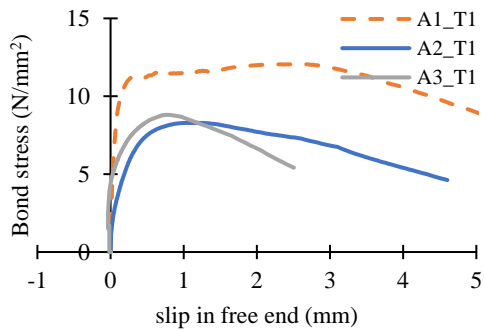
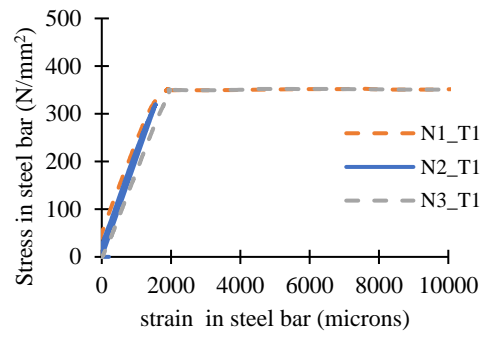
In the case of ASR specimens, the pullout force caused some of the rebars to yield in 28, 90 days and 150 days. The average bond strength was gradually improved by about 32% at the end of 150 days reaching about 11.28 N/mm^2 from 10.38 N/mm^2 at 28 days as shown in Table 5-6.

In the case of DEF, the bond strength on 28 days showed the yielding of steel in all the specimens. However, on 90 days, the strength was drastically reduced and was about 9.55 N/mm^2 and by 150 days it was reduced to 8.05 N/mm^2 .

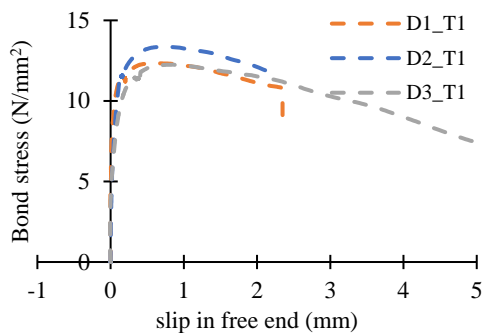
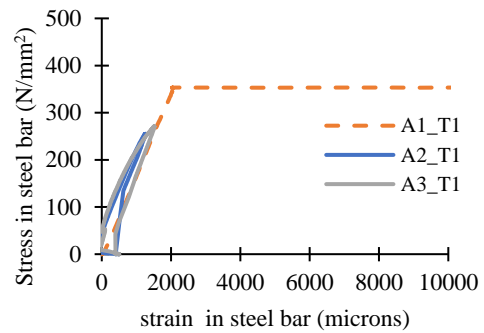
In the case of the DA specimen, the bond strength was low from the beginning. The initial strength was about 7.84 N/mm^2 . This was slightly improved by about 2% on 90 days, however, it eventually reduced by 3% on 150 days. The small change could be due to variability in the material and experimental error, the general trend should be gradual loss in the bond strength.



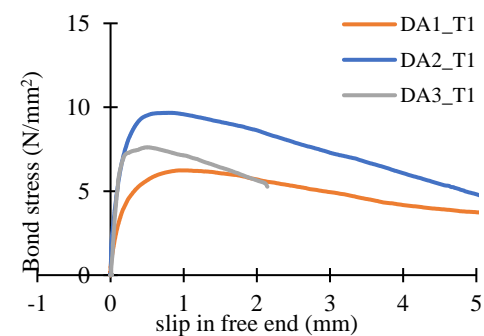
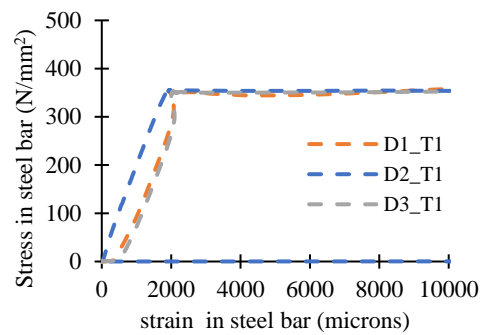
(a) Normal



(b) ASR



(c) DEF



(d) DA [*broken line indicates the specimen in which steel yielded]

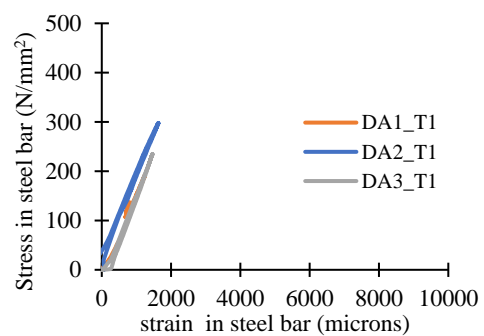
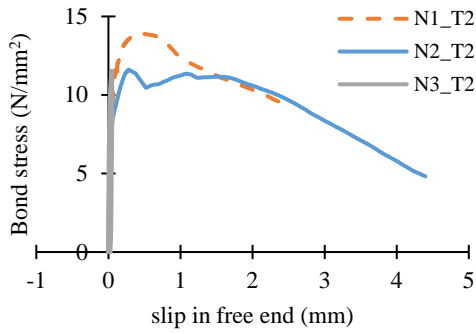
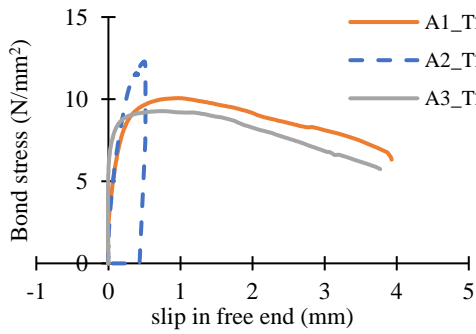
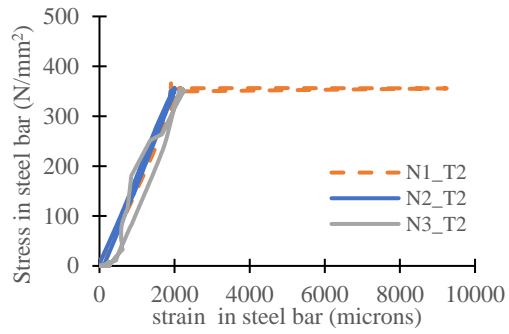


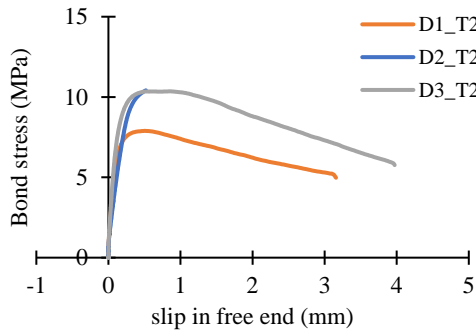
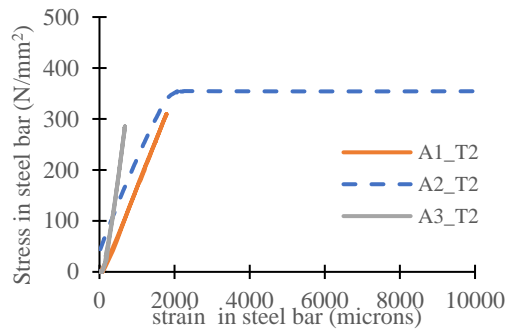
Figure 5-19 Bond stress and corresponding stress in steel rebar at 28 days



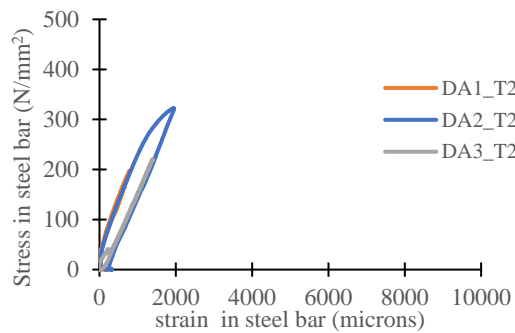
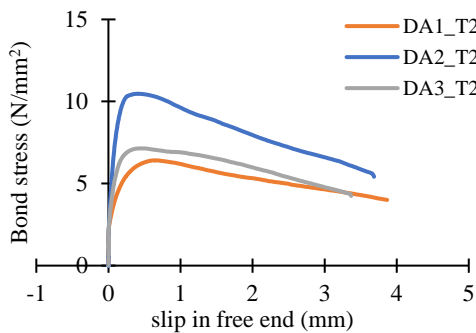
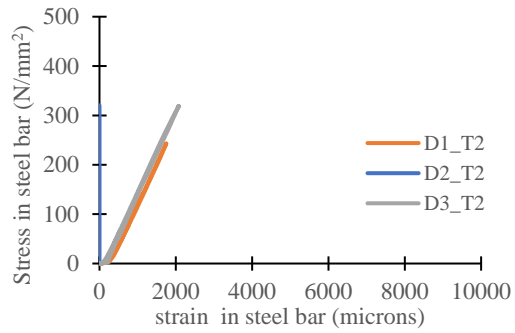
(a) Normal



(b) ASR

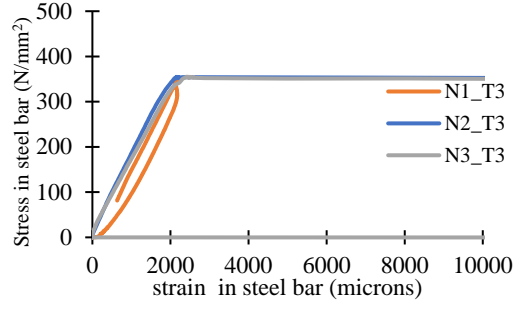
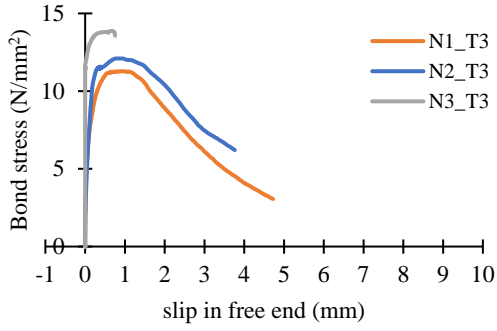


(c) DEF

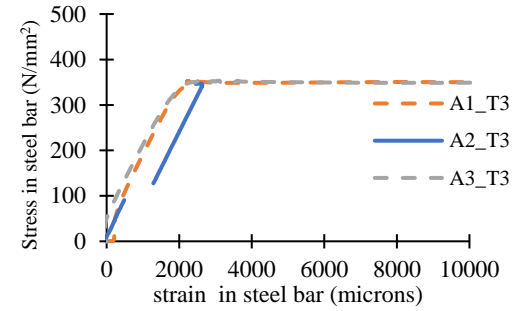
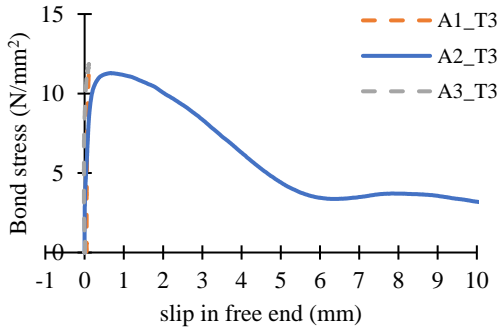


(d) DA [*broken line indicates the specimen in which steel yielded]

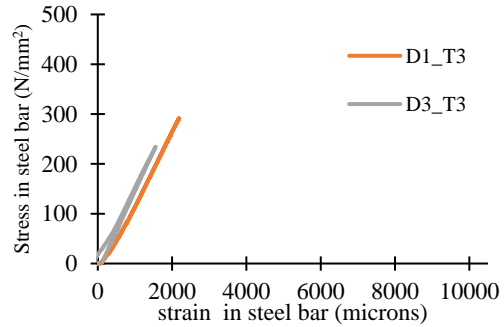
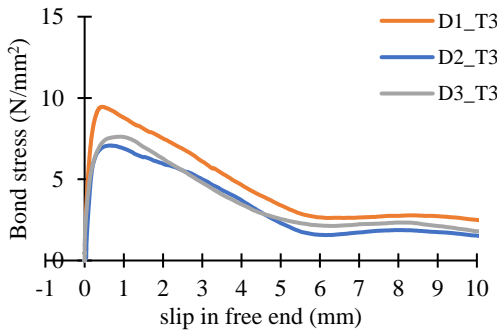
Figure 5-20 Bond stress and corresponding stress in steel rebar at 90 days



(a) Normal

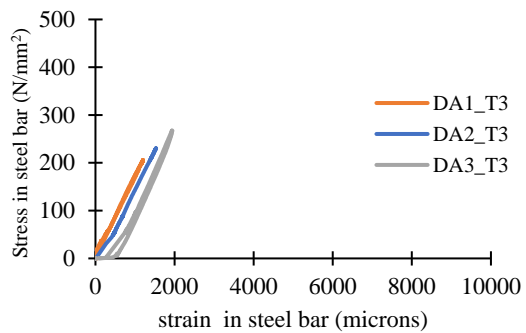
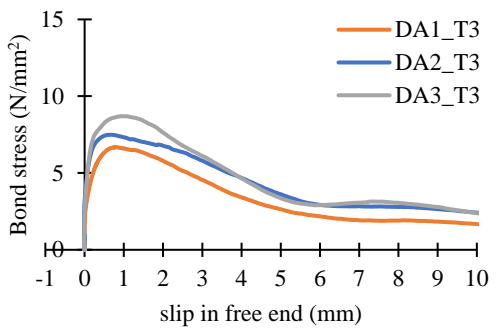


(b) ASR



(c) DEF

[strain gauge broke in one specimen]



(d) DA [*broken line indicates the specimen in which steel yielded]

Figure 5-21 Bond stress and corresponding stress in steel rebar at 150 days

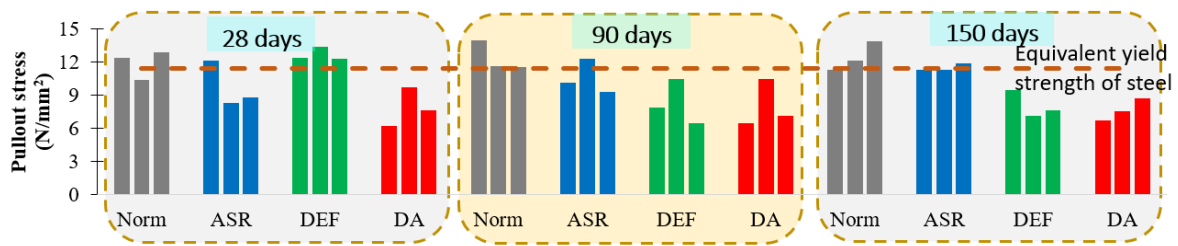


Figure 5-22 Peak pull out the stress of all specimens at 28 days, 90 days and 150 days

Table 5-6 Peak pullout strength and slip

	Normal	ASR	DEF	DA	
Age 28 days					
Bond strength (N/mm ²)		10.38	8.55	all yield	7.84
Slip at peak load (mm)		0.29	0.97	all yield	0.76
Age 90 days					
Bond strength (N/mm ²)		all yield	9.67	9.55	8.01
Slip at peak load (mm)		all yield	0.85	0.63	0.50
Age 150 days					
Bond strength (N/mm ²)		11.28	11.28	8.05	7.62
Slip at peak load (mm)		0.95	0.40	0.70	0.80

Note: The above table is based on only the specimens in which steel did not yield.

5.4. Discussion

5.4.1. Comparison of the evolution of strain

The evolution of the average expansive strain in the cylinder is shown in Figure 5-23. The summary of peak strain is shown in Table 5-7. Similar to the observation made in previous chapters, the rate and magnitude of strain evolution in DA specimen was the largest followed by DEF. The expansion in the ASR specimen reached about 1700 microns (0.17%) while the strain in the Normal specimen was negligible. If we compare the strain in the cylindrical specimen with the strain in the pull-out specimen shown in Figure 5-24, it can be observed that there is a significant reduction in expansion strain for DA and DEF specimens. The strain was reduced by up to 45%. The main reason for the reduction is due to the restraint effect by the main rebar and corner stirrups.

Among the pullout specimens which were restrained in all directions, the strain along the main rebar (H-direction) was lower compared to the perpendicular direction (V-direction). The ratio between strain in H and V direction lied between 0.7 to 0.9. In the previous studies by Bouzabata et al that DEF and DA expansion was found to be isotropic in stress-free condition (Bouzabata et al., 2012a) while it showed anisotropy in the presence of restraints (Bouzabata et al., 2012b). The expansion was reduced in the direction of restraint only and there was no

transfer of volumetric strain to other directions. Although there were no faces to measure the free expansion in this experiment, it can be inferred from the graphs that, the reduction in strain is directly related to the amount of steel present in that direction and does not influence the other direction.

The ASR specimen showed a larger expansion in the pullout specimens compared to cylinders indicating ASR expansion becomes larger in restraint cases. Similar to the observation was made in the previous chapters. The actual reason for such behaviour is unknown at this stage, nevertheless, it is hypothesized that it is due to the narrowing of cracks due to restraints that prevent leaching of ASR resulting in additional strain. This is further described in 5.4.2.

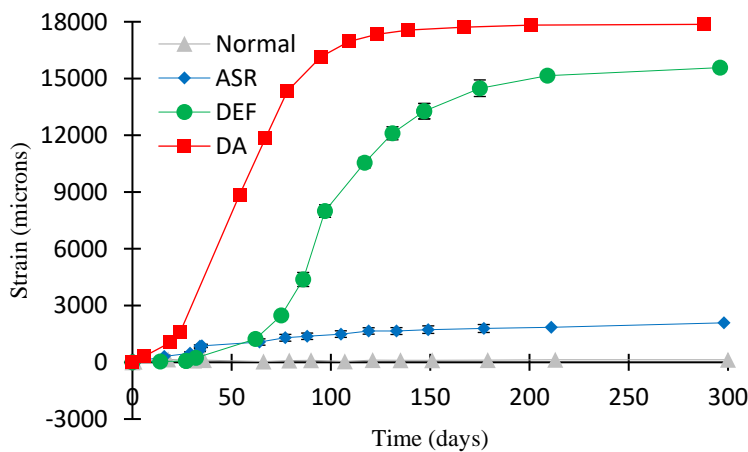


Figure 5-23 Evolution of strain in Normal, ASR, DEF and DA cylindrical specimens

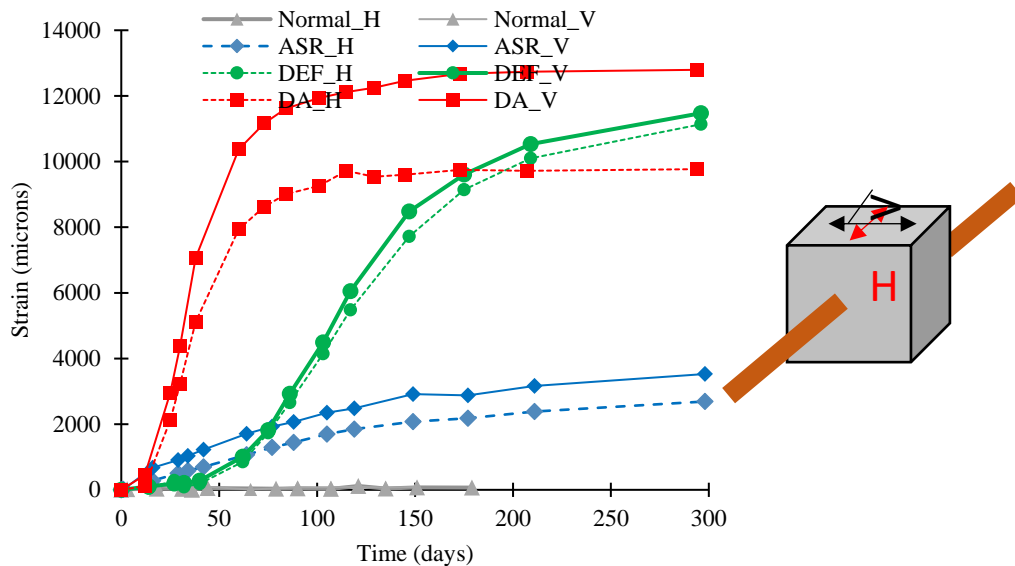


Figure 5-24 Evolution of strain in Normal, ASR, DEF and DA pullout specimens

Table 5-7 Expansive strain in cylindrical and pull out specimens

	Normal	ASR	DEF	DA
Cylinder	113	1,787	14,486	17,710
Pullout H-direction	67	2,178	9,143	9,745
Pullout V-direction	82	2,877	9,605	13,818

* *H-direction is parallel to the main rebar, V-direction is perpendicular to the main rebar*

5.4.2. Interaction of ASR and DEF reaction and expansion mechanism

The test result of ASR gel detection shown in Figure 5-12 and a similar result shown in Figure 3-14 indicates that ASR gel can move in the crack. It is clearly visible in the image of the cylindrical specimen in Figure 5-12 where the ASR gel is detected along a crack line. It can be seen that ASR infected cylindrical specimens had a larger amount of ASR gel compared to DA specimen even though the mix proportion in both specimens for ASR reaction, i.e. reactive aggregate and cement type, was similar. One of the reasons for the occurrence of lower ASR gel in more expanded concrete (DA specimens) could be due to leaching out of ASR gel through the pores by moisture exchange. This is evident from the fact that the amount of ASR gel was low in the samples taken near the surface of the specimen and also it was noticed that ASR gel distribution was uniform in cylindrical ASR specimen while in DA specimen, the concentration was near the surface as shown in Figure 5-22. When steel was present and expansion was low, in both pullout and internal restrained experiment (Figure 3-14), ASR gel distribution was uniform in both ASR and DA specimens. One possible reason for this behaviour is due to the restraint by reinforcement which prevented the opening of larger cracks from where ASR could be leached out.

From these observations, it can be said that in the initial stage of unreinforced specimens, both ASR and DEF contribute to expansion. When expansion exceeds some critical value, cracks become large enough and ASR gel is leached out. The void left by ASR gel leaching remains unaffected and hence the expansion in DA case become larger than DEF case in unreinforced case. A similar process occurs in the reinforced case at an early age, however, due to the presence of restraint, any void left by ASR leaching is used to accommodate the DEF expansion. The forcing of expansion into the voids helps to close the cracks and prevent further leaching of ASR gel. Hence in the reinforced case, the apparent expansion of DEF and DA specimens reaches a similar level.

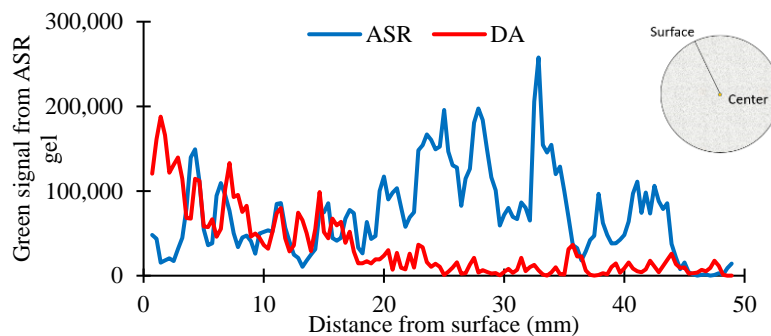
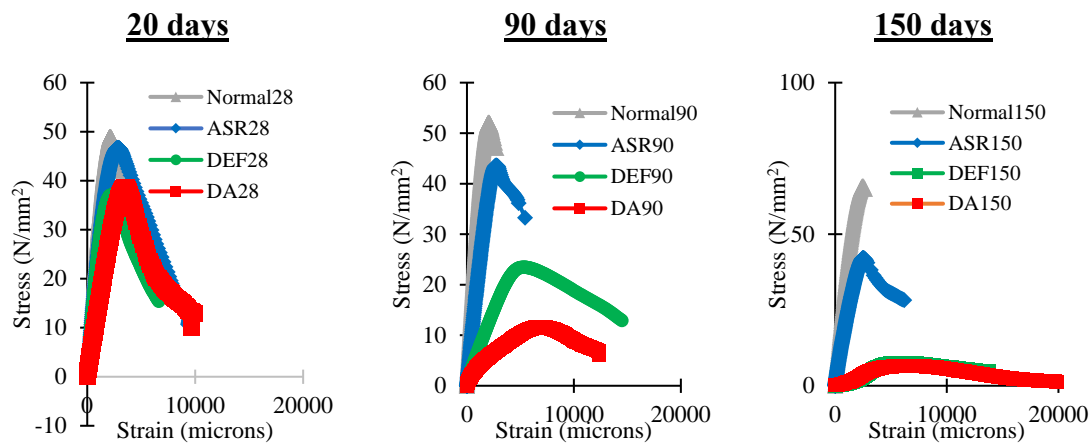


Figure 5-25 Distribution of ASR gel in ASR and DA cylinders

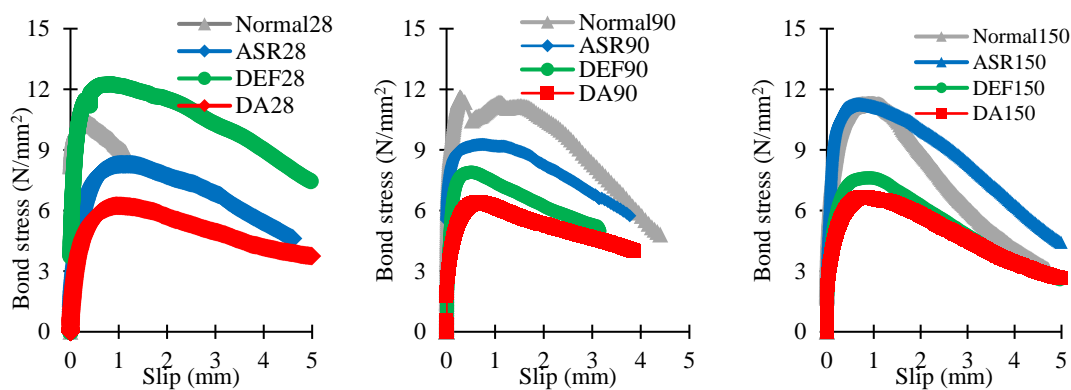
5.4.3. Relation between bond strength and compressive strength

The decrease in compressive strength is reflected in the gradual decrease in the pullout strength as shown in Figure 5-26. The corresponding relation between compressive and bond strength is shown in Figure 5-27. The numerical values can be found in Table 5-4 and Table 5-6.

In the Normal specimen, the increase in compressive strength only added to the yielding of steel, hence there was no change in the pull out strength. In the case of ASR, although there was no significant change in the compressive strength; the pullout strength was slightly improved. This is attributed to the prestressing effect at a lower expansion level Li et al. (2020). For the DEF specimen, the loss in compressive strength also resulted in the loss of pull-out strength; however, the reduction appeared to be stabilized at about 8 N/mm² as shown in Figure 5-27(a). In the case of DA specimens, the bond was reduced starting from 28 days. It is due to the large expansion that occurred in the specimen.

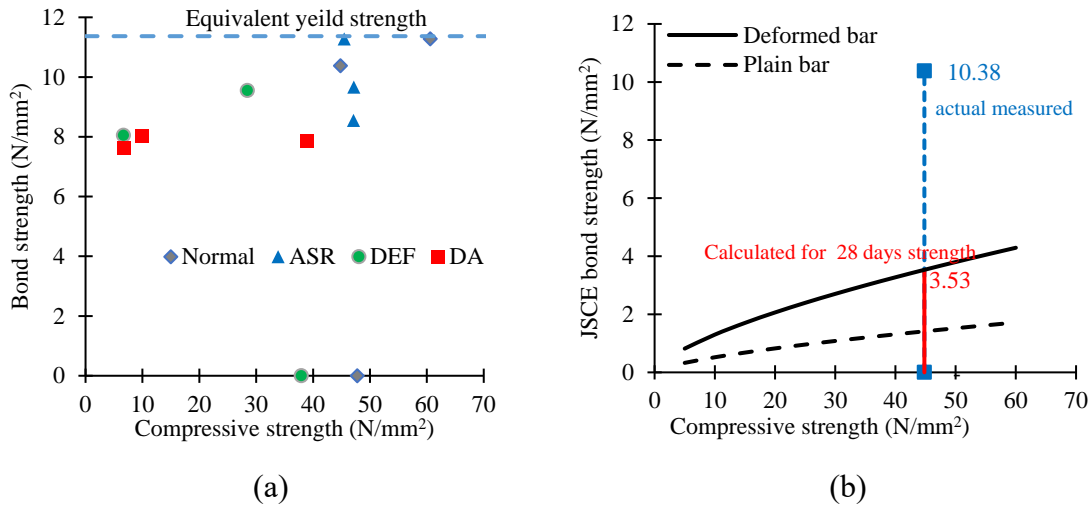


(a) Uniaxial compressive stress and strain



(b) Bond strength from pullout test

Figure 5-26 (a) Stress- slip curve and (b) stress in the embedded steel during pullout test at 28 days



* data point with zero bond strength refers to the set in which steel yielded in all the specimens

Figure 5-27 Relation between compressive strength and bond strength in (a) experiment and (b) based on JSCE code

5.4.4. Relation between expansion and strength

Figure 5-28 (a) shows a plot between the expansive strain and compressive strength of the cylindrical specimens and Figure 5-28 (b) shows a plot between the expansive strain and pullout strength based on the specimens that did not yield. Figure 5-29 shows the normalized form of the same information. The normalization is done by using the strength of the Normal specimen at 28 days as the base case. It must be noted that the normalized value gives the relative change in pullout strength.

The general tendency is that as the expansion increases, the compressive and bond strength reduces. The reduction in compressive strength is more significant compared to the bond strength. The loss in compressive strength could be as large as 80% at the expansion of about 10,000 microns (1%). This is in a similar range as described by Wang et al.,(2019) and other authors as described in Chapter 2. It was also observed that as the expansion progress the peak strain in the compressive test is increased. The increase in the peak strain is partially ascribed to the closing of pre-existing gaps (refer to Chapter 6).

The bond strength, however, was stabilized at about 60% and remained at the same level independent of the expansion. The reason for no further decrease in the bond strength is unclear, however, based on the fact that bonding occurs due to (a) adhesion between steel and concrete and (b) interlocking of ribs and concrete (Figure 5-30), it is anticipated that expansion damages the adhesion between steel and concrete by micro-cracks. These micro-cracks cannot damage mechanical interlocking because its size is small compared to the rib spacing in rebar and thus, the bond strength is contributed only by the interlocking of ribs. This hypothesis is indirectly verified by comparing the bond strength specified in the design codes, for example in JSCE (refer Figure 5-27(b)), the bond strength of a plain bar is specified as 40% of the bond strength of the deformed bars, which means the component of strength by the interlocking of the deformed bar is about 60%. A similar specification in British standards (BS 8110) results in about 43% of strength provided by the interlocking of deformed bars. Thus, it can be concluded

that the cracked zone contribute minimal adhesion and most of the force is resisted by the mechanical interlocking and thus the bond strength is stabilized at about 60%. This hypothesis should be verified in future by conducting a direct pullout test with plain rebars.

In the case of ASR, the bond strength was improved by about 5% at the expansion of about 3000 microns (0.3%). This expansion is far greater than reported by Li et al. (2020). This increase in bond strength is ascribed to the apparent increase in prestressing force at relatively low expansion. The prestressing occurs due to the confinement provided by shear stirrups at the edges and the main rebar in the centre of the specimen. At low expansion, ASR gel is not washed through the cracks as explained in section 5.4.2, which allows for the prestressing effect to occur. However, when the expansion is high, the gel is washed out which increase the porosity and decreases the strength. In this experiment, the ASR specimen had a low number of fine cracks in the surface, indicating that very few cracks in the inner concrete.

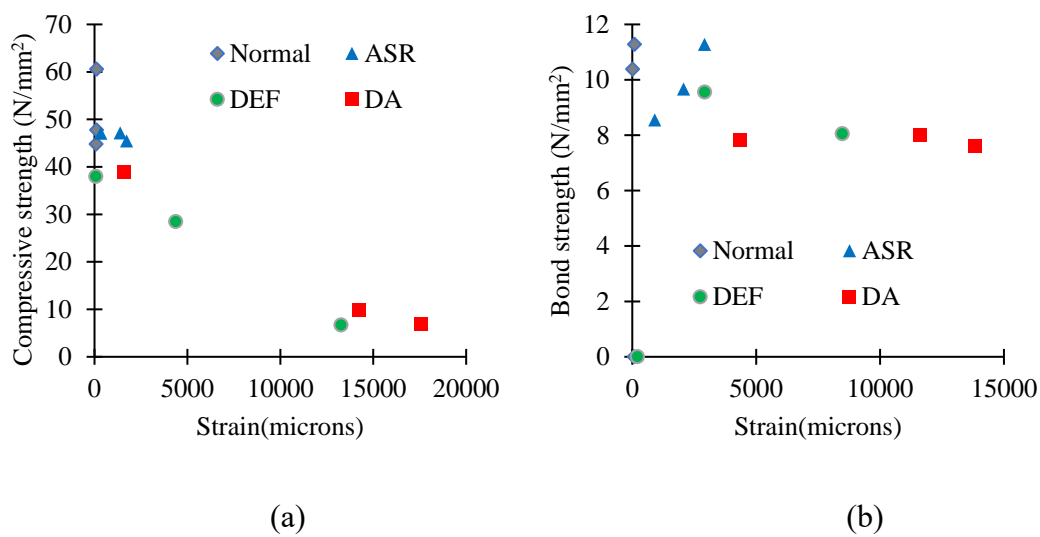


Figure 5-28 (a) Absolute compressive strength and (b) absolute peak pull out stress at various expansion levels based on specimens that did not yield

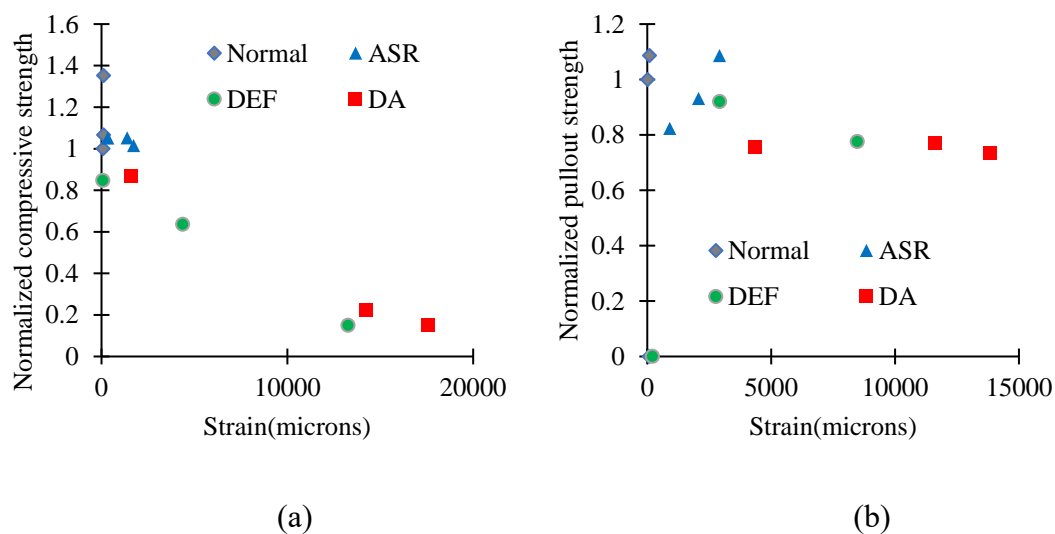


Figure 5-29 (a) Relative compressive strength and (b) relative peak pull out stress at various expansion levels based on specimens that did not yield

expansion levels based on specimens that did not yield

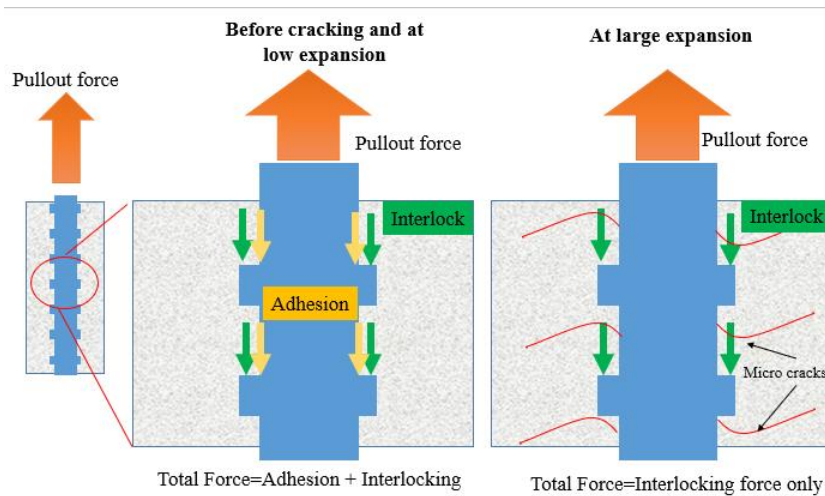


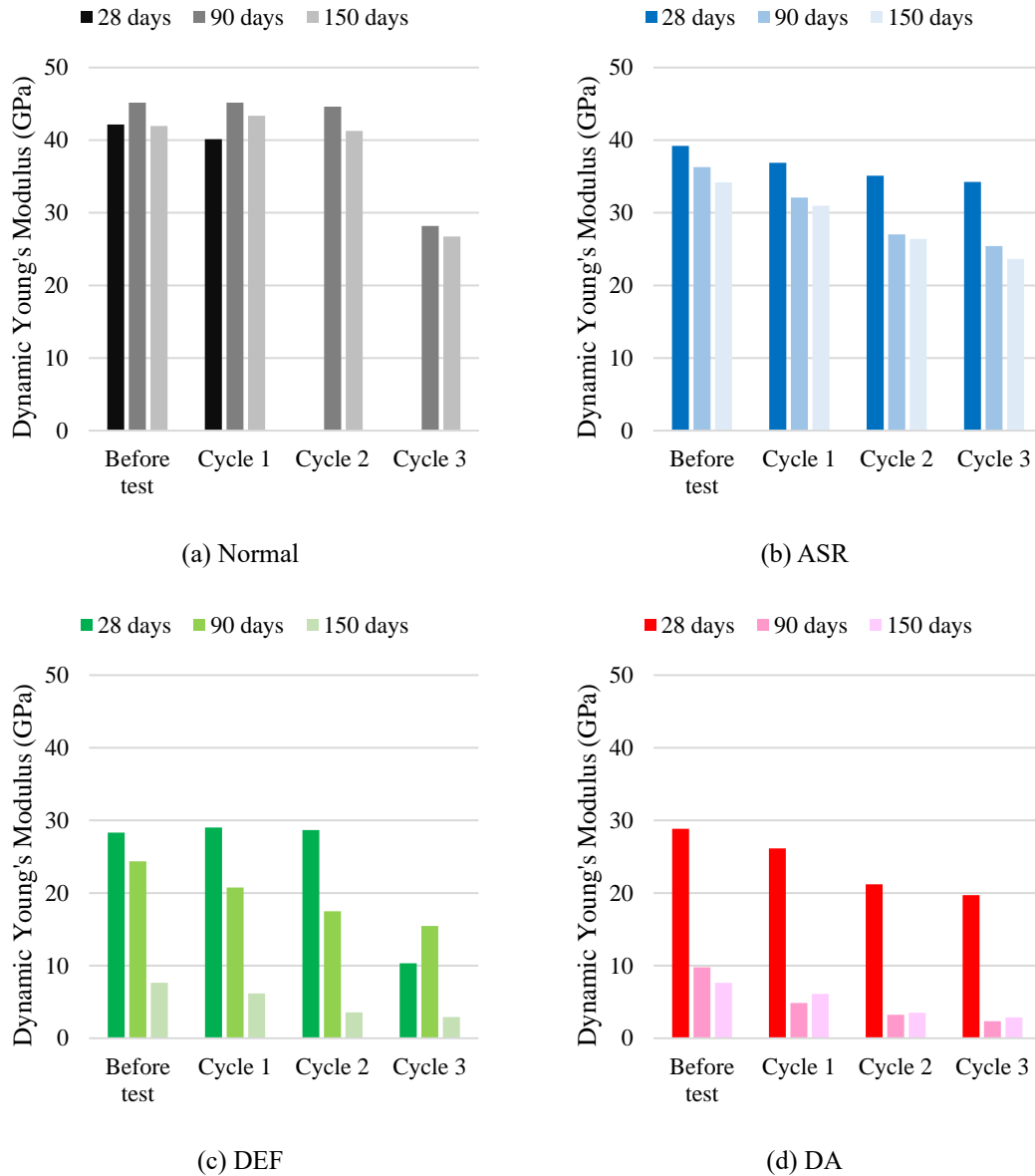
Figure 5-30 Mechanism of bond strength reduction

5.4.5. Evolution of damage in the affected concrete

Besides peak strength, it is of interest for structural analysis to know the value of elasticity of the material at various stress levels on the deteriorated concrete. For that, a stepwise loading test was done to measure the change in dynamic Young's modulus (E_d). The load was applied to induce stress of 25%, 50% and 75% of the peak load and resonance frequency was measured after each unloading.

The result of the experiment is shown in Figure 5-31. It can be seen that for the Normal specimens, the reduction occurred only in the last cycle i.e. at 75% strength level throughout the age of the specimen. The decrease in E_d in the ASR specimen was gradual (almost linear) with the stress. The tendency of the DEF specimen was similar to the Normal specimen at 28 days, however, from 90 days onwards, the reduction in E_d with stress was visible starting from the stress level of 25%. In the case of the DA specimen, the reduction of E_d was observed from the 28th day and it decreased gradually with the increase in stress.

Based on the above observation, it can be deduced that ASR, DEF and DA causes damage to the concrete even at a low-stress level. Not only the peak strength is reduced, but Young's modulus is also greatly affected. Thus, the structures affected with ASR needs more careful attention because, even though there is an apparent increase in the compressive and bond strength, the stiffness of the structure could be greatly reduced causing serviceability issue such as excessive deflection.



*Cycle 1 indicates 25% stress, Cycle 2 indicates 50% stress and Cycle 3 indicates 75% stress of the average peak strength

Figure 5-31 Impact on dynamic Young's modulus due to loading on affected structures.

5.5. Summary

In this chapter, the effect of ASR, DEF and DA in bond strength and compressive strength were studied. Based on the experiments and observations, the following conclusions are made:

- 1) The free expansion in the cylindrical ASR specimen converged at about 1,800 microns (0.18%). The strain in the DEF and DA specimen converged at about 15,000 microns (1.5%) and 18,000 microns (1.8%) respectively. The expansion due to DEF and DA was rapid compared to the ASR specimen.
- 2) In the pullout cube specimen, the strain in ASR reached about 2,200 microns (0.22%) and 3000 microns (0.3%) in longitudinal and lateral directions respectively. It was

8900 (0.89%) and 10,000 microns (1%) in DEF and 10,000 microns (1%) and 13000 microns (1.3%) in DA specimens respectively.

- 3) There was a significant reduction in expansive strain for DA and DEF specimens in the pullout test specimen due to the presence of reinforcement. The reduction in expansive strain was up to 45% compared to free expansion. In the pullout specimens, the strain along the main rebar was lower than in the perpendicular direction which was due to the additional restraint provided by the main rebar. The ratio between the expansive strain in longitudinal and lateral direction lied between 0.7 to 0.9.
- 4) The ASR specimen showed larger expansion in the pullout specimens compared to the free strains in the cylinders. This result was similar to that observed in the other chapters.
- 5) The uniaxial compressive strength was reduced to about 80% when expansion reached about 10,000 microns (1%) for DA and DEF specimens. The stress-strain curve gets flat and the plastic strain increased with the age of DA and DEF specimens. The strain at peak strength was also increased with expansion. In the case of ASR, the compressive strength did not change significantly.
- 6) In DA and DEF specimens, the bond strength gradually decreased with expansion and was stabilized at about 60% of initial bond strength. In the case of ASR, the bond strength was improved by about 5% at the expansion of about 3000 microns (0.3%). The increase in bond strength is ascribed to the apparent increase in prestressing force at relatively low expansion and the absence of larger cracks in the concrete.
- 7) ASR, DEF and DA affected concrete can experience internal damage starting from the low-stress level. The damage decreases Young's modulus. This can cause an unexpected change in stiffness and deflection of the structures even at the low-stress level. The structures affected with ASR needs careful attention because, even though there is an apparent increase in the compressive and bond strength, the stiffness of the structure could be greatly reduced causing serviceability issue such as excessive deflection.

6. Investigation in internal damage by X-ray CT

In Chapters 3 to 5, experiments on the mechanical strength reduction due to ASR/DEF were described. It was noted that the swelling of concrete causes a gradual loss in compressive strength and an increase in the peak strain. The physical reason for such behaviour, however, remains unclear from those experiments alone. There exist some indirect methods such as proposed by Sanchez et al. (2018) which estimates the level of damage in expanding concrete by measuring cracks under a microscope or by observing the loss in stiffness by applying cyclic loading. It is desirable to know the underlying mechanism for such behaviour by direct observation. For that, an X-ray computed tomography (CT) study was conducted to investigate the internal mechanism of compressive failure of highly expanded concrete. The main objectives of this experiment are as follows:

- a) to analyze the effect of pre-existing cracks on the compressive strength.
- b) to study the effect of various types of compressive stress on the evolution and propagation of cracks

For the experiment, DEF affected specimens that had undergone a large free expansion of over 20,000 microns (=2%) were used. These specimens were tested under monotonic, stepped, cyclic, and sustained loadings to obtain the stress-strain in order to examine the effect of loading pattern and stress level on the internal damage. The specimen preparation and CT scanning were done in Port and Airport Research Institute (PARI).

6.1. Methodology

6.1.1. Specimens

For the experiment, cylindrical specimens of 100 mm diameter and 200 mm height were prepared with the concrete mix shown in Table 6-1. The water-cement ratio was 0.5. The heat treatment was based on Famy et al.(2002) in which the temperature was set at 20°C for the first 4.5 hours after casting, it was then followed by a gradual increase to 90°C in the next 4 hours. After maintaining the same temperature for 11 hours, the temperature was gradually decreased to 20°C in the next 15 hours. The specimens were sealed up to an age of 21 days and stored in water at room temperature then after. The mean uni-axial compressive strength at the age of 28 days was 32.3 N/mm² and Young's modulus of elasticity was 28,600 N/mm². The expansion of the specimens was measured regularly for about 3 years, after the age of about 400 days the strain remained constant at about 20,000 microns (=2%) as shown in Figure 6-2. The expansion strain for two of the specimens used in CT experiment for the loading test was not directly measured however, it could exhibit almost the same expansion owing to the same mixing and curing conditions for the group coming from the same mix.

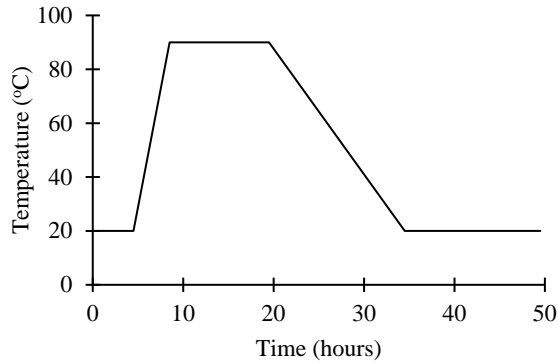


Figure 6-1 Heat treatment of the specimens

Table 6-1 Mix Proportion of DEF/ASR specimens

Cement (kg/m ³)	Sand (kg/m ³)	Coarse Aggregate (kg/m ³)	SO ₃ content (% of cement)	w/c ratio
337	798	965	8.65	0.50

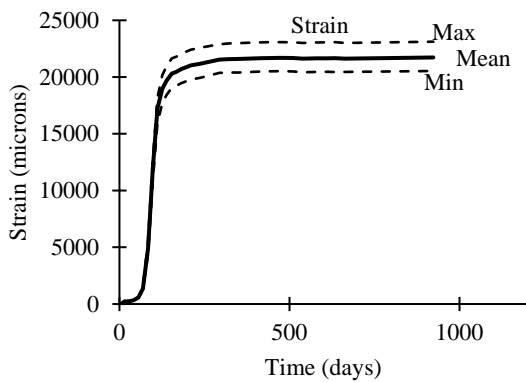


Figure 6-2 Strain and weight change of specimen over time

6.1.2. Mechanical tests

Four types of compressive loading were selected for the mechanical test to mimic various scenarios of loading in the real world. The first was monotonic loading that was done to estimate the compressive strength of the deteriorated specimens. The other three types of loadings are shown in Figure 6-3. The stepped loading type shown in Figure 6-3 (a) was done to evaluate the crack propagation process under several stress levels. The stress level was based on the monotonically loaded specimen which was about 4.7 N/mm² (~ 40 kN) Similarly, cyclic loadings shown in Figure 6-3 (b) and (c) were done to test crack propagation under repetitive loads. For the first type of cyclic load, two loading levels of 20 kN(= 50% of strength), 30 kN (= 75% of strength) were chosen. Additionally, another cyclic load was done at 30 kN to see the effect of cyclic load at higher stress. At the end of the cyclic load, the load was sustained for about 45 minutes without increasing the load. The sustaining of load at the end of the cyclic load was done to evaluate the behaviour of plastic strain coupling with the accumulated internal

crack propagation due to repeated load. Finally, a stepwise sustained loading was done as shown in Figure 6-3 (d) to combine monotonic and sustain loadings. The load was increased to a specific value (15, 30, 45 kN) and retained until the strain become stable, i.e., $d\epsilon/dt \approx 0$. Once strain reached became constant, additional load was applied. This test was done to examine the stability of internal cracks. CT scans were taken at the start, intermediate cycles, and end of the tests.

The strain stress was measured using a compressometer and a load cell with a setup shown in Figure 6-4. The dynamic Young's modulus was measured using the acoustic method described in ASTM-E1875-08.

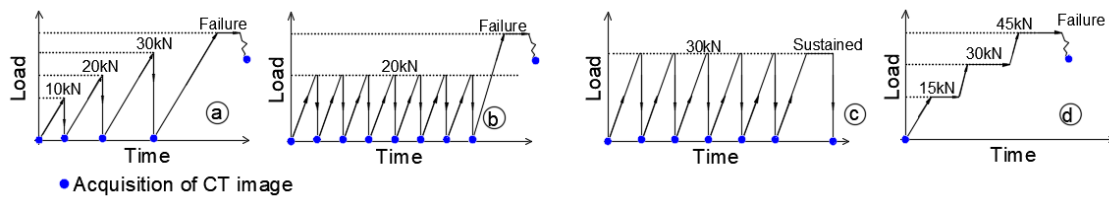


Figure 6-3 Types of loading procedure adopted during the experiment (a) stepped incremental loading, (b) cyclic loading (c)cyclic and sustained loading and (d) incremental sustained loading. The circular dot shows the timing of acquiring CT image

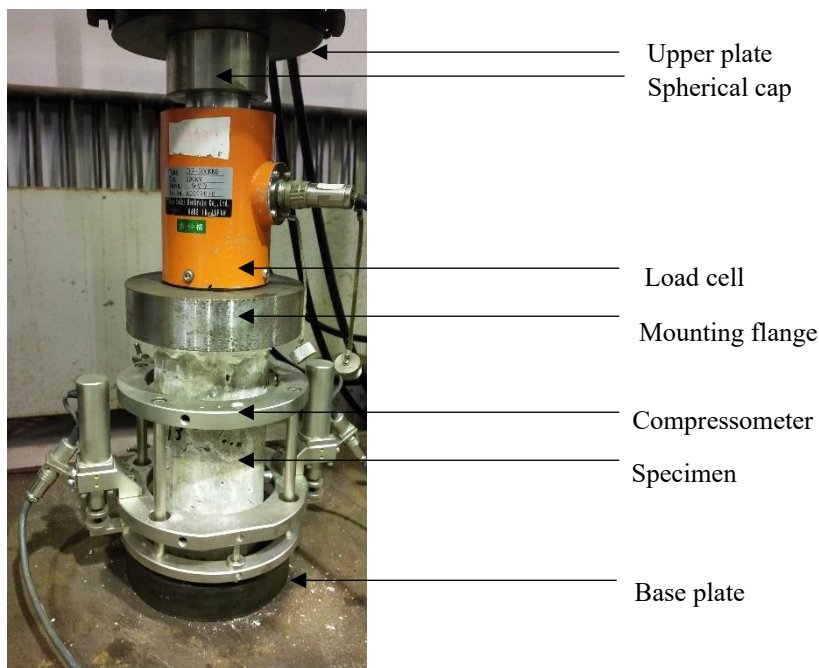


Figure 6-4 Setup for compression test

6.1.3. X-ray CT scan

The X-ray CT scans were carried out to visualize the internal cracks. The scans were taken using a μ -XCT (ScanXmate-D200RSS900) with a setup shown in Figure 6-5. The scanner took a series of 2D planer images along the specimen's height. The source voltage and

current of the x-ray was 160 kV and 0.2 mA respectively. The image was captured in a 418mm x 418mm flat panel with a resolution of 1504 px x 1504 px giving the image resolution of 163 $\mu\text{m}/\text{pixel}$ in the scanning plane. The slice thickness was 0.13 mm in the vertical direction. The CT images were combined to create a 3D model.

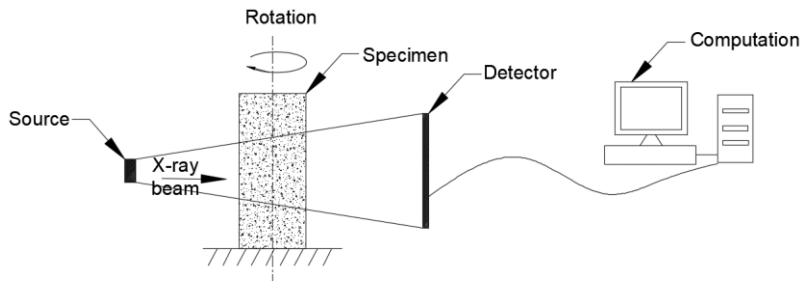


Figure 6-5 X-Ray CT scan setup

6.2. Specimen condition before the mechanical test

Figure 6-6 shows the state of some of the specimens before the mechanical examination. The specimens had degraded significantly, with cracks measuring up to 2.0 mm in width when examined under a microscope at a magnification of 25 times. In random spots and along the crack, an efflorescence of white deposits could be seen. Figure 6-7 shows the expansive strain and dynamic Young's modulus of the specimens used in this experiment. Since the dynamic Young's modulus of the specimens for loading types A and D were not significantly different from that of the others, the expansion strain before loading should be similar in all the specimens.



Figure 6-6 Condition of specimens before the mechanical test

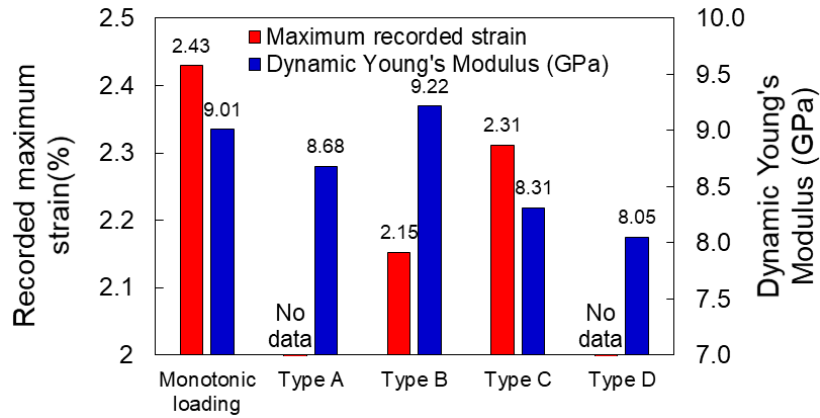


Figure 6-7 Dynamic Young's Modulus and maximum DEF strain of specimens before the mechanical test used for various loading types

6.3. Measurement of elasticity

The degradation of dynamic Young's modulus of elasticity was evaluated using an acoustic method in which acoustic waves of various frequencies are passed through the specimen and the one with the highest return (i.e. resonance frequency) is used to calculate Young's modulus. This dynamic Young's modulus is given by the following relation:

$$E_d = 4 * L^2 * f^2 * \rho$$

Where L is the length of the cylinder, ρ is the density and f is the resonance frequency.

6.4. Crack characterization

The images from X-ray CT scans were used for the analysis of crack volume and crack size distribution. The crack was identified in the CT image by using a thresholding method. This method is based on the detection of a difference in the pixel brightness which arises due to the difference in density of the concrete phases (Skarżyński et al., 2019). Firstly, the 2D images acquired from CT scans were stacked and passed through filters and thresholding. Based on several trials and recommendations from similar prior works by other researchers, the bandpass FFT filter was found to be suitable for crack detection (Stoev, 2012). The background noise is removed by the filter. It also blurs the image by removing high spatial frequencies. After that, thresholding was done to isolate the cracked area. Figure 6-8 shows the processes. The discretized image is a binary image that has the pixel intensity of either 0 or 255 that represents a crack and no crack area respectively. In this process, the air voids are also registered as black pixels. The image processing and calculation were done using ImageJ, an open-source software (Schindelin et al., 2012).

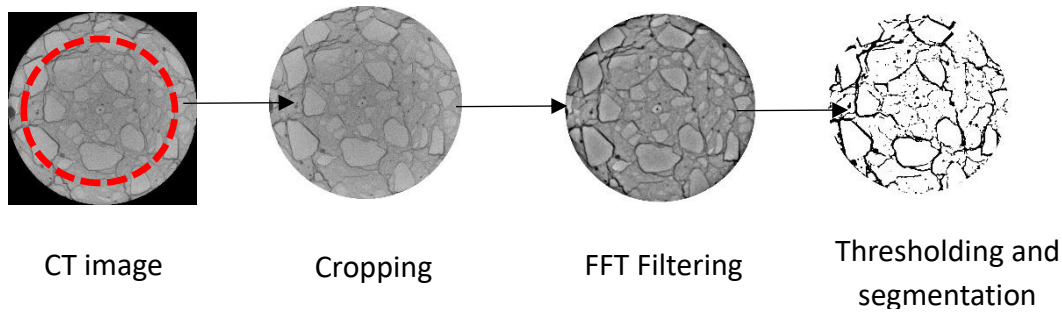


Figure 6-8 Steps for image analysis

The thresholding level can differ based on user preference and experience (Mardia & Hainsworth, 1988). To minimize input bias, a sensitivity analysis was done. Three ranges viz. 0-110, 0-120 and 0-130 of thresholding levels were selected and tests were done. Figure 6-9 shows the crack volume detected at different thresholding for various types of loadings. Figure 6-10 shows a typical case of crack detected with that thresholding. It can be seen that 0-110 thresholding underestimates the amount of crack, while 0-120 and 0-130 delimitates the crack zone. While checking with Otsu’s method on random 150 CT images, as proposed by Zhang et al. (P. Zhang et al., 2017), the recommended thresholding level was in the range of 0-112 to 0-120. Based on this finding, a threshold value of 0-120 was used in this study.

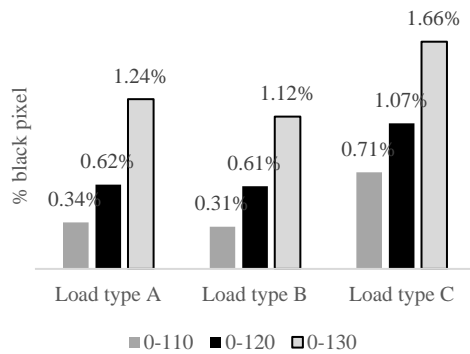


Figure 6-9 Sensitivity of thresholding for specimens after failure for mid stack

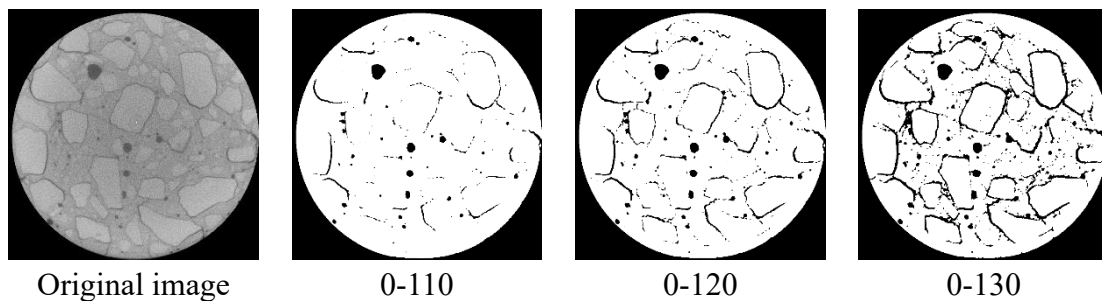


Figure 6-10 Crack detected at threshold values of 0-110, 0-120 and 0-130

6.4.1. Separation of cracks and air voids

The cracks were separated from the air voids by conducting two-stepped processing of

the binary images as shown in Figure 6-11. This method is similar to the one described by Mac et al. (2021) which was used to separate fine cracks from the air voids. However, some modification was necessary to correctly isolate the DEF cracks because the DEF cracks are larger having their size in the range of small air voids. The separation was done as follows. Firstly, particle analysis was done based on the size and circularity of the black pixels. Minimum size of 12 sq. pixels and circularity between 0.70-1.00 (1 indicates a perfect circle) was considered for the analysis. This process generates an image mask showing circular air voids. Secondly, to remove the air voids that were connected to the DEF cracks and/or that were non-spherical, a binary erosion was done by using minimizing filter of size 3 pixels. The process effectively isolates the air voids from cracks, however, it also erodes the boundary of the air voids making them smaller than the actual size. To regenerate the boundary of such voids, a Gaussian blur with a deviation of 4 was applied followed by binarizing the image. Finally, the image showing air voids was subtracted from the original image to isolate the cracks. A typical 3d view after the completion of the separating process is shown in Figure 6-12.

6.4.2. Crack volume

The crack volume was estimated based on the cumulative area of black pixels on the binary image multiplied by the thickness of the slice. The crack volume of the specimens was calculated using the mid 5cm of the specimen to prevent boundary effect. For comparison, the 10 cm was also calculated.

6.4.3. Crack width

The width of the crack was determined by analyzing the intensity of the image as described in Tomczak et al. (Tomczak et al., 2017). For the analysis, the mid 5 cm (376 slices) were used. Firstly, sample lines were drawn as shown in Figure 6-13, each covering 20 ° zone. The intensity of each pixel was then plotted along each sample line and the crack width was calculated by counting the number of black pixels encountered along the sample line. Only cracks of 2 pixels or more (~326 μm) were counted because a single isolated pixel could be a noise arising from thresholding. The process was repeated for each 10th slice of 376 slice stack. The summation of crack count is reported here.

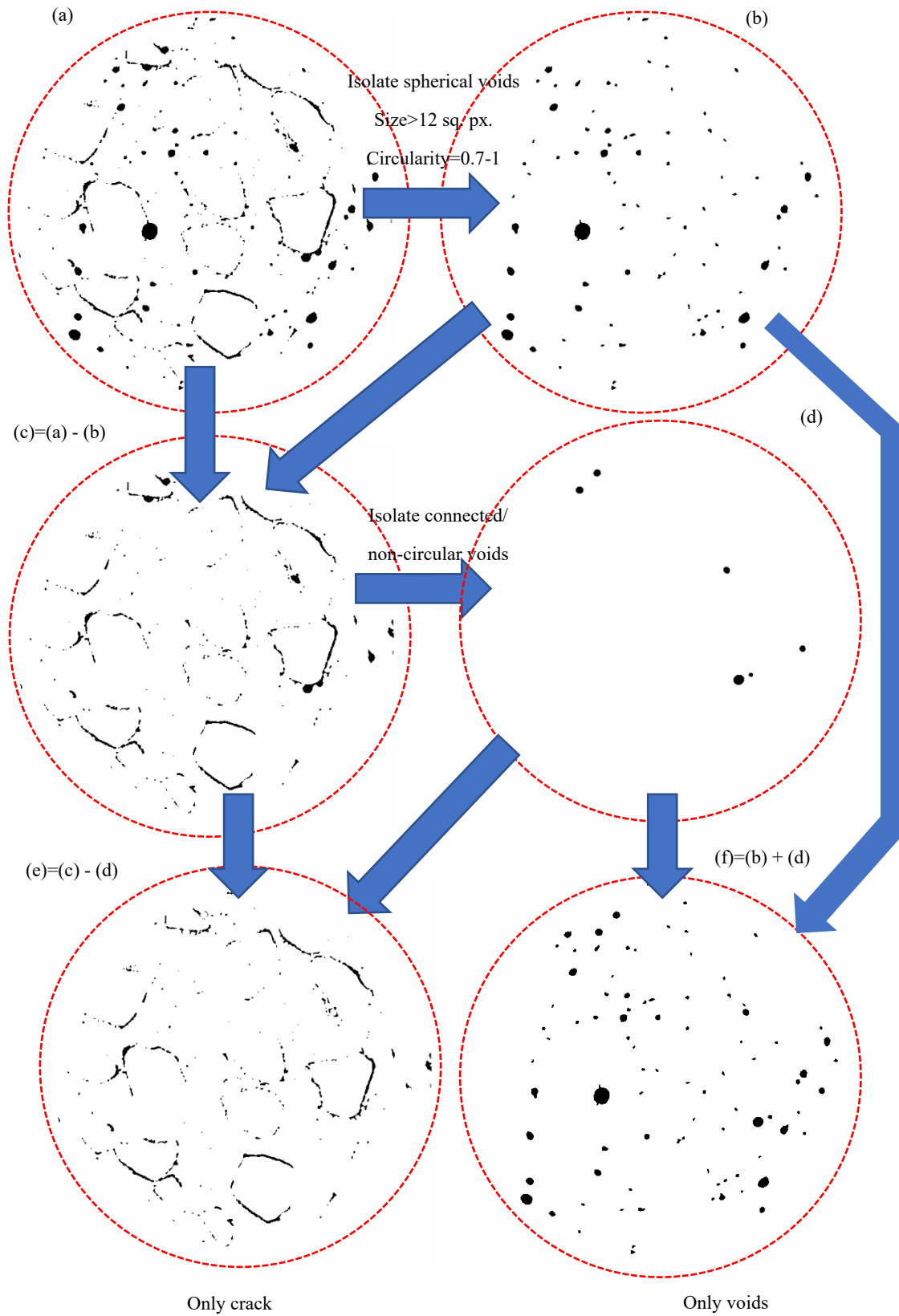


Figure 6-11 Process of separating air voids and cracks

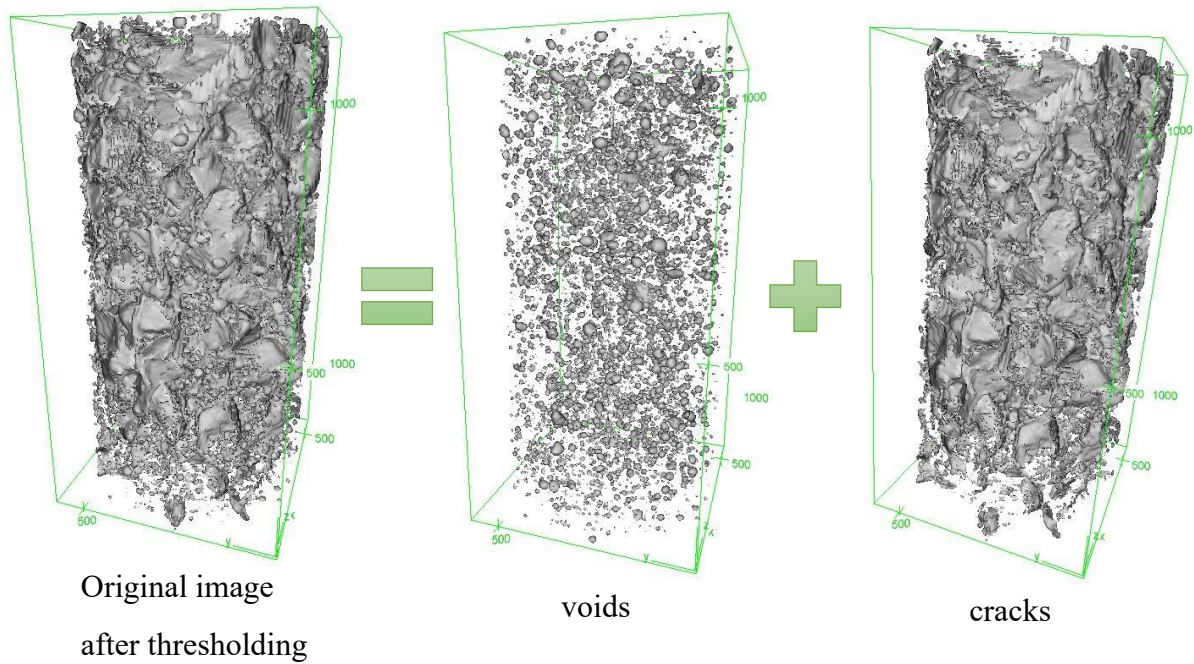


Figure 6-12 3d view of voids and cracks

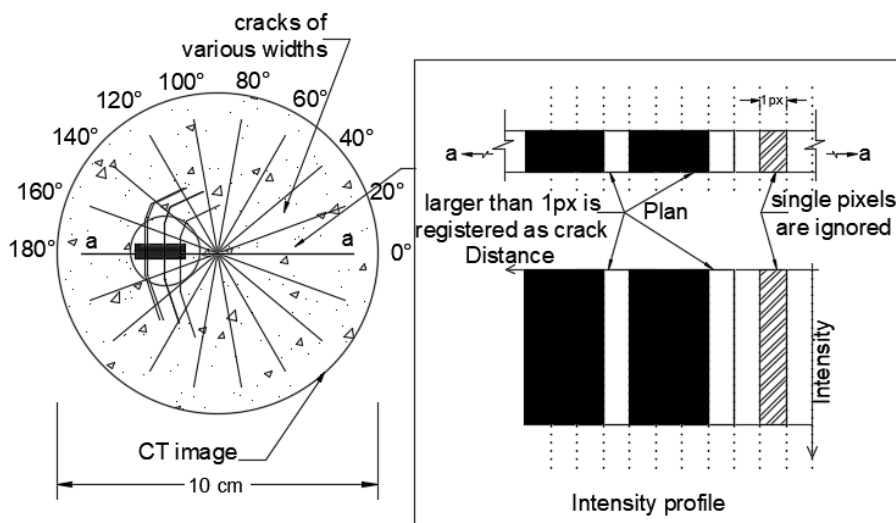
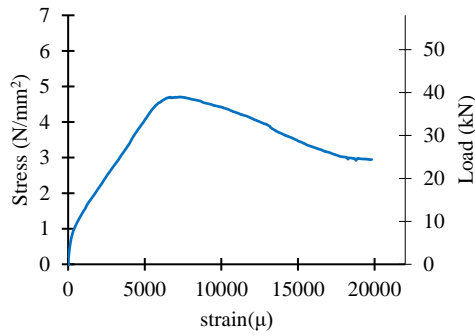


Figure 6-13 Determination of crack width

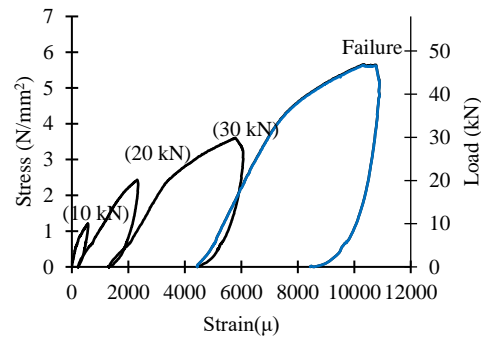
6.5. Results

6.5.1. Stress-strain relationships of concrete with DEF expansion under various compressive loading patterns

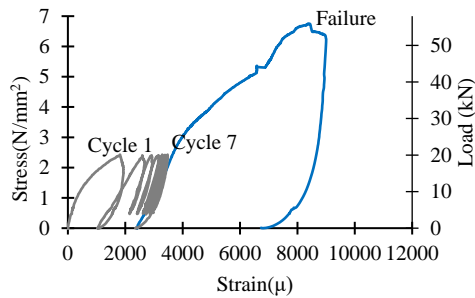
The stress and strain behaviour under various loading types are shown in Figure 6-14.



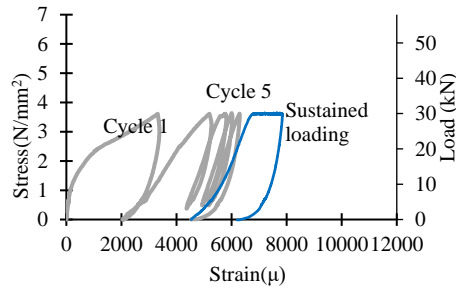
(o) Monotonic loading



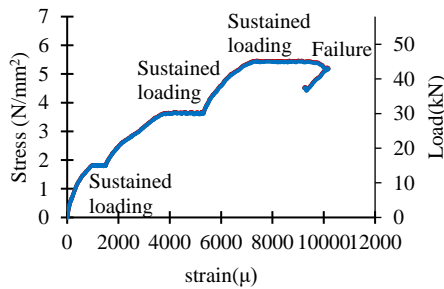
(a) Step loading



(b) Cyclic loading of 20 kN (= 2.40 N/mm²)



(c) Cyclic loading of 30 kN (=3.61 N/mm²)



(d) Sustained loading at 15 kN (=1.82 N/mm²), 30 kN (=3.64 N/mm²) and 45 kN (=5.46 N/mm²)

Figure 6-14 Relationships between stress and strain under various compressive loading patterns

In the monotonic loading, the peak stress was 4.70 N/mm^2 as shown in Figure 6-14 (o). The 28 days mean strength was 32.3 N/mm^2 , which means a reduction of about 85% compressive strength. The axial strain, in the vertical direction, at the peak load was about 6200 microns (6.2%). For comparison, the strain at peak load for a non-damaged specimen lies in the range of about 1700-2200 microns (De Nicolo et al., 1994). This indicates that the internal damage by DEF can increase the plastic strain. A nonlinear stress-strain relationship was observed from the beginning of loading in Figure 6-15 and the elastic behaviour at the low-stress level was not observed.

As shown in Figure 6-14 (a), the residual strain at unloading increased in all steps of

incremental loading indicating an increase of plastic strain with loading in each step. The initial stiffness was not changed even though the step load increased. The stiffness during cyclic loading was steeper than that at 1st loading or re-loading (refer to Figure 6-14 (b) and (c)). Figure 6-14 (d) shows that the strain gradually increased at sustained stress, which became larger at larger loads for the same loading duration. In the sustained loading case, the failure occurred when the load was sustained at 45 kN (=5.46 N/mm²) for few minutes.

The failure compressive strengths in the cases of step loading, cyclic loading with 20 kN (=2.40 N/mm²) and sustained loading are higher than that in the case of monotonic loading (4.70 N/mm²). This is attributed to the most significant DEF expansion in the monotonic loading's specimen as shown in Figure 6-7 even though the expansion of specimens for step and sustained loadings was not measured, they should have a lower value. In all the tests, the peak stress and strain at failure, except cyclic loading of 30 kN, were not significantly different from those under monotonic loading taking into account the variation of expansion DEF strain as shown in Figure 6-7. It suggests that the loading history may not have an effect on the final failure state of concrete when the DEF expansion is large.

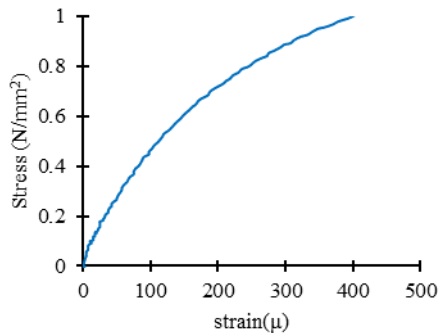


Figure 6-15 Enlarged initial stress-strain relationship for monotonic loading

6.5.2. Crack distribution and propagation after various loading

Owing to residual deformation resulting from plastic deformation and crack propagation, the position and angle of aggregate and crack in the cross-sectional picture after each loading is slightly different even in the same specimen in the image analysis. The distribution and propagation propensity of cracking after each loading, on the other hand, was consistent over a large number of images and the cumulative data.

Figure 6-16 shows the crack propagation after each unloading in the step-loading. Note that the figures shown in this section are the original binary image after thresholding (without air void separation) The gaps in the loading direction gradually closed with the increase of load while the gaps in the radial direction opened with the increase. When the load was about 64 % of strength, i.e., about 30 kN (=3.64 N/mm²), the cracks from aggregates started to propagate and then connected with other aggregates to form a network. At lower stress levels (about 2.42 N/mm² = 43% of strength), the pre-existing gaps around coarse aggregates can be vertically closed and horizontally opened due to the loading and Poisson's effect but it did not propagate to connect with the aggregates.

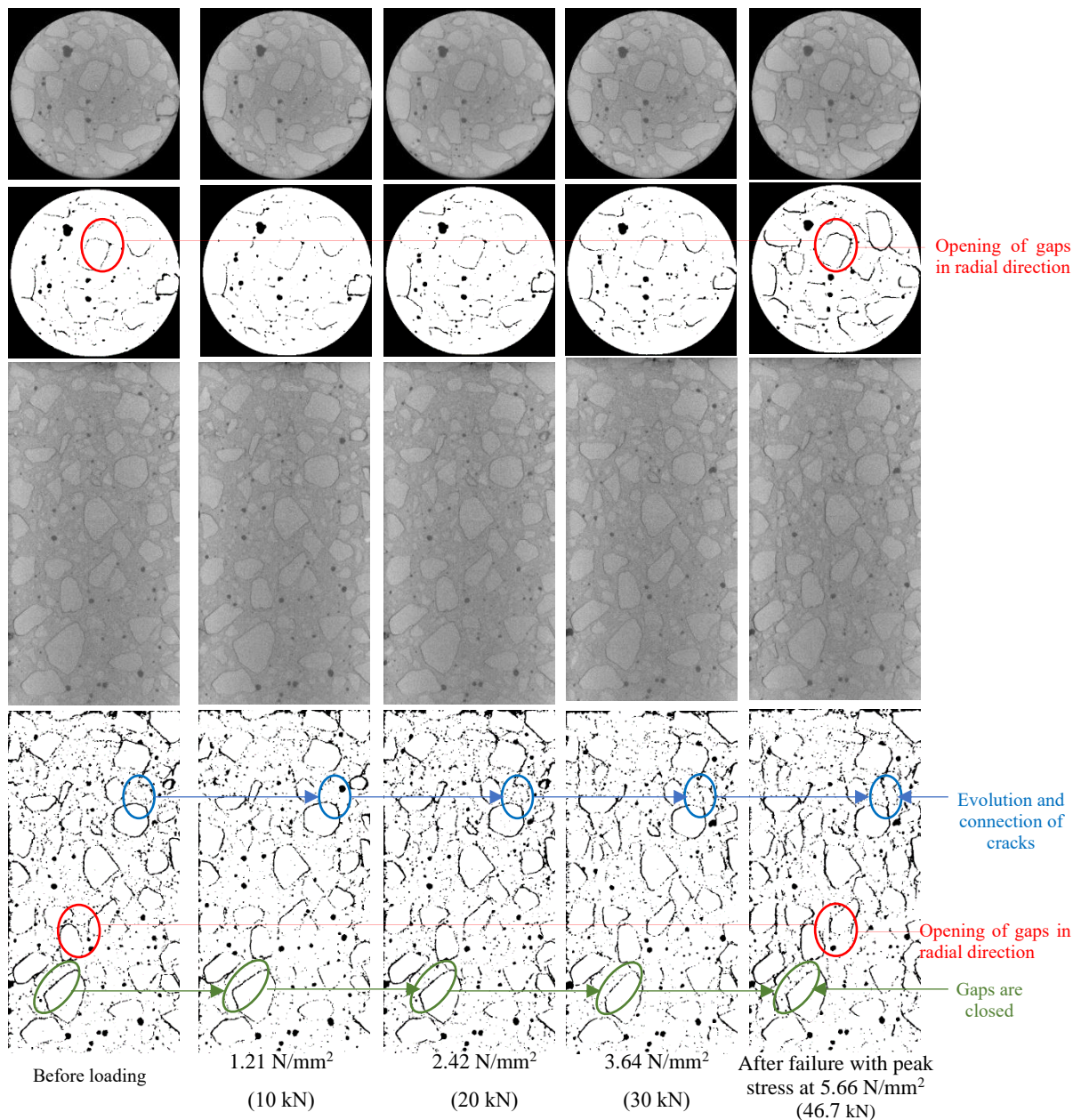


Figure 6-16 X-ray CT and binary image showing crack propagation due to stepwise loading

The crack distribution under cyclic loading of 20 kN ($=2.40 \text{ N/mm}^2$) is shown in Figure 6-16. The pre-existing gaps around aggregate due to DEF expansion were closed or opened depending on the stress direction as explained in the previous section. The crack propagation connecting the aggregates was observed at the failure, which suggests that the crack network in aggregates to cause the failure does not form at the low-stress level of 2.40 N/mm^2 (about 35.6 % of strength).

Figure 6-18 shows the crack distribution under cyclic loading with 30 kN ($=3.61 \text{ N/mm}^2$). The vertical cracks are formed after the 1st loading which propagated to connect with the aggregates with the additional cyclic loading. Similar to the 20 kN case, the existing gaps around the aggregate were vertically closed and horizontally opened. As discussed earlier, the crack network leading to the failure can evolve at the high-stress level of 3.61 N/mm^2

corresponding to about 75 % of the strength of monotonic loading. An additional crack network connecting neighbour aggregates was formed under sustained loading of 30 kN after 5 cycles.

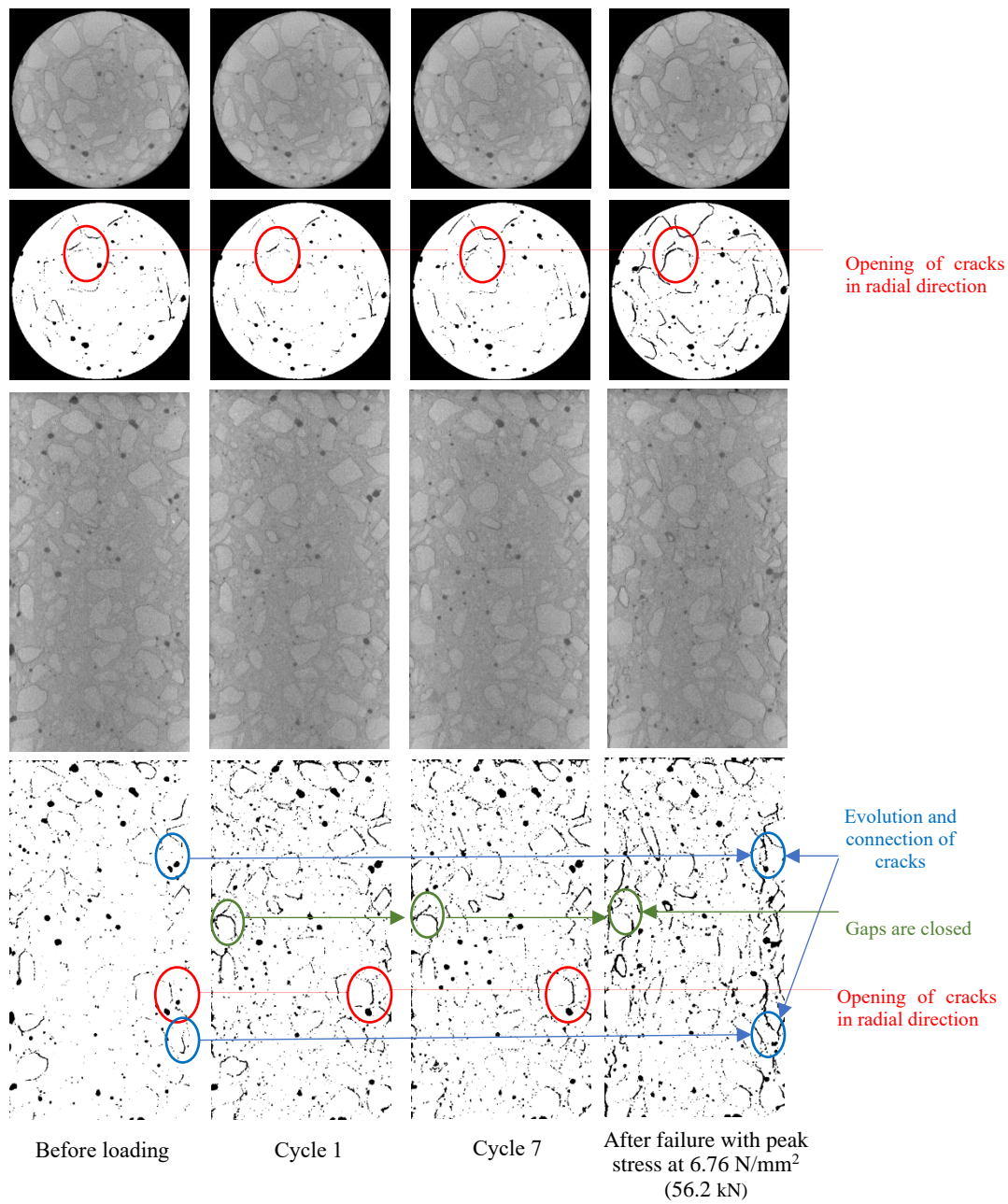


Figure 6-17 CT and Binary images showing crack propagation due to cyclic loading of 20 kN (= 2.40 N/mm²)

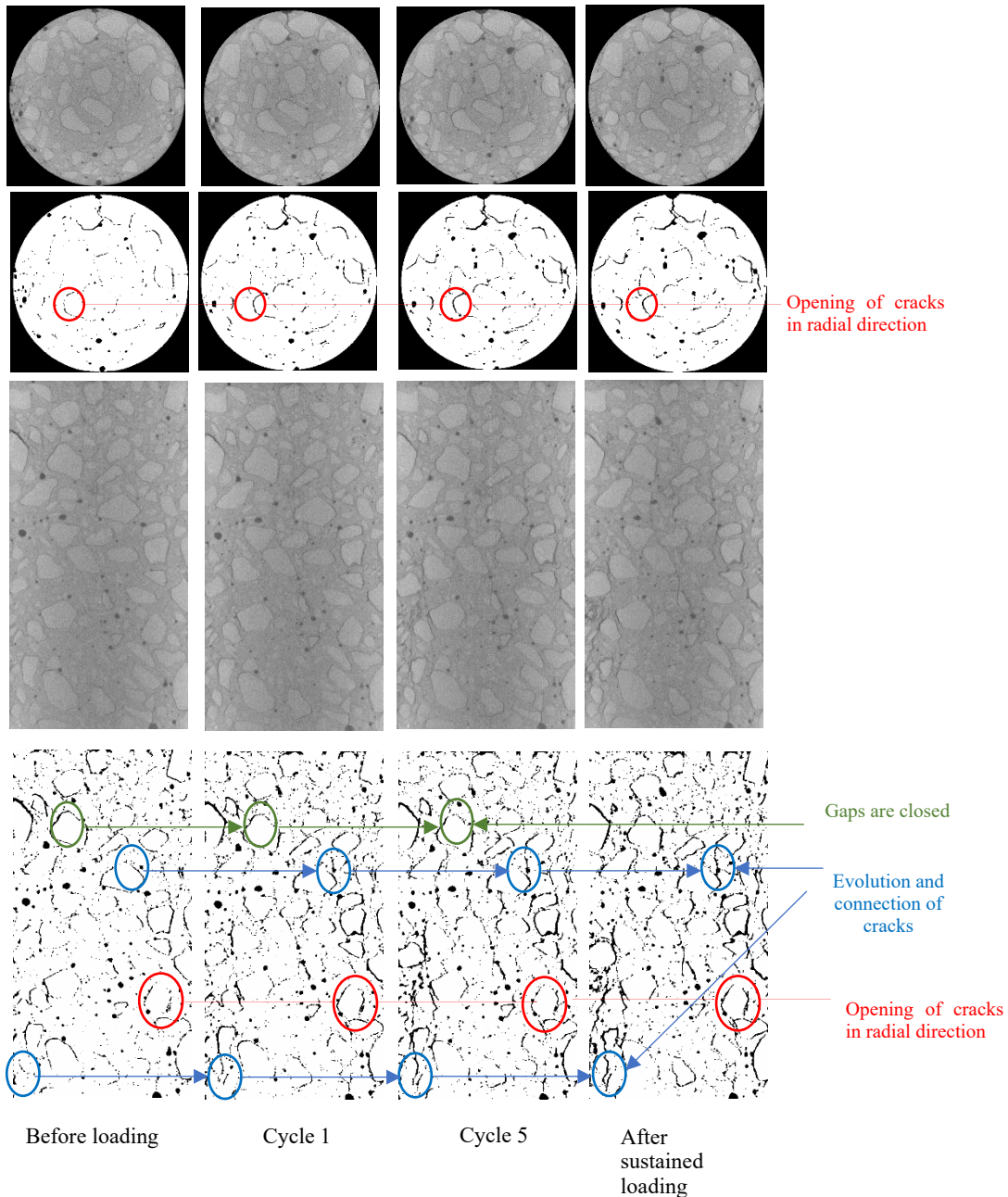


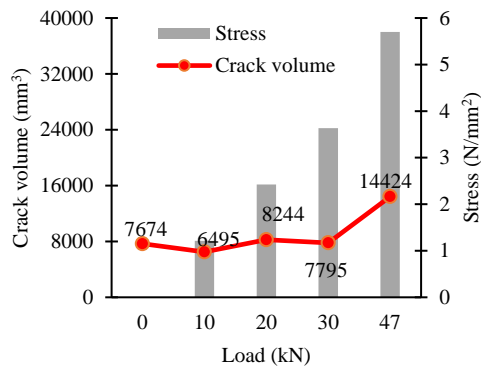
Figure 6-18 CT and Binary images showing crack propagation due to cyclic loading of 30 kN (= 3.61 N/mm²)

6.5.3. Crack volume and crack size based on X-ray CT scan

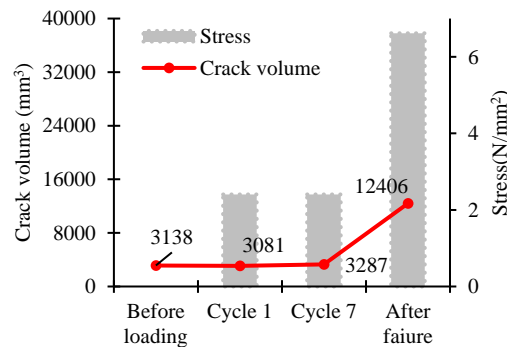
Figure 6-19 shows the crack volume calculated using the X-ray CT scanning images in the mid 50 mm after each unloading for various loading cases. The calculation is based on the DEF cracks only and any voids have been subtracted. The crack volume due to DEF expansion before loading was between 3,000 mm³ to 7,000 mm³ in the sliced zone of 50 mm with a concrete volume of about 400,000 mm³ without considering radial expansion. This indicates about 0.8 to 1.8 % of the concrete volume is pre-existing cracks (excluding air voids). The calculated crack volume corresponds to the DEF expansion (2 %).

Figure 6-19 (a) shows that the crack volume does not increase even with the increase in

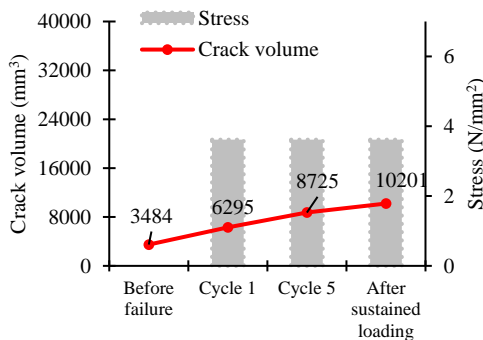
stress at low stresses level. It was then slightly increased after failure under step loading. For the cyclic loading of 20 kN shown in Figure 6-19 (b), the crack volume increased at the failure from the 7th cyclic loading of 20 kN while there was no increase of crack volume during the cyclic loading. Figure 6-19 (c) shows that the crack volume increased after 1st loading and increased further under the cyclic loading of 30 kN ($=3.61 \text{ N/mm}^2$). The crack volume increased significantly in the case of sustained loading as shown in Figure 6-19 (d), which can be attributed to the accumulated damage under sustained loading of 45 kN near the failure.



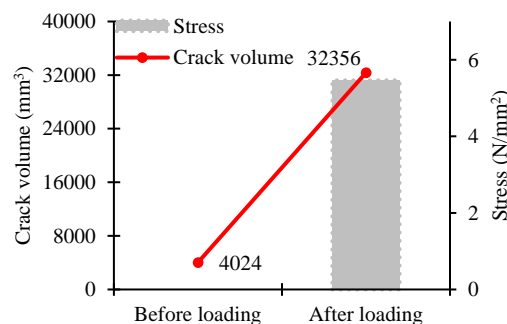
(a) Step loading



(b) Cyclic loading of 2.5 N/mm² (20 kN)



(c) Cyclic loading of 3.74 N/mm² (30 kN)



(d) Sustained loading

Figure 6-19 Crack volume under various compressive loading patterns for mid 5 cm

For comparison, the crack volume for the mid 10 cm of the specimen is shown in Figure 6-20. The tendency is the same as that for 5 cm thickness, and the absolute volume is approximately twice that for 5 cm.

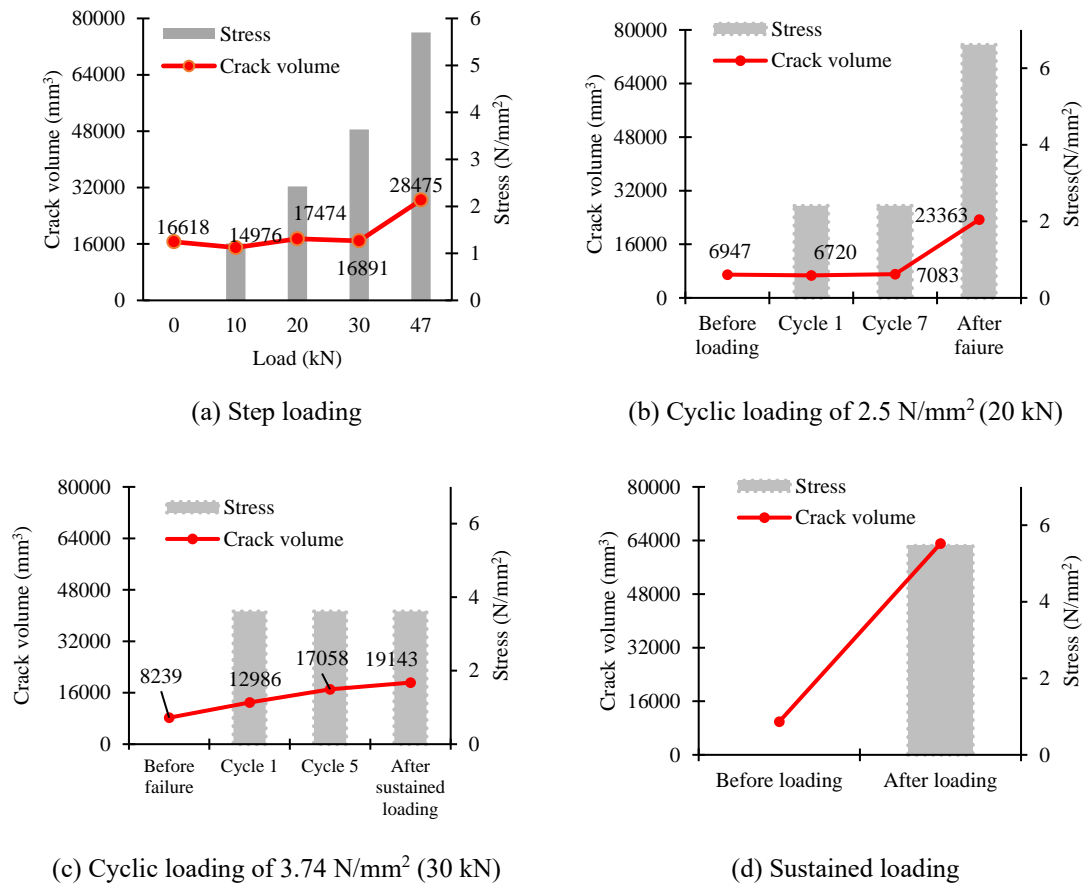


Figure 6-20 Crack volume under various compressive loading patterns for mid 10cm

The count of cracks with different widths under various loading patterns is shown in Figure 6-21. The error bar in the graph is the standard error.

In the case of step loading (Figure 6-21(a)) when the load was less than 30 kN, the crack count is reduced or remained the same even with the increase of loading. As discussed above, some of the preexisting gaps around aggregate can close in the loading direction decreasing the count of the smaller cracks. Even though the gap opened with the increase of load (Figure 6-16), the effect on the increase in the crack count and volume would be smaller compared to the effect of crack closing before the failure.

Figure 6-21 (b) shows that the crack count did not increase under cyclic loading of 20 kN (=2.40 N/mm²) while in Figure 6-21 (b), the count of cracks with a width less than 1 mm was reduced at 1st loading of 30 kN cycle and it gradually increased. Figure 6-17 shows the gaps around aggregate can be vertically closed and horizontally opened under cyclic loading of 20 kN (=2.40 N/mm²). In the case of 30 kN (=3.61 N/mm²) cycle, the CT-scanning in Figure 6-18 showed that the vertical cracks can form at the 1st loading which gradually propagated to connect at the high-stress level to increase the crack count and volume even though the gaps around the aggregate can be closed in the axial direction. The crack count at 30 kN was not changed in the case of step loading however it increased in the case of cyclic loading comparing to that before loading. This can be attributed to the more crack count and volume before loading

in the specimen for step loading, which may contribute to the additional gap closing effect.

In the case of sustained loading, the crack count of all widths was significantly increased compared to the number of cracks before loading which was also reflected in the significant increase in the crack volume.

For confidence, the crack width analysis was also done for mid 10 cm which is shown in Figure 6-22. It indicates the trend remains similar, only the count is doubled.

Sensitivity of thresholding on crack count

Crack width analysis for different thresholding values is shown in Figure 6-23. It can be observed that the number of cracks increases with thresholding however, the tendency remains similar.

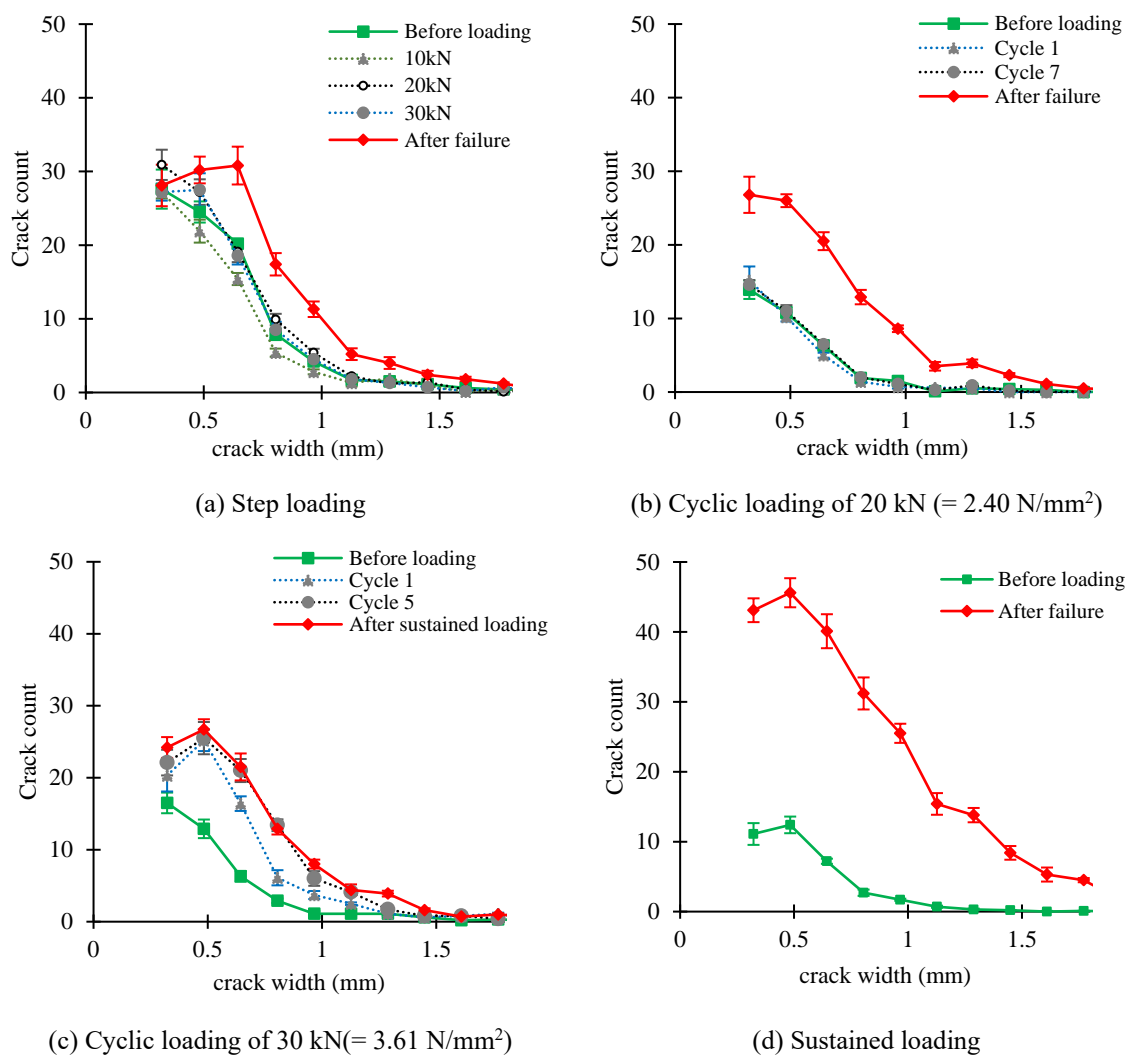


Figure 6-21 Crack count of various widths under different compressive loading patterns for mid 5 cm

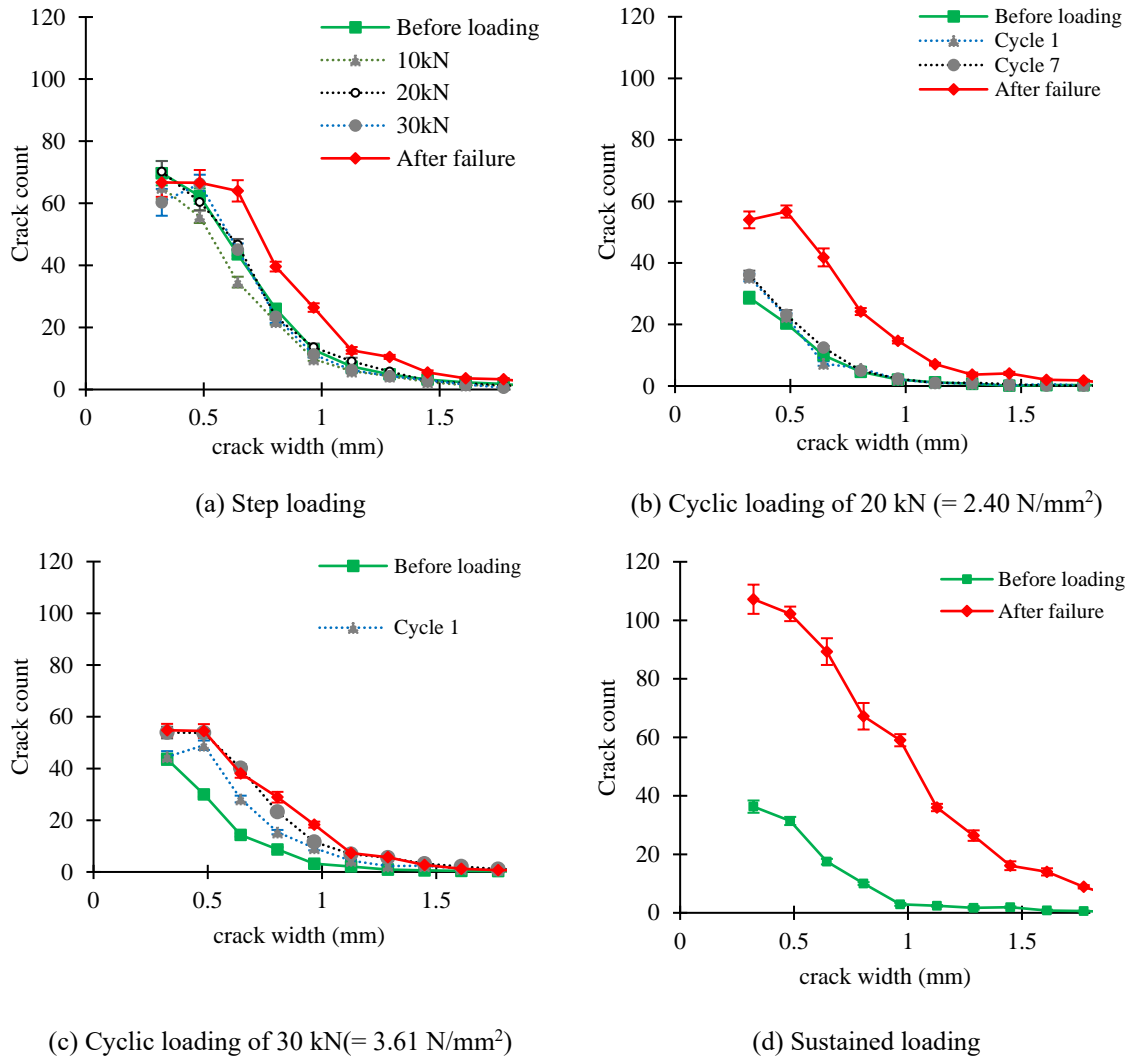


Figure 6-22 Crack count of various widths under different compressive loading patterns using mid 10 cm

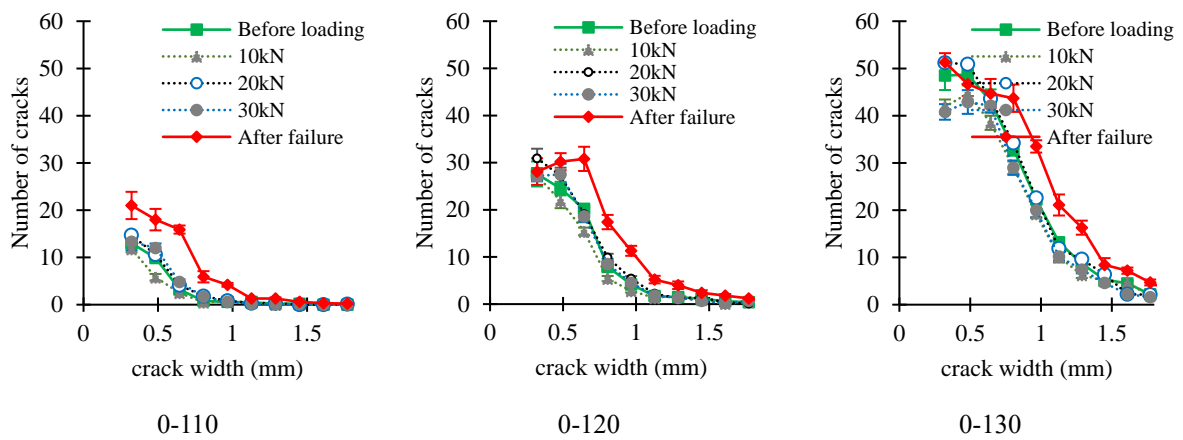


Figure 6-23 Crack distribution for threshold values of 0-110, 0-120 and 0-130

6.6. Discussion

6.6.1. Crack propagation

Under compressive stress, the plastic deformation can occur from the beginning of loading due to pre-existing gaps around the aggregate as observed in the CT scanning. The gap can close at a low-stress level and increases plastic deformation. The gap closing in the cyclic loading can reduce subsequent plastic deformation in the reloading thus decreasing the stiffness. The gap can widen in the perpendicular direction. From the image analysis, it is speculated that the gap closing or opening at a low-stress level does not increase the crack volume and crack count larger than 326 μm .

The load over 30 kN (corresponding to about 75 % of strength by monotonic loading), caused the crack to connect with the neighbour aggregates and propagated to increase the crack volume and count. The cracks over 0.5 mm can propagate due to the cyclic loading at a high-stress level of 30 kN as indicated in Figure 6-18 and image analysis.

It should be noted that the internal cracks focused on in this study are limited to be large cracks (more than 326 μm) due to the limitation of X-ray CT. The plastic deformation in the mortar with microcracking cannot be detected by the CT-scanning which can equally affect the non-linear stress-strain relationship and residual strain. The contribution from smaller microcracks and gaps needs to be further investigated as a future study using high-resolution image analysis for example by employing Digital Image Correlation (DIC) method (Miura et al., 2020).

6.6.2. Distribution of cracks

The CT image provided a unique opportunity to measure the crack distribution within the specimen. Wang et al. had predicted that in DEF expansion, the crack first appears in the outer region of the concrete surface and propagate inwards (Wang et al., 2019). The crack volume along the radius of the cylindrical specimen of this experiment is shown in Figure 6-24. Prior to the loading, the crack volume was largest in the region about 10 mm inside the concrete surface and it rapidly decreased towards the core and surface of the specimen. After the failure of the specimen, the crack volume was increased. While other loading cases generated more crack volume within the same region where the cracks were present prior to the loading, the sustained load opened more cracks even in the inner core of the concrete. The tendency remained similar.

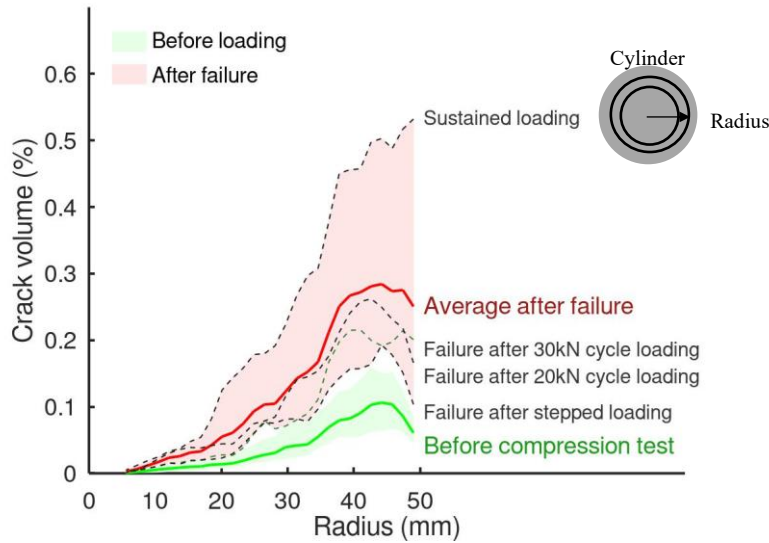


Figure 6-24 Distribution of crack from the core to the surface of cylindrical specimen before and after loadings

6.6.3. Relating SDI and PDI with internal damage

The definition of stiffness damage index (SDI) and plastic damage index (PDI) used by Sanchez et al. for indirect assessment of crack propagation is shown in Figure 6-25(a) (Sanchez et al., 2018). They recommended using four cycles of loading at 40% of compressive strength. However, other authors have used different loading conditions (Martin et al., 2017; Sanchez et al., 2016). For the analysis in this study, SDI and PDI are calculated for each loading-unloading step in the step loading case to understand the impact of loading history and stress levels on SDI and PDI. In the case of cyclic loading, the unloading was not returned to zero stress; in which case the SDI_{cycle} and PDI_{cycle} are defined by using the hysteresis area shown in Figure 6-25 (b).

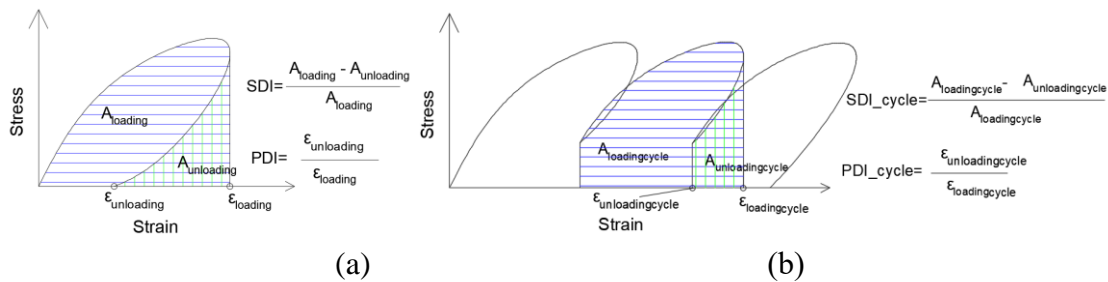


Figure 6-25 Definition of stiffness damage index and plastic damage index (a) for step loading (b) for cyclic loading in this study

SDI and PDI increased rapidly in the early stage of incremental stepped loading, while the crack volume was changed only slightly as shown in Figure 6-26. As the crack volume increased, the SDI was stabilized indicating that the stiffness does not get influenced by the propagation of the large crack. However, PDI kept on increasing up to about 80% of the peak load. Unlike Sanchez and Martin's explanation that PDI is mainly affected by crack

propagation (Martin et al., 2017; Sanchez et al., 2018), in this study, PDI was found to be affected not only by crack propagation but also by the closing of pre-existing DEF cracks.

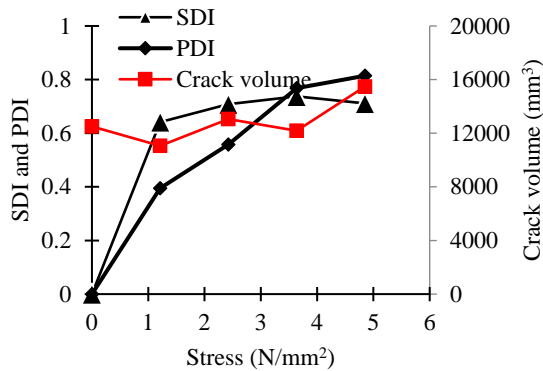


Figure 6-26 Damage index and plastic damage index for stepped incremental loading

SDI_{cycle} was reduced due to the cyclic load of 20 kN in the first three cycles from the large value at 1st loading. It was almost stabilized with the additional cycles as shown in Figure 6-27(a). In the case of the 30kN cyclic load, the SDI_{cycle} gradually decreased as shown in Figure 6-27 (b). The calculated crack volume before loading in the specimen for cyclic loading with 20 kN are smaller than those in the specimen for cyclic loading with 30 kN as shown in Figure 6-7 and Figure 6-19. As the magnitude of stiffness can be related to the closing of gaps around the aggregate, the subsequent smaller closing of fewer gaps with 20 kN may stabilize SDI_{cycle} rapidly. Furthermore, higher stress can propagate the cracks from aggregate as indicated by Figure 6-18, which may decelerate SDI_{cycle} reduction.

Meanwhile, PDI_{cycle} remained relatively unchanged during the cyclic loading with 20 kN while the cyclic loading with 30 kN increased PDI from 1st to 2nd cyclic and made a slight increase at the failure. This is due to the difficulty to close the gaps once it is already closed in the previous loading cycle. The cyclic loading of 20 kN did not increase the cracks which were suggested by the image analysis. This led to the stable PDI_{cycle}.

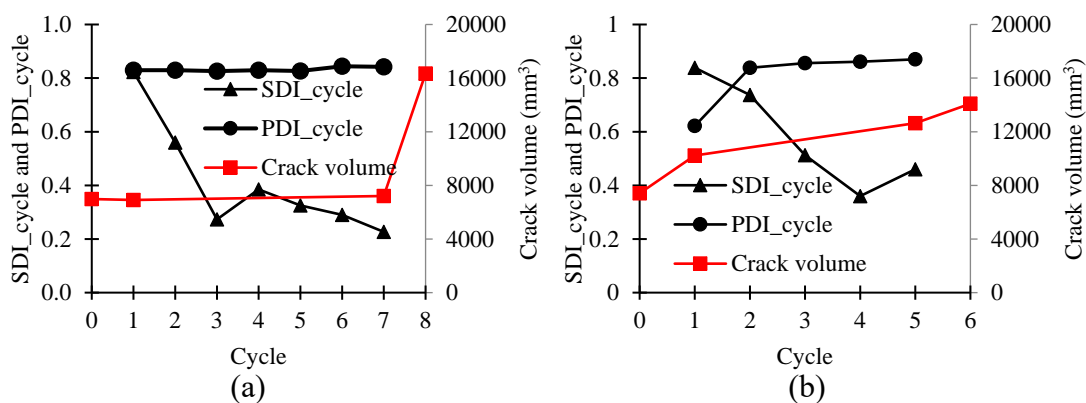


Figure 6-27 Damage index, plastic damage index and change in crack volume for cyclic loading of (a) 20kN and (b) 30 kN

6.6.4. Effect of sustained load

The creep effect was observed in the sustained loading type. The specific creep, defined as the ratio strain and applied stress can be used to quantify the creep effect (Mindess & Young, 1981, pp. 440–443). The calculated specific creep strain in the sustained loading case is shown in Figure 6-28. In the figure, the specific creep is similar at the beginning due to possible linear time dependency in the cement paste matrix, however, it gradually becomes larger at a higher stress level. It means that the rate of plastic deformation depends on the stress level.

For comparison, the specific creep at sustained 30 kN after 5th cyclic loading with 30 kN is also shown in Figure 6-28. It is noted that the specific creep after the cyclic loading was smaller than that at the same load of 30 kN in the sustained loading. This is due to the closing of the gap around aggregates during the cyclic loading leading to stiffer time-dependent deformation. A strong influence of loading history on the time-dependent deformation of DEF is indicated in the study.

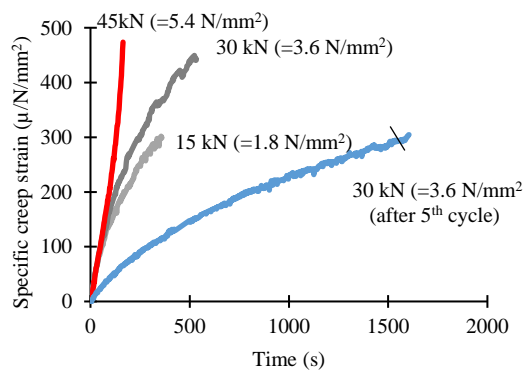


Figure 6-28 Evolution of specific strain.

6.6.5. Changes in elasticity

In one of the specimens with step loading, the dynamic Young's modulus was measured at each unloading. The damage of elasticity due to static loading of various intensities is shown in Figure 6-29(a). The dynamic Young's modulus was measured using resonance frequency and the mechanical Young's modulus was measured as a tangent modulus for the strain of 50 microns. It can be seen that the dynamic young's modulus remains higher than the mechanical young's modulus for all stress levels. The magnitude of both types of modulus gradually decreases. This is due to the increase in crack volume as shown in Figure 6-29 (b). As verified in the CT image, the number of smaller crack increase with stress level. The result is in congruence with the degradation effect of cracking on elasticity studied by Miura et al. (Miura et al., 2020). It must be noted, however, that fine cracks less than about 200 microns cannot be detected by CT. Hence at a low-stress level, the damage due to fine cracks cannot be captured.

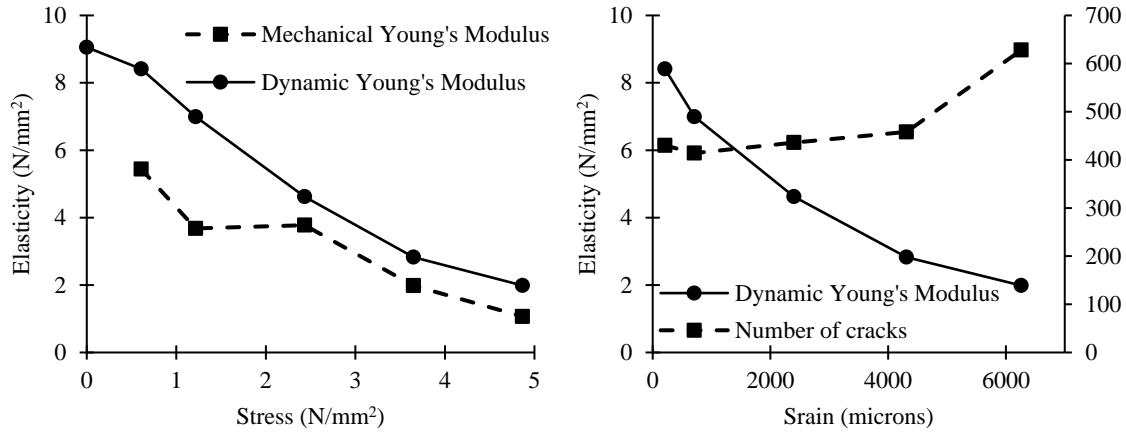


Figure 6-29 Reduction in elasticity at various levels of loading

6.7. Summary

This study focused on the mechanical testing of concrete specimens that had undergone an expansion of about 2% by DEF. Various loading cases were applied to understand the mechanism of internal crack propagation. The cracks were quantified by image analysis of X-ray CT images. Based on this study, the following conclusions are made:

- (1) DEF causes a significant reduction in peak strength. At the expansion of 2%, the reduction in strength was about 85% and the corresponding plastic strain was in the range of 8000 microns which is about 4 times more than the normal concrete.
- (2) At a stress level of less than about 50 % of the peak strength, the pre-existing gaps around aggregate can be opened or closed to not increase the volume of cracks with a width over 0.5 mm. However, it increases the plastic deformation of the concrete. When the stress exceeds about 75 % of strength, the large cracks propagate between the aggregates forming a fracture surface and leading to failure.
- (3) At a small load, there is a closing of gaps/cracks in the loading direction. When load increases, the cracks in the radial direction open. The closing of the gap in the axial direction causes additional plastic strain.
- (4) Steeped loading indicated that the number of smaller cracks decreases when low stress is applied which is due to the closing of pre-existing DEF cracks. At a higher stress level, new cracks are formed and the existing crack grows in size in the perpendicular direction. The cracks in the range of 0.5-1.0 mm also increases.
- (5) Cyclic loading test indicated that when low-stress cyclic loading (up to 50% of compressive strength) is applied, a plastic strain occurs, although there is no significant internal crack propagation and the peak load is not reduced. At the high-stress cyclic loading (75% of compressive strength), the peak load decreases significantly due to the rapid propagation of internal cracks.
- (6) The sustained type of loading causes the growth of all types of cracks – both smaller and larger cracks, showing that creep type of loading can cause the crack to grow. This indicated that the risk of the sustained type of loading in DEF deteriorated structures is high.

(7) Crack propagation correlated with SDI and PDI indicated the level of stress do not affect the values of SDI and PDI.

7. Numerical modelling

7.1. Background

In the previous chapters, experimental works were described that were focused to find the properties of swelling concrete. In this chapter, a numerical method is proposed to model the ASR/DEF deteriorated concrete.

In Chapter 2, it was described that previous researchers have proposed various mathematical models to represent the evolution of expansion. Some of these models describe about the reduction in strength and elasticity. However, it must be noted that deterioration due to ASR and DEF is distinctive. For instance, in the case of ASR, the strength is increased at the low level of expansion while the elasticity is reduced at the same time. Similarly, the DEF and DA expansion can cause a large plastic strain at the peak load. These kinds of behaviour cannot be captured by the previous models. To overcome this situation, a hybrid model is proposed which combines the stress-strain relation and damage model by Mazar (Mazars & Pijaudier-Cabot, 1989) with the time-dependent deterioration expansion model by Larive, described in Chapter 2 (Larive & Laboratoire Central des Ponts et Chaussees, 1998). The hybrid model also incorporates the change in strength and elasticity to match with the experimental observations.

The main objectives of this study are:

- a) develop a model to combine the time-dependent expansion with a strength model
- b) implement the model to perform sample analysis

7.2. Time dependent expansion model of Larvie

The time dependent expansion model by Larvie is described in Section 2.8.

7.3. Strength model of Mazar

Mazars' model is used to study the damage in concrete when a mechanical load is applied at the particular instant of the time-expansion curve. The model is a continuum damage model and considers concrete as isotropic material. In the model, the damage is tracked by a set of internal variables. The stress-strain relationship is formulated by gradually changing Young's modulus based on the damage at that instant (De Falco et al., 2018; Mazars & Pijaudier - Cabot, 1989; Pituba & Lacerda, 2012). The stress is considered to be directly related to the strain and Young's modulus as:

$$\sigma = E_d \epsilon \quad (7-1)$$

where σ is stress, ϵ is strain and E_d is the elasticity at that instant of loading.

The damage in elasticity is given by

$$E_d = (1 - d) * E_o \quad (7-2)$$

where E_o is the undamaged modulus of elasticity and

d is the damage parameter

The damage is activated when $\epsilon_{eq} \geq \epsilon_{do}$. The value of ϵ_{do} is the deformation at the maximum tensile stress in uni-axial tension tests. The equivalent strain (ϵ_{eq}) is given as the sum of the square of positive eigenvalues of the strain tensor

$$\epsilon_{eq} = \sqrt{\langle \epsilon_1^2 \rangle_+ + \langle \epsilon_2^2 \rangle_+ + \langle \epsilon_3^2 \rangle_+} \quad (7-3)$$

The total damage 'd' is the sum of damage in compression and tension given as

$$d = \alpha_t^\beta d_t + \alpha_c^\beta d_c \quad (7-4)$$

Where d_t and d_c are the damage areas in tensile and compressive zones respectively given by

$$d_t = 1 - (1 - A_t) * \frac{\epsilon_{do}}{\epsilon_{eq}} - A_t * e^{-B_t(\epsilon_{eq} - \epsilon_{do})} \quad (7-5)$$

$$d_c = 1 - (1 - A_c) * \frac{\epsilon_{do}}{\epsilon_{eq}} - A_c * e^{-B_c(\epsilon_{eq} - \epsilon_{do})} \quad (7-6)$$

where A_t , B_t , A_c and B_c are material parameters based on uniaxial tension and compression tests respectively.

And, α_t and α_c are weighing coefficients such that

$$\alpha_t = \begin{cases} 1 & \text{when tension is active} \\ 0 & \text{when compressin is active} \end{cases} \quad (7-7)$$

$$\alpha_c = \begin{cases} 0 & \text{when tension is active} \\ 1 & \text{when compressin is active} \end{cases} \quad (7-8)$$

The exponent β is usually fixed at 1.10.

The material parameters A_t , B_t , A_c and B_c are calculated with the following relationships. A_c is obtained by solving $f'(\epsilon_c)=0$, and B_c by solving $f_cj=f(\epsilon_c)$

$$A_t = 0.9 \quad (7-9)$$

$$B_t = \frac{f_{tj}}{E_o} \quad (7-10)$$

$$A_c = \frac{\left(\frac{f_{cj} * nu * \sqrt{2}}{E_{ij}} - \epsilon_{do} \right)}{(\epsilon_c * nu * \sqrt{2} * e^{B_c * (\epsilon_{do} - \epsilon_c * nu * \sqrt{2})}) - \epsilon_{do}} \quad (7-11)$$

$$B_c = \frac{1}{(\epsilon_c * nu * \sqrt{2})_o} \quad (7-12)$$

Since the tensile test on ASR/DEF specimen in the advanced stage of expansion is

difficult to obtain, it can be indirectly estimated by using Eurocode or a similar empirical equation. For the study in this thesis, Eurocode-2 is used to estimate the tensile strength and initial Young's modulus based on the following relations(BSI, 2004):

$$\text{Undamaged Young's modulus, } E_o = 22 * 10^3 * \left(\frac{f_{cj}}{10}\right)^{0.3} \text{ in MPa} \quad (7-13)$$

$$\text{Undamaged tensile strength, } f_{tj} = 0.3 * f_{cj}^{\frac{2}{3}} \text{ in MPa} \quad (7-14)$$

$$\text{Deformation at peak strength, } \epsilon_c = 0.7 * \frac{f_{cj}^{0.31}}{1000} \quad (7-15)$$

where f_{cj} is the compressive strength of the concrete. Incorporating time dependency in Mazar's model

The time dependency in Mazar's model can be incorporated by defining modification parameters for peak strength, strain at peak strength and Young's modulus of elasticity based on the level of expansion. The data showing the variation of these variables with time are not numerous. In one of the studies by Wang et al. (2019), they collected data from various researchers for ASR and DEF studies which is similar to the data set indicated in Chapter 2. These data are shown in Figure 7-1 and Figure 7-2. These figures also show the experiment result of this thesis from Chapter 5. It can be seen that at small expansion, there is an increase in strength and Young's modulus of elasticity for both ASR and DEF specimens. Once the expansion strain is increased there is a rapid drop in their values and after a certain level of expansion, the values get stabilized.

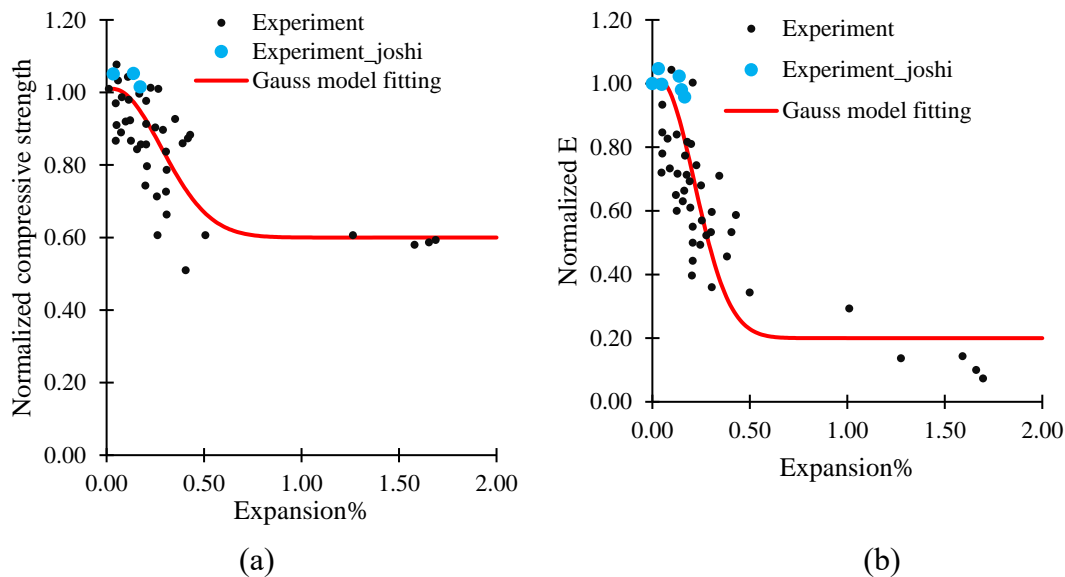
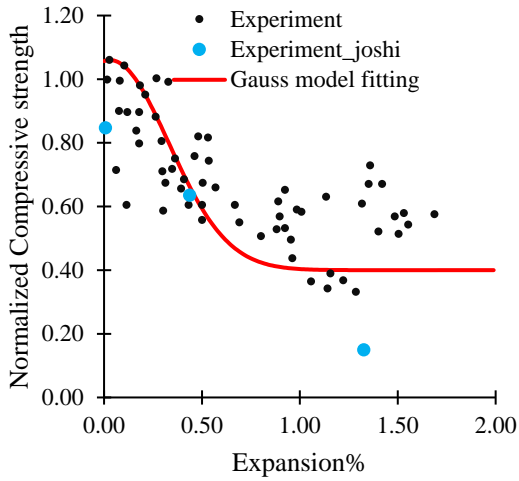
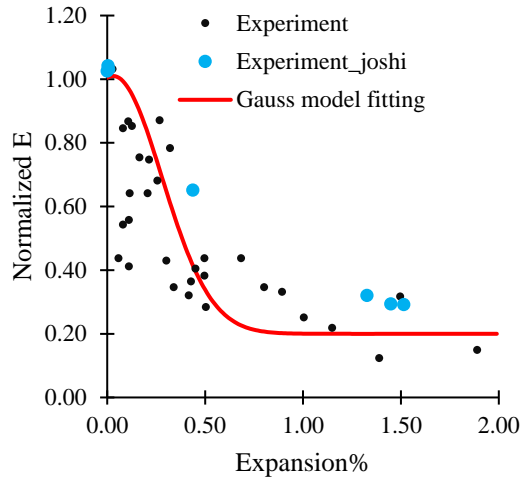


Figure 7-1 Evolution of (a) compressive strength and (b) Young's modulus with expansion in ASR affected concrete



(a)



(b)

Figure 7-2 Evolution of (a) compressive strength and (b) Young’s modulus with expansion in DEF affected concrete

To capture such phenomena mathematically, various trials and errors were done to fit the data. It was observed that the parameters can be modelled with a Gaussian function in the form shown below.

$$\phi = a \cdot e^{-\frac{(bx-c)^2}{d^2}} + r \quad (7-16)$$

Where ϕ is the modification parameter and x is the expansion strain. Similarly, a , b , c and d are Gaussian’s parameters and r is a constant. The typical shape represented by the Gaussian’s equation is shown in Figure 7-3.

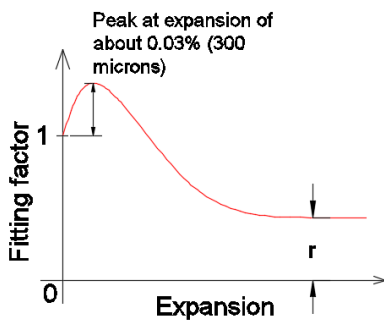


Figure 7-3 Evolution of Gaussian function

7.3.1. Change in peak strength

As discussed in Chapter 2, there is a slight increase in strength and other engineering properties when the expansion is small. This was also observed in the experiment described in Chapter 5. The strength increases by about 5-10% strength when the strain is about 350 microns (P. Li et al., 2020). Once this limit exceeds, the strength reduces rapidly with an increase in expansion. However, after about 10,000 microns (i.e.1% strain) expansion, there is no further decrease and strength stays constant. To convey this physical phenomenon in a mathematical

model, a Gaussian function in the form shown below is proposed:

$$\phi_{\sigma} = a_{\sigma} e^{-(b_{\sigma} x - c_{\sigma})^2 / d_{\sigma}^2} + r_{\sigma} \quad (7-17)$$

Where a_{σ} , b_{σ} , c_{σ} and d_{σ} are Gaussian's parameters and r_{σ} is residual compressive strength after severe expansion.

The strength, i.e. uniaxial compressive strength, at an expansion level of ϵ_{τ} is then calculated as

$$\sigma_{c_j\tau}(\epsilon_{\tau}) = \sigma_o * \phi_{\sigma} \quad (7-18)$$

Where ϵ_{τ} is the expansion observed at time τ .

7.3.2. Change in Young's modulus

Similar to the peak strength, the modulus of elasticity slightly increase and then gradually reduce with expansion. After about expansion of about 10,000 microns, the elasticity stabilizes which is about 20% of the original (refer to Chapter 5). The reduction is modelled by the following equation

$$\phi_E = a_E e^{-(b_E x - c_E)^2 / d_E^2} + r_E \quad (7-19)$$

The residual strength at an expansion level is calculated as

$$E_{o\tau}(\epsilon_{\tau}) = E_o * \phi_E \quad (7-20)$$

Where a_E , b_E , c_E and d_E are Gaussian's parameters and r_E is residual Young's modulus after severe expansion.

The Young's modulus at an expansion level of ϵ_{τ} is calculated as

$$E_{o\tau}(\epsilon_{\tau}) = E_o * \phi_E \quad (7-21)$$

Where ϵ_{τ} is the expansion observed at time τ .

7.3.3. Change in peak strain

The next parameter that controls the behaviour of the material is the strain at peak compressive strength. It has been observed from the experiment that as the expansion becomes large, the peak strain (or plastic strain) also becomes large. One of the main reason for larger plastic strain is the occurrence of cracks and gaps which needs to be overcome while loading the affected specimen (refer Chapter 6). This means the peak strain is related to the expansive strain. Hence, a relation of the form shown below is proposed. This equation is similar to the equation proposed by Ulm et al. (2000).

$$\epsilon_{c\tau} = \epsilon_{co} + \epsilon_{cmax} * \frac{1 - e^{-\left(\frac{\tau}{\tau_c}\right)}}{1 + e^{-\left(\frac{\tau - \tau_l}{\tau_c}\right)}} \quad (7-22)$$

Where ϵ_{co} is the peak strain in compression for an undamaged concrete

ϵ_{cmax} is the peak strain of severely damaged concrete. It must be noted that beyond a certain level of expansion, the peak strain does not change significantly.

7.4. Model implementation

The data shown in Figure 7-1 and Figure 7-2 are fitted with the proposed equations for ASR and DEF cases separately. The values of the parameters are shown in Table 7-1. It was noted that for a given expansion level, the tendency of DA specimen was similar to DEF specimen in Chapter 5, hence the values of DEF can also be used for DA analysis with some modification based on experiment. The curve represented by the fitted equation is shown by a continuous line in Figure 7-1 and Figure 7-2. The model was then implemented in Code-Aster FEM software for structural analysis.

Table 7-1 Gaussian parameters for time-dependent strength analysis

Parameters for peak strength		
	ASR	DEF
a_{σ}	0.41	0.66
b_{σ}	0.03	0.03
c_{σ}	0.25	0.3
d_{σ}	0.6	0.35
Parameters for Young's modulus of elasticity		
	ASR	DEF
a_E	0.81	0.81
b_E	0.035	0.03
c_E	0.18	0.25
d_E	0.2	0.2
Parameters for Peak strain		
	ASR	DEF
ϵ_{cmax}	0.0012 (=1200 microns)	0.008 (=8000 microns)
$\epsilon(\tau_c)$	0.4	0.2
$\epsilon(\tau_l)$	0.5	0.3

7.5. Application of the model

This section describes two application examples based on the test results carried out in Chapter 3 and Chapter 5 and one typical beam analysis for its flexure and shear capacity.

7.5.1. Concrete prism with and without steel

In this test, the concrete prism described in Chapter 3 was used to calculate the free expansion independent of external loading. Two cases were simulated, viz with steel and without steel rebar with the dimension shown in Figure 7-4.

Evolution of expansive strain

To simulate the evolution of expansive strain, first, the expansion kinetics was found by fitting the experimental data to match with Larvie's equations. The fitted parameters are shown in Table 7-2. These values give the ultimate strain, characteristic time and lag time, based on which the expansion at a given instant can be calculated. The boundary condition was applied by restraining one of the edges in each direction of the prism (an alternative approach using

random nodes as a fixed boundary is given in Appendix E). The expansion kinetics along with strength parameters of Table 7-1 was used to calculate the expansion.

Next, the expansion of the reinforced concrete specimen was simulated using the same fitted parameters. Figure 7-5 and Figure 7-6 shows the result of numerical simulation. The free expansion was well captured because the same data was used to fit the model. The expansion of the reinforced specimen had some deviation. By re-calibrating the model, more accuracy can be obtained which is shown in the same figure by broken lines.

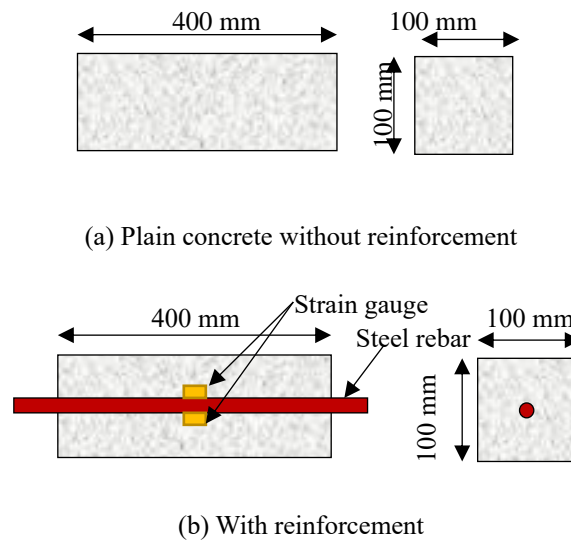


Figure 7-4 Dimension of prismatic specimens used in the simulation

Table 7-2 Strain evolution parameters for free expansion of prismatic specimens

Parameters	ASR	DEF	ASR Steel calibrated	DEF Steel calibrated
Latency time (τ_L), days	35	140	10	160
Characteristics time (τ_c), days	5	25	5	35
Ultimate strain, microns	275	9350	303	6000

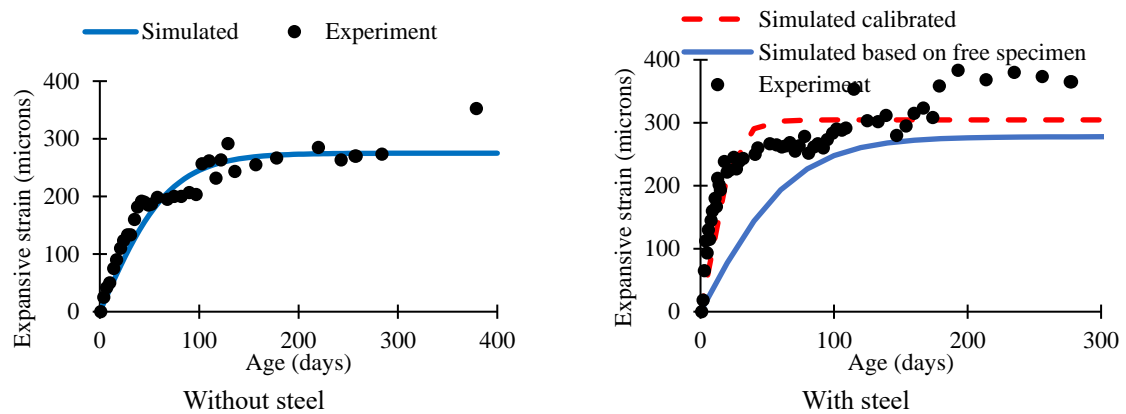


Figure 7-5 Evolution of free expansion of ASR infected concrete with and without reinforcement

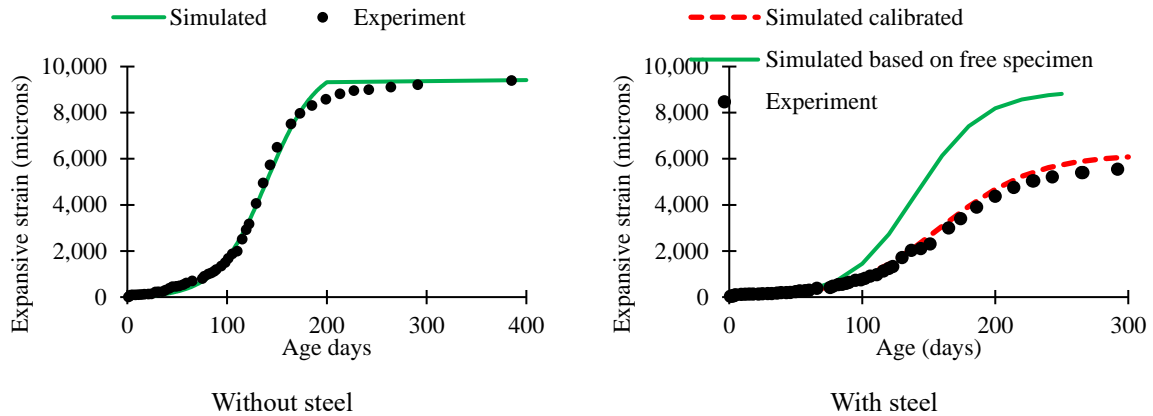


Figure 7-6 Evolution of free expansion of DEF infected concrete with and without reinforcement

Transfer of strain in steel

Figure 7-7 shows the principal stress in the reinforced specimen in ASR and DEF specimen at the age of 150 days. It can be seen that the steel experiences tensile stress due to the expansion in concrete in the range of about 50 N/mm². The evolution of strain in the interface of steel and concrete is shown in Figure 7-8. The concrete and steel expand together when expansion is relatively small. When the larger expansion occurs, a gradual reduction in strain occurs which was also verified by the experiment data. Physically, this indicates slipping of steel rebar could be due to micro-cracking of concrete in the steel-rebar interface as explained in Section 5.4.4.

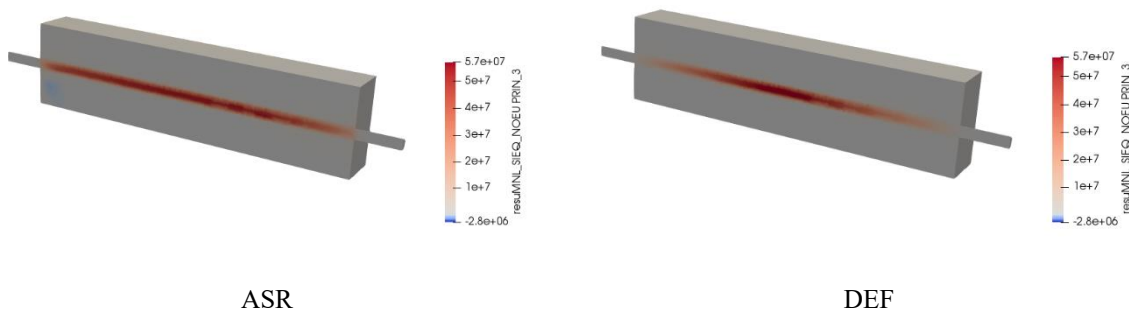


Figure 7-7 Evolution of principal strain at the age of 150 days for free specimen

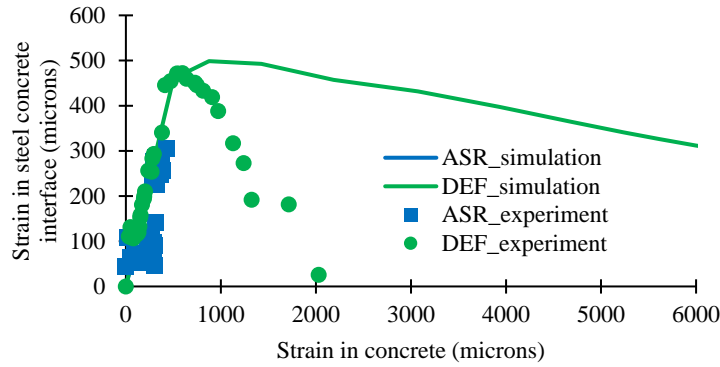


Figure 7-8 Evolution of strain in steel-concrete interface due to concrete expansion

7.5.2. Compressive strength of concrete cylinders at various ages

A cylinder of diameter 100 mm and height of 200 mm was used for this example. This example is based on the specimen described in Chapter 5.

The numerical analysis was done in two stages. In the first stage, the free expansion of the concrete was calculated with the kinetic parameters shown in Table 7-3. The boundary condition was applied by considering the edge of the lower face as fixed. The time-step for the analysis was taken as 1 day. At every step, the damage was calculated.

Table 7-3 Strain evolution parameters for free expansion of cylindrical specimens

Parameters	ASR	DEF
Latency time (τ_L), days	50	100
Characteristics time (τ_c), days	25	20
Ultimate strain, microns	1,760	14,850

In the second stage, uniaxial compressive loading at the age of 90 days and 150 days were simulated. The bottom of the specimen was considered fixed while the displacement of 0.025 mm is added at each step of the non-linear analysis. The reaction forces and concrete stress were calculated for each step.

Evolution of expansive strain

The evolution of expansion in the free specimen i.e. when there is no load, is shown in Figure 7-9. The evolution is well captured by the model.

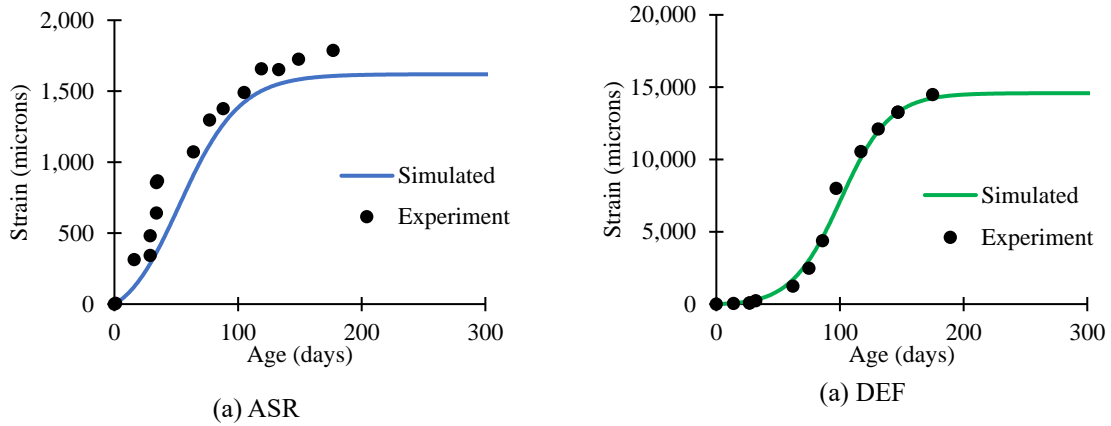


Figure 7-9 Evolution of free expansion in ASR and DEF specimens

Uniaxial compressive strength at various age

The stress-strain relation in the uniaxial compressive test is shown in Figure 7-10 and Figure 7-11 for ASR and DEF respectively. The peak stress and strain are well captured by the model especially when the expansive strain is small (e.g. 90 days ASR). At larger strain, there was some discrepancy between the experiment and simulated values which was mainly observed for DEF specimens. The discrepancy occurred because in the experiment the actual strength of the specimen was lower than the data set used to fit the model (Refer Figure 7-1 and Figure 7-2). The discrepancy for the DEF specimens was reduced if the actual values of the experiment were used to calibrate the model as shown by the red lines in Figure 7-11.

Figure 7-12 shows the equivalent strain (damage strain) as defined in Mazar’s model. The slipping angle at failure was higher for ASR, while the DEF specimens failed with a lower angle. A similar tendency was observed in the experiment as shown in Figure 7-13.

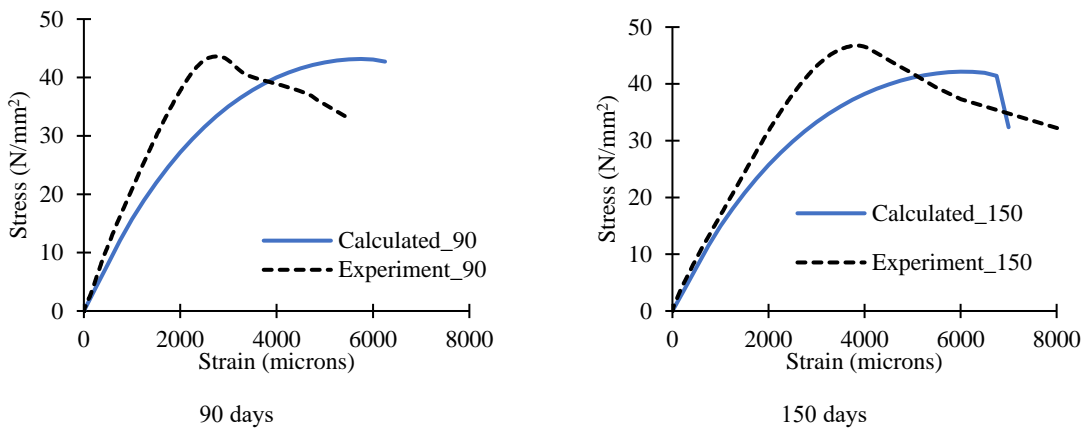
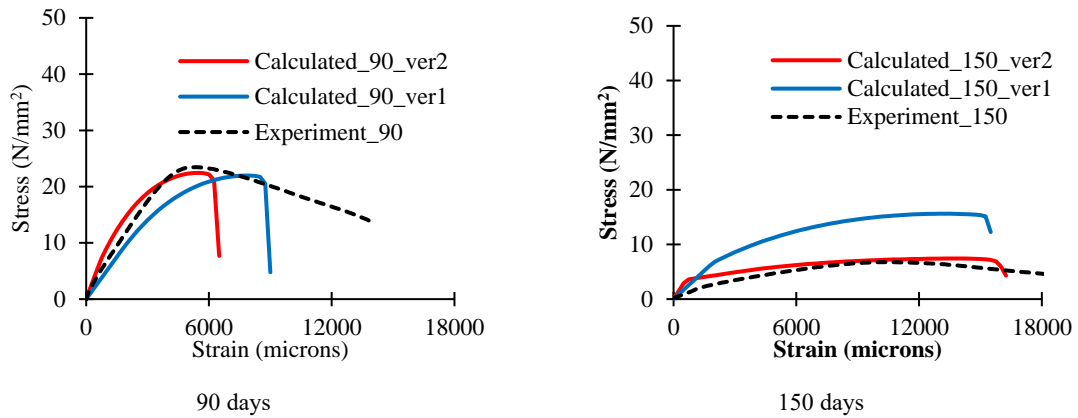


Figure 7-10 Comparison of uniaxial compressive test for ASR specimens at 90 days and 150 days



Ver1= based on the main data set;

Ver2= based on the actual experiment data

Figure 7-11 Comparison of uniaxial compressive test for DEF specimens at 90 days and 150 days

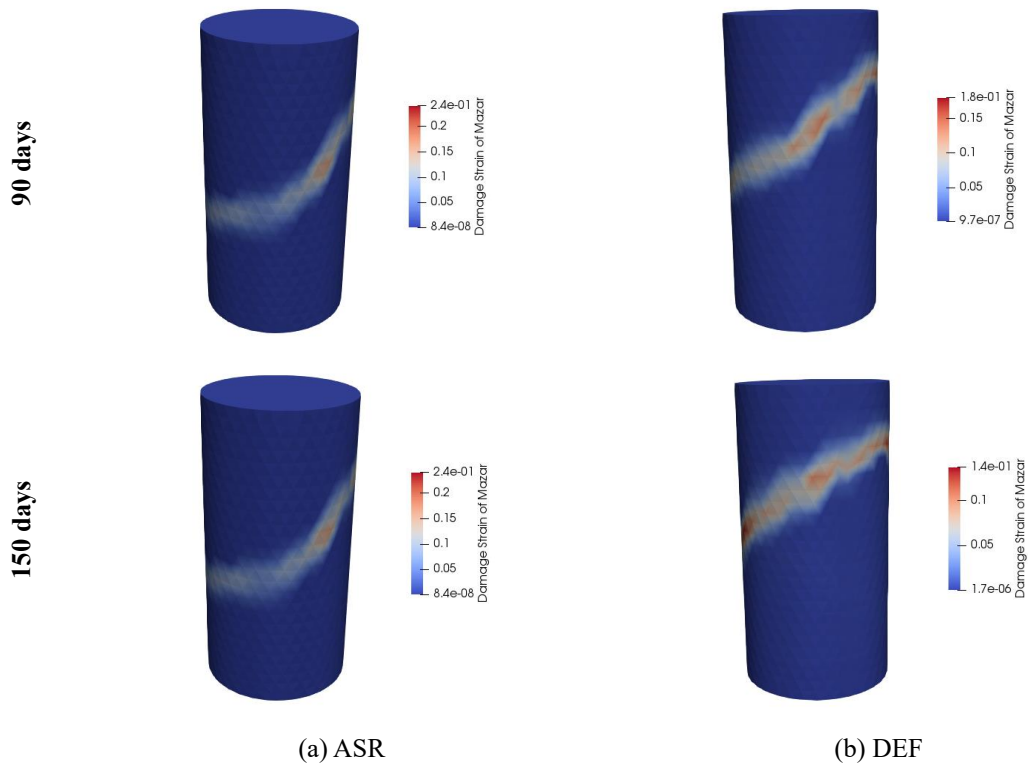


Figure 7-12 Damage evolution in (a) ASR and (b) DEF specimens due to uniaxial compression at 90 days and 150 days



(a) ASR



(b) DEF

Figure 7-13 Damage in (a) ASR and (b) DEF specimens in experiment due to uniaxial compression at 150 days

7.5.3. Evolution of loading capacity of DEF affected beam

In this example, the loading capacity of a typical reinforced concrete beam is simulated for various levels of expansion. The cross-section of the beam was considered to be 200 mm x 150 mm and the length of the beam was 1800 mm. The clear cover was 40 mm on each side. The reinforcement was arranged such that it undergoes flexure failure in the first case and shear failure in the second case as shown in Figure 7-14 (a) and (b) respectively. The undamaged strength of the concrete was set at 39 N/mm² and the yield stress of steel was set at 400 N/mm². Two D16 steel bars were used as the main bar on the bottom of the beam and two D6 bar was used in the top. The shear stirrups were ring-shaped made with D7 steel rebars.

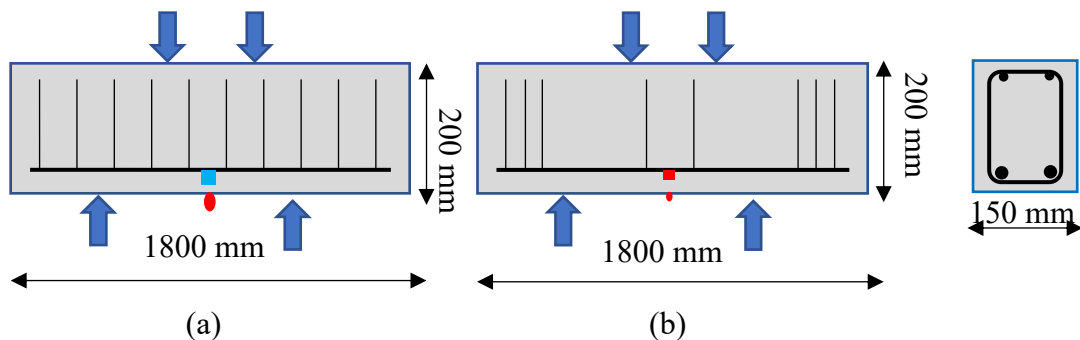


Figure 7-14 Beam for analysing (a) flexure failure and (b) shear failure

Simulation of compressive test of concrete

Before conducting the simulation of the beam, the compressive strength of the concrete was simulated to verify the DEF expansion at 0 microns (0.0%), 5000 microns (0.5%) and 10,000 microns (1.0%). The result is shown in Figure 7-15. As expected, with increased expansion, the peak strength was reduced and peak strain was increased.

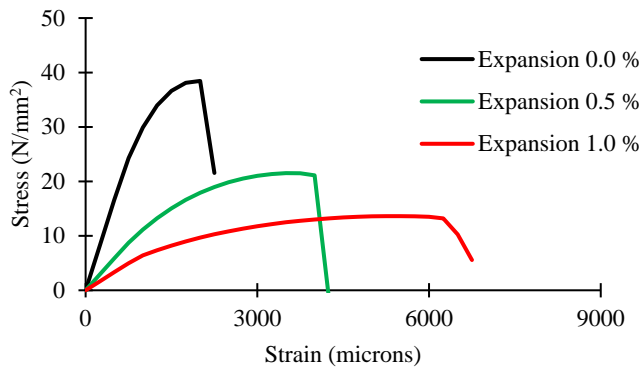


Figure 7-15 Simulated stress-strain relation of a DEF affected cylinder at various expansion

Loading capacity of the beam and failure mechanism

The simulated load deflection for both cases is shown in Figure 7-16. The corresponding stress in the steel rebar measured at the middle span of the beam is shown in Figure 7-17.

In the case of flexure failure, it was observed that there was an increase in the deflection of the beam, however, the ultimate load was not reduced significantly (Figure 7-16 a). In each simulation case, steel had yielded (Figure 7-17 a). The reason for no significant reduction in loading capacity even though the concrete strength was reduced is due to the high peak strain of concrete (Figure 7-15). The larger peak strain in concrete allowed the beam to deflect more. This allowed the steel to take more load until it yielded.

In the case of shear failure, the load capacity of the beam was reduced significantly with the increase in the expansion (Figure 7-16 b). In all simulation cases, the beam failed in compression as indicated in Figure 7-17 b because in all cases steel did not yield. Higher expansion caused failure to occur in smaller loads. The main reason for the reduction in loading capacity was due to the lack of confinement effect by shear reinforcement.

From this numerical analysis, it is predicted that even though the strength of concrete is reduced, ductile failure can be achieved owing to the large plastic strain if shear reinforcement is adequate. If the shear reinforcement is lacking, the structures are likely to undergo brittle/compressive failure, especially at high expansion.

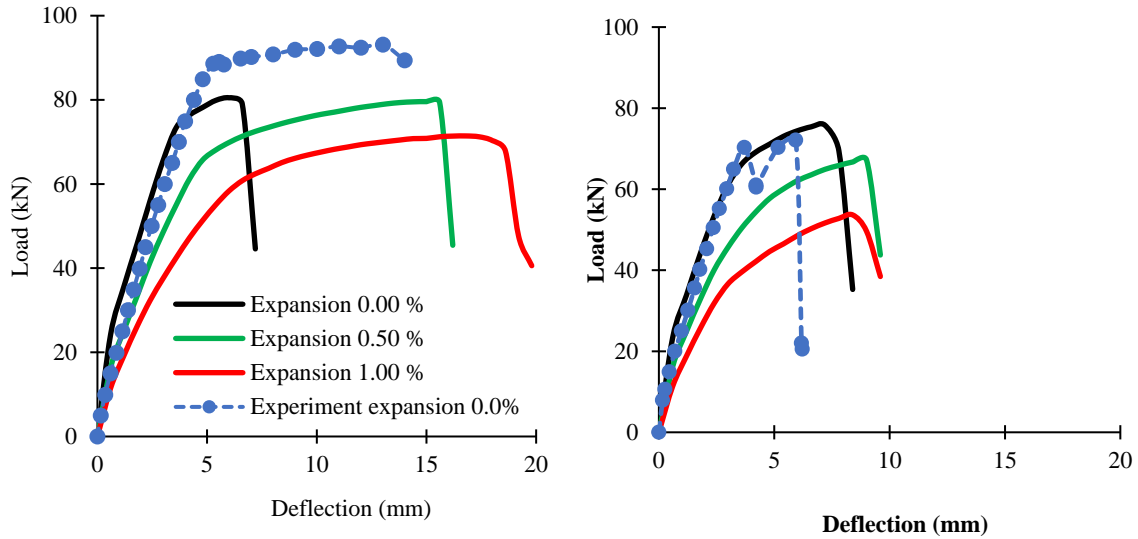


Figure 7-16 Load deflection curve for (a) flexure failure (b) shear failure

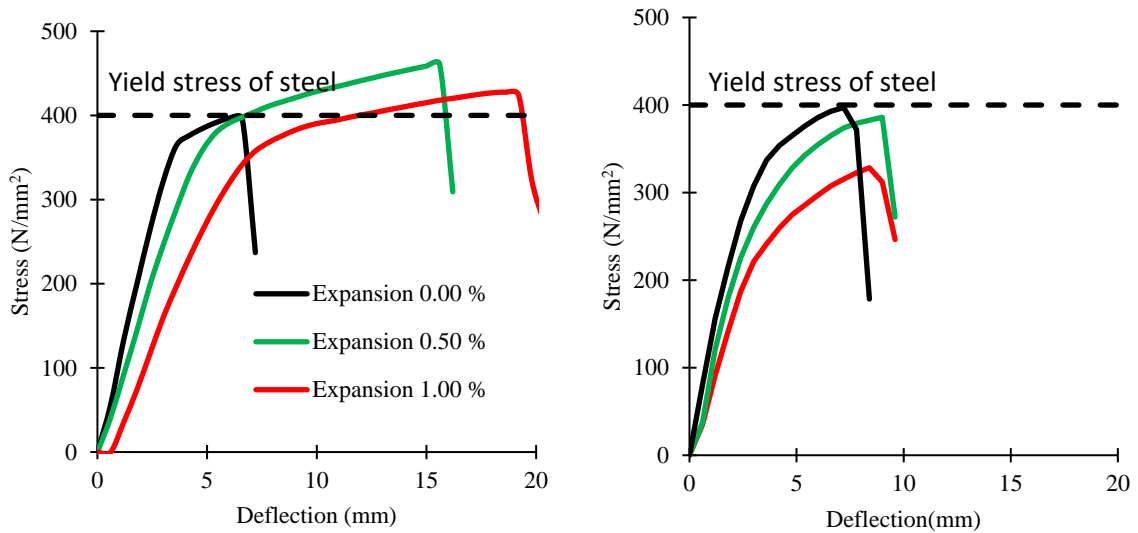


Figure 7-17 Stress in steel for (a) flexure failure (b) shear failure

7.6. Summary

In this chapter, a method was proposed to incorporate time-dependent deterioration in Mazar's model. The parameters of the proposed model were based on the Gaussian function. The numerical model was implemented and tested in Code Aster. It was found that the model has the good potential to predict the strain and strength. Following are the key outcomes:

- a) The proposed model mainly has two parts. The first part of the model calculates the expansion of concrete based on experimental observations of expansion which is generally based on the ingredients, heat treatment and restraint condition. The second part of the model calculates the strength parameters such as compressive strength, young modulus and peak strain of concrete based on the expansion of the concrete.

The model parameters are based on the experiment data of previous researchers and this dissertation.

- b) The model was used to successfully calculate the evolution of an expansive strain of unreinforced and reinforced concrete by calibrating the model with the experiment data.
- c) The bond strain in the interface of steel and concrete calculated using the model was in-line with the experiment results.
- d) The reduction in peak strength and increase in peak strain of concrete with increasing expansion could be well simulated. The simulated stress-strain curve was similar to the experiment results.
- e) The model was used to simulate the behaviour of flexure failure and shear failure of a reinforced beam. It is predicted that there will be no significant reduction in beam strength if sufficient shear reinforcement is provided. When shear reinforcement is insufficient, the loading capacity of the beam is significantly reduced and it will undergo brittle compressive failure. This simulation has to be verified with experiments in the future.

8. Case Study: Structural response of massive structure by internal expansion reaction

8.1. Background

The discussion in the previous chapters was focused on the strength and loading capacity of the structures. However, there are cases when the serviceability, such as deflection and cracking of the structures, becomes more important than the strength. A small internal expansion can have a significant impact on the serviceability of a massive concrete structure. To understand the effect of such expansion, one of the concrete dams in Thailand (Figure 8-1) that had been undergoing ASR expansion was studied. The dam is showing a gradual deflection that is increasing over time. It is believed that there are no safety-related issues, however, the possible loss of serviceability due to excessive deflection and cracking dam needed to be assessed.

The dam has an arch shape with a maximum height of 154 m. The crest width is 486 m. The dam was constructed in 1964 to use the impounded water for irrigation and hydroelectricity.

The main objectives of this study are as follows:

- a) to identify and confirm the cause of expansion
- b) conduct numerical modelling to predict the future deformation and to identify the susceptible region for cracking and conduct sensitivity analysis to check the dam's serviceability in various cases

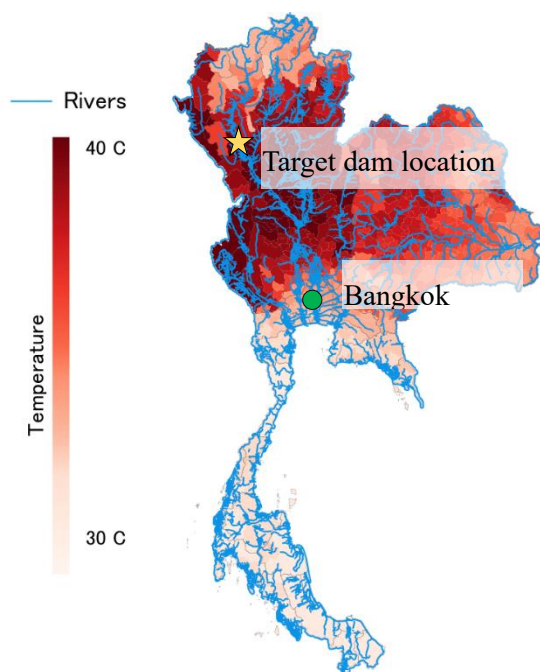


Figure 8-1 Location of the dam in Thailand. The distribution of maximum average temperature is also shown based on Souris (2000)

8.2. Diagnosis of the problem

The deflection of the dam was monitored using a plumb line installed in block 12 at the centre of the dam body as shown in Figure 8-2. The deflection is gradually increasing in the upstream direction. The expected behaviour for an arch dam is that the radial deflection occurs in the direction of load i.e. downstream direction during all normal hydrostatic loadings (Ghanaat, 1993). Even when concrete creep is considered, the deflection should increase in the downstream direction (Yin et al., 2019), although the creep effect should be small because the dam concrete uses a large volume of large-sized aggregates to reduce hydration heat, and the relative humidity remains stable (Neville, 1996). However, the observed deflection is in the opposite direction than expected.

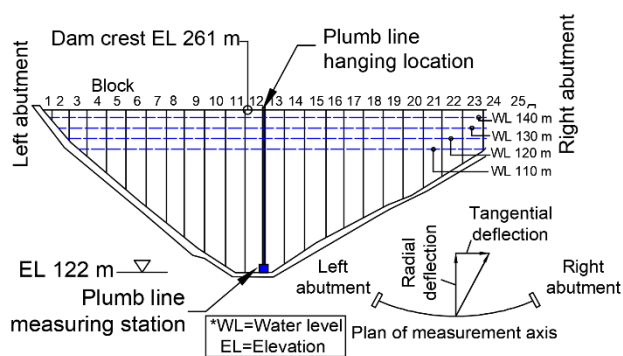


Figure 8-2 Location of deflection measurement station in the dam

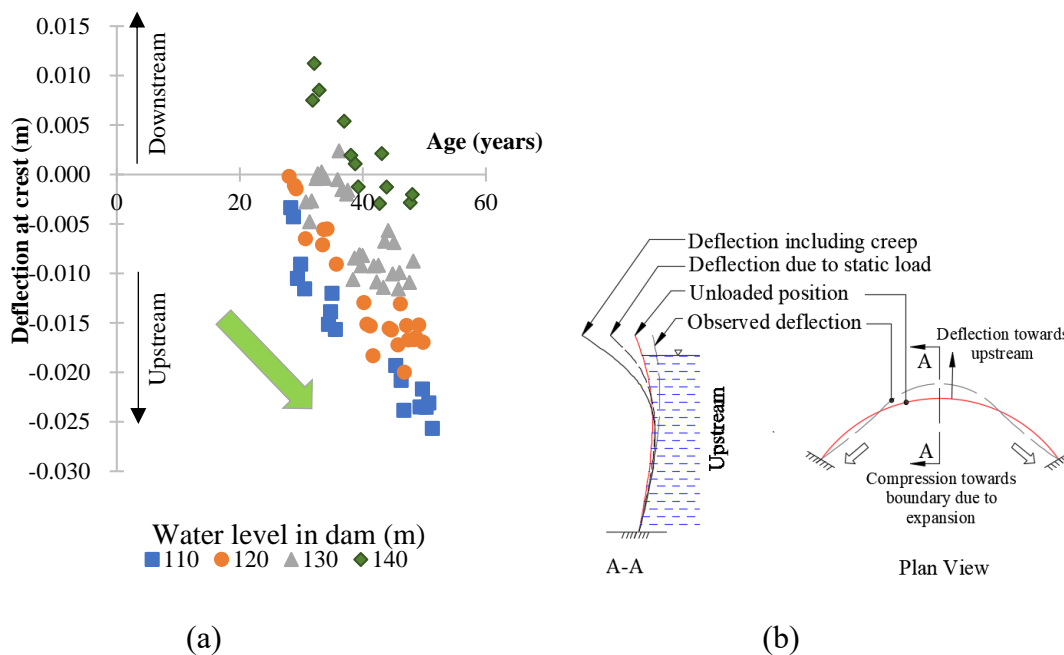


Figure 8-3 (a) Deflection of the dam at the crest (based on Bui Anh (2018)) and (b) mechanism of expansion

Deflection can occur in the upstream direction by the expansion of the dam concrete. The expansion can push the concrete in all directions; however, because of the arch geometry of the dam, the downstream deflection is restricted, and thus, the dam deflects in the upstream direction, as shown in Figure 8-3(b).

A thermal expansion could be one of the phenomena to cause deflection. The thermal expansion due to the ambient temperature rise is not monotonic, which means that the expansion should be recovered when the temperature is lowered. However, such a monotonic temperature rise has not been reported in Thailand. Furthermore, the thermal expansion should become stable after approximately three thermal cycles by the opening of cracks (Roth & Dolice, 2017). Furthermore, in the case of the target dam, thermal cracks have not been detected on the dam surface (Bui et al., 2019). Thus, the expansion by the rise in temperature can be ignored.

Another expansive phenomenon could be swelling due to water absorption. In the case of a dam having a massive concrete body, the moisture content can remain uniform throughout its body except at the outer face, whose thickness can be neglected with respect to the overall size of the structure (Steffens et al., 2003). Thus, the possibility of expansion by moisture absorption is low. Conversely, some part of the data shows that deflection decreases when the water level rises (Figure 8-3 (a)), even though increased moisture absorption should lead to a higher deflection. Thus, this mechanism can be omitted.

An expansive chemical reaction is another possible mechanism that can cause an increase in volume. Given the hot tropical climate of Thailand (Figure 8-1), the possibility of temperature rise owing to mass concreting and easy availability of moisture in the hardened phase, Delayed Ettringite Formation (DEF), can be suspected (Bouzabata et al., 2012a). Aggregate in Thailand also has potential for the ASR (Sujjavanich, 2017; Yamada et al., 2013). ASR has been reported in highway bridges (Sujjavanich et al., 2012), however, ASR in the dams have not been reported in Thailand. For testing the condition of the concrete, core samples were extracted from the dam by using a rotary drill: one from a depth of 0.00–0.300 m (C1) and another from a depth of 0.70–1.00 m (C2) near the right abutment and the petrographic analysis was carried out.

8.2.1. Petrographic analysis

Petrographic analysis can identify the constituent minerals and examine the possibility of ASR and DEF. The cutting surface taken from the core was observed using a stereoscopic microscope to identify the fine and coarse aggregates, aggregate geometry, and ASR gel. A thin section was cut (20×30 mm, the thickness of about $15 \mu\text{m}$) and polished to observe under the polarizing microscopy and identify the rock types. This would also identify the location of reactions and the extent and sequence of ASR in concrete (Godart *et al.* 2012).

Figure 8-4 shows the cutting surface of C1 sample and its magnified surfaces. Similarly, Figure 8-5 shows the cutting surface of C2 sample and its magnified surfaces. From the analysis, the rock types of both fine and coarse aggregates were found to be gneiss. In both of the core samples, a seepage of ASR gel was found around the aggregate. Figure 8-6 shows the polarizing microscopic observation of coarse aggregates in C2 specimen; C1 specimen had a similar

tendency. Both C1 and C2 had a part of gneiss in the coarse and fine aggregate which were of calcareous to pelitic/arenaceous types. The main minerals were calcite, dolomite, quartz, microcrystalline to cryptocrystalline quartz, biotite, muscovite, plagioclase, tremolite, potash-feldspar, and diopside. The coarse aggregate of pelitic/arenaceous gneiss was found to have fine cracks filled with ASR gel products, as shown in Figure 8-7. The products in the crack under SEM showed the presence of Si with Ca, Na, and K, which are components of typical ASR gel products. The microcrystalline-cryptocrystalline quartz reacted with alkali in the cement to precipitate the ASR gel. The deterioration stage can be evaluated as weak or moderate, corresponding to the cryptic or developing stage according to the definition of previous studies (Katayama et al., 2004).

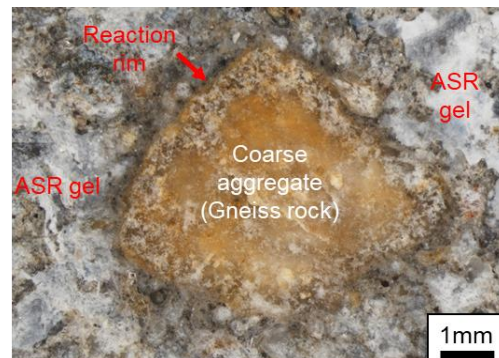
Furthermore, under the polarizing microscope, no gaps were found around the aggregate or surrounding cracks in the cement paste, which are typical characteristics of DEF. Even in the C2 sample, wherein a large hydration heat would be generated at a greater depth (Wang et al., 2019) no effect of DEF was found. Thus, the possibility of DEF is quite low as per the petrographic analysis.



(a) Cutting surface

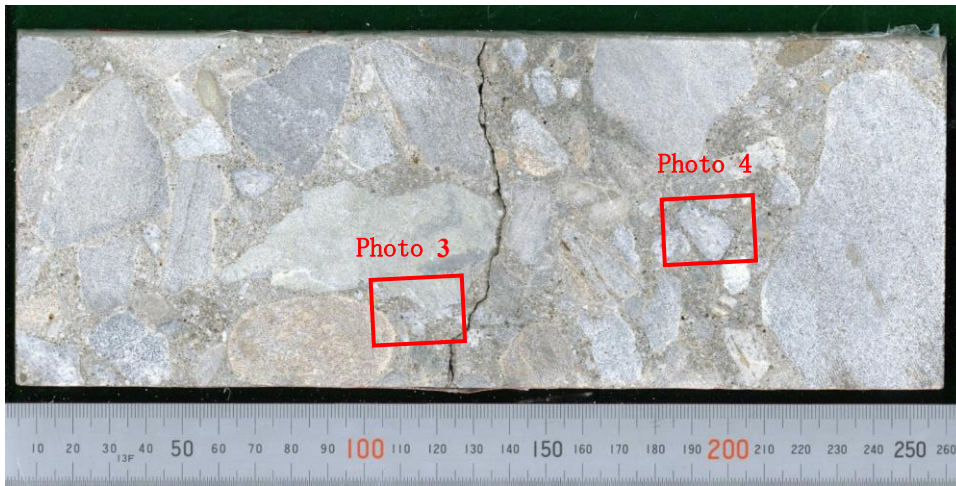


(b) Magnified surface (Photo 1)



(c) Magnified surface (Photo 2)

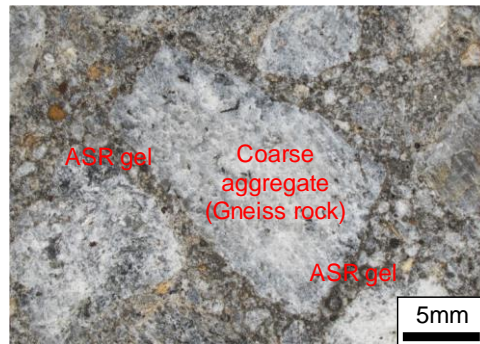
Figure 8-4 Cutting surface and magnified surface of C1 core sample (based on (Joshi et al., 2021))



(a) Cutting surface

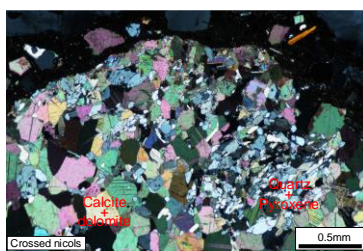


(b) Magnified surface (Photo 3)

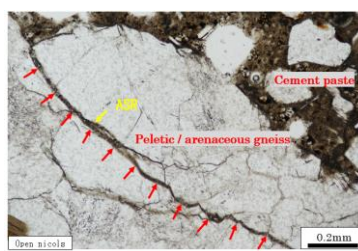


(c) Magnified surface (Photo 4)

Figure 8-5 Cutting surface and magnified surface of C2 core sample (based on (Joshi et al., 2021))



Calcareous gneiss



Pelitic/arenaceous gneiss

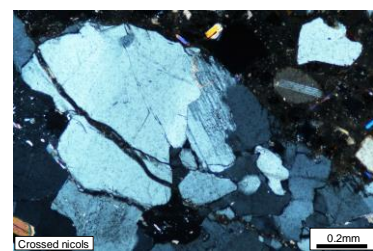


Figure 8-6 Polarizing microscopic observation of coarse aggregate in the C2 core sample (based on (Joshi et al., 2021))

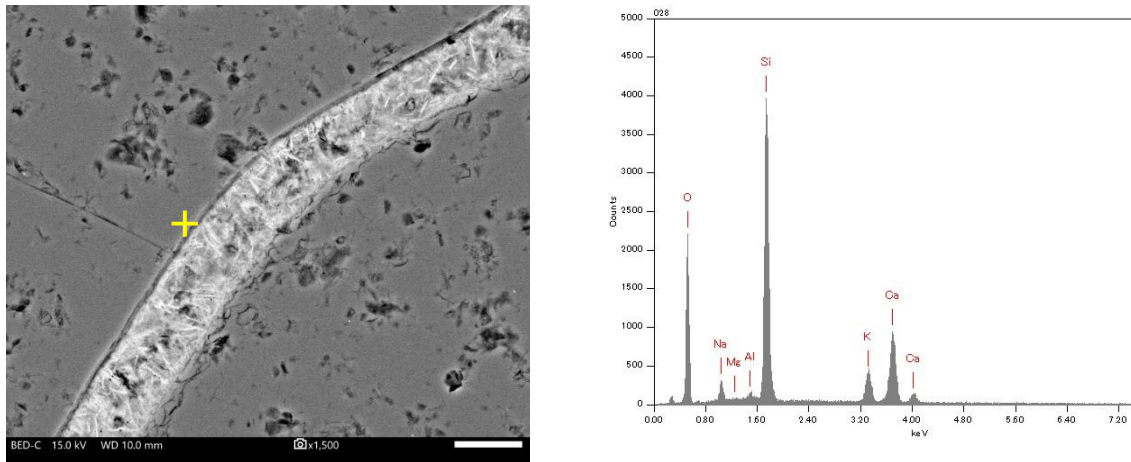


Figure 8-7 SEM observation of ASR gel and qualitative analysis by EDS in the coarse aggregate of C2 sample (based on (Joshi et al., 2021))

8.2.2. Residual expansion test

Concrete cores of 10 cm diameter were taken from the dam body and conditioned in water at 20 °C until they were completely saturated and expansion due to water absorption became stable. It took 150 days and the strain was 0.045% and 0.035% for C1 and C2, respectively. At this point, zero readings were taken and the cores were submerged in NaOH solution (1M concentration) at 80 °C.

The expansion recorded is shown in Figure 8-8. The maximum strain was 0.15% and 0.12% for C1 and C2 respectively, at the age of approximately 90 days. Specimen C1 extracted near the surface (0.0–0.3 m) showed larger expansion compared to C2 (0.7–1.0 m). It can be suggested that C2 had undergone a high temperature owing to the heat of hydration at a greater depth that can accelerate ASR during early service life, and thus, causing a small residual expansion. Without the high-temperature incidence in C1 which was near the dam surface exhibited a lower expansion.

This test indicated that both core samples have a residual ASR expansion potential. According to the ASTM C1260 guidelines (mortar bar test), an expansion between 0.1% and 0.2% in 16 days indicates that the specimen has a potential for ASR. Because specimens C1 and C2 are concrete specimens, the test performed in this experiment does not entirely conform to ASTM; nonetheless, similar accelerated tests performed by other authors, such as Kuroda et al.(2008) and Thomas et al. (2008) have shown such method is also applicable to predict the potential ASR expansion.

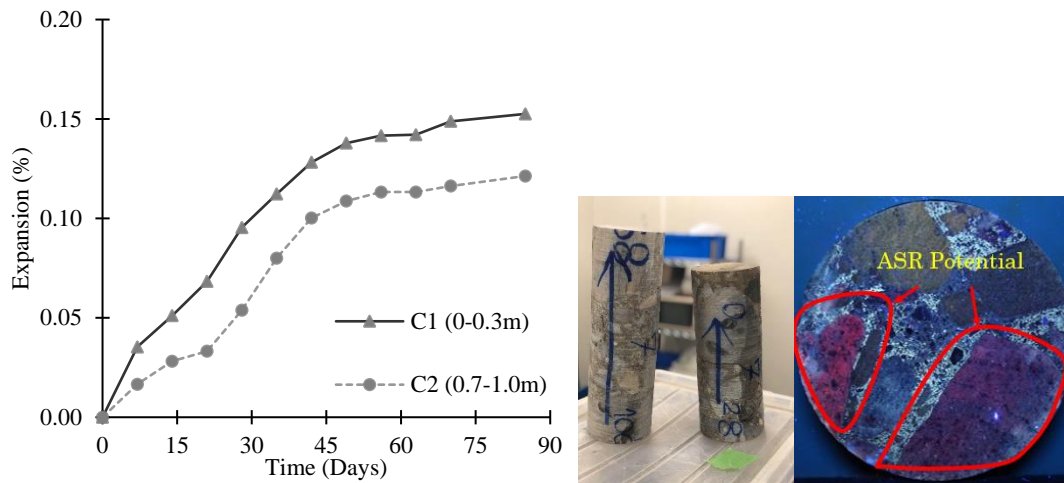


Figure 8-8 Expansion owing to accelerated ASR test for core samples taken from a depth of 30 cm (C1) and 100 cm (C2) (based on (Sriprasong, 2020))

8.3. Numerical analysis for time-dependent deformation

The numerical modelling is based on the model described in Chapter 2.

In this study, the numerical model was implemented in an open-source finite element software, Code_Aster, which has the capability of coupled analysis of thermal, mechanical, and acoustic behaviours (de France, 1989).

A three-dimensional model was used. The mesh size of the model was optimized by sensitivity analysis. Once the mesh size was fixed, thermal analysis was performed to calculate the temperature distribution inside the dam body. The temperature from the thermal analysis was used to calculate the latency and characteristic time for each element inside the dam body. The free strain and stress were calculated. The stress field was applied to the model, and mechanical analysis was performed. Since cracks have not been observed on the dam surface, linear analysis was used in this study. The possible restraint effect due to the reinforcement was not incorporated because the percentage of reinforcement is low for mass concrete of the dam. The numerical analysis was done and calibrated to match the observed deflections.

8.3.1. Model implementation

Thermal analysis

The first step in the numerical analysis is to determine the temperature distribution in the dam body. The fluctuation of monthly air temperature at the dam location from 2014 to 2020 is shown in Figure 8-9. Based on the historical data, the average monthly temperature was calculated. The maximum temperature was found to occur in April (32.1 °C) and the minimum temperature in January (24.5 °C).

The ambient temperature was applied to the dry surface of the dam. Due to differences in water conductivity, there is a time lag between ambient and water temperatures to gain equilibrium, which results in a low temperature in the reservoir side of the dam during summer and a high temperature during winter. However, to keep the analysis simple, the time lag was neglected and the relation between air and water temperature was approximated using a linear

function $\theta_{\text{water}} = 0.965 \times \theta_{\text{air}}$, where the temperature is in Kelvin (Stefan & Preud'homme, 1993). Other properties are listed in Table 8-1. The temperature distribution inside the dam body for March, February, and October is shown in Figure 8-10; other months had a similar distribution.

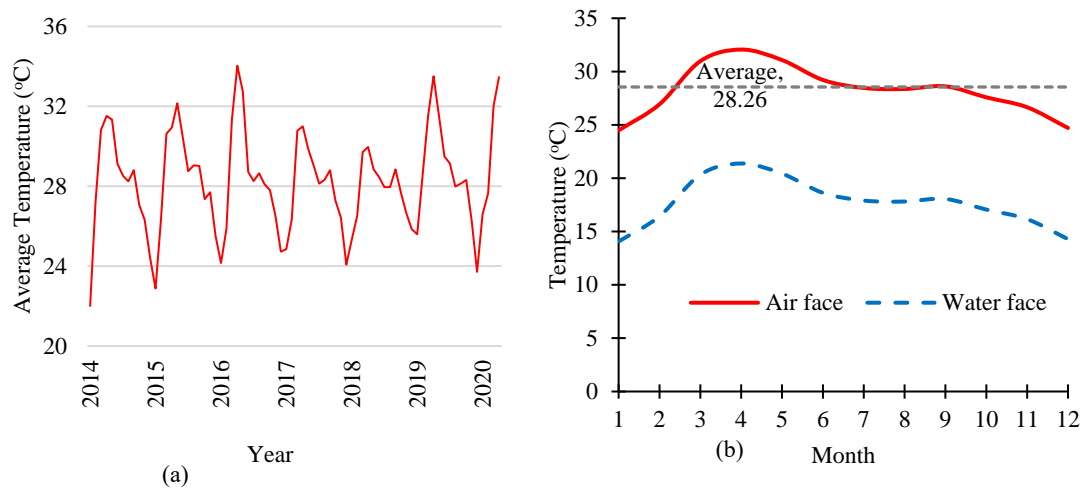


Figure 8-9 Fluctuation of temperature from 2014 to 2020; (b) average annual temperature fluctuation used in the numerical model

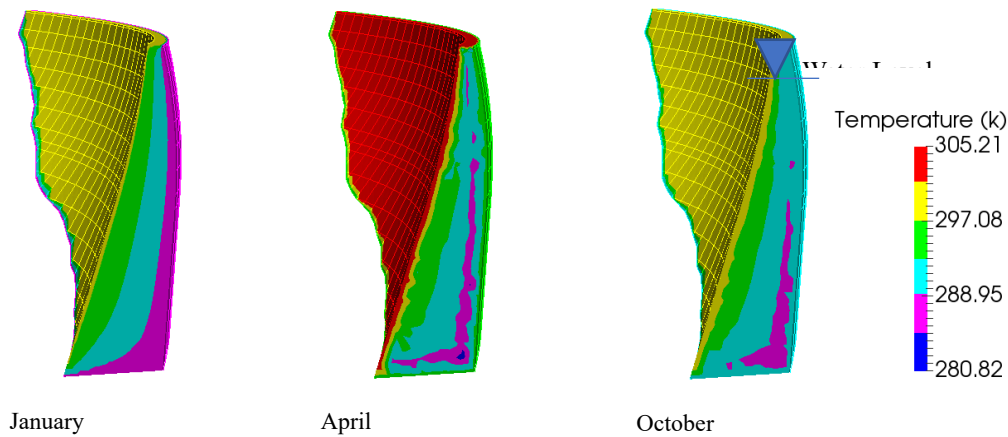


Figure 8-10 Temperature distribution inside the dam body at various months

ASR parameters

Based on the temperature distribution, the average latency time (τ_L) and characteristics (τ_c) times were calculated at each node. The latency time and characteristic time control the rate of strain evolution. The age at which ASR manifests can vary significantly. ASR is slow in the case of large dams and can take an appreciable amount of time until it becomes apparent. It takes even a long time to manifest this expansion into serious damage. The summary of the age of the dam at which the ASR was identified is shown in Figure 8-11 which is based on data of 40 dams around the world collected by (Charlwood & Sims, 2016) and (Sellier et al., 2017) (also see Appendix). The mean is approximately 30.8 years, and the standard deviation is 14.3 years. This is only an indicative value, the actual values used in the analysis was found by calibrating the model. In the targeted dam where analysis was carried out, the ASR evolution

was much slower, which is discussed in the calibration section.

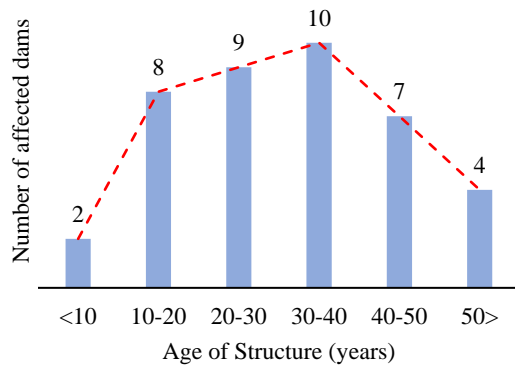


Figure 8-11 Age of dam when ASR occurred in various dams

The next main parameter for the model is the value of ultimate strain. It can be measured in the laboratory with prescribed tests, such as RILEM TC 191-ARP or ASTM C1260-07. However, large inconsistencies occur between field measurements and laboratory predictions (Hooton et al., 2013). The inconsistency is mainly due to the exposure condition and the specimen's size. Therefore, the expansion evolution parameters should be suitably modified to be applied in the numerical model. This strain value used in the analysis is described in the calibration section.

Table 8-1 Parameters used for analysis

Parameters	Values	Unit
Thermal conductivity of concrete, K	1.75	W/m ² /K
Specific heat capacity of concrete, C	0.75	KJ/Kg/K
Thermal expansion coefficient of concrete, α	10×10^{-6}	/K
U_c	5400	K
U_L	9400	K
Initial temperature, θ_0	301.41 (28.26)	K (°C)
$\tau_L(\theta_0)$	30	years*
$\tau_C(\theta_0)$	60	years*
Undamaged modulus of elasticity E_0	44.18	GPa ^o

* based on calibration

o based on the core sample

Boundary conditions

The boundary condition of the numerical model was determined based on the geological features. The dam lies on bedrock with an average modulus of elasticity of 34.5 GPa. Bui

(2018) studied the effect of elastic foundation in the instantaneous deflection of the same dam and reported a radial displacement of 3.5 cm at the crest. When the numerical model of this study was tested with a rigid boundary, a similar result was obtained and hence, a rigid boundary was used in this study.

8.4. Model calibration

The model was calibrated using the observed deflection data collected by Bui (2018). For reliability, the deflection data were tallied with the measurement by Thongthamchart & Raphitphan (n.d.). Both data were found to match with reasonable accuracy, as shown in Figure 8-12. The water level data show that the operation level remains at or below 120 m (EL 234 masl) for approximately 70% of the time; hence, this water level is considered as the reference level for the analysis.

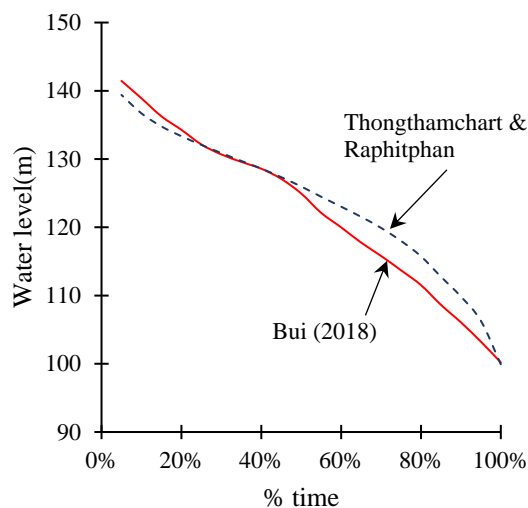


Figure 8-12 Water level comparison between Bui (2018) and Thongthamchart & Raphitphan (n.d.)

The calibration process consists of determining mainly three parameters: viz. $\epsilon(\infty)$, τ_c and τ_L . After several trials and errors, the value of $\epsilon(\infty)$ was set at 0.075%, τ_c to 30 years, and τ_L was changed from 50 to 70 years because this setting could incorporate all the observed values, as shown in Figure 8-13(a). For other analyses, τ_c and τ_L were set at 30 years and 60 years, respectively, as the base case. A similar method was used by Pan et al. (2013). After setting the parameters, the deflection of the dam for various water levels was calculated, as shown in Figure 8-13 (b), and it was found to match the observed values. The standard error of estimation for observed and predicted deflection lies between 2.6 to 6.0 mm for the water level of 110 m to 140 m respectively as shown in Table 8-2. The correlation coefficient between the observed and calculated deflection for the water level of 120 m was greater than 0.9 indicating a good prediction.

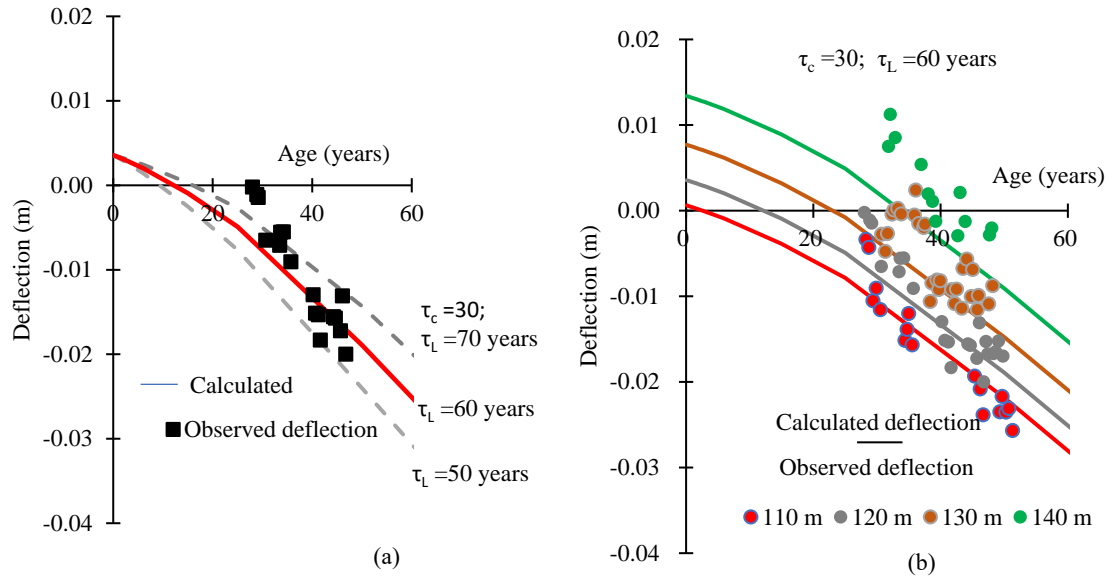


Figure 8-13 (a) Calibration of the model at a water level of 120 m; (b) estimation of deflection for various water levels; the full line is the calculated values while the observed values are shown by dots.

Table 8-2 Standard error of estimation of deflection for various water level

Water level	110 m	120 m	130 m	140 m
	(EL 224 m)	(EL 234 m)	(EL 244 m)	(EL 254 m)
Correlation coefficient	0.95	0.91	0.77	0.89
Standard error of estimate (mm)	2.62	3.23	4.05	6.03

8.5. Sensitivity analysis

In this section, various factors influencing the behaviour of the dam are discussed.

8.5.1. Effect of elasticity

Equations 7 and 8 indicate that Young’s modulus of elasticity (E) will gradually degrade over time as ASR progresses. To compare the difference between the analysis that utilizes constant E and the one that uses degrading E was carried out because the degradation is small, approximately 4 GPa in 100 years. As shown in Figure 8-14(a), there is no significant difference between the two series. The two-parameter Kolmogorov–Smirnov test shows that $D(= 0.071) < D_{lim}(= 0.464)$; hence, the two series are statistically similar (Pratt & Gibbons, 2012). The radial deflection along the dam height, shown in Figure 8-14 (b), is also identical. This result is similar to the observations by Saouma et al. (2007).

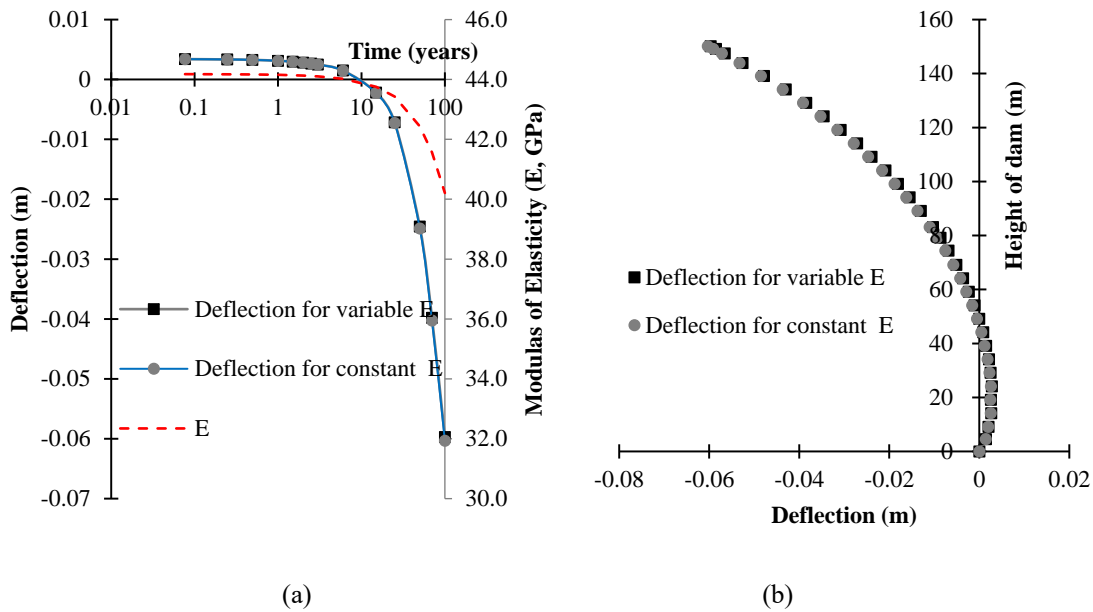


Figure 8-14 (a) Effect of modulus of elasticity on the evolution of deflection, and (b) deflection of the dam for a water level of 120 m along its height at the age of 100 years

8.5.2. Effect of varying monthly temperature

The numerical model can be simplified if a static value of average temperature can be used instead of varying monthly temperatures. Thus, to verify, an analysis was carried out using the average temperature of 28.26 °C. The evolution of deflection is shown in Figure 8-14 (a). The radial deflection along the dam height is shown in Figure 8-14 (b). A slightly higher deflection will inevitably be calculated at the advanced age of the dam for the constant temperature because the exponential terms of Equations 3 and 4 vanish while considering the constant average temperature. This reduces the average value of τ_c and τ_L , and increases the strain rate. The total effect is an increase in deflection at the later age of the dam. However, it can be observed that the trends of the two curves are similar. The two-parameter Kolmogorov–Smirnov test shows $D(= 0.143) < D_{lim}(= 0.464)$; hence, the two series are statistically similar. Thus, in the absence of reliable temperature data, a single temperature model can be used without losing appreciable precision.

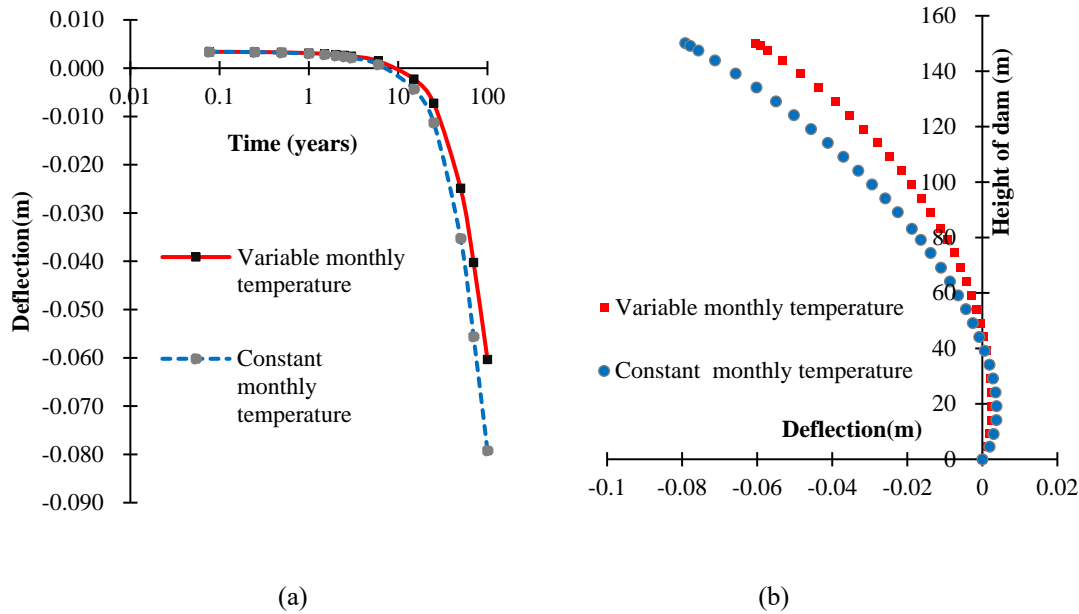


Figure 8-15 (a) Evolution of deflection overtime for a water level of 120 m; (b) the deflection pattern of the dam at the age of 100 years

8.5.3. Effect of ambient temperature

Another analysis was carried out to check the effect of varying temperatures on the deflection of the dam. This hypothetical analysis could be of interest to monitor the pattern of deflection when the dam is subjected to a larger differential temperature. For the analysis, the base temperature was set at 20 °C and the environmental temperature was set from 20 to 40 °C. The maximum radial deflections are shown in Figure 8-16(a). In all cases, the deflection gradually increased and flattened out at the age of approximately 70 years. Similarly, the evolution of the maximum deflection, including the thermal strain, is shown in Figure 8-16 (b). Because the ASR expansion is superimposed by the thermal expansion, a slightly higher deflection is seen at the higher temperature; the evolution curve for 20 °C remains unchanged as the base temperature remains the same.

A detailed comparison of the maximum radial deflection at the age of 50 and 100 years for various water levels and temperatures is shown in Table 8-3. The deflection can increase by about 45% for a temperature differential of 20 °C when thermal strain is added, which is significant. However, the temperature differential over 20 °C throughout the life of the dam is hypothetical and may not occur under normal circumstances. The actual annual temperature difference is 7.58 °C for the target dam, which results in a 4% and 12% increase in deflection at the age of 50 and 70 years when thermal strains are accounted for. However, the thermal strain recovers when the temperature drops; thus, in normal cases, it can be neglected, as discussed previously.

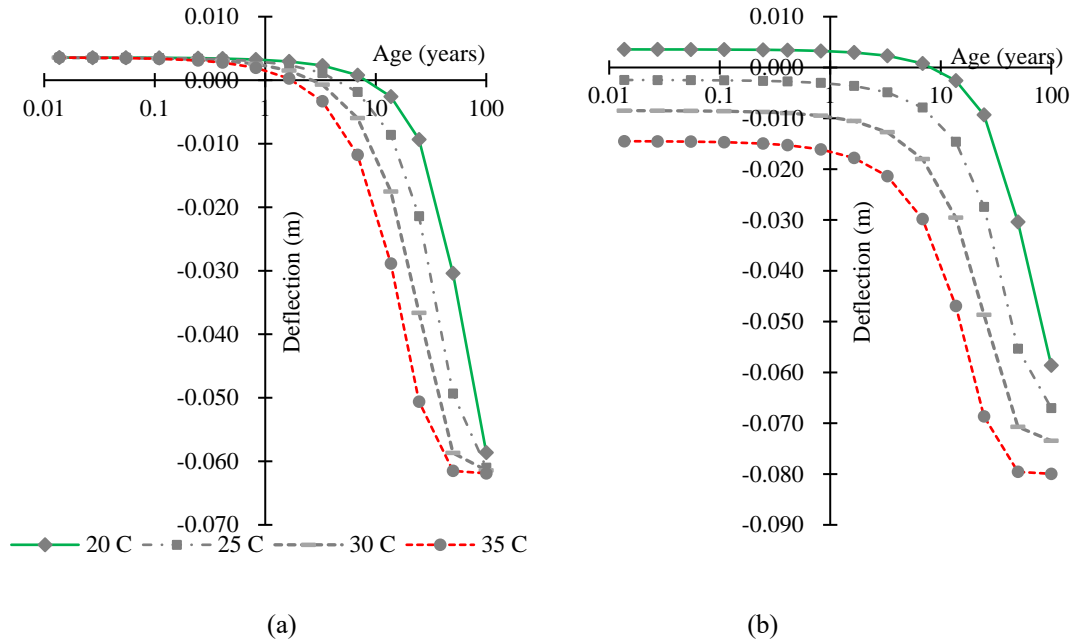


Figure 8-16 Evolution of maximum radial deflection at the crest for various temperatures and water level of 120 m owing to (a) ASR strain (b) ASR strain combined with the thermal strain

Table 8-3 Comparison of deflection with and without thermal strain for various water levels and temperature

Deflection with ASR only (without thermal expansion) (m)										
Water level	50 years					100 years				
	20 °C	25 °C	30 °C	35 °C	40 °C	20 °C	25 °C	30 °C	35 °C	40 °C
110 m (EL 224 m)	-0.037	-0.057	-0.068	-0.071	-0.072	-0.068	-0.070	-0.071	-0.071	-0.072
120 m (EL 234 m)	-0.034	-0.054	-0.065	-0.068	-0.069	-0.064	-0.067	-0.068	-0.068	-0.069
130 m (EL 244 m)	-0.029	-0.050	-0.060	-0.063	-0.065	-0.060	-0.063	-0.063	-0.064	-0.065
140 m (EL 254 m)	-0.023	-0.043	-0.054	-0.057	-0.058	-0.054	-0.056	-0.057	-0.057	-0.058
Deflection with ASR and thermal expansion (m)										
110 m (EL 224 m)	-0.037	-0.064	-0.081	-0.090	-0.099	-0.068	-0.077	-0.084	-0.091	-0.099
120 m (EL 234 m)	-0.034	-0.061	-0.078	-0.087	-0.095	-0.064	-0.074	-0.081	-0.088	-0.095
130 m (EL 244 m)	-0.029	-0.056	-0.073	-0.083	-0.091	-0.060	-0.069	-0.076	-0.083	-0.091
140 m (EL 254 m)	-0.023	-0.050	-0.067	-0.076	-0.084	-0.054	-0.063	-0.070	-0.077	-0.085

8.5.4. Effect of strain

The magnitude of the ultimate ASR strain (ϵ_{∞}) is one of the major parameters used for calibration. Thus, an analysis was carried out by applying a strain from 0.00045 to 0.0015 that corresponds to 30% to 100% of 0.0015 strain value (measured during the accelerated test). Because the accelerated test was done at 80°C in 1 mol/l NaOH solution which could produce a low viscous ASR gel with high alkali content and thus give higher expansion than the actual field strain. Thus its effect on the displacement of the dam is an important consideration. For this sensitivity analysis, the temperature and other variables were set constant. The evolution of radial deflection at the crest for a hydrostatic load of 120 m and various input strains is shown in Figure 8-17(a). As expected, the magnitude of deflection increased with an increase in the ultimate strain. This is true for water levels from 110 m to 140 m, as shown in Figure 8-17 (b). Note that the model calibrated at 50% of ultimate strain yielded the optimum result. Interestingly, in the experiment by (Kawabata, Yamada, et al., 2021), the ASR-DEF-affected specimens manifested approximately 50% of the expansive strain in the field compared to the specimens in the laboratory, which suggests the existence of a similar correlation for ASR affected structures. This should be further studied.

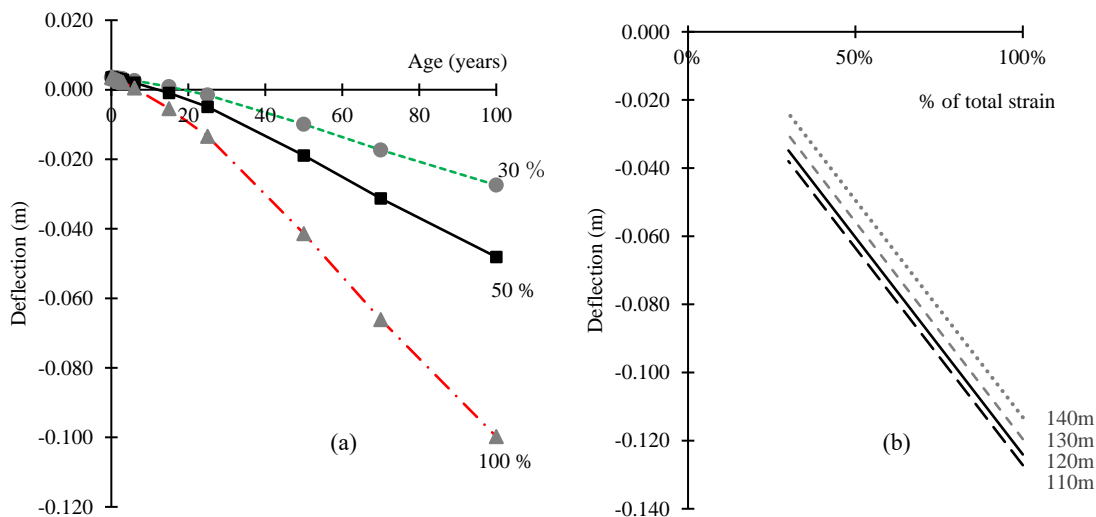


Figure 8-17 (a) Evolution of deflection owing to various levels of ASR strain for a water level of 120 m; (b) deflection of the dam for various water levels at the age of 100 years

8.6. Deflection prediction

Two approaches were used to predict the future deflection of the dam. In the first approach, a deterministic method was used by setting τ_c as 30 and τ_L as 50, 60, and 70 years. These values are selected based on the model calibration as they predicted the observed values correctly. The radial deflection at the dam centre line, using the deterministic approach, for a water level of 120 m is shown in Figure 8-18(a), and the distribution of deflection for various ages are shown in Figure 8-18 (b). At the age of 100 years, the deflection will lie between 54

and 66 mm.

The second method was the probabilistic method (Monte Carlo). In this method, the input parameters, $\epsilon(\infty)$, τ_c , and τ_L , are assumed to have a normal distribution as shown in Table 8-4. In practice, these three parameters are not known; thus, they have to be estimated based on historic data of similar structures as was done earlier in the calibration section.

The result of the probabilistic analysis is shown in Figure 8-19(a). The mean deflection is 61.68 mm and the standard deviation of deflection is 28.04 mm. Deflections for other cases are shown in Table 8-4 and graphically shown in Figure 8-19 (b).

Table 8-4 Variation of input and output parameters

Parameters	Mean	Standard deviation
$\epsilon(\infty)$	0.00075	0.00025
τ_c (year)	30	10
τ_L (year)	60	20

Deflection at dam crest at the age of 70 years for various water level			
Water Level	Mean (mm)	Standard deviation (mm)	deviation (mm)
110 m (EL 224 m)	45.71	23.47	
120 m (EL 234 m)	42.57	23.31	
130 m (EL 244 m)	37.70	23.47	
140 m (EL 254 m)	31.05	23.72	

Deflection at dam crest at the age of 100 years for various water level			
Water Level	Mean (mm)	Standard deviation (mm)	deviation (mm)
110 m (EL 224 m)	64.72	28.21	
120 m (EL 234 m)	61.68	28.04	
130 m (EL 244 m)	57.14	28.40	
140 m (EL 254 m)	50.53	28.52	

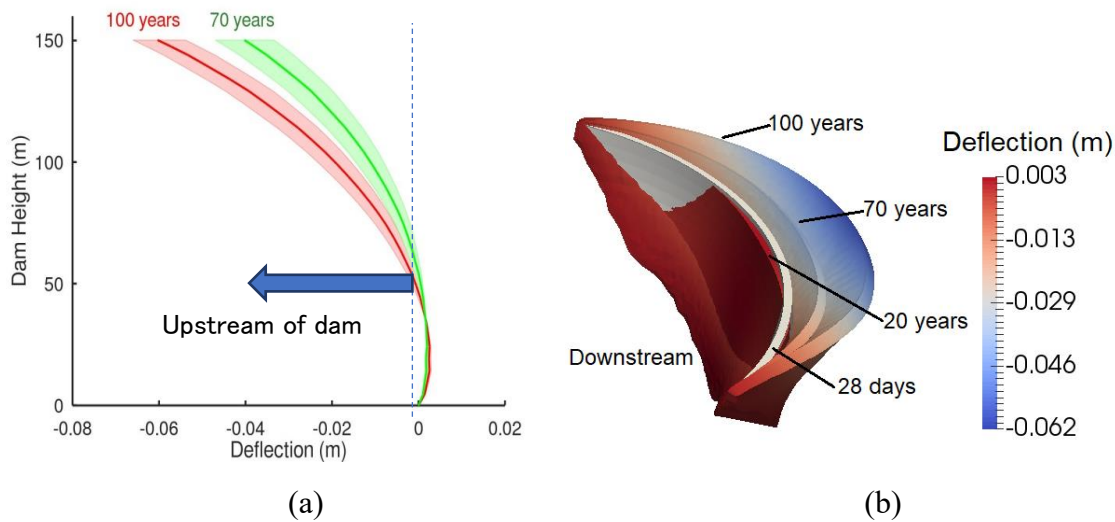


Figure 8-18 (a) Prediction of deflection of the dam at the age of 70 years and 100 years using a deterministic approach for the water level of 120 m; (b) deflection of the dam for various ages (Joshi et al., 2021)

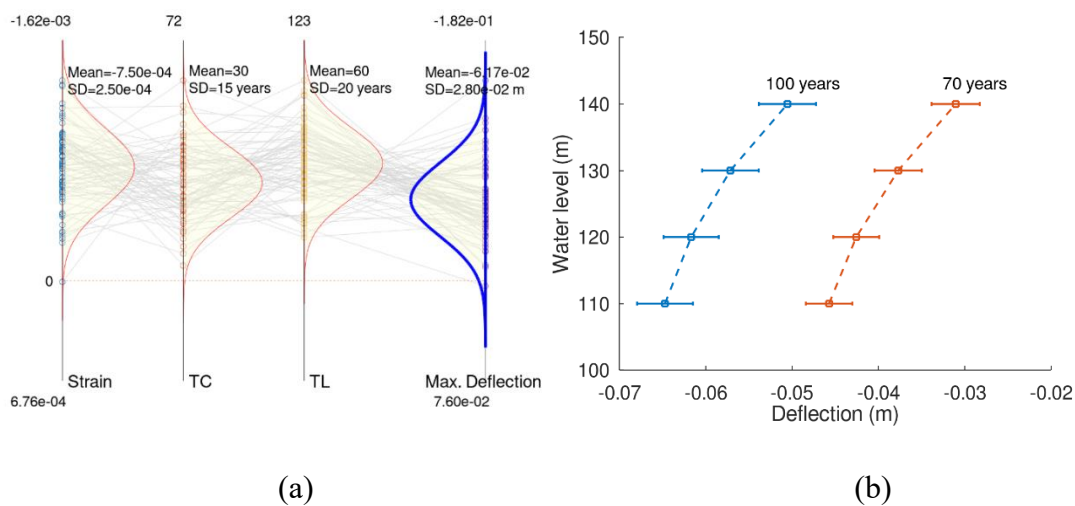


Figure 8-19 (a) Probabilistic prediction of the deflection of the dam for the water level of 120 m; (b) deflection for various water levels with the standard error at the age of 100 and 70 years. (Joshi et al., 2021)

8.7. Crack susceptibility

The other major parameter of interest is the crack-susceptible zone in the dam. The area exceeding the tensile or compressive strength of the concrete has a potential for cracking. The distribution of principal stress in the dam body is shown in Figure 8-20. Due to the arch shape, the increase in the ASR strain increases the compressive stress, whereas small tensile stress (less than 1 N/mm²) is generated without ASR expansion. Thus, there is less likelihood of tensile cracks owing to the expansion. However, in the future, if the ASR expansion occurs beyond the predicted values, some compressive cracks may appear in the downstream face. The estimated maximum compressive stress at the age of 100 years in the downstream face is about 15 N/mm², which is small enough to avoid compressive cracking.

The effect of reinforcement steel has not been considered in this analysis due to the lack of data and its low percentage. A recent study has shown that steel can partially resist the expansion and provide safety against cracking when the ASR is at its early age, that is when the stress level is low (P. Li et al., 2020). This will provide additional safety against the crack formation.

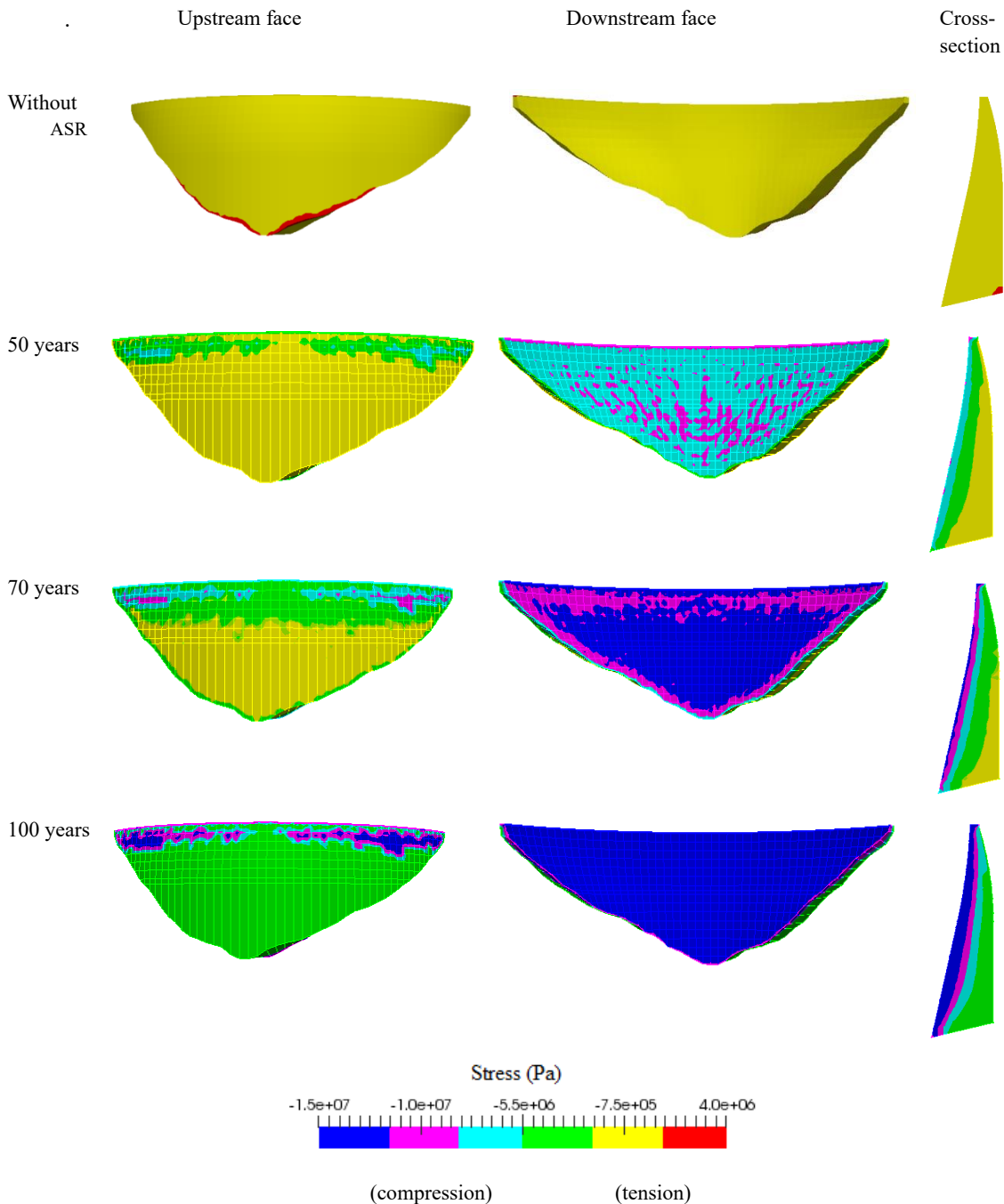


Figure 8-20 Distribution of major principal stress in the dam body without the effect of ASR and with ASR at the age of 50 years, 70 years and 100 years for hydrostatic loading of 120 m (Joshi et al., 2021)

8.8. Summary

In this study, an arch dam was diagnosed with ASR based on petrographic analysis and SEM imaging of the concrete. The residual expansion was measured by conducting an accelerated ASR test which revealed the possibility of expansion of about 0.15%. To assess the dam behaviour, a time-dependent analysis was carried out.

A coupled thermo-chemo-mechanical analysis was implemented in finite element software. Using the temperature data, the ASR strain and stress were calculated. The deflection and principal stresses in the dam were estimated by calibrating the model with the observed deflections. The variation of the model was accounted for by providing a possible range of deflection values instead of a single value.

It is predicted that, at the age of 100 years (i.e. in 2064) of the dam, the maximum deflection will lie between approximately 54–66 mm towards the upstream direction. The probabilistic analysis further verified that the estimated upstream deflection of 61 mm with a standard deviation of 28 mm. Both methods gave similar values.

The principal stress distribution in the dam showed that the dam is predominantly in compression and safe against cracking at the current rate of reaction. This study predicts the possible region where problems may occur if the reaction is accelerated beyond the currently expected values.

9. Conclusion and recommendation

This dissertation was focused to fill the gap in knowledge in the field of concrete engineering related to the deterioration caused by expansion of concrete by alkali-silica reaction (ASR), delayed ettringite formation (DEF) and their combination (DA). The inspiration for the study was based on the observation that although there have been many studies to understand the mechanism of those reactions which are helpful to prevent the expansion in new construction, there are very few studies on the impact of expansion on the serviceability and safety of existing structures. Thus, a series of experiments and numerical studies were done in this dissertation to understand the interaction between expansion and change in engineering behaviour of infected concrete.

The dissertation was broadly divided into two parts. The first part was focused on the experimental study on the change in the mechanical behaviour of expanding concrete caused by ASR, DEF and DA. The second part of the dissertation involved numerical modeling and a case study of ASR affected massive dam structure. The general conclusion of each part of the study is given in the following subsections.

9.1. Part A: Experimental works

In the first part of the dissertation, various experiments were carried out to understand the interaction between concrete expansion and mechanical properties of infected concrete. Experiments were carried out to check the following:

- effect of internal and external steel restraints on the expansion,
- change in bond strength due to the expansion and
- mechanism of cracks propagation in a highly expanded concrete by using X-ray CT

The major finding of the study are as follows:

- 1) In prismatic specimen (100 mm x 100 mm x 400mm) cured at 80 °C, the free expansion due to DA was the highest followed by DEF and ASR. The free expansion in the DA could reach 18,000 microns (1.8%), in DEF could reach about 9,000 microns (0.9%) and in ASR could reach about 300 microns (0.03%). When cured at 90 °C, the free expansion also reached a similar level.
- 2) The expansion due to DEF and DA was much rapid compared to the ASR specimen.
- 3) The internal restraint by reinforcement or the external restraint by steel plates could significantly reduce the expansion by up to 45%. Even though the free expansion was different for DEF and DA, the restraint caused both types of expansion to converge at a similar level. The expansion in DA started earlier than DEF.
- 4) The expansion could instigate tensile stress in the rebar in the case of internal restraints. The tensile strain could reach up to about 500 microns, after which the strain in rebar was reduced. This was attributed to the microcracking between steel and concrete interfaces.

- 5) The external restraining frame also experienced significant stress. The stress was about 158.3 N/mm² and 95.4 N/mm² in DEF and DA specimens respectively and the corresponding stress in the concrete was about 11.2 N/mm² and 6.7 N/mm² respectively. The expansion could bend the restraining end plates which were verified by a numerical calculation.
- 6) As of the current measurement, the ASR specimen showed a larger expansion in the restrained condition than the free cases. The reason for such behaviour is unclear at this stage. It could be possible that given sufficient time to expand, the free expansion can exceed the restrained one.
- 7) The uniaxial compressive strength could reduce to about 80-85% when expansion reached about 10,000 microns (1%) for DA and DEF specimens. The stress-strain curve gets flat and the plastic strain increased with the increase in free expansion. The strain at peak strength was also increased with expansion. In the case of ASR, the compressive strength did not change significantly.
- 8) In DA and DEF specimens, the bond strength gradually decreased with expansion and was stabilized at about 60% of initial bond strength. In the case of ASR, the bond strength was improved by about 5% at the expansion of about 3000 microns (0.3%). The increase in bond strength is ascribed to the apparent increase in prestressing force at relatively low expansion and the absence of larger cracks in the concrete.
- 9) ASR, DEF and DA affected concrete can experience internal damage due to external load even at the low-stress level. The damage reduced the dynamic of Young's modulus. This shows that deflection of the structures can increase rapidly at the low-stress level in the affected structures. However, it is unclear at this stage if the same will be true for the reinforced specimen because the damage experiment was done in an unreinforced specimen.
- 10) The structures affected with ASR needs careful attention because, even though there is an apparent increase in the compressive and bond strength, the stiffness of the structure could be greatly reduced causing serviceability issue such as excessive deflection.
- 11) The X-ray CT scanning of highly deformed cylinders (20,000 microns or 2% expansion) revealed that at a stress level of less than about 50 % of the peak strength, the pre-existing gaps around aggregate can be opened or closed without increasing the apparent crack volume. The stress exceeding about 75 % of peak strength, the large crack could propagate between the aggregates forming a fracture surface and leading to failure. When the load is small, there is a closing of gaps/cracks in the loading direction. When the load increases, the cracks in the radial direction open. The closing of the gap in the axial direction was the main reason for the additional plastic strain. At a higher stress level, new cracks are formed and the existing crack grows in size towards the perpendicular direction. The cracks in the range of 0.5-1.0 mm also increases.

- 12) The sustained type of loading on highly expanded concrete can cause the growth of both smaller and larger cracks, showing that creep type of loading can cause the crack to grow. This points out the risk of the sustained type of loading in DEF deteriorated structures is high.

9.2. Part B: Numerical modelling for strength and serviceability evaluation

The second part of the dissertation was focused on developing and testing a structural modelling for ASR and DEF affected concrete. The time-dependent expansion by ASR/DEF was modelled using Larvie's equations and the strength model of concrete at a particular instant was modelled using Mazer's model. The model was connected together by fitting the expansion-strength and expansion-elasticity relationship with a Gaussian function. The non-linear numerical model was implemented in Code Aster and tested for various example cases.

It was found that the model can predict strength and deformation. The model was used to successfully calculate the evolution of expansive strain of unreinforced and reinforced concrete by calibrating it with the experiment data. The bond strain in the interface of steel and concrete predicted using the model had similar values to the experiment results. The stress-strain behaviour of deteriorated concrete encountered in the experiment in which the peak strength is reduced while peak strain is increased could be well simulated. The model was also used to predict the behaviour of a reinforced beam. It is estimated that there will be no significant reduction in beam strength if sufficient shear reinforcement is provided. When shear reinforcement is insufficient, the loading capacity of the beam can significantly reduce and can undergo brittle compressive failure which becomes pronounced with the expansion. This simulation has to be verified with an experiment in the future.

The time-dependent expansion model was also used to perform a case study for an ASR affected massive dam structure. The main focus of the study was to check the serviceability of the structure. Using the temperature data, the ASR expansion and stress were calculated. The deflection and principal stresses in the dam were estimated by calibrating the model with the observed deflections. The variation of the model was accounted for by providing a possible range of deflection values instead of a single value. It is predicted that, at the age of 100 years (i.e. in 2064) of the dam, the maximum deflection will lie between approximately 54–66 mm towards the upstream direction. The probabilistic analysis further verified that the estimated upstream deflection of 61 mm with a standard deviation of 28 mm. The principal stress distribution in the dam showed that the dam is predominantly in compression and safe against cracking at the current rate of reaction. This study predicted the possible region where problems may occur if the reaction is accelerated beyond the currently expected values.

The finding of the dissertation is expected to be useful for the engineers tackling the issues of the structural performance of ASR/DEF affected structures.

9.3. Recommendation for future study

Based on the study carried, the following are recommended for future study.

- The stress induced in the steel rebar by the concrete expansion in the direction of rebar showed a gradual tension followed by compression in Chapter 3 i.e. the stress was reversed during the expansion. Although this behaviour was observed made in several specimens, there is still a suspicion that it could be an experimental error. Thus, it is suggested to reconfirm this observation.
- The stress in concrete was in the range of 6.7 to 11.2 N/mm² (Chapter 4) which is much higher than reported by other authors such as 1.9 to 3.9 N/mm² by Kawabata, et al. (2021) even though the expansive strain was similar (about 20,000 microns or 2%). It is believed that this discrepancy could be due to the difference in mix design, however, the actual reason is not clear. Thus experiment with various mix proportions is recommended to be carried out.
- The expansion of the ASR specimen was found to be greater in the restrained condition in all the experiments (Chapter 3, 4 and 5). This is a contradictory behaviour because in general, the expansion should be reduced as shown by DEF and DA expansion. This point needs to be confirmed or falsified by future experiments. It is suggested to carry out an experiment with various reinforcement percentages.
- In the bond strength experiment, only single rebar and one concrete mix were used. For generality, it is recommended to conduct an experiment with rebars of different diameters and different concrete mixes. Furthermore, tests shall also be done with plain rebars. The pullout strength of a normal specimen shall be checked in a trial experiment.
- The numerical model described in Chapter 8 needs to be further tested by applying with other experiment results, especially at the structural level.

References

- Ahmed, T., Burley, E., & Ridgen, S. (1999). Effect of alkali-silica reaction on tensile bond strength of reinforcement in concrete tested under static and fatigue loading. *Materials Journal*, 96(4), 419–428. <https://doi.org/10.14359/641>
- Ahmed, T., Burley, E., Rigden, S., & Abu-Tair, A. I. (2003). The effect of alkali reactivity on the mechanical properties of concrete. *Construction and Building Materials*, 17(2), 123–144. [https://doi.org/10.1016/S0950-0618\(02\)00009-0](https://doi.org/10.1016/S0950-0618(02)00009-0)
- Al Shamaa, M., Lavaud, S., Divet, L., Colliat, J. B., Nahas, G., & Torrenti, J. M. (2016). Influence of limestone filler and of the size of the aggregates on DEF. *Cement and Concrete Composites*, 71, 175–180. <https://doi.org/10.1016/j.cemconcomp.2016.05.007>
- Al Shamaa, M., Lavaud, S., Divet, L., Nahas, G., & Torrenti, J. M. (2014). Coupling between mechanical and transfer properties and expansion due to DEF in a concrete of a nuclear power plant. *Nuclear Engineering and Design*, 266, 70–77. <https://doi.org/10.1016/j.nucengdes.2013.10.014>
- Alexander, M. G., Blight, G., & Lampacher, B. (1992). *Pre-demolition tests on structural concrete damaged by AAR. I*, 1–10.
- Allard, A., Bilodeau, S., Pissot, F., Fournier, B., Bastien, J., & Bissonnette, B. (2018). Expansive behavior of thick concrete slabs affected by alkali-silica reaction (ASR). *Construction and Building Materials*, 171, 421–436. <https://doi.org/10.1016/j.conbuildmat.2018.03.159>
- Alnaggar, M., Cusatis, G., & Luzio, G. D. (2013). Lattice discrete particle modeling (LDPM) of alkali silica reaction (ASR) deterioration of concrete structures. *Cement and Concrete Composites*, 41, 45–59. <https://doi.org/10.1016/j.cemconcomp.2013.04.015>
- Awasthi, A., Matsumoto, K., Nagai, K., Asamoto, S., & Goto, S. (2017). Investigation on possible causes of expansion damages in concrete. *Journal of Asian Concrete Federation*, 3(1), 49–66. <https://doi.org/10.18702/acf.2017.06.3.1.49>
- Baillemont, G., Delaby, J.-B., Brouxel, M., & Rémy, P. (2000). *Diagnosis, treatment and monitoring of a bridge damaged by AAR*. 1099–1108.
- Baingam, L., Saengsoy, W., Choktaweekarn, P., & Tangtermsirikul, S. (2012). Diagnosis of a combined alkali silica reaction and delayed ettringite formation. *Science & Technology Asia*, 17(4), 22–35.
- Barbosa, R. A., Hansen, S. G., Hansen, K. K., Hoang, L. C., & Grell, B. (2018). Influence of alkali-silica reaction and crack orientation on the uniaxial compressive strength of concrete cores from slab bridges. *Construction and Building Materials*, 176, 440–451. <https://doi.org/10.1016/j.conbuildmat.2018.03.096>
- Bergol, L., Di Pace, G., Rocco, C., Szeimberg, S., & Zitzer, L. (2003). Use of fracture mechanics parameters to monitor concrete deterioration due to delayed ettringite reformation. *Special Publication*, 212, 181–196.
- Bouzabata, H., Multon, S., Sellier, A., & Houari, H. (2012a). Swellings due to alkali-silica reaction and delayed ettringite formation: Characterisation of expansion isotropy and effect of moisture conditions. *Cement and Concrete Composites*, 34(3), 349–356. <https://doi.org/10.1016/j.cemconcomp.2011.10.006>
- Bouzabata, H., Multon, S., Sellier, A., & Houari, H. (2012b). Effects of restraint on expansion sferdue to delayed ettringite formation. *Cement and Concrete Research*, 42(7), 1024–

1031. <https://doi.org/10.1016/j.cemconres.2012.04.001>
- Brown, P. W., & Bothe, J. V. (1993). The stability of ettringite. *Advances in Cement Research*, 5(18), 47–63.
- Brunetaud, X., Divet, L., & Damidot, D. (2008). Impact of unrestrained Delayed Ettringite Formation-induced expansion on concrete mechanical properties. *Cement and Concrete Research*, 38(11), 1343–1348. <https://doi.org/10.1016/j.cemconres.2008.05.005>
- Brunetaud, X., Linder, R., Divet, L., Duragrin, D., & Damidot, D. (2007). Effect of curing conditions and concrete mix design on the expansion generated by delayed ettringite formation. *Materials and Structures*, 40(6), 567–578. <https://doi.org/10.1617/s11527-006-9163-3>
- BS 7543:2015 *Guide to durability of buildings and building elements, products and components*. (2015).
- BSI. (1997). *Structural use of concrete*.
- BSI. (2004). *Eurocode 2: Design of concrete structures: Part 1-1: General rules and rules for buildings*. British Standards Institution.
- Bui, K. A. (2018). *Finite element simulation of static structural behavior of a concrete arch dam*. Thammasat University.
- Bui, K. A., Pakawat, S., Ganchai, T., Somnuk, T., & Pruettha, N. (2019). An evaluation of thermal effects on behavior of a concrete arch dam. *Songklanakarin Journal of Science and Technology*, 41, 1059–1068. <https://doi.org/10.14456/SJST-PSU.2019.133>
- Canadian Standards Association. (2000). Guide to the evaluation and management of concrete structures affected by alkali-aggregate reaction. *CSA A864-00*. Ontario, Canada.
- Ceary, M. (2007). *Characterization of delayed ettringite formation in Maryland bridges*. <https://drum.lib.umd.edu/handle/1903/6816>
- Chana, P. S. (1989). Bond strength of reinforcement in concrete affected by alkali silica reaction. *Transport and Road Research Laboratory (TRRL), CR 1*. <https://trid.trb.org/view/314058>
- Charlwood, R., & Sims, I. (2016). Expansive chemical reactions in dams and hydroelectric projects. *Proceedings of the Institution of Civil Engineers - Construction Materials*, 169(4), 197–205. <https://doi.org/10.1680/jcoma.15.00083>
- Charlwood, R., & Sims, I. (2017). Review of the effectiveness of strategies to manage expansive chemical reactions in dams and hydro projects. *Proceedings of the Dam Swelling Concrete DSC*.
- Chatterji, S., & Christensen, P. (1990). Studies of alkali-silica reaction. Part 7. Modelling of expansion. *Cement and Concrete Research*, 20(2), 285–290. [https://doi.org/10.1016/0008-8846\(90\)90082-9](https://doi.org/10.1016/0008-8846(90)90082-9)
- Chrisp, T., Waldron, P., & Wood, J. (1993). Development of a non-destructive test to quantify damage in deteriorated concrete. *Magazine of Concrete Research*, 45(165), 247–256. <https://doi.org/10.1680/mac.1993.45.165.247>
- Christensen, A. N., Jensen, T. R., & Hanson, J. C. (2004). Formation of ettringite, $\text{Ca}_6\text{Al}_2(\text{SO}_4)_3(\text{OH})_{12}\cdot 26\text{H}_2\text{O}$, AFt, and monosulfate, $\text{Ca}_4\text{Al}_2\text{O}_6(\text{SO}_4)\cdot 14\text{H}_2\text{O}$, AFm-14, in hydrothermal hydration of Portland cement and of calcium aluminum oxide—Calcium sulfate dihydrate mixtures studied by in situ synchrotron X-ray powder diffraction. *Journal of Solid State Chemistry*, 177(6), 1944–1951. <https://doi.org/10.1016/j.jssc.2003.12.030>
- Colleparidi, M. (1999). Damage by delayed ettringite formation. *Concrete International*, 21(1),

- Day, R. L. (1992). *The effect of secondary ettringite formation on the durability of concrete: A literature analysis*.
- De Falco, A., Mori, M., & Sevieri, G. (2018, October 22). *Mazars' damage model for masonry structures: A case study of a church in Italy*. 2018 COMSOL Conference.
- de France, E. (1989). Finite element code aster, analysis of structures and thermomechanics for studies and research. *Open Source on Wwww. Code-Aster. Org, 2017*.
- De Nicolo, B., Pani, L., & Pozzo, E. (1994). Strain of concrete at peak compressive stress for a wide range of compressive strengths. *Materials and Structures, 27*(4), 206–210. <https://doi.org/10.1007/BF02473034>
- Dent Glasser, L. S., & Kataoka, N. (1981). The chemistry of 'alkali-aggregate' reaction. *Cement and Concrete Research, 11*(1), 1–9. [https://doi.org/10.1016/0008-8846\(81\)90003-X](https://doi.org/10.1016/0008-8846(81)90003-X)
- Deschenes, D., Bayrak, O., & Folliard, K. (2009). Shear capacity of large-scale bridge bent specimens subject to alkali-silica reaction and delayed ettringite formation. *Structures Congress 2009, 1–9*. [https://doi.org/10.1061/41031\(341\)116](https://doi.org/10.1061/41031(341)116)
- Diamond, S. (1996). Delayed ettringite formation—Processes and problems. *Cement and Concrete Composites, 18*(3), 205–215. [https://doi.org/10.1016/0958-9465\(96\)00017-0](https://doi.org/10.1016/0958-9465(96)00017-0)
- Diamond, S. (1989). ASR-another look at mechanisms. *Proc. 8th Intl. Conf. on Alkali-Aggregate Reaction, 115–119*.
- Diamond, S., & Thaulow, N. (1974). A study of expansion due to alkali—Silica reaction as conditioned by the grain size of the reactive aggregate. *Cement and Concrete Research, 4*(4), 591–607. [https://doi.org/10.1016/0008-8846\(74\)90009-X](https://doi.org/10.1016/0008-8846(74)90009-X)
- Ekolu, S. O., Thomas, M. D. A., & Hooton, R. D. (2007). Implications of pre-formed microcracking in relation to the theories of DEF mechanism. *Cement and Concrete Research, 37*(2), 161–165. <https://doi.org/10.1016/j.cemconres.2006.10.014>
- Esposito, R., & Hendriks, M. (2019). Literature review of modelling approaches for ASR in concrete: A new perspective. *European Journal of Environmental and Civil Engineering, 23*(11), 1311–1331. <https://doi.org/10.1080/19648189.2017.1347068>
- Famy, C., Scrivener, K. L., Atkinson, A., & Brough, A. R. (2002). Effects of an early or a late heat treatment on the microstructure and composition of inner C-S-H products of Portland cement mortars. *Cement and Concrete Research, 32*(2), 269–278. [https://doi.org/10.1016/S0008-8846\(01\)00670-6](https://doi.org/10.1016/S0008-8846(01)00670-6)
- Fan, S., & Hanson, J. M. (1998). Length expansion and cracking of plain and reinforced concrete prisms due to alkali-silica reaction. *Materials Journal, 95*(4), 480–487.
- Farny, J. A., & Kosmatka, S. H. (1997). *Diagnosis and control of alkali-aggregate reactions in concrete*. Portland Cement Association Skokie, IL.
- Figueira, R. B., Sousa, R., Coelho, L., Azenha, M., de Almeida, J. M., Jorge, P. A. S., & Silva, C. J. R. (2019). Alkali-silica reaction in concrete: Mechanisms, mitigation and test methods. *Construction and Building Materials, 222*, 903–931. <https://doi.org/10.1016/j.conbuildmat.2019.07.230>
- Fournier, B., Berube, M.-A., Folliard, K. J., & Thomas, M. (2010). *Report on the diagnosis, prognosis, and mitigation of alkali-silica reaction (ASR) in transportation structures (dot:42869)*. FHWA-HIF-09-004. <https://rosap.nrl.bts.gov/view/dot/42869>
- Fu, Y. (1996). *Delayed ettringite formation in Portland cement products*. [Thesis, University of Ottawa (Canada)]. <http://dx.doi.org/10.20381/ruor-7976>

- Fu, Y., Ding, J., & Beaudoin, J. (1997). Expansion of Portland cement mortar due to internal sulfate attack. *Cement and Concrete Research*, 27(9), 1299–1306.
- Gautam, B. P., & Panesar, D. K. (2017). The effect of elevated conditioning temperature on the ASR expansion, cracking and properties of reactive Spratt aggregate concrete. *Construction and Building Materials*, 140, 310–320. <https://doi.org/10.1016/j.conbuildmat.2017.02.104>
- Gautam, B. P., Panesar, D. K., Sheikh, S. A., & Vecchio, F. J. (2017). Multiaxial Expansion-Stress Relationship for Alkali Silica Reaction-Affected Concrete. *ACI Materials Journal*, 114(1). <https://doi.org/10.14359/51689490>
- Ghanaat, Y. (1993). *Theoretical manual for analysis of arch dams (Technical report ITL-93-1)*. US Army Corps of Engineers.
- Giaccio, G., Zerbino, R., Ponce, J. M., & Batic, O. R. (2008). Mechanical behavior of concretes damaged by alkali-silica reaction. *Cement and Concrete Research*, 38(7), 993–1004. <https://doi.org/10.1016/j.cemconres.2008.02.009>
- Giannini, E. R. (2012). *Evaluation of concrete structures affected by alkali-silica reaction and delayed ettringite formation* [Thesis]. <https://repositories.lib.utexas.edu/handle/2152/ETD-UT-2012-08-6081>
- Giannini, E. R., Sanchez, L. F. M., Tuinukuafe, A., & Folliard, K. J. (2018). Characterization of concrete affected by delayed ettringite formation using the stiffness damage test. *Construction and Building Materials*, 162, 253–264. <https://doi.org/10.1016/j.conbuildmat.2017.12.012>
- Godart, B., & Divet, L. (2013). Lessons learned from structures damaged by delayed ettringite formation and the French prevention strategy. *Fifth International Conference on Forensic Engineering*, 12.
- Godart, B., & Divet, L. (2017). The revision of the French recommendations for the prevention of Delayed Ettringite formation. *Proceedings of the JCI-RILEM International Workshop on Control of Cracking in Concrete Structures 5*, 10-p.
- Grattan-Bellew, P. E., Beaudoin, J. J., & Vallée, V.-G. (1998). Effect of aggregate particle size and composition on expansion of mortar bars due to delayed ettringite formation. *Cement and Concrete Research*, 28(8), 1147–1156. [https://doi.org/10.1016/S0008-8846\(98\)00084-2](https://doi.org/10.1016/S0008-8846(98)00084-2)
- Hanehara, S., Kawabata, Y., Ogawa, S., Hyodo, H., & Yoshida, N. (2019). *Technical committee on delayed ettringite formation*. 22.
- Hanehara, S., & Oyamada, T. (2010). *Reproduction of delayed ettringite formation (DEF) in concrete and relationship between DEF and alkali silica reaction*. 6.
- Hobbs, D. W. (1986). *Some tests on fourteen year old concrete affected by the alkali-silica reaction*. 7, 342–346.
- Hobbs, D. W., & Gutteridge, W. A. (1979). Particle size of aggregate and its influence upon the expansion caused by the alkali-silica reaction. *Magazine of Concrete Research*, 31(109), 235–242. <https://doi.org/10.1680/mac.1979.31.109.235>
- Hooton, R. D., Rogers, C., MacDonald, C. A., & Ramlochan, T. (2013). Twenty-year field evaluation of alkali-silica reaction mitigation. *Materials Journal*, 110(5), 539–548. <https://doi.org/10.14359/51685905>
- Huang, Q., Gardoni, P., Trejo, D., & Pagnotta, A. (2014). Probabilistic model for steel-concrete bond behavior in bridge columns affected by alkali silica reactions. *Engineering Structures*, 71, 1–11. <https://doi.org/10.1016/j.engstruct.2014.03.041>

- Imai, H., Yamasaki, T., Maehara, H., & Miyagawa, T. (1986). The deterioration by alkali-silica reaction of Hanshin expressway concrete structures—Investigation and repair. *Proceedings of the 7th International Conference on Concrete Alkali-Aggregate Reactions*.
- Islam, M. S., & Ghafoori, N. (2018). A new approach to evaluate alkali-silica reactivity using loss in concrete stiffness. *Construction and Building Materials*, *167*, 578–586. <https://doi.org/10.1016/j.conbuildmat.2018.02.047>
- Jensen, V., & Sujjavanich, S. (2016). *ASR and DEF in concrete foundations in Thailand*. 15th International Conference on Alkali-Aggregate Reaction in Concrete. São Paulo: UNES.
- Joshi, N. R., Sriprasong, T., Asamoto, S., & Sancharoen, P. (2021). Time-dependent deformation of a concrete arch dam in Thailand—Numerical study on effect of alkali silica reaction on deflection of arch. *Journal of Advanced Concrete Technology*, *19*(3), 181–195. <https://doi.org/10.3151/jact.19.181>
- JSCE. (2007). *Standard specifications for concrete structures-2007 “Design.”*
- Karthik, M. M., Mander, J. B., & Hurlbauss, S. (2016). ASR/DEF related expansion in structural concrete: Model development and validation. *Construction and Building Materials*, *128*, 238–247. <https://doi.org/10.1016/j.conbuildmat.2016.10.084>
- Karthik, M. M., Mander, J. B., & Hurlbauss, S. (2018). Experimental Behavior of Large Reinforced Concrete Specimen with Heavy ASR and DEF Deterioration. *Journal of Structural Engineering*, *144*(8), 04018110. [https://doi.org/10.1061/\(ASCE\)ST.1943-541X.0002102](https://doi.org/10.1061/(ASCE)ST.1943-541X.0002102)
- Katayama, T., Tagami, M., Sarai, Y., Izumi, S., & Hira, T. (2004). Alkali-aggregate reaction under the influence of deicing salts in the Hokuriku district, Japan. *Material Characterization*, *53*(2-4), 105–122.
- Kawabata, Y., Dunant, C., Yamada, K., & Scrivener, K. (2019). Impact of temperature on expansive behavior of concrete with a highly reactive andesite due to the alkali–silica reaction. *Cement and Concrete Research*, *125*, 105888. <https://doi.org/10.1016/j.cemconres.2019.105888>
- Kawabata, Y., Ueda, N., Miura, T., & Multon, S. (2021). The influence of restraint on the expansion of concrete due to delayed ettringite formation. *Cement and Concrete Composites*, *121*, 104062. <https://doi.org/10.1016/j.cemconcomp.2021.104062>
- Kawabata, Y., Yamada, K., Ogawa, S., & Sagawa, Y. (2021). Mechanisms of internal swelling reactions: Recent advances and future research needs. *Bridge Maintenance, Safety, Management, Life-Cycle Sustainability and Innovations*, 2599–2607.
- Kelham, S. (1996). The effect of cement composition and fineness on expansion associated with delayed ettringite formation. *Cement and Concrete Composites*, *18*(3), 171–179. [https://doi.org/10.1016/0958-9465\(95\)00013-5](https://doi.org/10.1016/0958-9465(95)00013-5)
- Kelham, S. (1997). *Effect of cement composition and hydration temperature on volume stability of mortar*. 4, 4.
- Kelham, S. (2004). Effects of cement parameters on expansion associated with DEF. *International RILEM Workshop on Internal Sulfate Attack and Delayed Ettringite Formation*, 197–211.
- Kreitman, K. L. (2011). *Nondestructive evaluation of reinforced concrete structures affected by alkali-silica reaction and delayed ettringite formation*.
- Kuroda, T., Inoue, S., Yoshino, A., Nishibayashi, S., & Miyagawa, T. (2008). Effects of accelerated test conditions on ASR expansion of concrete core. *Dimension*, *40*(60), 80.

- Larive, C., & Laboratoire Central des Ponts et Chaussées, 75-Paris (France); (1998). *Combined contribution of experimentation and modeling to the understanding of the Alkali Reaction and its mechanical effects*.
- Larsen, S., Lindgård, J., Thorenfeldt, E., Rodum, E., & Haugen, M. (2008). *Experiences from extensive condition survey and FEM-analyses of two norwegian concrete dams with ASR*. Proceedings of the 13th International Conference on Alkali-Aggregate Reaction in Concrete, Citeseer, Trondheim, Norway.
- Lawrence, B. L., Moody, E. D., Guillemette, R. N., & Carrasquillo, R. L. (1999). Evaluation and mitigating measures for premature concrete distress in Texas Department of Transportation concrete elements. *Cement, Concrete and Aggregates*, 21(1), 73–81.
- Li, P., Tan, N., An, X., Maekawa, K., & Jiang, Z. (2020). Restraint effect of reinforcing bar on ASR expansion and deterioration characteristic of the bond behavior. *Journal of Advanced Concrete Technology*, 18(4), 192–210.
- Li, Z., Afshinnia, K., & Rangaraju, P. R. (2016). Effect of alkali content of cement on properties of high performance cementitious mortar. *Construction and Building Materials*, 102, 631–639. <https://doi.org/10.1016/j.conbuildmat.2015.10.110>
- Locher, F., & Sprung, S. (1973). Ursache und Wirkungsweise der Alkalireaktion. *Beton*, 7, 303–306.
- Lothenbach, B., Matschei, T., Möschner, G., & Glasser, F. P. (2008). Thermodynamic modelling of the effect of temperature on the hydration and porosity of Portland cement. *Cement and Concrete Research*, 38(1), 1–18. <https://doi.org/10.1016/j.cemconres.2007.08.017>
- Ma, K., Long, G., & Xie, Y. (2017). A real case of steam-cured concrete track slab premature deterioration due to ASR and DEF. *Case Studies in Construction Materials*, 6, 63–71. <https://doi.org/10.1016/j.cscm.2016.12.001>
- Mac, M. J., Yio, M. H. N., Wong, H. S., & Buenfeld, N. R. (2021). Analysis of autogenous shrinkage-induced microcracks in concrete from 3D images. *Cement and Concrete Research*, 144, 106416. <https://doi.org/10.1016/j.cemconres.2021.106416>
- Mardia, K. V., & Hainsworth, T. J. (1988). A spatial thresholding method for image segmentation. *IEEE Transactions on Pattern Analysis and Machine Intelligence*, 10(6), 919–927. <https://doi.org/10.1109/34.9113>
- Martin, R. P., Bazin, C., Billo, J., Estivin, M., Renaud, J. C., & Toutlemonde, F. (2012). Experimental evidence for understanding DEF Sensitivity to early-age thermal history. *RILEM-JCI International Workshop on Crack Control of Mass Concrete and Related Issues Concerning Early-Age of Concrete Structures*, 10p.
- Martin, R. P., Sanchez, L., Fournier, B., & Toutlemonde, F. (2017). Evaluation of different techniques for the diagnosis & prognosis of Internal Swelling Reaction (ISR) mechanisms in concrete. *Construction and Building Materials*, 156, 956–964. <https://doi.org/10.1016/j.conbuildmat.2017.09.047>
- Marzouk, H., & Langdon, S. (2003). The effect of alkali-aggregate reactivity on the mechanical properties of high and normal strength concrete. *Cement and Concrete Composites*, 25(4), 549–556. [https://doi.org/10.1016/S0958-9465\(02\)00094-X](https://doi.org/10.1016/S0958-9465(02)00094-X)
- Mazars, J., & Pijaudier-Cabot, G. (1989). Continuum damage theory—Application to concrete. *Journal of Engineering Mechanics*, 115(2), 345–365. [https://doi.org/10.1061/\(ASCE\)0733-9399\(1989\)115:2\(345\)](https://doi.org/10.1061/(ASCE)0733-9399(1989)115:2(345))
- Mindess, S., & Young, J. F. (1981). *Concrete* (2nd ed.). Prentice-Hall.

- Miura, T., Sato, K., & Nakamura, H. (2020). The role of microcracking on the compressive strength and stiffness of cracked concrete with different crack widths and angles evaluated by DIC. *Cement and Concrete Composites*, *114*, 103768. <https://doi.org/10.1016/j.cemconcomp.2020.103768>
- Miyagawa, T., Seto, K., Sasaki, K., Mikata, Y., Kuzume, K., & Minami, T. (2006). Fracture of reinforcing steels in concrete structures damaged by alkali-silica reaction-Field survey, mechanism and maintenance. *Journal of Advanced Concrete Technology*, *4*(3), 339–355. <https://doi.org/10.3151/jact.4.339>
- Mohammadi, A., Ghiasvand, E., & Nili, M. (2020). Relation between mechanical properties of concrete and alkali-silica reaction (ASR); a review. *Construction and Building Materials*, *258*, 119567. <https://doi.org/10.1016/j.conbuildmat.2020.119567>
- Monette, L. J., Gardner, N. J., & Grattan-Bellew, P. E. (2002). Residual strength of reinforced concrete beams damaged by alkali-silica reaction—Examination of damage rating index method. *Materials Journal*, *99*(1), 42–50. <https://doi.org/10.14359/11315>
- Morenon, P., Multon, S., Sellier, A., Grimal, E., Hamon, F., & Bourdarot, E. (2017). Impact of stresses and restraints on ASR expansion. *Construction and Building Materials*, *140*, 58–74. <https://doi.org/10.1016/j.conbuildmat.2017.02.067>
- Mullick, A. (1991). Alkali-silica reaction—Indian experience. *The Alkali-Silica Reaction in Concrete*, 307.
- Multon, S., Seignol, J.-F., & Toutlemonde, F. (2005). Structural behavior of concrete beams affected by alkali-silica reaction. *ACI Materials Journal*, *102*(2), 67.
- Multon, S., & Toutlemonde, F. (2010). Effect of moisture conditions and transfers on alkali silica reaction damaged structures. *Cement and Concrete Research*, *40*(6), 924–934. <https://doi.org/10.1016/j.cemconres.2010.01.011>
- Munir, M. J., Abbas, S., Qazi, A. U., Nehdi, M. L., & Kazmi, S. M. S. (2017). Role of test method in detection of alkali-silica reactivity of concrete aggregates. *Proceedings of the Institution of Civil Engineers - Construction Materials*, *171*(5), 203–221. <https://doi.org/10.1680/jcoma.16.00058>
- Nanayakkara, A. (2011). *Importance of controlling temperature rise due to heat of hydration in massive concrete elements*. 8.
- Natesaiyer, K., & Hover, K. C. (1988). In situ identification of ASR products in concrete. *Cement and Concrete Research*, *18*(3), 455–463. [https://doi.org/10.1016/0008-8846\(88\)90080-4](https://doi.org/10.1016/0008-8846(88)90080-4)
- Neville, A. M. (1996). *Properties of concrete*. John Wiley & Sons.
- Oberholster, R. E., & Davies, G. (1986). An accelerated method for testing the potential alkali reactivity of siliceous aggregates. *Cement and Concrete Research*, *16*(2), 181–189. [https://doi.org/10.1016/0008-8846\(86\)90134-1](https://doi.org/10.1016/0008-8846(86)90134-1)
- Odler, I. (1981). *Interaction between gypsum and the CSH phase formed in C3S hydration*. *4*, 493–495.
- Pan, J., Feng, Y., Xu, Y., Jin, F., Zhang, C., & Zhang, B. (2013). Chemo-damage modeling and cracking analysis of AAR-affected concrete dams. *Science China Technological Sciences*, *56*(6), 1449–1457.
- Pituba, J. J. C., & Lacerda, M. M. S. (2012). Simplified damage models applied in the numerical analysis of reinforced concrete structures. *Revista IBRACON de Estruturas e Materiais*, *5*(1), 26–37. <https://doi.org/10.1590/S1983-41952012000100004>
- Pourbehi, M. S., & van Zijl, G. P. A. G. (2019). Seismic analysis of the Kleinplaas dam affected

- by alkali-silica reaction using a chemo-thermo-mechanical finite element numerical model considering fluid structure interaction. *Journal of Advanced Concrete Technology*, 17(8), 462–473. <https://doi.org/10.3151/jact.17.462>
- Powter, A. (1978). History, deterioration, and repair of cement and concrete in nineteenth century fortifications constructed by the Royal Engineers. *Bulletin of the Association for Preservation Technology*, 10(3), 59. <https://doi.org/10.2307/1493668>
- Price, W. H. (1951). Factors influencing concrete strength. *Journal Proceedings*, 47(2), 417–432. <https://doi.org/10.14359/12003>
- Ramlochan, T., Zacarias, P., Thomas, M. D. A., & Hooton, R. D. (2003). The effect of pozzolans and slag on the expansion of mortars cured at elevated temperature: Part I: Expansive behaviour. *Cement and Concrete Research*, 33(6), 807–814. [https://doi.org/10.1016/S0008-8846\(02\)01066-9](https://doi.org/10.1016/S0008-8846(02)01066-9)
- Rivard, P., Fournier, B., & Ballivy, G. (2000). Quantitative petrographic technique for concrete damage due to ASR: Experimental and application. *Cement, Concrete and Aggregates*, 22(1), 63–72. <https://doi.org/10.1520/CCA10465J>
- Rocco, C., Giandrasso, F., Bergol, L., Di Pace, G., & Planas, J. (2004). *Fracture properties of concrete exposure to delayed ettringite formation*. 1–8.
- Roth, S.-N., & Dolice, D. (2017). *Thermal cracking of a concrete arch dam*. 6–8.
- Sahu, S., & Thaulow, N. (2004). Delayed ettringite formation in Swedish concrete railroad ties. *Cement and Concrete Research*, 34(9), 1675–1681. <https://doi.org/10.1016/j.cemconres.2004.01.027>
- Sanchez, L. F. M., Drimalas, T., Fournier, B., Mitchell, D., & Bastien, J. (2018). Comprehensive damage assessment in concrete affected by different internal swelling reaction (ISR) mechanisms. *Cement and Concrete Research*, 107, 284–303. <https://doi.org/10.1016/j.cemconres.2018.02.017>
- Sanchez, L. F. M., Fournier, B., Jolin, M., Bastien, J., & Mitchell, D. (2016). Practical use of the Stiffness Damage Test (SDT) for assessing damage in concrete infrastructure affected by alkali-silica reaction. *Construction and Building Materials*, 125, 1178–1188. <https://doi.org/10.1016/j.conbuildmat.2016.08.101>
- Saouma, V., Martin, R. A., Hariri-Ardebili, M. A., & Katayama, T. (2015). A mathematical model for the kinetics of the alkali-silica chemical reaction. *Cement and Concrete Research*, 68, 184–195. <https://doi.org/10.1016/j.cemconres.2014.10.021>
- Saouma, V., Perotti, L., & Shimpo, T. (2007). Stress analysis of concrete structures subjected to alkali-aggregate reactions. *ACI Structural Journal*, 104(5), 532–541.
- Schindelin, J., Arganda-Carreras, I., Frise, E., Kaynig, V., Longair, M., Pietzsch, T., Preibisch, S., Rueden, C., Saalfeld, S., Schmid, B., Tinevez, J.-Y., White, D. J., Hartenstein, V., Eliceiri, K., Tomancak, P., & Cardona, A. (2012). Fiji: An open-source platform for biological-image analysis. *Nature Methods*, 9(7), 676–682. <https://doi.org/10.1038/nmeth.2019>
- Scrivener, K., & Lewis, M. (1997). *A microstructural and microanalytical study of heat cured mortars and delayed ettringite formation*. 4, 4iv061.
- Seignol, J.-F., & Baghdadi, N. (2009). *A macroscopic chemo-mechanical model aimed at re-assessment of delayed-ettringite-formation affected concrete structures*. 20.
- Sellier, A., Grimal, É., Multon, S., & Bourdarot, E. (2017). *Swelling concrete in dams and hydraulic structures: DSC 2017*. John Wiley & Sons.
- Shayan, A., & Ivanusec, I. (1996). An experimental clarification of the association of delayed

- ettringite formation with alkali-aggregate reaction. *Cement and Concrete Composites*, 18(3), 161–170. [https://doi.org/10.1016/0958-9465\(96\)00012-1](https://doi.org/10.1016/0958-9465(96)00012-1)
- Shayan, A., & Quick, G. (1994). *Alkali-aggregate reaction in concrete railway sleepers from Finland*.
- Shi, Z., Shi, C., Wan, S., & Ou, Z. (2017). Effect of alkali dosage on alkali-silica reaction in sodium hydroxide activated slag mortars. *Construction and Building Materials*, 143, 16–23. <https://doi.org/10.1016/j.conbuildmat.2017.03.125>
- Shimada, Y. (2005). *Chemical path of ettringite formation in heat-cured mortar and its relationship to expansion*.
- Sims, I., & Poole, A. B. (2017). *Alkali-aggregate reaction in concrete: A world review*. CRC Press.
- Skarżyński, Ł., Marzec, I., & Tejchman, J. (2019). Fracture evolution in concrete compressive fatigue experiments based on X-ray micro-CT images. *International Journal of Fatigue*, 122, 256–272. <https://doi.org/10.1016/j.ijfatigue.2019.02.002>
- Smaoui, N., Bérubé, M. A., Fournier, B., Bissonnette, B., & Durand, B. (2005). Effects of alkali addition on the mechanical properties and durability of concrete. *Cement and Concrete Research*, 35(2), 203–212. <https://doi.org/10.1016/j.cemconres.2004.05.007>
- Souris, M. (2000). *Thailand meteorological datas*. <http://www.savgis.org/thailand.htm#>
- Sriprasong, T. (2020). *Expansion mechanism associated with ASR and DEF and numerical analysis of mass concrete dam time-dependent deformation by ASR expansion*.
- Sriprasong, T., Asamoto, S., & Joshi, N. R. (2020). Study on the combined alkali silica reaction and delayed ettringite formation. *International Journal of GEOMATE*, 19(75), 84–91. <https://doi.org/10.21660/2020.75.38051>
- Stark, J., & Bollmann, K. (1999). *Delayed ettringite formation in concrete*.
- Stefan, H. G., & Preud'homme, E. B. (1993). Stream temperature estimation from air temperature. *Journal of the American Water Resources Association*, 29(1), 27–45. <https://doi.org/10.1111/j.1752-1688.1993.tb01502.x>
- Steffens, A., Li Kefei, & Coussy Olivier. (2003). Aging approach to water effect on alkali-silica reaction degradation of structures. *Journal of Engineering Mechanics*, 129(1), 50–59. [https://doi.org/10.1061/\(ASCE\)0733-9399\(2003\)129:1\(50\)](https://doi.org/10.1061/(ASCE)0733-9399(2003)129:1(50))
- Stoev, K. (2012). *Comparison of radiographic image processing algorithms*. Atomic Energy of Canada Limited.
- Structural effects of alkali-silica reaction*. (1992). The Institution of Structural Engineers. <https://www.istructe.org/resources/guidance/structural-effects-alkali-silica-reaction/>
- Sujjavanich, S. (2017). Investigation of potential alkali-silica reactivity of aggregate sources in Thailand. *International Journal of GEOMATE*, 13(35), 108–113. <https://doi.org/10.21660/2017.35.6712>
- Sujjavanich, S., Won-In, K., Wongkhamchan, W., & Dararutana, P. (2012). The application of fluoresced gel for the first Alkali Silica Reaction evidence in Thailand. *Advanced Materials Research*, 368(373), 613–616. <https://doi.org/10.4028/www.scientific.net/AMR.368-373.613>
- Swamy, R. N., & Al-Asali, M. M. (1986). Influence of alkali-silica reaction on the engineering properties of concrete. In *Alkalies in Concrete*. ASTM International.
- Talley, K. G. (2009). *Assessment and strengthening of ASR and DEF affected concrete bridge columns*.
- Taylor, H. F. W., Famy, C., & Scrivener, K. L. (2001). Delayed ettringite formation. *Cement*

- and Concrete Research*, 31(5), 683–693. [https://doi.org/10.1016/S0008-8846\(01\)00466-5](https://doi.org/10.1016/S0008-8846(01)00466-5)
- Thiebaut, Y., Multon, S., Sellier, A., Lacarriere, L., Boutillon, L., Belili, D., Linger, L., Cussigh, F., & Hadji, S. (2018). *Effects of delayed ettringite formation on reinforced concrete structures*. <https://hal.insa-toulouse.fr/hal-02155138>
- Thomas, M. (1998). Delayed ettringite formation in concrete: Recent developments and future directions. *American Ceramic Society, Inc., Materials Science of Concrete VI(USA), 2001*, 435–481.
- Thomas, M., Folliard, K., Drimalas, T., & Ramlochan, T. (2008). Diagnosing delayed ettringite formation in concrete structures. *Cement and Concrete Research*, 38(6), 841–847. <https://doi.org/10.1016/j.cemconres.2008.01.003>
- Thomas, M., Folliard, K. J., Fournier, B., Rivard, P., Drimalas, T., & Garber, S. I. (2013). *Methods for evaluating and treating ASR-affected structures: Results of field application and demonstration projects: Volume I-Summary of findings and recommendations*. United States. Federal Highway Administration.
- Thomas, P., Ha Hau, V., Vessalas, K., Sirivivatnanon, V., & South, W. (2019). *Assessment of aggregate reactivity using slurry tests*. 29th Biennial National Conference of the Concrete Institute of Australia.
- Thongthamchart, C., & Raphitphan, N. (n.d.). *Performance of Bhumibol concrete arch dam after 50 years of operation*.
- Tomczak, K., Jakubowski, J., & Fiołek, P. (2017). Method for assessment of changes in the width of cracks in cement composites with use of computer image processing and analysis. *Studia Geotechnica et Mechanica*, 39(2), 73–80. <https://doi.org/10.1515/sgem-2017-0017>
- Tosun, K. (2006). Effect of SO₃ content and fineness on the rate of delayed ettringite formation in heat cured Portland cement mortars. *Cement and Concrete Composites*, 28(9), 761–772. <https://doi.org/10.1016/j.cemconcomp.2006.06.003>
- Tracy, S. L., Boyd, S. R., & Connolly, J. D. (2004). Effect of curing temperature and cement chemistry on the potential for concrete expansion due to DEF. *PCI Journal*, 49(1), 46–57. <https://doi.org/10.15554/pcij.01012004.46.57>
- Ulm, F.-J., Coussy, O., Kefei, L., & Larive, C. (2000). Thermo-chemo-mechanics of ASR expansion in concrete structures. *Journal of Engineering Mechanics*, 126(3), 233–242. [https://doi.org/10.1061/\(ASCE\)0733-9399\(2000\)126:3\(233\)](https://doi.org/10.1061/(ASCE)0733-9399(2000)126:3(233))
- Wang, Y., Meng, Y., Jiradilok, P., Matsumoto, K., Nagai, K., & Asamoto, S. (2019). Expansive cracking and compressive failure simulations of ASR and DEF damaged concrete using a mesoscale discrete model. *Cement and Concrete Composites*, 104, 103404. <https://doi.org/10.1016/j.cemconcomp.2019.103404>
- Wood, J., Young, J. S., & Ward, D. E. (1986). The structural effects of alkali-aggregate reaction on reinforced concrete. *Proceedings of the 7th International Conference on Concrete Alkali-Aggregate Reactions*. <https://trid.trb.org/view/296502>
- Xi, Y., Bažant, Z. P., Molina, L., & Jennings, H. M. (1994). Moisture diffusion in cementitious materials Moisture capacity and diffusivity. *Advanced Cement Based Materials*, 1(6), 258–266. [https://doi.org/10.1016/1065-7355\(94\)90034-5](https://doi.org/10.1016/1065-7355(94)90034-5)
- Yamada, K., Hirono, S., & Ando, Y. (2013). ASR problems in Japan and a message for ASR problems in Thailand. *Journal of Thailand Concrete Association*, 1(2), 1–18.
- Yan, P., Zheng, F., Peng, J., & Qin, X. (2004). Relationship between delayed ettringite

- formation and delayed expansion in massive shrinkage-compensating concrete. *Cement and Concrete Composites*, 26(6), 687–693. [https://doi.org/10.1016/S0958-9465\(03\)00060-X](https://doi.org/10.1016/S0958-9465(03)00060-X)
- Yin, W., Zhao, E., Gu, C., Huang, H., & Yang, Y. (2019). A nonlinear method for component separation of dam effect quantities using kernel partial least squares and pseudosamples. *Advances in Civil Engineering*. <https://doi.org/10.1155/2019/1958173>
- Yurtdas, I., Chen, D., Hu, D. W., & Shao, J. F. (2013). Influence of alkali silica reaction (ASR) on mechanical properties of mortar. *Construction and Building Materials*, 47, 165–174. <https://doi.org/10.1016/j.conbuildmat.2013.04.046>
- Zhang, P., Lu, S., Li, J., Zhang, P., Xie, L., Xue, H., & Zhang, J. (2017). Multi-component segmentation of X-ray computed tomography (CT) image using multi-Otsu thresholding algorithm and scanning electron microscopy. *Energy Exploration & Exploitation*, 35(3), 281–294. <https://doi.org/10.1177/0144598717690090>
- Zhang, Z., Olek, J., & Diamond, S. (2002a). Studies on delayed ettringite formation in early-age, heat-cured mortars: I. Expansion measurements, changes in dynamic modulus of elasticity, and weight gains. *Cement and Concrete Research*, 32(11), 1729–1736. [https://doi.org/10.1016/S0008-8846\(02\)00862-1](https://doi.org/10.1016/S0008-8846(02)00862-1)
- Zhang, Z., Olek, J., & Diamond, S. (2002b). Studies on delayed ettringite formation in heat-cured mortars: II. Characteristics of cement that may be susceptible to DEF. *Cement and Concrete Research*, 32(11), 1737–1742. [https://doi.org/10.1016/S0008-8846\(02\)00894-3](https://doi.org/10.1016/S0008-8846(02)00894-3)

Acknowledgement

First and foremost, I would like to express my deep gratitude to my supervisor Assoc. Prof. Dr. Shingo Asamoto for his continuous support, patience, kindness, motivation, enthusiasm, and understanding throughout my PhD study. His guidance helped me throughout the research and writing of the thesis and journal papers. Moreover, I am grateful to him for pushing me to do better, to improve myself and to become a competent researcher. I will always remember his word that getting a PhD is only a beginning of a research carrier. His encouragement has greatly increased my devotion for science and engineering.

I am also grateful to my dissertation committees, Prof. Dr. Takashi Maki, Prof. Dr. Yasunao Matsumoto and Prof. Dr. Masahiko Osada, for their kind support, valuable feedback, and profound ideas for this research work. I also thank Asst. Prof. Dr. Chandra Shekhar Goit for inspiring and training to use Code-Aster for the research activities. It has given a deeper understanding of FEM. Support from Asst. Prof. Dr. Yao Luan was always an inspiration.

I would like to extend my gratitude to Dr. Yuichiro Kawabata from Port and Airport Research Institute Japan (PARI) for providing the reactive aggregate for the experiment and allowing us to use equipment for X-ray CT analysis. A brief yet thoughtful discussion with Dr. Miura Taito inspired to seek perfection.

My special thanks go to all lab members over the last three years. Although due to Covid19, the social life was halted, the interaction with lab members fulfilled the gaps. I want to extend my special thanks to Ayumu Matsumoto for his support during the experimental works. I also want to thank my senior and colleague Dr. Thanadet Sriprasong for a wonderful collaboration and Dr. Dagvabazar Gombosuren for various discourses in the lab. Prasanthan Thiyagaraja kindly helped to proof read the final manuscript. The thoughtful discussion with Dr. Nabaraj Shrestha and Dr. Arjun Baniya on various topics was always useful whenever I was stuck in a problem.

I would also like to thank my teachers in Nepal for their effort to plant the seed of education in me.

Similarly, my gratitude goes to MEXT, for their financial support to carry out the research.

Last but not the least, my heartfelt thanks go to my mother, sister and Nilar for their unconditional love, patience and support.

Joshi Nirmal Raj
Saitama University, Japan

Appendix

- Effect of cement type on the free expansion
- Photographs of specimens of Chapter 3 (Internal restrains)
- Photographs of specimens of Chapter 4 (External restrains)
- Photographs of specimens of Chapter 5 (Bond test)
- Alternate analysis of prism based on random nodes
- Sample code for analysis in Code-Aster
- List of some infrastructures infected by internal expansion reaction

A. Effect of cement type on the free expansion

The effect of cement type in expansion, elasticity and mass gain by comparing the findings of the experiment of Chapter 1 with that of Sriprasong et al. (2020) are shown in Figure A1, Figure A2 and Figure A3 respectively. Sriprasong et al.'s specimens were prepared with OPC having a composition shown in Table A1.

It can be observed in Figure A1 that in the case of ASR, the expansion for the HPC case was smaller even though the alkali content was higher. The clear reason for such behaviour is not understood. One possible reason for the larger expansion in the OPC case could be contributed by the higher content of MgO as indicated in Table A1 (1.48% for HPC and 2.34% in OPC). In the case of DEF and DA, it was observed that in the early stage (up to about 300 days) HPC could instigate much higher expansion. The difference, however, became smaller for the DEF specimen made by OPC because it started to expand again after about 300 days. This means that the DEF expansion is inhibited by OPC and it can manifest later when favourable conditions are met.

The change in elasticity was rapid for HPC as shown in Figure A2; the effect was significant for DA specimens, however, in ASR specimens, the behaviour was not noticeable. The mass gain for HPC cement was also higher for the specimen with HPC cement than OPC cement.

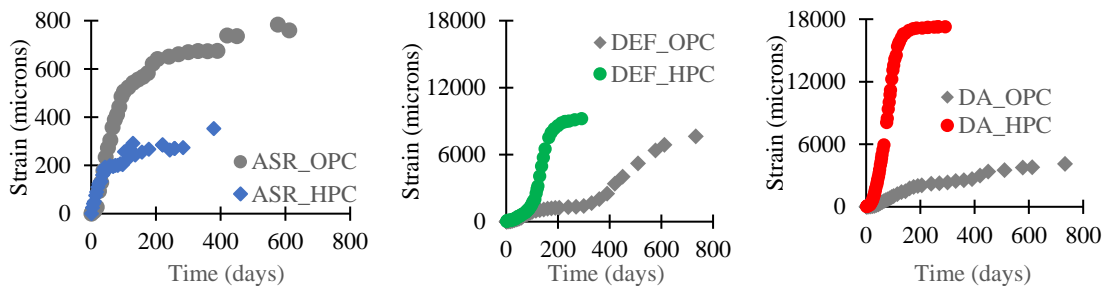


Figure A1 Comparison of strain evolution in (a) ASR, (b) DEF and (c) DA specimens for OPC and HPC

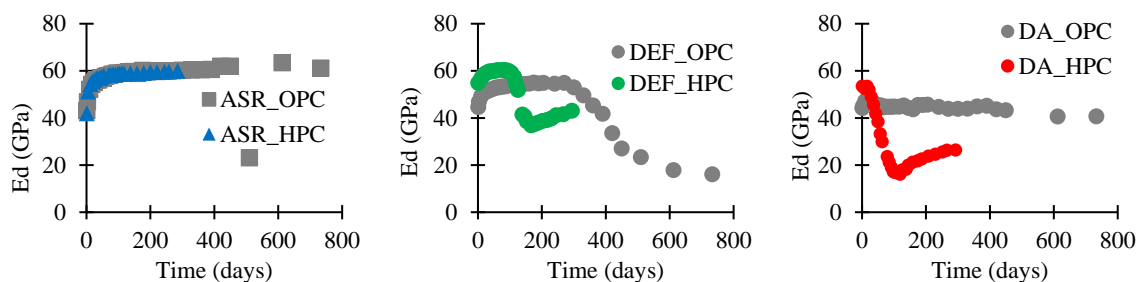


Figure A2 Comparison of dynamic modulus of elasticity (E_d) evolution in (a) ASR, (b) DEF and (c) DA specimens for OPC and HPC

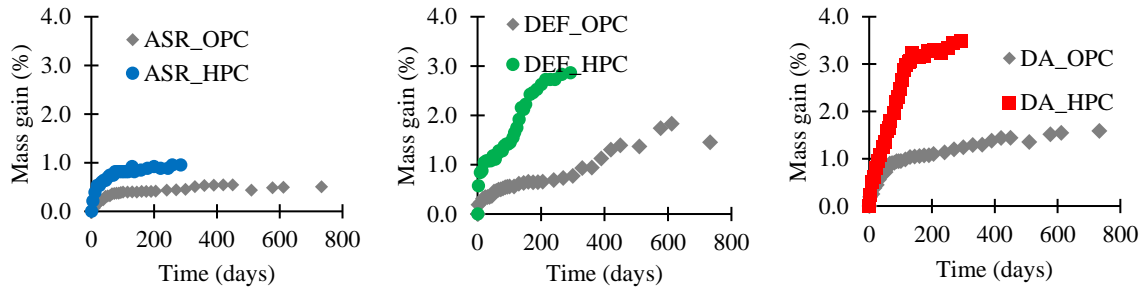


Figure A3 Comparison of mass gain evolution in (a) ASR, (b) DEF and (c) DA specimens for OPC and HPC

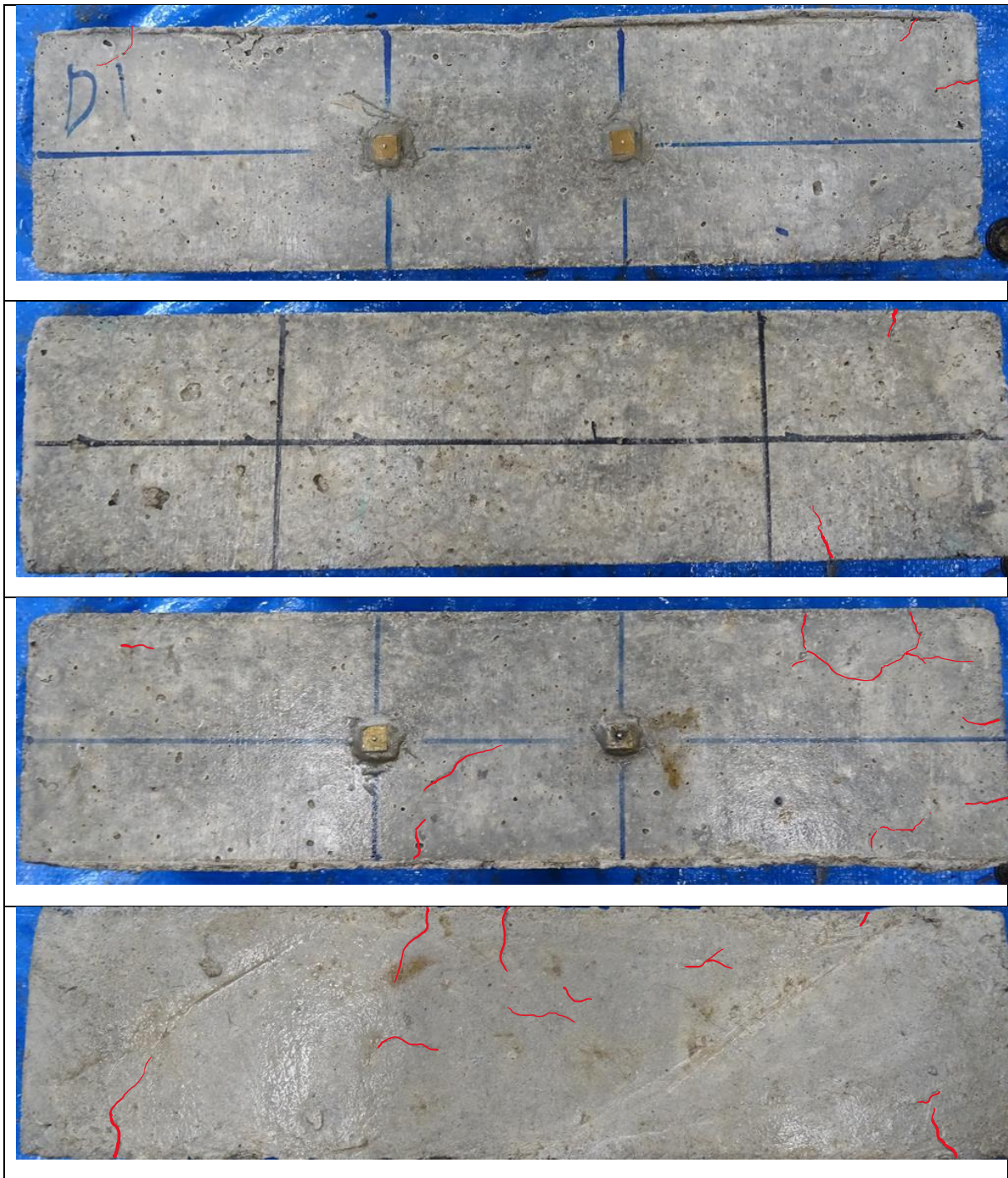
Table A1 Cement composition

SN	Chemical composition	Percentage by mass	
		HPC	OPC
1	Loss on ignition (ig.loss)	0.77	2.25
2	Silicon Dioxide (SiO ₂)	20.49	20.61
3	Aluminum Oxide (Al ₂ O ₃)	5.13	5.11
4	Iron Oxide (Fe ₂ O ₃)	2.58	3.04
5	Calcium Oxide (CaO)	64.82	64.27
6	Magnesium Oxide (MgO)	1.48	0.95
7	Sulphur Trioxide (SO ₃)	3.01	2.05
8	Sodium Oxide (Na ₂ O)	0.30	0.35
9	Potassium Oxide (K ₂ O)	0.38	0.30
10	Chloride (Cl ⁻)	0.005	0.023

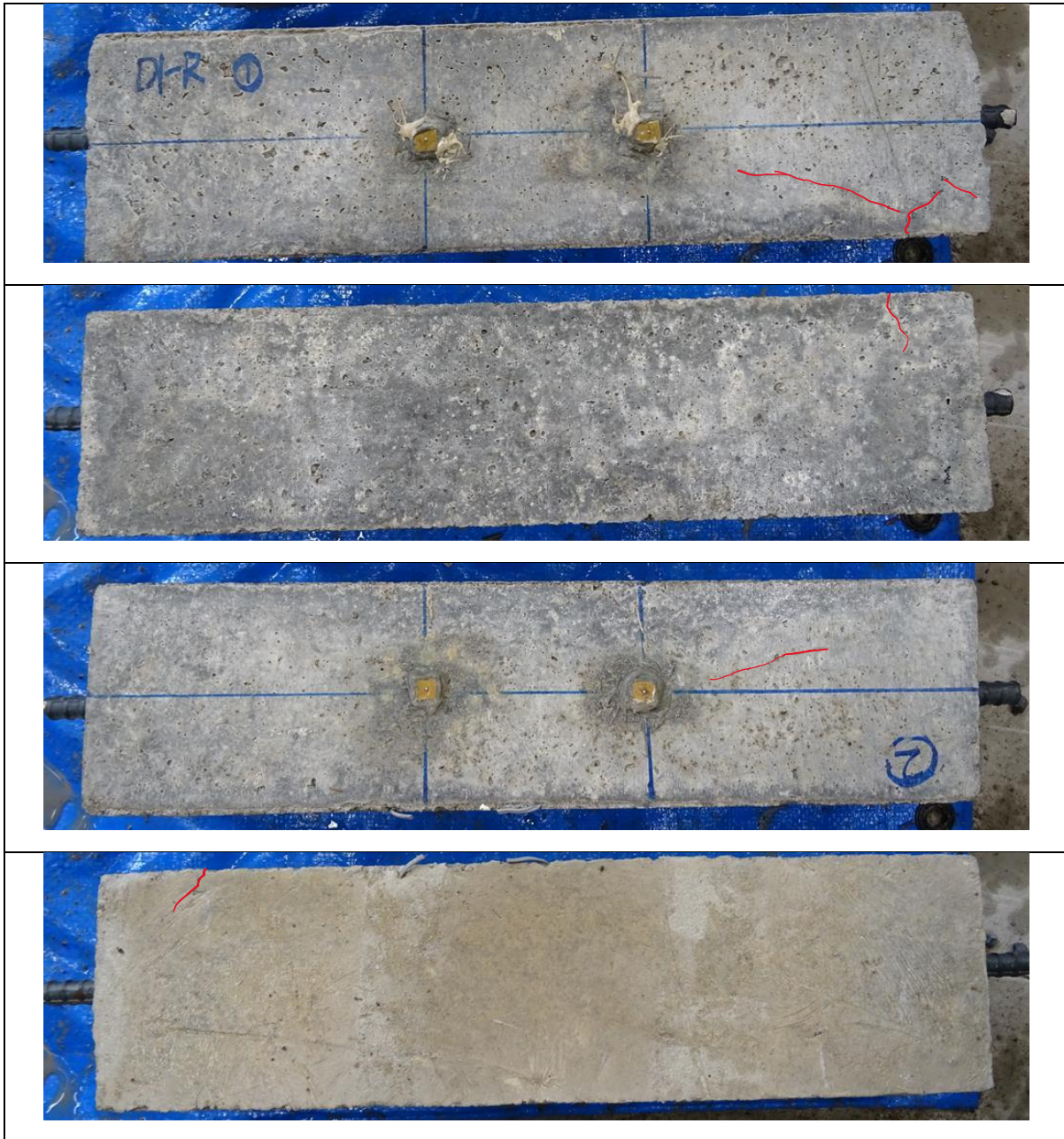
B. Photographs of specimens of Chapter 3 (Internal restrains)

Some selected specimens are shown in the photos below

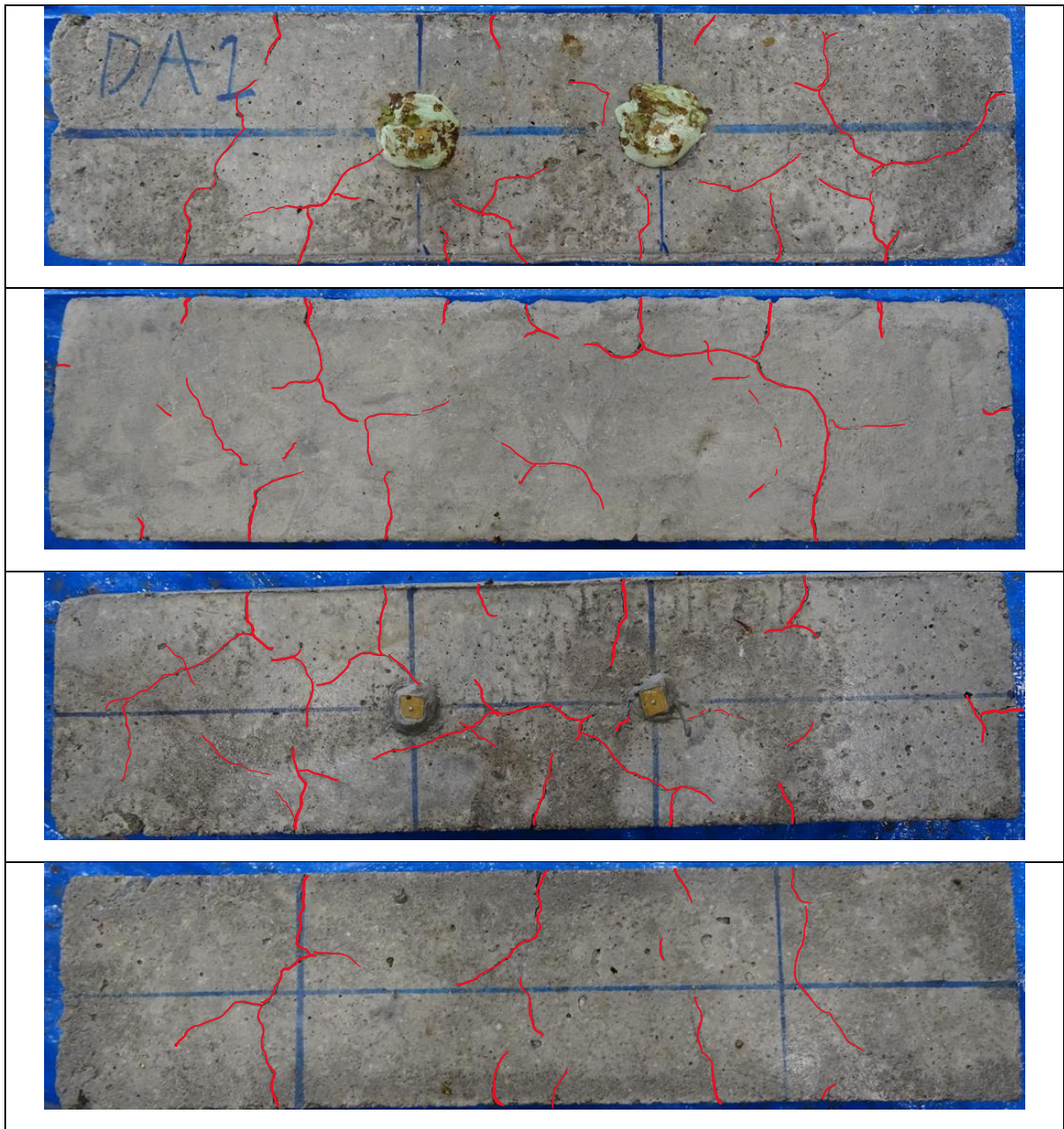
Specimen DEF Unreinforced (100 x 100 x 400 m)



Specimen DEF reinforced (100 x 100 x 400 m)



Specimen ASR+DEF Unreinforced (100 x 100 x 400 m)

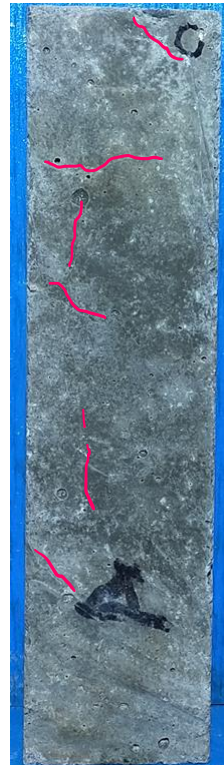


Specimen ASR+DEF Reinforced (100 x 100 x 400 m)



C. Photographs of specimens of Chapter 4 (External restrains)

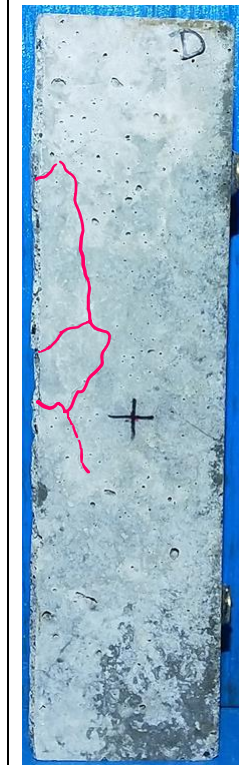
Free expansion specimens (40x40x160 mm)

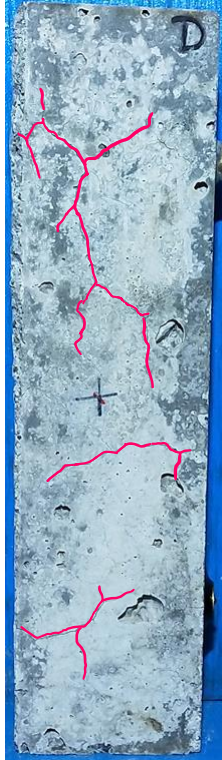
ASR1	Side 1	Side 2	Side 3	Side 4
				

ASR2	Side 1	Side 2	Side 3	Side 4
				

ASR3	Side 1	Side 2	Side 3	Side 4
				

DEF1	Side 1	Side 2	Side 3	Side 4
				

DEF2	Side 1	Side 2	Side 3	Side 4
				

DEF3	Side 1	Side 2	Side 3	Side 4
				

DA1	Side 1	Side 2	Side 3	Side 4
				

DA2	Side 1	Side 2	Side 3	Side 4
				

DA3	Side 1	Side 2	Side 3	Side 4
				

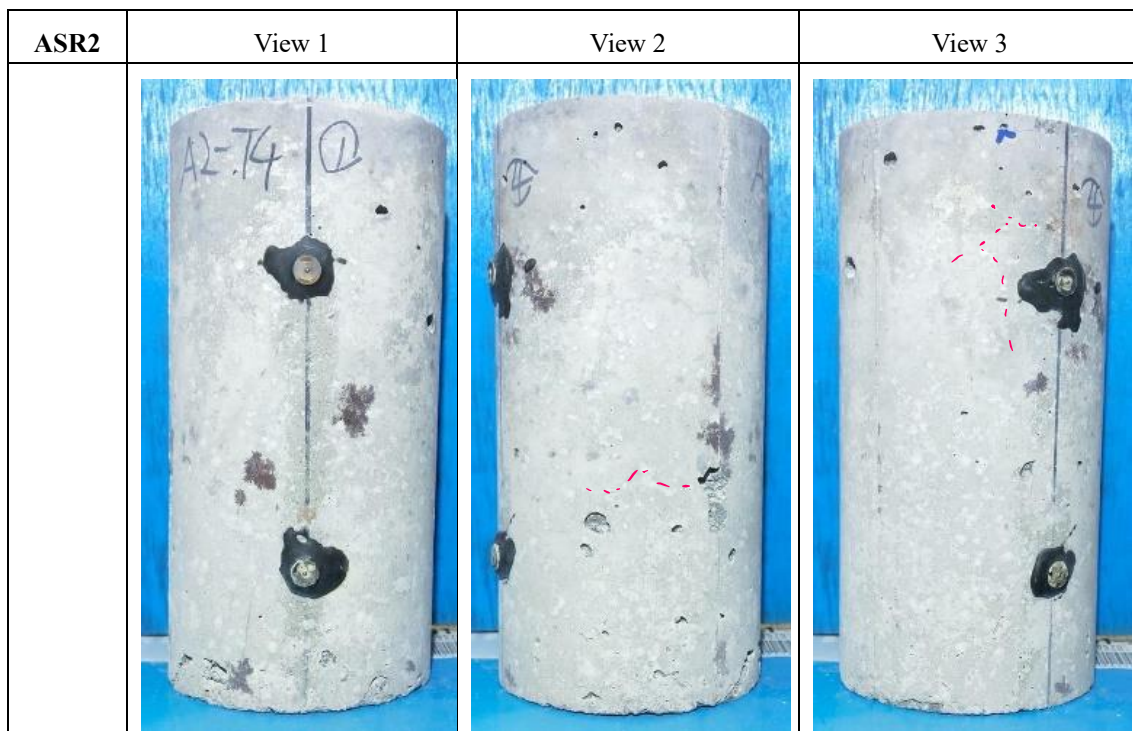
Restrained specimens (40x40x160 mm)

No cracks were seen in Normal and ASR specimens

Specimen	DEF specimens	DA specimens
DEF 4		
DEF 5		
DEF 6		

D. Photographs of specimens of Chapter 5 (Bond test)

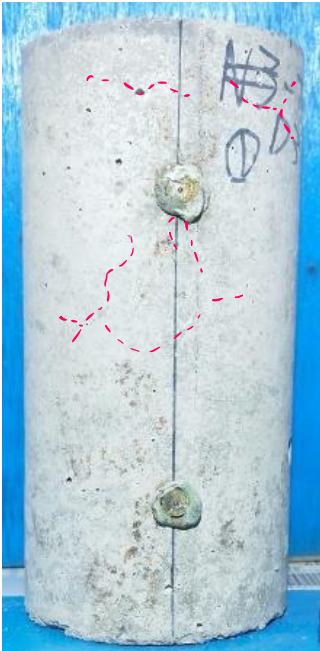
Cylindrical specimens (At 150 days)

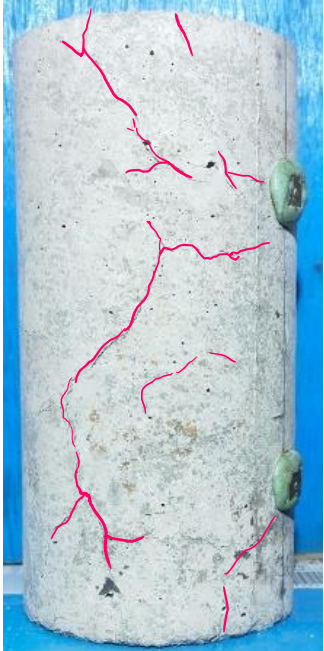
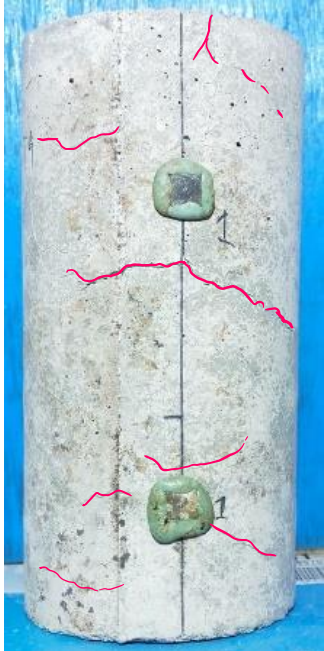


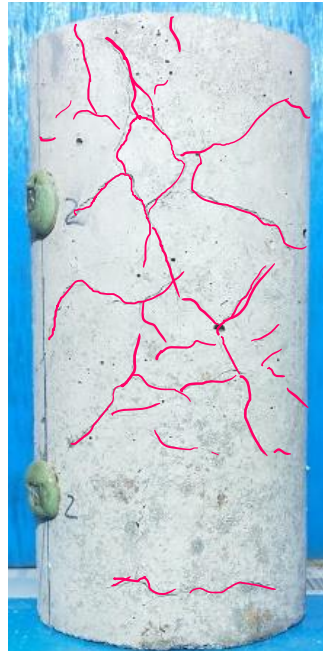
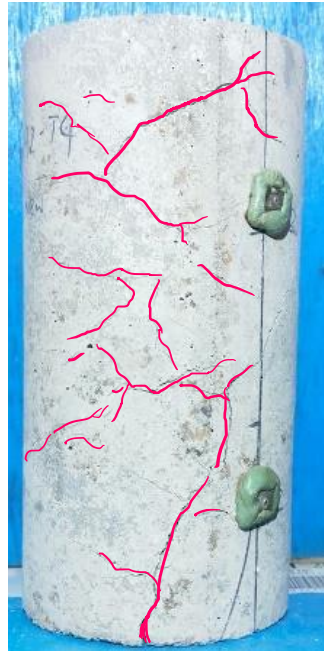
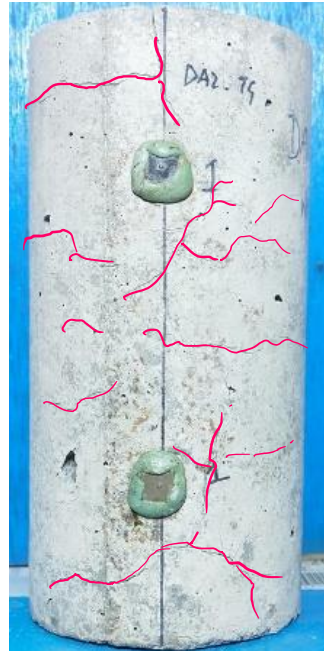
ASR 3	View 1	View 2	View 3
			

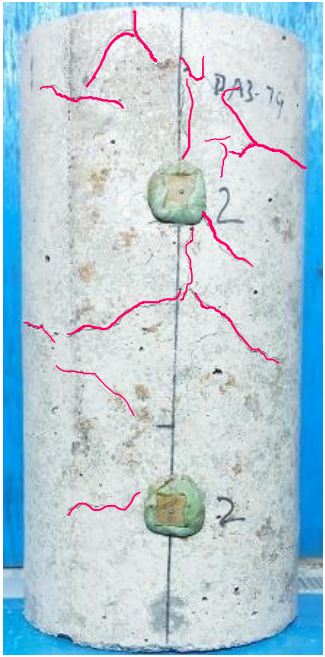
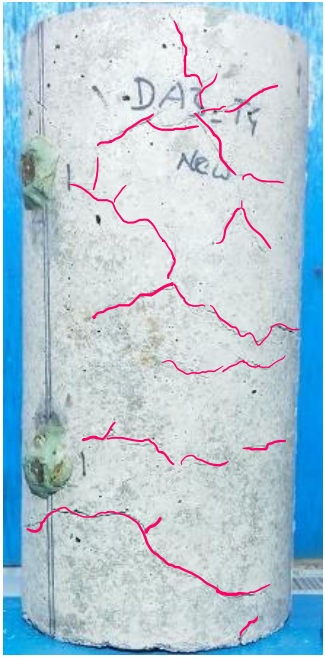
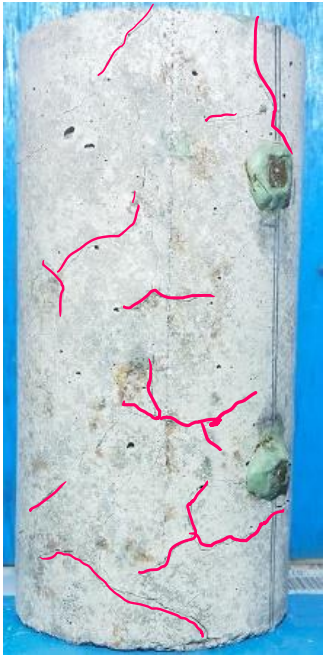
DEF 1	View 1	View 2	View 3
			

DEF 2	View 1	View 2	View 3
			

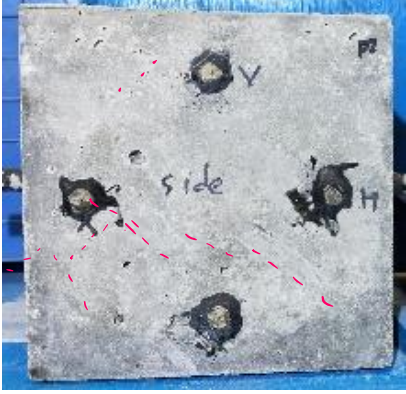
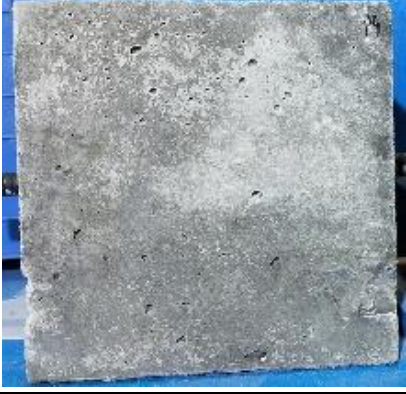
DEF 3	View 1	View 2	View 3
			

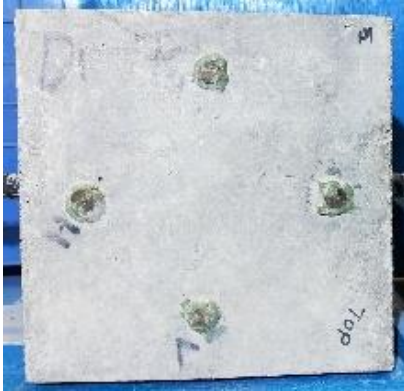
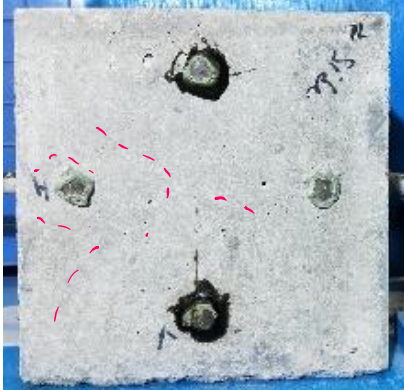
DA1	View 1	View 2	View 3
			

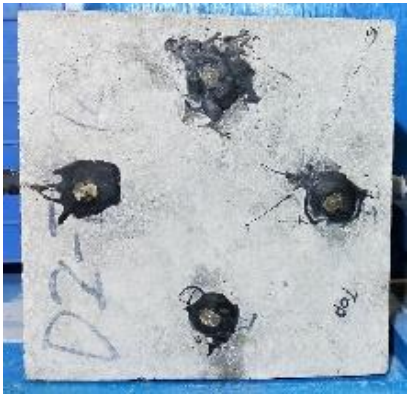
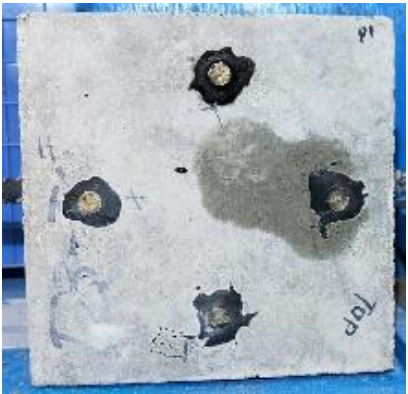
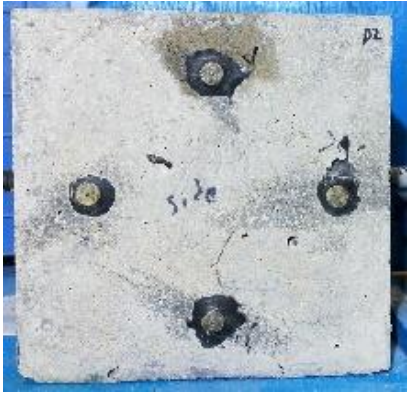
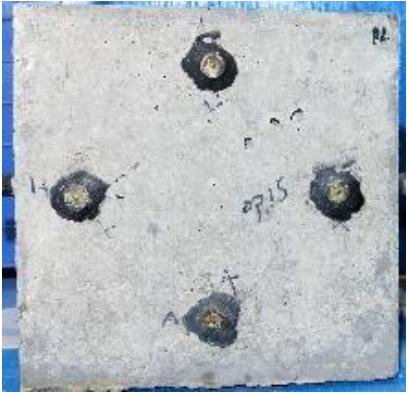
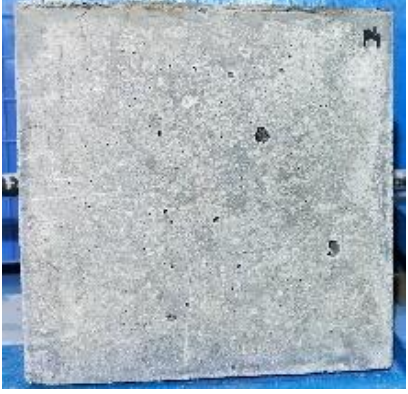
DA 2	View 1	View 2	View 3
			

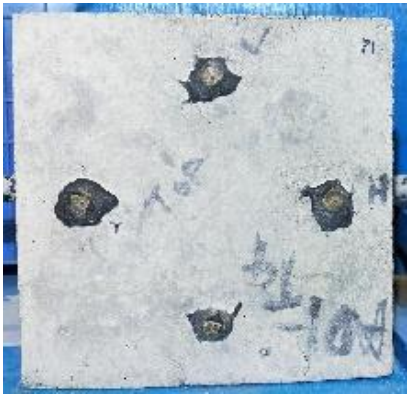
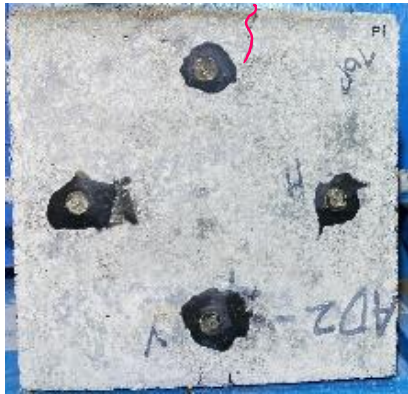
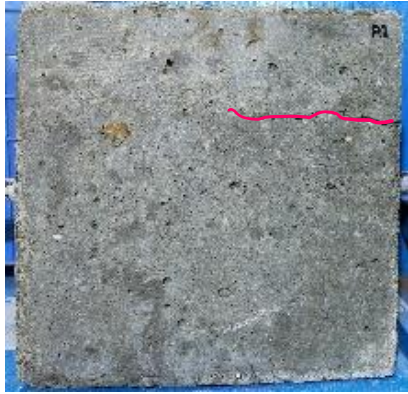
DA 3	View 1	View 2	View 3
	 <p>View 1 shows a concrete cylinder with two green sensors. Red lines mark cracks. Handwritten text includes "DA3-79" at the top and the number "2" next to each sensor.</p>	 <p>View 2 shows a concrete cylinder with two green sensors. Red lines mark cracks. Handwritten text includes "DA3-79" and "New" near the top.</p>	 <p>View 3 shows a concrete cylinder with two green sensors. Red lines mark cracks.</p>

Pull out specimens (at 150 days)

	ASR 1	ASR 2
Side 1		
Side 2		
Side 3		
Side 4		

Side	ASR 3	DEF 1
Side 1		
Side 2		
Side 3		
Side 4		

Side	DEF 2	DEF 3
Side 1		
Side 2		
Side 3		
Side 4		

Side	DA1	DA2
Side 1		
Side 2		
Side 3		
Side 4		

Side	DEF 03
Side 1	
Side 2	
Side 3	
Side 4	

E. Alternate analysis of prism based on random nodes

In Chapter 7, the edge of prisms were used as fixed boundary. However, in reality the evolution of expansive by ASR and DEF is not uniform across the specimen causing non-uniform cracking. To capture such physical behaviour, an alternative method is proposed in this Appendix. It is done by simulating the expansion by randomly selecting about 1% of node points and setting them as fixed. Using the same parameters given in Table 7-1 expansion was calculated.

The result of simulation for the expansion of unreinforced ASR and DEF (shown in Figure E1) is shown in Figure E2 and E3 respectively. Similar to the observation made in Chapter 7, the parameters used for simulation of unreinforced specimen had to be recalibrated to simulate the reinforced concrete. The stress and strain in ASR and DEF specimen at the age of 150 days are shown in Figure E4 and Figure E5 respectively. Similar to the real specimen, the potential crack location is randomly distributed. The map cracking pattern, however, was not distinctly visible in the simulation. This should be refined in the future study.

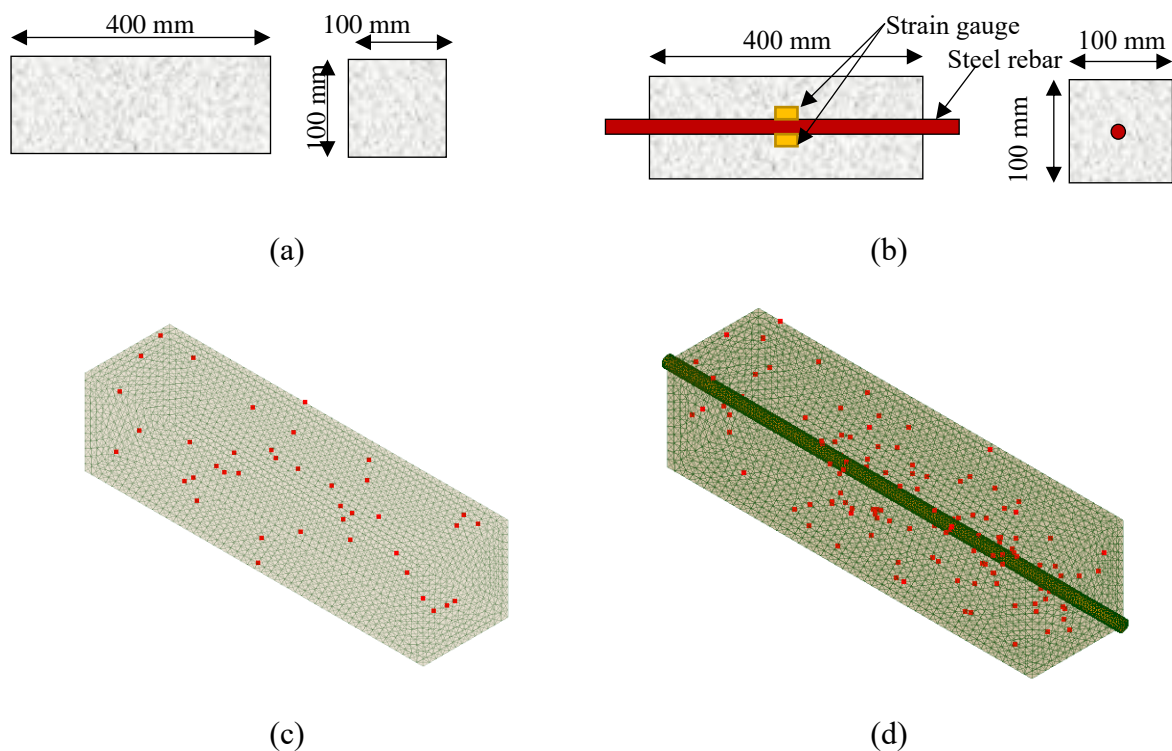


Figure E1 (a) Unreinforced prism, (b) Reinforced prism, (c) and (d) random nodes (in red) that were set fixed for FEM analysis

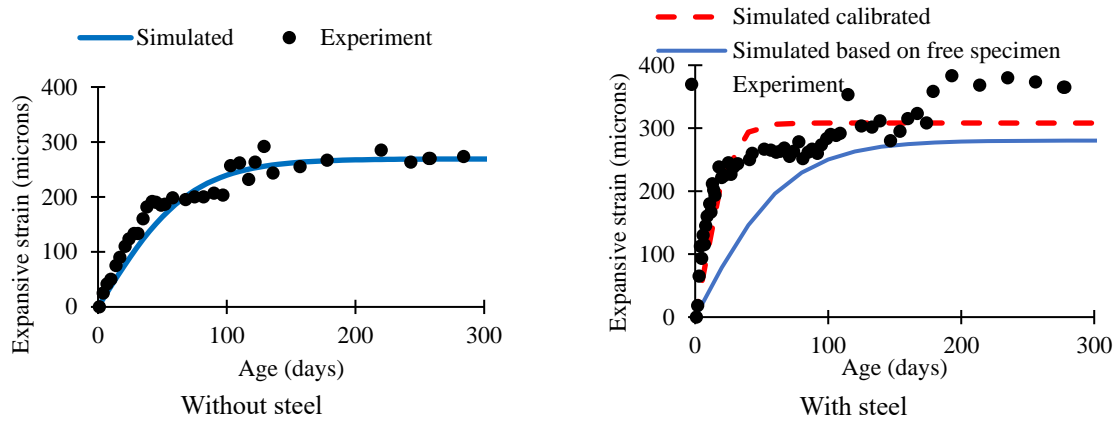


Figure E2 Evolution of free expansion of ASR infected concrete with and without reinforcement

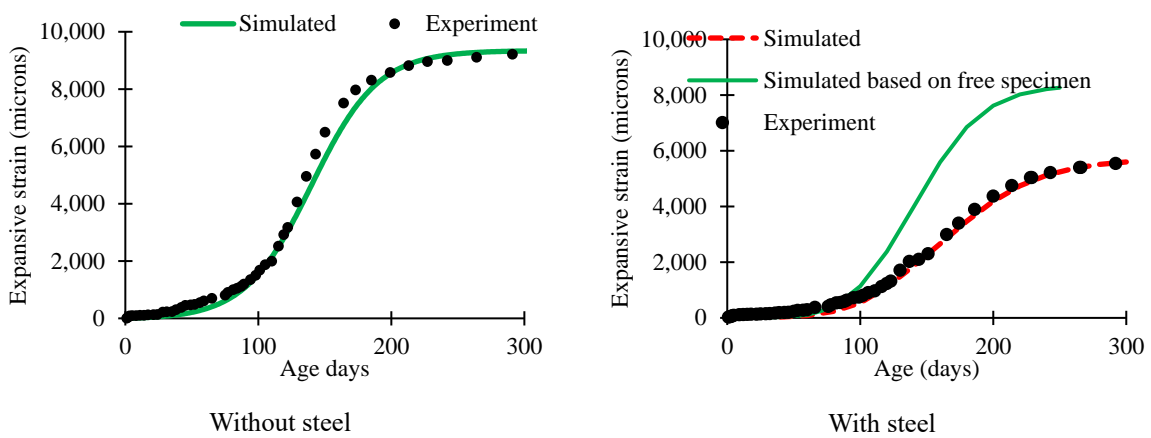


Figure E3 Evolution of free expansion of DEF infected concrete with and without reinforcement

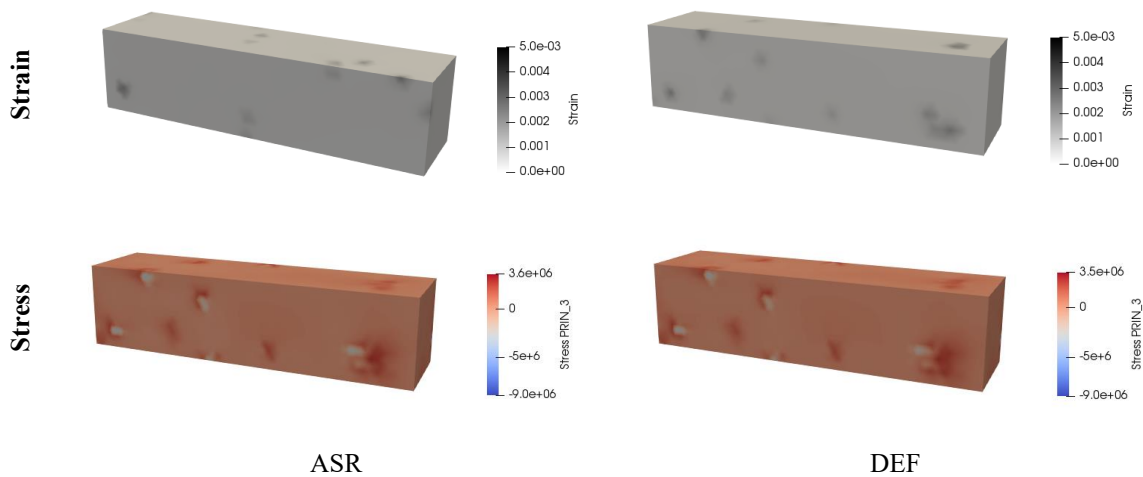


Figure E4 Evolution of principal strain at the age of 150 days for free specimen

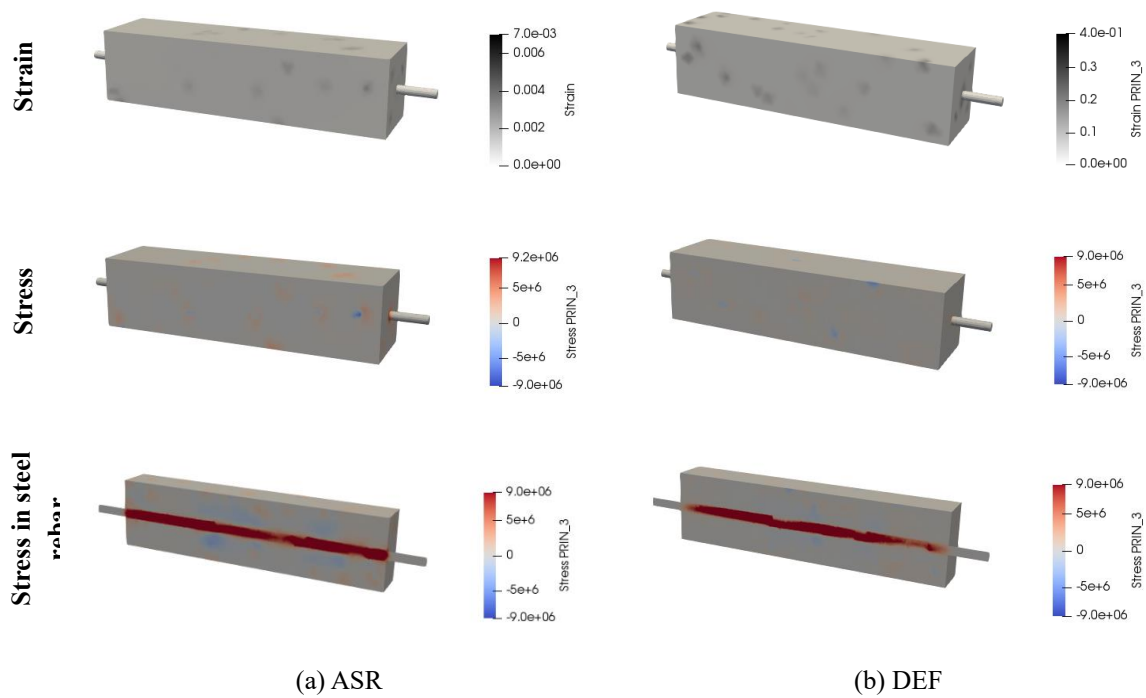


Figure E5 Evolution of principal strain at the age of 150 days for reinforced specimen

F. Sample script of Code-Aster used in Chapter 8

Stage 1: Expansion simulation

```
DEBUT(LANG='EN')

mesh = LIRE_MALLAGE(FORMAT='MED',
    UNITE=20)

modelT = AFFE_MODELE(AFFE=_F(MODELISATION=('3D', ),
    PHENOMENE='THERMIQUE',
    TOUT='OUI'),
    MAILLAGE=mesh)

modelM = AFFE_MODELE(AFFE=_F(MODELISATION=('3D', ),
    PHENOMENE='MECANIQUE',
    TOUT='OUI'),
    MAILLAGE=mesh)

listr = DEFI_LIST_REEL(DEBUT=0.0,
    INTERVALLE=_F(JUSQU_A=400.0,
    PAS=1.0))

fEij = DEFI_FONCTION(NOM_PARA='TEMP',
    NOM_RESU='fEij',
    PROL_DROITE='LINEAIRE',
    PROL_GAUCHE='LINEAIRE',
    VALE=(0.0, 34545098469.0, --0.540675540644, *truncated*, 54.9993799737, 30503699999.9))

fEPSDo = DEFI_FONCTION(NOM_PARA='TEMP',
    PROL_DROITE='LINEAIRE',
    PROL_GAUCHE='LINEAIRE',
    VALE=(0.0, 0.000101572189438, 0.540675540644, 0.000101580361044, *truncated*, 54.9993799737,
    0.000110828365933))

fBeta = DEFI_CONSTANTE(NOM_RESU='fBeta',
    VALE=1.1)

fBT = DEFI_FONCTION(NOM_PARA='TEMP',
    PROL_DROITE='LINEAIRE',
    PROL_GAUCHE='LINEAIRE',
    VALE=(0.0, 9845.21457625, 0.540675540644, 9844.42258054, *truncated*, 54.9993799737, 9022.96078789))

fAT = DEFI_CONSTANTE(NOM_RESU='fAT',
    VALE=0.9)

fBC = DEFI_FONCTION(NOM_PARA='TEMP',
    PROL_DROITE='LINEAIRE',
    PROL_GAUCHE='LINEAIRE',
    VALE=(0.0, 1551.89054518, *truncated*, 54.9993799737, 1016.48061053))
```

```

fAC = DEFI_FONCTION(NOM_PARA='TEMP',
    PROL_DROITE='LINEAIRE',
    PROL_GAUCHE='LINEAIRE',
    VALE=(0.0, 1.28405751624, *truncated*, 54.9993799737, 0.815434987511))
fK = DEFI_CONSTANTE(NOM_RESU='fK',
    VALE=0.7)
fTheta = DEFI_FONCTION(NOM_PARA='INST',
    NOM_RESU='fTheta',
    PROL_DROITE='LINEAIRE',
    PROL_GAUCHE='LINEAIRE',
    VALE=(0.0, 0.0, 2.0, *truncated*, 804.0, 55.0))
fNU = DEFI_CONSTANTE(NOM_RESU='fNU',
    VALE=0.2)
fRHO = DEFI_CONSTANTE(NOM_RESU='fROH',
    VALE=2480.0)
fAlpha = DEFI_CONSTANTE(NOM_RESU='fAlpha',
    VALE=3.2e-05)
concrete = DEFI_MATERIAU(ELAS_FO= _F(ALPHA=fAlpha,
    E=fEij,
    NU=fNU,
    RHO=fRHO,
    TEMP_DEF_ALPHA=0.0),
    MAZARS_FO= _F(AC=fAC,
    AT=fAT,
    BC=fBC,
    BT=fBT,
    EPSD0=fEPSDo,
    K=fK),
    THER= _F(LAMBDA=1.75,
    RHO_CP=750.0))
affeT = AFFE_MATERIAU(AFFE= _F(MATER=(concrete, ),
    TOUT='OUI'),
    MODELE=modelT)
loadT = AFFE_CHAR_THER_F(MODELE=modelT,
    TEMP_IMPO= _F(TEMP=fTheta,
    TOUT='OUI'))
fixM = AFFE_CHAR_MECA(DDL_IMPO= _F(GROUP_NO=('Group_fixNodes', ),
    LIAISON='ENCASTRE'),

```

```

MODELE=modelM)
resuT = THER_LINEAIRE(CHAM_MATER=affeT,
    EXCIT=_F(CHARGE=loadT),
    INCREMENT=_F(LIST_INST=listr),
    MODELE=modelT)
affeM = AFFE_MATERIAU(AFFE=_F(MATER=(concrete, ),
    TOUT='OUI'),
    AFFE_VARC=_F(EVOL=resuT,
        NOM_CHAM='TEMP',
        NOM_VARC='TEMP',
        PROL_DROITE='LINEAIRE',
        PROL_GAUCHE='LINEAIRE',
        VALE_REF=0.0),
    MODELE=modelM)
resuMNL = STAT_NON_LINE(CHAM_MATER=affeM,
    COMPORTEMENT=_F(RELATION='MAZARS'),
    CONVERGENCE=_F(ARRET='NON',
        ITER_GLOB_ELAS=50,
        ITER_GLOB_MAXI=50,
        RESI_GLOB_RELA=0.0001),
    EXCIT=_F(CHARGE=fixM),
    INCREMENT=_F(LIST_INST=listr),
    METHODE='NEWTON',
    MODELE=modelM,
    NEWTON=_F(MATRICE='ELASTIQUE',
        PREDICTION='TANGENTE'))
resuMNL = CALC_CHAMP(reuse=resuMNL,
    CONTRAINTE=('SIGM_NOEU', ),
    CRITERES=('EPEQ_NOEU', 'SIEQ_NOEU'),
    DEFORMATION=('EPSI_NOEU', ),
    RESULTAT=resuMNL,
    VARI_INTERNE=('VARI_NOEU', ))
tabObsN = POST_RELEVE_T(ACTION=_F(GROUP_NO=('Group_topNode', ),
    INTITULE='deplz1',
    NOM_CHAM='DEPL',
    NOM_CMP=('DZ', ),
    OPERATION=('EXTRACTION', ),
    RESULTAT=resuMNL),

```

```

_F(GROUP_NO=('Group_bottomNode' ,),
  INTITULE='DEPLZ2',
  NOM_CHAM='DEPL',
  OPERATION=('EXTRACTION' ,),
  RESULTANTE=('DZ' ,),
  RESULTAT=resuMNL)))
tabStrm = POST_RELEVE_T(ACTION=( _F(GROUP_NO=('Group_midNode' ,),
  INTITULE='stressZ',
  NOM_CHAM='SIGM_NOEU',
  NOM_CMP=('SIZZ' ,),
  OPERATION=('EXTRACTION' ,),
  RESULTAT=resuMNL),
_F(GROUP_NO=('Group_midNode' ,),
  INTITULE='StrainZ',
  NOM_CHAM='EPSI_NOEU',
  NOM_CMP=('EPZZ' ,),
  OPERATION=('EXTRACTION' ,),
  RESULTAT=resuMNL)))
IMPR_RESU(FORMAT='MED',
  RESU=( _F(RESULTAT=resuT),
  _F(RESULTAT=resuMNL)),
  UNITE=4)
IMPR_TABLE(FORMAT='TABLEAU',
  SEPARATEUR=';',
  TABLE=tabObsN,
  UNITE=5)
IMPR_TABLE(FORMAT='TABLEAU',
  SEPARATEUR=';',
  TABLE=tabStrm,
  UNITE=3)
FIN()

```

Stage 2: Compression simulation

```
DEBUT(LANG='EN')
mesh = LIRE_MALLAGE(FORMAT='MED',
    UNITE=3)
modelM = AFFE_MODELE(AFFE=_F(MODELISATION=('3D', ),
    PHENOMENE='MECANIQUE',
    TOUT='OUI'),
    MAILLAGE=mesh)
concrete = DEFI_MATERIAU(ELAS=_F(E=30700000000.0,
    NU=0.2),
    MAZARS=_F(AC=0.812,
    AT=0.9,
    BC=1016.0,
    BT=9062.67,
    EPSD0=0.00011,
    K=0.7))
affeM = AFFE_MATERIAU(AFFE=_F(MATER=(concrete, ),
    TOUT='OUI'),
    MODELE=modelM)
listr = DEFI_LIST_REEL(DEBUT=0.0,
    INTERVALLE=_F(JUSQU_A=1.0,
    NOMBRE=200))
fload = DEFI_FONCTION(NOM_PARA='INST',
    PROL_DROITE='LINEAIRE',
    PROL_GAUCHE='LINEAIRE',
    VALE=(0.0, 0.0, 1.0, 1.0))
fixM = AFFE_CHAR_MECA(DDL_IMPO=_F(GROUP_MA=('Group_bottomFace', ),
    LIAISON='ENCASTRE'),
    MODELE=modelM)
load = AFFE_CHAR_MECA(DDL_IMPO=_F(DZ=-0.005,
    GROUP_MA=('Group_topface', )),
    MODELE=modelM)
resuMNL = STAT_NON_LINE(AFFICHAGE=_F(INFO_RESIDU='OUI'),
    ARCHIVAGE=_F(PAS_ARCH=1),
    CHAM_MATER=affeM,
    COMPORTEMENT=_F(RELATION='MAZARS'),
    CONVERGENCE=_F(ARRET='NON',
    ITER_GLOB_ELAS=100,
```

```

ITER_GLOB_MAXI=20,
RESI_GLOB_RELA=0.0001),
EXCIT=(_F(CHARGE=fixM),
_F(CHARGE=load,
FONC_MULT=fload)),
INCREMENT=_F(LIST_INST=listr),
METHODE='NEWTON',
MODELE=modelM,
NEWTON=_F(MATRICE='ELASTIQUE',
PREDICTION='TANGENTE'))
resuMNL = CALC_CHAMP(reuse=resuMNL,
CONTRAINTE=('SIGM_NOEU', ),
CRITERES=('EPEQ_NOEU', 'SIEQ_NOEU'),
DEFORMATION=('EPSI_NOEU', ),
FORCE=('REAC_NODA', ),
RESULTAT=resuMNL,
VARI_INTERNE=('VARI_NOEU', ))
tabObsN = POST_RELEVE_T(ACTION=( _F(GROUP_NO=('Group_topNode', ),
INTITULE='deplz1',
NOM_CHAM='DEPL',
NOM_CMP=('DZ', ),
OPERATION=('EXTRACTION', ),
RESULTAT=resuMNL),
_F(GROUP_NO=('Group_bottomNode', ),
INTITULE='deplz2',
NOM_CHAM='DEPL',
OPERATION=('EXTRACTION', ),
RESULTANTE=('DZ', ),
RESULTAT=resuMNL)))
tabStrn = POST_RELEVE_T(ACTION=( _F(GROUP_NO=('Group_midNode', ),
INTITULE='stressz',
NOM_CHAM='SIGM_NOEU',
NOM_CMP=('SIZZ', ),
OPERATION=('EXTRACTION', ),
RESULTAT=resuMNL),
_F(GROUP_NO=('Group_midNode', ),
INTITULE='strainZ',
NOM_CHAM='EPSI_NOEU',

```

```

    NOM_CMP=('EPZZ', ),
    OPERATION=('EXTRACTION', ),
    RESULTAT=resuMNL),
_F(GROUP_NO=('Group_bottomFaceNodes', ),
    INTITULE='reaction',
    NOM_CHAM='REAC_NODA',
    OPERATION=('EXTRACTION', ),
    RESULTANTE=('DZ', ),
    RESULTAT=resuMNL)))
IMPR_RESU(FORMAT='MED',
    RESU=_F(RESULTAT=resuMNL),
    UNITE=80)
IMPR_TABLE(FORMAT='TABLEAU',
    SEPARATEUR=',',
    TABLE=tabObsN,
    UNITE=2)
IMPR_TABLE(FORMAT='TABLEAU',
    SEPARATEUR=',',
    TABLE=tabStrn,
    UNITE=4)
FIN()

```

G. List of some infrastructures infected by internal expansion reaction

SN	Location	Structure	Year of Construction	Date of Expansion noticed	Problems
1	Pakistan	Warsak GS dam	1960	1970s	Deformation and cracking in the powerhouse structure
2	India	Hirakud (Orissa) dam	1957	1973	Snapping of bolts at sluice gate roller tracks, deflection of sidewalls of the adit gallery
3	India	Powerhouse of Rihand Dam (U.P.)	1962	1987	Misalignment of machinery, difficulties in the operation of gates, cranes and passenger lifts. The rotor assembly sunk and there was a horizontal displacement of 3 cm at crane level
4	Canada	Mactaquac gravity intake	1967	1970s	Diagonal cracking in end pier
5	Canada	Mactaquac GS	1968	1970s	Loss of spillway gate clearances
6	Canada	Mactaquac GS	1969	1970s	Opening of the longitudinal vertical crack in the powerhouse Diagonal cracks in intake and draft tube piers
7	Canada	La Tuque dam	1940	1992	Cracking at the junction of gravity dam with intake
8	Canada	Otto Holden dam	1952	1970	Reduction of runner clearance Misalignment of turbine/generator assembly Misalignment of crane rails
9	USA	Center Hill dam	1948	1974	Loss of shear strength of horizontal lift joints
10	USA	Fontana dam	1946	1970	Cracking at curved section due to longitudinal expansion
11	USA	Copper basin	1938	1950	Upstream deformation and diagonal cracking near abutment
12	USA	Owyhee	1932	1948	Horizontal cracks at lift joints
13	USA	Center Hill dam – spillway	1948	1967	Loss of spillway gate clearances
14	USA	Chickamauga dam – spillway	1940	1964	Loss of spillway gate clearances
15	USA	Hiwassee dam	1940	1949	Impacts on gate clearances
16	USA	Terry lock dam	1969	2004	Severe cracking of piers
17	USA	Stewart Mountain	1930	1943	Minor crack and deflection
18	USA	Seminole	1939	1970	Horizontal and diagonal cracks in the downstream face

SN	Location	Structure	Year of Construction	Date of Expansion noticed	Problems
19	USA	Friant	1942		Damage in crest, spillway, walls and gallery
20	USA	Roanoke Rapid	1955	1995	Problem in spillway gate Misalignment of powerhouse Leakage in gallery
21	USA	Santeetlah	1927	1938	Surface cracking Displacement of arch and thrust block
22	Brazil	Moxoto	1977	1979	Cracks in wall and slab Stress accumulation in turbine parts
23	Brazil	Pedra	1968	1991	Map cracking Lateral thrust on end pillars cause the operating problem
24	Brazil	Billings-Pedra	1936	1992	Operation problem in the flood gate Surface cracking even after repair
25	Brazil	Furnas	1963	1970	Crack in spillway and powerhouse
26	Zimbabwe/Zambia	Kariba	1959	1983	Body, spillway sluice Concerns with stop-log and vertical gate guide integrity
27	Mozambique	Cahora Bassa	1974	1994	Diagonal cracks on crown parts. Deformation of spillway gate supports
28	Uganda	Nalubaale	1954		Generator foundation, spiral casing in powerhouse showed severe cracks
29	South Africa	Kleinplass	1982		Swelling and carking at horizontal joints in the spillway section
30	South Africa	Kouga	1969	1972	Horizontal crack near crown
31	Angola	Matala Dam	1954		Deformation of spillway pier and gate pedestals
32	Nigeria	Asejiri dam	1968	1982	Loss of spillway gate clearances
33	Italy	Pantelessio		1955	Horizontal cracks in inspection gallery
34	Italy	Poglia dam	1950	1970s	Deformations at the junction with wing wall
35	Spain	San Estaban dam	1955	1970s	Movement and cracking of horizontal lift joints
36	Spain	Tavascan dam	1965	1975	Cracking of spillway piers
37	Portugal	Alto Ceira dam	1949	1953	Upstream deformations Diagonal cracking near abutments
38	Portugal	Pracana dam	1951	1950s	Horizontal cracks in the upstream face, cracks at heads of buttresses Diagonal cracks in buttresses
39	Switzerland	Salanfe dam	1953	1970s	Cracking at the bend in gravity dam segments

SN	Location	Structure	Year of Construction	Date of Expansion noticed	Problems
40	Switzerland	Illsee dam	1962	1970s	Horizontal cracking on the downstream face
41	Switzerland	Isola dam	1960	1978	Crack in central downstream face Crack in upstream face Crack in upper gallery
42	Switzerland	Salanfe	1953		Upstream movement Surface cracking in the downstream face and access gallery
43	France	Temple-sur-lot	1951	1960	Crack in spillway pier Difficulty in the operation of bulkhead gate Disruption of embedded parts
44	France	Chambon dam	1934	1952	Deformation and cracking at a curved section near abutment
45	Norway	Stolsvatn dam	1948		Extensive surface cracking leading to reinforcement corrosion